DEVELOPMENT OF A DEDICATED HYBRID K-EDGE DENSITOMETER FOR PYROPROCESSING SAFEGUARDS MEASUREMENTS USING MONTE CARLO SIMULATION MODELS

A Dissertation
Presented to
The Academic Faculty

by

George Spencer Mickum

In Partial Fulfillment
of the Requirements for the Degree
Doctor of Philosophy in the
School of Mechanical Engineering
Nuclear and Radiological Engineering Program

Georgia Institute of Technology
December 2015

DEVELOPMENT OF A DEDICATED HYBRID K-EDGE DENSITOMETER FOR PYROPROCESSING SAFEGUARDS MEASUREMENTS USING MONTE CARLO SIMULATION MODELS

Approved by:

Dr. Nolan Hertel, Advisor
School of Mechanical Engineering,
Nuclear and Radiological Engineering Program
Georgia Institute of Technology

Dr. Adam Stulberg
School of International Affairs
Georgia Institute of Technology

Dr. Chaitanya Deo
School of Mechanical Engineering,
Nuclear and Radiological Engineering Program
Georgia Institute of Technology

Dr. Franklin DuBose
School of Mechanical Engineering,
Nuclear and Radiological Engineering Program
Georgia Institute of Technology

Dr. Anna Erickson
School of Mechanical Engineering,
Nuclear and Radiological Engineering Program
Georgia Institute of Technology

Dr. Robert McElroy
Nuclear Security and Isotope Technology Division
Oak Ridge National Laboratory

Date Approved: October 8, 2014

To my wife, Megan:
If I am the cup, then she is the water that fills the empty space inside.

ACKNOWLEDGEMENTS

I would like to start by thanking my advisor, Dr. Nolan Hertel, whose ability to combine patience, support and encouragement have tremendously assisted me during the development of my dissertation and the development of myself. His technical and academic guidance has been invaluable. I count myself very lucky to have worked with and learned from him during my time as a graduate student. In addition I have to thank Dr. Robert McElroy, who served as my co-advisor on my dissertation. I have been amazed by his knowledge and have greatly benefited from many conversations with him balancing physics, mathematics, and engineering. I am a better engineer today due in considerable part to his mentoring.

Special words of thanks are due to my dissertation advisors Dr. Chaitanya Deo, Dr. Anna Erickson, Dr. Adam Stulberg, and Dr. Franklin DuBose for giving their advice and being part of my dissertation committee. I am very grateful for their guidance throughout the duration of my academic and research endeavors in graduate school.

I would like to thank Trond Bjornard for being my mentor and friend at the outset of my work in research, and for nurturing my interest in the field of nuclear safeguards. The encouragement and help I received throughout my graduate career from Shaheen Dewji was to such a great extent that thanks alone could never suffice, so chocolate was required. I would also like to thank the support I received from Dr. Stephen Croft, Steve Cleveland, and Tyler Guzzardo at Oak Ridge National Laboratory for their support and help with planning and setting up experiments on the ORNL HKED.

TABLE OF CONTENTS

LIST OF TABLES

LIST OF FIGURES

LIST OF SYMBOLS AND ABBREVIATIONS

Am	Americium
ANM	Alternate Nuclear Material
CAD	Computer Assisted Design
Cm	Curium
DA	Destructive Assay
EBR-II	Experimental Breeder Reactor - II
ER	Electrorefiner
FWHM	Full Width at Half Maximum
HKED	Hybrid K-Edge Densitometer
HPGe	High Purity Germanium
IAEA	International Atomic Energy Agency
ICP-MS	Inductively Coupled Plasma – Mass Spectrometry
IDMS	Isotope Dilution Mass Spectrometry
INL	Idaho National Laboratory
IFR	Integral Fast Reactor
KAERI	Korean Atomic Energy Research Institute
KED	K-Edge Densitometry
Kr	Krypton
LCC	Liquid Cadmium Cathode
LEGe	Low Energy Germanium
LWR	Light Water Reactor
MCNP	Monte Carlo N-Particle code

MOX	Mixed Oxide Fuel
MUF	Material Unaccounted For
NDA	Non-Destructive Assay
NIST	National Institute of Standards and Technology
NNWS	Non-Nuclear Weapons State
Np	Neptunium
ORNL	Oak Ridge National Laboratory
PUREX	Plutonium URanium EXtraction
Pu	Plutonium
REDC	Radiochemical Engineering Development Complex
ROK	Republic of Korea
SQ	Significant Quantity
TRU	Transuranic
U	Uranium
UNF	Used nuclear fuel
Xe	Xenon
XRF	X-Ray Fluorescence

SUMMARY

Pyroprocessing is an electrochemical method for recovering actinides from used nuclear fuel and recycling them into fresh nuclear fuel. It is posited herein that proposed safeguards approaches on pyroprocessing for nuclear material control and accountability face several challenges due to the unproven plutonium-curium inseparability argument and the limitations of neutron counters. Thus, the Hybrid K-Edge Densitometer is currently being investigated as an assay tool for the measurement of pyroprocessing materials in order to perform effective safeguards. This work details the development of a computational model created using the Monte Carlo N-Particle code to reproduce HKED assay of samples expected from the pyroprocesses. The model incorporates detailed geometrical dimensions of the Oak Ridge National Laboratory HKED system, realistic detector pulse height spectral responses, optimum computational efficiency, and optimization capabilities. The model has been validated on experimental data representative of samples from traditional reprocessing solutions and then extended to the sample matrices and actinide concentrations of pyroprocessing. Data analysis algorithms were created in order to account for unsimulated spectral characteristics and correct inaccuracies in the simulated results. The realistic assay results obtained with the model have provided insight into the extension of the HKED technique to pyroprocessing safeguards and reduced the calibration and validation efforts in support of that design study. Application of the model has allowed for a detailed determination of the volume of the sample being actively irradiated as well as provided a basis for determining the matrix effects from the pyroprocessing salts on the HKED assay spectra.

CHAPTER 1

INTRODUCTION

Pyroprocessing is an electrochemical method for recovering actinides from both oxide and metallic used nuclear fuel (UNF) for further use as burnable fuel in fast reactors. Given rising global interest in recycling used nuclear fuel with electrometallurgical reprocessing, or pyroprocessing, efforts to prepare appropriate safeguards strategies for future pyroprocessing facilities have begun. Pyroprocessing presents a unique challenge to traditional safeguards techniques due to the nature of the process and the harsh environment in which it takes place. Thus both timely and robust accountancy approaches are being investigated that may be effective under such an environment. One such approach is a plan to develop the hybrid K-edge densitometer (HKED) instrument to extend it to safeguards assay of pyroprocessing materials.

Oak Ridge National Laboratory is home to a hybrid K-edge densitometry system, which may be used to support safeguards verification measurements during pyroprocessing activities for nuclear material accountancy. The feasibility and role of the HKED for pyroprocessing safeguards measurements has not yet been established, and several technological and practical challenges need to be addressed. Transition to using the HKED will depend on simulations that could assist in the extension of this assay method to predict the detector response to the new sample types and configurations. The limited availability of representative solution standards expected from pyroprocessing molten salts have spurred efforts to develop a Monte Carlo model to facilitate algorithm development and optimize the measurement configuration of the HKED system.

The goal of this work was to develop a model using the Monte Carlo N-Particle (MCNP) code that incorporated detailed geometrical dimensions of the HKED, realistic detector response tallies, optimum computational efficiency, and optimization capabilities to be able to reproduce the resultant HKED assay of samples expected from the pyroprocesses. To ensure the fidelity of the MCNP model, the model was validated against experimental data of representative samples from traditional sample solutions before extending the model to pyroprocessing samples. An assessment of the underlying physics models and data libraries of MCNP was performed to ascertain the validity of the generated x-ray fluorescence and K-edge spectral results. A post-processing algorithm to modify the simulated data was required to correct for several deficiencies of the model.

Analysis was undertaken to investigate any potential biases originating from the extension of the simulation method beyond the known calibration range. Capabilities and limitations are discussed herein for extending the HKED system beyond aqueous solutions with uranium and plutonium ratios of 100:1 to include salt based samples from pyroprocessing where uranium and plutonium ratios approach 1:1. Completion of this study resulted in high confidence that the simulation provided realistic HKED assay results for materials with complex mixtures of pyroprocessing salts and actinide elements over a wide concentration range.

The finalized work provides the ability to examine the impact of actinide concentrations and ratios encountered with pyroprocessing sampling as well as assess the impact on the measurement from non-standard sample matrices and non-homogeneities. It presents an analysis of the impact on the assay results from spectral interferences due to matrix effects. Additionally, it offers a fully operational computational model as a means of determining the volume within the HKED sample where the K-edge x-rays are generated in order to optimize the sample vial size for pyroprocessing measurements. This work

constitutes a major advancement in support of the design study for optimizing the HKED instrument for safeguards assay of pyroprocessing material.

CHAPTER 2

PYROPROCESSING

2.1 Pyroprocessing Background

Pyroprocessing is an electrochemical method for recovering actinides from both oxide and metallic used nuclear fuel (UNF) for further use as burnable fuel in fast reactor design concepts, potentially in the Generation IV set of fast reactors [1, 2]. The separation of actinides from fission products in UNF leads to the capability of fabricating recycled fuel useable in advanced nuclear reactors. Such fuel is capable of burning long-lived actinides thereby reducing their overall inventory in UNF. Pyroprocessing enables closing the nuclear fuel cycle with the use of a proliferation-resistant process while reducing the quantity of waste at commercial nuclear power plants and in repositories.

Pyroprocessing was first investigated in the 1950's and 1960's at Argonne National Laboratory as an alternative to the aqueous Plutonium URanium EXtraction (PUREX) process. The major drawbacks of PUREX are that its organic solvent had limited stability in the presence of strong ionizing radiation and it produced fully separated U and Pu streams [3, 4]. Pyroprocessing offered more reagent stability in high radiation fields, while retaining an inherently proliferation-resistant characteristic for producing Pu that always was comingled with U. In its initial stage, pyrochemical processing was developed to process recycle fuel-melt as part of the U.S. Integral Fast Reactor (IFR) program's Experimental Breeder Reactor II (EBR-II) program at Idaho National Laboratory (INL). The IFR program was canceled in 1994, but pyroprocessing work continued at the IFR's Fuel Conditioning Facility (FCF) and demonstrated robust proliferation resistant, highly efficient actinide recovery (99.9%) of uranium and uranium coupled with transuranics (U/TRU) [4, 5], and repository-extending waste minimization.

Currently, long-term storage of used nuclear fuel is being compared to strategies for conversion of the hazardous radionuclides into short-lived elements of smaller, more manageable sizes. The ongoing debate about the back end options for storing used nuclear fuel has spurred interest in the partitioning and transmutation (P&T) of the actinides within the fuel in order to lessen the expected storage time and minimize the amount of waste. Through this debate, the technology of pyroprocessing has been investigated as an approach to reprocess the used nuclear fuel while mitigating the concerns of putting separated plutonium into circulation. For the pyroprocessing technology to feasibly reduce the storage concerns for used nuclear fuel, it would need to be coupled with a fleet of fast reactors serving as the transmutation component for P&T of the actinides. Moreover, even assuming that the proliferation concerns of separated plutonium can be decreased, the economics have not been proven to favor reprocessing over long-term repository storage.

Although various countries have explored pyroprocessing extensively (including the United States, Republic of Korea, Russia, India, and Japan), development of a full-scale facility is still in its infancy. Currently, efforts are at the prototype stage with several proposals in the works for full-scale facilities [6-8]. Notably, the Korea Atomic Energy Research Institute (KAERI) has been developing pyroprocessing technology for the Pyroprocess Integrated Inactive Demonstration (PRIDE) and Engineering Scale Pyroprocess Facility (ESPF) [8] in order to develop an indigenous capability acceptable to the global community from a nonproliferation standpoint. Notable work has been accomplished by the KAERI as part of their effort to reduce their reliance on long-term storage of the domestic used nuclear fuel. Current cooperation between the Republic and Korea and the United States in the form of an ongoing joint fuel-cycle study is looking to

quantify the likelihood of pyroprocessing being safely and securely industrialized within the safeguarding requirements of the International Atomic Energy Agency (IAEA).

The largest development of pyroprocessing technologies is coming out of Russia, where they are developing a closed fuel cycle set to be fully implemented by 2020 coupling fast reactor fuels with a unique approach to pyroprocessing that will accept oxide-matrix fuels directly to the electrorefiner [9]. Testing on non-aqueous reprocessing methods began back in the early 1960s at the Research Institute of Atomic Reactors (RIAR) in Dimitrovgrad with the goal of developing the closed fuel cycle for the fast breeder reactor. Today, the Dimitrovgrad Dry Process developed at RIAR under the DOVITA programme (Dry reprocessing, Oxide fuel, Vibropac, Integral, Transmutation of Actinides) is a cornerstone of the Strategy of Nuclear Power Development in Russia in the First Half of the 21st Century [10]. Additional interest in pyroprocessing has been displayed by France, the United Kingdom, and China, where alternating levels of investigations are presently ongoing.

Although yet to be demonstrated on a large scale, laboratory-scale and engineering-scale development has highlighted several reasons countries find pyroprocessing attractive. The storage size of used nuclear fuel and the time needed to keep it in a repository are both reduced through a pyroprocessing facility coupled with a fast reactor. The batch process is capable of fabricating a comingled uranium-plutonium product, constituting a major reason some countries are approaching such an immature technology, compared to mature approaches such as PUREX. The replacement of aqueous and organic process materials with molten salt materials that do not efficiently moderate neutrons leads to improved criticality safety and the replacement of miles of tubing with an inline batch process may prove to have appreciable economic benefits.

The fundamental principle driving pyroprocessing is the exploitation of the difference in the Gibbs free energies between fission products and actinides. Separation is possible by applying an electrochemical potential to metallic or oxide-reduced UNF to separate constituent species of fission products and actinides in a molten salt medium. Pyroprocessing is more compact than its aqueous counterparts (PUREX), opening the possibility of recycling UNF on the reactor site and negating issues associated with spent fuel security, storage and long-term high-level waste. Pyroprocessing is conducted in a highly shielded hot cell facility under inert atmospheric conditions. The process occurs under high-temperature conditions and can be applied to high burn-up fuel with little cooling time. Compared to PUREX, which operates in continuous mode in an aqueous medium, pyroprocessing is a dry process, which operates in batch-mode.

Two types of pyroprocessing have been proposed [6]:

1) Metal oxide refining in a fluoride or chloride media; and
2) Oxide electrorefining via a chloride media.

Pyroprocessing is applied more readily to metallic rather than oxide fuels since the original process developed at the IFR was intended for metallic UNF from fast reactors. Additional processing steps are required for oxide fuels in preparation for electrorefining, as shown in Figure 2.1. Oxide fuel must first be converted to elemental form before separation of fission products and actinides can occur in the electrorefiner. The oxide reduction process involves several stages as shown in Figure 2.2.

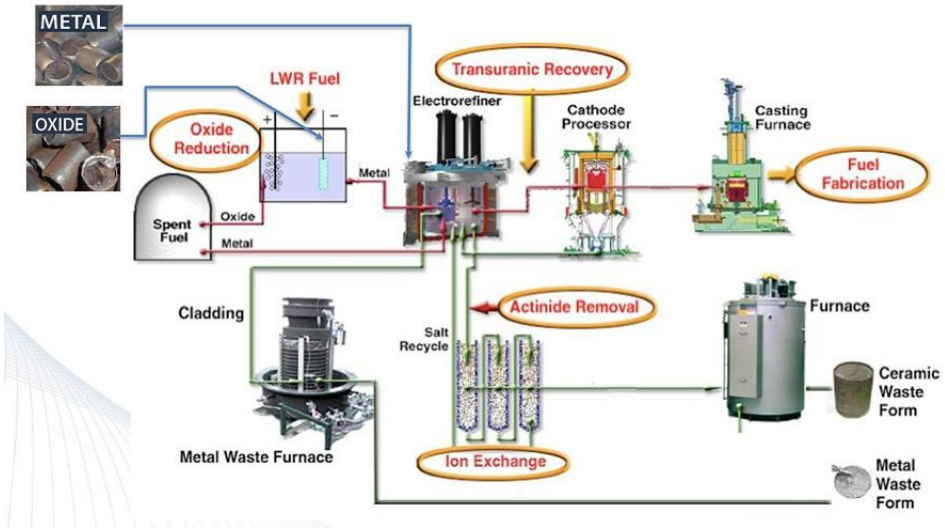

Figure 2.1. Pyroprocessing treatment of used nuclear fuel.

Reproduced from [11].

However, the current research efforts in Russia plan to avoid the oxide reduction process entirely and input an oxide form directly into the electrorefiner for reprocessing [9]. Thus the initial products of the electrorefining process are plutonium and uranium oxides in the form of powder. This output form benefits the Russian nuclear fuel cycle plans as it can be recycled into fuel pins using the vibropac process [9]. While this oxide method is planned for Russian development, the majority of the current pyroprocessing developments use the metallic method resulting in the need for voloxidation and electrolytic reduction to reduce oxides to metal form before input into the electrorefiner.

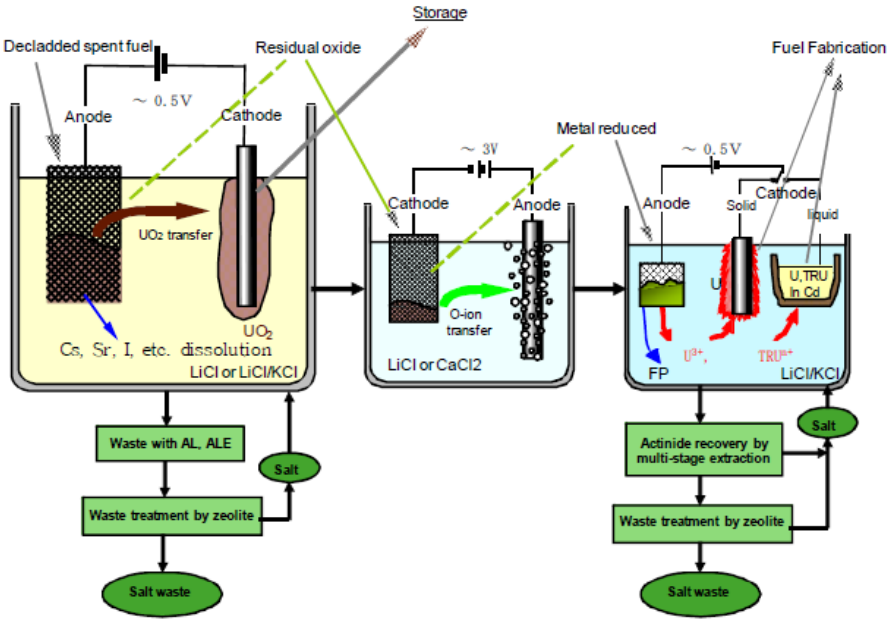

Figure 2.2. Pyroprocessing treatment of light water reactor oxide used nuclear fuel.

Reproduced from [6].

2.1.1 Fuel Decladding/Chopping (Metallic/Oxide)

Spent fuel assemblies are disassembled and sheared or mechanically chopped into short segments of about 2-5 cm that will fit in the electrorefiner or molten salt dissolver [5], then further undergoes a pulverization step to reduce the granular rubble into a fine grain powder. The fuel assembly hardware is transferred to metal waste processing while noble off-gasses from the fission products (Xe and Kr) are captured separately and directed into the respective waste stream. Iodine released at this stage can be captured in zeolite in preparation for waste storage. Oxide fuel must then undergo voloxidation in order to be converted to a metallic form, whereas metallic fuel from fast reactors is already in a suitable form to undergo electrorefining.

2.1.2 Voloxidation (Oxide)

Following decladding, oxide fuels are directed to a voloxidation process, where UO_2 is converted to U_3O_8, resulting in a homogeneous powder. This process increases the rate at which U_3O_8 is converted to metallic uranium by decreasing the density and increasing surface area of the fuel to increase the reaction rate over the larger surface area. The efficiency of the following reduction step is increased when the U_3O_8 solute is completely dissolved into the molten salt solvent. This dissolution can be accomplished when the fuel is crushed into a fine powder before introduction into the reduction vessel, the small surface area of the particles mitigates the formation of a metallic surface layer building up on the surface of the particles and hindering reduction of the inner area of the particle. Oxide fuel undergoes this voloxidation process via the following reaction:

$$3UO_2 + O_2 \rightarrow U_3O_8 \qquad \text{Equation 2.1}$$

Voloxidation consequently decreases the density of UO_2 of 11.0 g/cm^3 to U_3O_8 at 8.3 g/cm^3 [12]. Furthermore, gaseous fission products, such as tritium, krypton, iodine and xenon, in addition to some metal elements (cesium, technetium, etc.) are transformed into volatile oxides and removed via an off-gas system [12].

2.1.3 Electrolytic Reduction

The actinides and fission products from voloxidation must be reduced into metallic form prior to subsequent electrorefining. Over a decade ago, an electrochemical process was developed for converting these metal oxides to an elemental form through an electrolytic reduction process [5]. In electrolytic reduction, a LiCl-Li_2O molten salt at 650^{o}C serves as the electrolyte in an electrochemical cell. In this cell, the cathode is the oxide fuel powder with an inert anode of platinum or conductive ceramic spiral wound. As current is passed between the electrodes, electrons reduce the metal ions of the actinide and most

lanthanide oxides in the fuel to collect as base metals at the cathode. As depicted in Figure 2.3, oxide ions are released into the electrolyte and produce oxygen gas. Both calcium and lithium based systems were considered by researchers at the Central Research Institute of Electric Power Industry (CRIEPI) in Japan and Idaho National Laboratory with the calcium system operating at a higher temperature (800^{o}C) but with a more stable oxide ion than lithium. However, the lithium reducing system was favored based on its lower operating temperature and its compatibility with the electrorefining salt and has been adopted in the pilot Korean system.

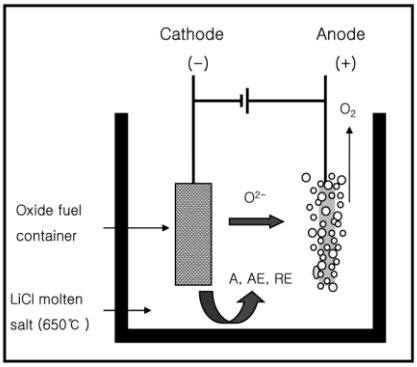

Figure 2.3. Electrolytic reduction of oxide fuel.

Reproduced from [12].

The following chemical reactions occur in electrolytic reduction for the metal ion *(M)* to be reduced [5] [12]:

Cathode Reaction:

$$Li^{+} + e^{-} \rightarrow Li \qquad \text{Equation 2.2}$$

$$M_xO_y(s) + 2y\ Li \rightarrow x\ M(s) + y\ Li_2O \qquad \text{Equation 2.3}$$

Anode Reaction:

$$2O^{2-} \rightarrow O_2(g) + 4e^- \qquad \text{Equation 2.4}$$

In addition, actinide oxides and most lanthanide oxides are reduced via LiCl to form Li_2O and metal chlorides. For example, the reaction with the cesium (Cs) fission product proceeds as follows:

$$Cs_2O + 2LiCl \rightarrow Li_2O + 2CsCl \qquad \text{Equation 2.5}$$

This reaction with Cs is important corresponding to the high capture of fission products in the electrolyte after the formation of highly stable chlorides such as CsCl.

The analytical results from electrolytic reduction runs at INL were acquired by extracting the post-run fuel and dissolving the fuel sample with elemental bromine in an ethyl acetate medium to separate the oxide and metallic fuel phases. Only preliminary results of the overall difference in weight percent between metal fuel and remaining oxide fuel were reported. Based on INL's experimental data, the yields from electrolytic reduction were as follows [13]:

Rare Earth:

- Nd: 36-43%
- Ce: 40-49%

Actinides:[1]

- U: 98-99%
- Pu: 93-96%

---

[1] Yields for ^{241}Am and ^{237}Np were obtained via Inductively Coupled Plasma Mass Spectrometry **(**ICP-MS). These isotopic values are the dominant forms of the elements' yield, as other isotopes have decayed away due to short half-lives.

- Pr: 38-47%
- Sm: 27-33%
- Y: 34-40%
- ^{237}Np: 97-98%
- ^{241}Am: 77-84%

The elements that do not collect on the solid cathode remain in the electrolyte, thus 60-66% of the yttrium is removed from the electrolyte during waste processing. The overall efficiency of this process is a 99.5% reduction yield with only 0.05% of the input uranium oxide not being reduced to metal and instead left in solution [14].

As a result, the bulk of actinides are deposited on the solid cathode, while the bulk of fission products remain in the salt and are consolidated to form a metallic waste. The fission products and a small amount of transuranics dissolved in the electrolyte form a solid matrix, which is hot pressed into a ceramic composite and eliminated as high-level waste. The bulk of the remaining LiCl-Li_2O remains in the electrolytic reduction cell for reuse. The cathodes from electrolytic reduction contain the bulk of metallic U, minor actinides and lanthanides, and metallic fission products, which are subsequently directed into an electrorefiner.

2.1.4 Electrorefining (Metallic)

At the heart of pyroprocessing is the electrorefining process. Historically, the electrorefiner developed at INL was the Mark IV refiner designed specifically for metallic spent fuel. The anode basket and cathode both rotated. With a single cathode and dual node anode assemblies, each anode was able to hold a batch size of 8 kg U [1] [15]. The successor to the Mark IV is the Mark V, which is capable of treating blanket fuel up to 5 MTHM/yr. The Mark V has four anode assemblies, each with a 37 kg U capacity. Electrorefining exploits differences in the Gibbs free energies of actinides and fission products to separate the constituent elements. The Gibbs free energy at 500^{o}C of fission

products (Cs, Y, etc.), which are relatively stable in the chloride salt phase, ranges from -87.8 to -65.1 kcal/mol (-367.4 to -272.4 kJ/mol); electrotransportable actinides (Pu, Np, U) range in free energy from -62.4 to -55.2 kcal/mol (-261.1 to -231.0 kJ/mol) [4]. The free energy of chlorides and fluoride formation with actinides (with respect to the applied potentials) is predicted by the Nernst equation, governing the distribution of species between liquid metal and the molten eutectic salt [1].

Electrorefining employs an electrochemical cell normally using LiCl-KCl eutectic salt (with UCl_3 added) and two cathodes employed sequentially in the process: a solid graphite cathode and a liquid cadmium (Cd) cathode; the system operates at 500°C[2] [14]. A mesh basket containing the metallic fuel from electrolytic reduction serves as the anode (Figure 2.4). As a small, negative electric potential (-1.4V) is applied between the anode and cathode, the uranium ions are transported as metal through the eutectic salt to the graphite cathode where they preferentially form metallic dendritic deposits, as shown in Figure 2.5. Only they deposit in quantity on the cathode because the higher stability (in Gibbs free energy) of the dissolved transuranic and rare earth chlorides prevents them from also reducing to metals on the cathode. Thus depending upon the free energies of the chloride formation, the active metals and fission products will stay as stable chlorides in the eutectic salt, to be electrotransported to the two cathodes, or remain oxidized as metals in the anode basket (Table 2.1).

[2] 650°C if the electrolyte is LiCl salt.

Table 2.1. Free Energies of Chloride Formation at 500 °C, - kcal/g-eq[3]

Elements that remain in salt (very stable chlorides)		Elements efficiently electrotransported		Elements that remain as metals (less stable chlorides)	
$BaCl_2$	87.9	$CmCl_3$	64.0	$ZrCl_2$	46.6
CsCl	87.8	$PuCl_3$	62.4	$CdCl_2$	32.3
RbCl	87.0	$AmCl_3$	62.1	$FeCl_2$	29.2
KCl	86.7	$NpCl_3$	58.1	$NbCl_5$	26.7
$SrCl_2$	84.7	UCl_3	55.2	$MoCl_4$	16.8
LiCl	82.5			$TcCl_4$	11.0
NaCl	81.2			$RhCl_3$	10.0
$CaCl_2$	80.7			$PdCl_2$	9.0
$LaCl_3$	70.2			$RuCl_4$	6.0
$PrCl_3$	69.0				
$CeCl_3$	68.6				
$NdCl_3$	67.9				
YCl_3	65.1				

Reproduced from [15].

2.1.4.1 Uranium and Plutonium Deposition

The actinides build up in the eutectic salt in the electrorefiner over time and uranium on the solid cathode is removed after each batch. This initial separation of uranium on the

[3] The term kcal/g-eq is to be read as kilocalories per mass in grams of the material interacting with one mole of electrons. For elements with a valence of one the mass is just the atomic weight in grams; for trivalent substances, uranium for example, the mass is one third of the atomic weight; and so on.

solid cathode is preferential due to the uranium chloride molecule undergoing more advantageous chemical reactions (uranium reduction at very low electric potential) in the molten salt then the other spent fuel ions with more stable chlorides. Upon depositing on the solid cathode, the other spent fuel ions immediately react with the uranium chloride remaining in the salt, causing electrodeposition of the uranium and the transport of the more stable ions back into the salt. The electrodeposition of the uranium on the solid cathode allows it to be selectively removed and over time this drawdown of uranium from the electrorefining vessel varies the actinide concentration and uranium to plutonium ratio in the salt. As the uranium concentration reduces in the eutectic salt, the reaction of plutonium chloride with uranium chloride begins to become significant – thereby commingling on the solid cathode. This contamination on the solid cathode by plutonium and other transuranics may be monitored through analysis of the uranium metal product deposited on the solid cathode or by cyclic voltammetry measurement of the actinide concentrations in the electrorefiner vessel. When the ratio of actinide molecules to uranium molecules in the eutectic salt exceeds four, the liquid cadmium cathode is introduced, electric potential is increased slightly, and actinides are deposited therein [15].

The ongoing drawdown of uranium and the subsequent buildup of TRU in the eutectic salt are important when considering the U to Pu ratios for TRU product removal since the uranium and plutonium chlorides in the salt are in constant dynamic flux. Any safeguards on the eutectic salt will need to be able to accommodate the wide expected ranges of U to Pu. The TRU product is not removed from the salt with the liquid Cd cathode until the plutonium contamination reaches equilibrium in the eutectic salt – occurring when the uranium chloride to plutonium chloride ratio reaches 1:4.1 [15]. This ratio corresponds to the equilibrium point when the rate of the forward reaction to preferentially deposit uranium on the solid cathode is equal to the rate of the reaction to deposit plutonium on

the solid cathode. At the equilibrium concentration ratio of 1:4.1 for UCl_3 to $PuCl_3$ in the eutectic salt, the U to Pu ratio in the liquid cadmium phase is 1:1.55 [15]. This U to Pu ratio in the cadmium of 1.55 is a factor of 2.56 less than the 4.1 ratio of plutonium chloride to uranium chloride highlighting the difficulty to remove a pure product. Thus the liquid cadmium cathode product will be degraded from the anode feed material by a considerable amount.

2.1.4.2 Electrowinning

Once most of the U has been removed from the salt, the solid cathode is replaced by the liquid Cd cathode (Figure 2.6), and the potential is increased to -1.8V [12]. Under these conditions, co-deposited U and TRU (Np, Pu, and Gd-Am) respectively begin to anodically dissolve and form transuranic chlorides in the electrolyte through an electrowinning process [5] [12]. The electrowinning process entails the removal of TRU deposits with a liquid cadmium cathode. Similarly, lanthanides anodically dissolve as soluble chlorides; however, this achieves poor separation of minor actinides and rare earth elements, since the cell is operated such that lanthanides are not deposited on either cathode. The deposition of U is periodically scraped and removed from cathodes in the electrorefiner, with a yield of ~99.68%, where the TRU from electrowinning yields ~97.83% [14]. These yields describe the weight percent of input material that is successfully removed from the electrorefining vessel and not recovered from the salt. The yield from electrowinning is slightly lower since the collected weight percentage of actinides drops for higher atomic number elements, which require a larger negative voltage to increase collection efficiency. At the end of electrorefining, the fuel baskets contain noble metals and cladding which are fabricated into a suitable waste form.

2.1.5 Salt Purification, Actinide Drawdown and Uranium Processing

Following the recovery of U in electrorefining, the molten salt still contains residual uranium. Electrorefining is truncated in order to prevent the contamination of U from TRU or rare earth elements. Yet, up to 15 wt% of the U removed on the graphite cathode is composed of the eutectic salt [5]. Uranium purification from the salt is accomplished via a distillation process at 800^{o}C to recover the salt from dendritic uranium. Following salt removal, the U is consolidated into a metal ingot by heating the dendrites to 1200^{o}C. A similar process allows separation of the eutectic salt from the TRU product off of the liquid cadmium cathode.

The mixture of actinides (U, Np, Pu, Am, and Cm) remaining the molten salt must be extracted in order to prevent the TRU from being lost in waste streams. The electrolyte can be separated from the metal salt mixture using a bottom-pour crucible and the U/TRU is then formed into ingots and used for subsequent fuel fabrication. The salt is collected and treated in actinide drawdown via an electrolysis process.

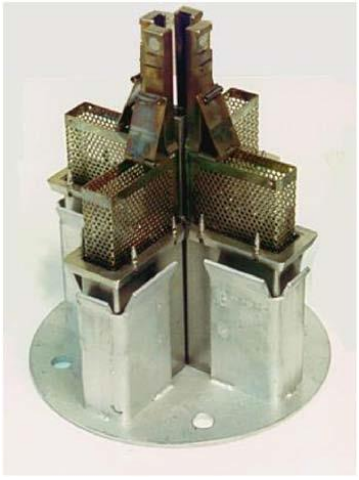

Figure 2.4. Anode basket.

Reproduced from [11].

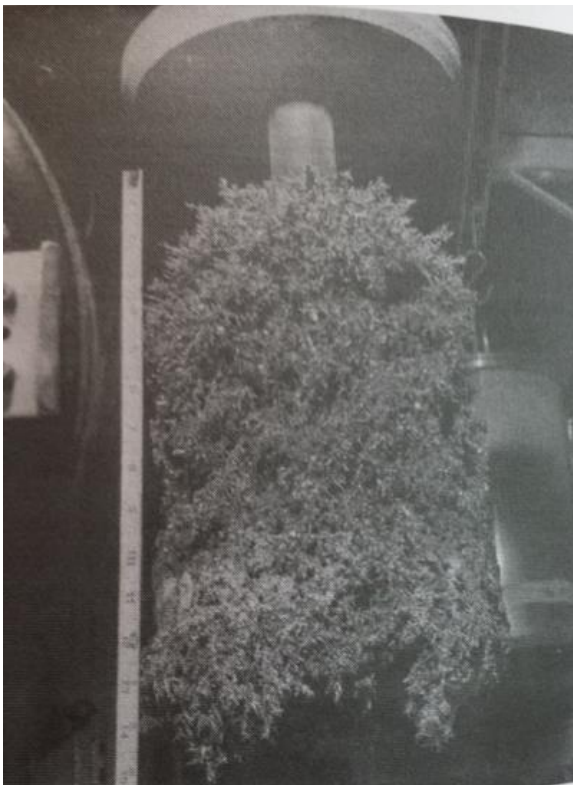

Figure 2.5. Dendritic deposition of uranium on solid cathode.

Reproduced from [15].

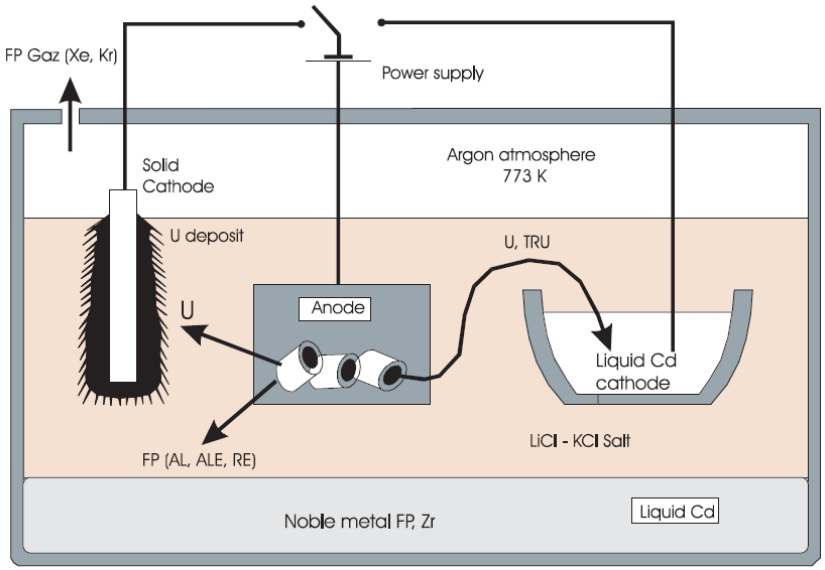

Figure 2.6. Electrorefining and electrowinning processes in electrochemical cell.

Reproduced from [16].

2.2 Policy Views on Pyroprocessing

2.2.1 United States Reprocessing Policy

In 2011, President Obama requested a study be performed to review policies for nuclear waste management and recommend strategies moving forward. The Blue Ribbon Commission of America's Nuclear Future took on these duties and subsequently stated that it would be "premature for the United States to commit … to closing the nuclear fuel cycle given the large uncertainties that exist about the merits and commercial viability of different fuel cycles and technology options", and encouraged "prompt efforts to develop one or more consolidated storage facilities" to manage the domestic used nuclear fuel in need of storage [17]. Since this report was published, the United States has yet to implement the commission's storage facility recommendations but continues to restrict the reprocessing of its supply of nuclear fuel used in other countries interested in closing their own fuel cycle. Yet there still exists a group of countries supporting the future application of pyroprocessing technologies to close the nuclear fuel cycle.

With such interest in pyroprocessing around the world increasing, the impact of the spread of technologies for enrichment or reprocessing, such as pyroprocessing, continues to be investigated. The issue of the more countries using the back end technologies of the nuclear fuel cycle such as reprocessing continues to be a sensitive matter to the nonproliferation regime as the dissemination of such technologies can remove barriers from pathways to nuclear weapons acquisition. Thus, while deterrence through safeguards on fissile material is arguably a reliable method for nonproliferation, there is no argument that if used fuel is never processed it will never be used to create weapons. In this way, the United States has formulated its current policy on denial of access to the fissile material as well as a denial of the capabilities for reprocessing technologies.

2.2.1.1 Policy Options

The United States is strictly focused on nuclear non-proliferation regulation at the global level. The American policy to avoid a domestic pursuit of implementing new nuclear fuel cycle technologies is meant to inspire other countries to emulate the same approach and thus reduce the spread of nuclear material enrichment and reprocessing. To date, this US policy to not allow reprocessing has worked to deter its non-nuclear weapons state (NNWS) partners from potential weapons programs.

But the US hold on global nuclear governance is fading. While politics have often caused the delay of development of nuclear infrastructure within the United States, the clear dearth of new nuclear investment was noticeable before the US shale revolution kicked off or even before the Fukushima accident occurred. With the Yucca Mountain nuclear waste repository mothballed, there is a lack of current investment and no long term plan for a nuclear future within the United States. And with growing concerns over energy security, an uneasy dependence on fossil fuels, or a fight against climate change still factoring into the energy supply calculus of other nations, this has compelled countries interested in a nuclear power option to turn to other nations for support and guidance.

Russia and China have succeeded in becoming major players in the market for emerging nuclear technologies. While politics have stalled nuclear development within the United States, nuclear development has become a pillar of the government's platform in each of these countries. The export of nuclear technology, goods, and services has been a large part of the Russian economy since the late 1990s [18]. The number of China's nuclear power reactors has doubled in the last decade and they expect to join the nuclear market as one of the few countries capable of producing heavy components in the nuclear supply chain [19]. Each of these countries is a nuclear weapons state and thus the nuclear technologies being developed domestically do not greatly change the nuclear

nonproliferation regime. However, Russians commonly do not ask for strong security guarantees or safety measures from the countries to which they export nuclear technology, a concerning prospect for the nuclear market [20]. Additionally, the French have on record noted the lack of an adequate safety culture within Chinese nuclear developments [21]. The need to ensure above average safety measures are taken at nuclear power and nuclear fuel facilities is critical to maintaining the correct nuclear safety culture that drives countries from the top down to be responsible and accountable within their nuclear industry. This lack of safety consciousness may spread to the security and safeguards requirements Russia and China place on the countries to which they export new nuclear technologies.

Since the competitiveness of the industry may soon overshadow the nonproliferation implications of providing nuclear technology to emerging economies, the US may find the changes in the global nuclear non-proliferation, security, and safety regimes unwelcome. More importantly, the US may already be losing its impact on directing the global nuclear development process. Efforts by the US to counterbalance this trend may be required in order to maintain the strict focus on nuclear non-proliferation regulation at the global level. Such efforts would provide a powerful approach to renewing US-lead safeguarding practices at existing and future nuclear fuel cycle facilities.

One such effort could be a joint US-ROK program to develop pyroprocessing. The Republic of Korea's desire for a more comprehensive nuclear capacity has caused friction with the US. Washington's strong opposition is because of global proliferation concerns. But American opposition to this or any NNWS unilaterally developing and implementing this technology may create a distinct rift between itself and countries which decide to close their nuclear fuel cycle through bilateral means. Since it has been published that Koreans are expected to have a positive response to other nuclear energy countries

providing pyroprocessing services [22], a partnership between the US and the ROK with the US taking the lead may become feasible. A joint US-ROK pyroprocessing development program hosted by the United States will signal that the US will be involved with the future global nuclear governance and put those countries aggressively pursuing advanced nuclear fuel cycle options on alert that the US will no longer be leading from behind.

Introducing this approach is multifaceted: (i) this multilateral approach may diffuse concerns of future weapons programs being grown within countries interested in broadening their own nuclear fuel cycle options; (ii) it has the opportunity to reinvigorate the US commercial nuclear market and reestablish its economic interest in nuclear power supply promotion; (iii) and it maintains the US focus on reducing global proliferation concerns in an organic way that continues to involve the United States in future global nuclear fuel cycle developments. Analysis is needed to determine if a fundamental shift from the US strict focus on nuclear non-proliferation to an embrace of championing safeguards may create a more secure role for the US and its nuclear standards in future nuclear facility operations.

Currently, the US and the ROK recently announced in April of 2015 an extension of the 123 Civil Nuclear Agreement committing the countries to continue to ensure a supply of US enriched nuclear fuel to South Korea. The agreement considered the issues of advanced consent for reprocessing or enrichment in detail and did not expressly require the ROK to renounce forever the right to such technical capabilities [23]. In this way, the door has been left open for future cooperation between the United States and the Republic of Korea on matters of closing the fuel cycle. South Korean scientists with cooperation from United States will continue work on investigating the economic and proliferation resistant benefits of pyroprocessing.

CHAPTER 3

SAFEGUARDS ON PYROPROCESSING

3.1 Overview

3.1.1 Need for Safeguards

To date experience with pyroprocessing has been limited to laboratory or pilot-scale unit operations such that, an acceptable approach for nuclear material safeguarding at these facilities must still be developed and agreed upon. Pyroprocessing has been accepted as possessing more nonproliferation characteristics compared to its aqueous counterpart, inherently making some view it as proliferation resistant [6] [24]. The features that give proliferation resistance include:

- High radiation and high temperature environments, as well as hot, corrosive salt and metal products;
- Small throughput of pilot-scale facilities ~ 1 MTHM/yr in dry batch-mode process [14] [24];
- Fewer processing units;
- Isotopic abundance of ^{240}Pu (thermal output, neutron generation); and
- Composition of actinides (U/TRU) during electrorefining deposited on the cathode have trace amounts of fission products making it more difficult to separate fissile – most notably Pu – material from intermediate or final products.

Recent work has examined the design of a commercial-scale pyroprocessing facility [25]; included is the basis of a safeguards model for such a facility and the key challenges for safeguarding such facilities compared to its aqueous counterpart [6] [3] [24]:

- High temperatures as well as corrosive salt and metal products make the environment challenging for instrumentation;
- Lack of accountability input tank at front end as seen with aqueous processes, making material balance (input/output) difficult. It could be possible to assay the UNF after shredding or homogenized spent fuel powder after voloxidation as proposed by KAERI [3];
- Inability to flush out plant to determine hold-up for material accountancy. Extraction of U/TRU can only occur once TRU content is built up in steady-state conditions, making it infeasible to flush out actinides in electrorefiner;
- Inability to flush out requires near real-time accountancy (NRTA) with proposed material balance conducted in parallel with 24-hour operations cycle. Potential for inline monitoring would reduce the requirement for continuous on-site inspection; and
- Process system settings must be monitored since operating at different voltages can potentially deposit TRU instead of U. When pulsing the voltage instead of operating in steady-state conditions, plutonium deposition on the solid cathode is improved [26].

3.1.2 Lessons from Aqueous Reprocessing Facilities

The pyroprocessing environment presents unique challenges for nuclear material accountancy – types of problems that were addressed decades ago for aqueous PUREX processing facilities on a commercial scale. Pivotal differences exist between the aqueous and dry recycling processes themselves, which will require new applications of measurement technologies or new approaches to measurement and safeguards, as summarized in Table 3.1. Compared to aqueous processes, pyroprocessing is much more compact and more highly radiation resistant, hence is capable of processing UNF with

shorter cooling times while producing minimal waste for long-term storage. PUREX processing occurs in an aqueous medium, permitting continuous processing, whereas pyroprocessing is conducted in a dry medium in batch operations. The aqueous medium also facilitates remote sampling techniques involving small side streams. Although pyroprocessing occurs in a high-radiation field behind highly-shielded hot cell walls (like that for PUREX), its high-temperature, inert atmosphere refining vessel introduces additional constraints (notable, remotely sampling a eutectic salt), making *in-situ* material accountancy measurements especially challenging when considering transposing instrumentation and techniques refined for aqueous facilities into the pyroprocessing environment.

Although the paradigms established for aqueous facilities - such as practices at Rokkasho Reprocessing Plant, Sellafield and La Hague, [27] - may not directly overlap with those of pyroprocessing, the safeguards approaches and methods can be extended [24]. This includes potential extension of existing capabilities for nuclear material accountancy, including those of the Hybrid K-Edge Densitometer (HKED).

Similar to safeguards approaches developed for aqueous facilities, material balance areas (MBAs) and key measurement points (KMPs) must be established for tracking the flow and inventory of nuclear material. The KMPs within these MBAs must be considered specific to the processes and intermediary products produced in pyroprocessing. Once mapped, evaluation of instrumentation for making independent safeguards verification measurements must be examined from the inventory of existing instrumentation/ techniques.

Table 3.1. Comparative Features of Aqueous Reprocessing and Pyroprocessing.

Process	Aqueous	Pyroprocessing (Metallic Fuel)	Pyroprocessing (Oxide Fuel)
Nature of operations	Continuous	Batch	Batch
Solvent	Organic, HNO_3	LiCl-KCl, Cd, Bi	NaCl-KCl, CsCl-NaCl
Operating temperatures (K)	<373	623-773	903-973
Pu recovery (%)	>99.9	>99.5 (theory)	>99.3-99.7
Nuclear Material Accounting	Continuous	Batch system required	Batch system required
Technological maturity	High	Demonstrated on laboratory- and pilot-scales	Demonstrated on laboratory- and pilot-scales

Extracted from [6].

3.1.3 Key Measurement Points and Material Balance Areas

The interest in pyroprocessing utilized as a recycling technology may soon necessitate a full-scale monitoring regime in preparation for full-scale plant constructions. Safeguarding this new technology requires the identification of diversion pathways, monitored at KMPs. Timely detection of undeclared events as well as an extensive process monitoring infrastructure to verify the facility is operated as declared will rely on accurate accounting as well as innovative monitoring technology.

Fuel reprocessed via pyroprocessing may be either oxide or metallic fuel. Safeguards accountancy primarily follows the plutonium products. As highlighted by Durst *et al.*, metallic spent fuel from fast reactors has a higher fraction of actinides due to higher burnup by hard spectrum reactors; consequently, accounting of minor actinides (Np, Am, Cm) becomes increasingly relevant alongside Pu and U [24]. Material accountancy strategies employed in pyroprocessing must optimize the measurement systems employed to provide continuity of knowledge of the actinides in various processing stages. In the case of the U/TRU products of pyroprocessing, the IAEA can more readily accomplish its mission by verifying the absence of weapons-useable material rather than proving its existence [6].

Recent studies have attempted to determine KMPs within designated material balance areas to provide continuity of knowledge through safeguards verification measurements of intermediary products [3] [14, 24, 25] [28-34]. As a result, nuclear material accountancy safeguards in pyroprocessing must focus on at least three key products: 1) Input spent fuel; 2) Pu and TRU-bearing intermediary materials; and 3) Output Pu and TRU [24].

The safeguards approach by KAERI for the conceptual Reference Pyroprocessing Facility (REPF) has identified five conceptual MBAs which provide a basis from which nuclear material accountancy can occur (Figure 3.1) [30] [31] [33] [34]:

- MBA-1 Spent Fuel Receiving and Storage: Disassembling, chopping, Decladding, voloxidation, and homogenization of UNF;
- MBA-2 Main Pyroprocess Area: Electrolytic reduction, electrorefining, electrowinning, and waste treatment;
- MBA-3 U Product Storage: U metal ingot;

- MBA-4 TRU Product Storage: TRU metal ingot; and
- MBA-5 Waste Storage: Metal/salt waste.

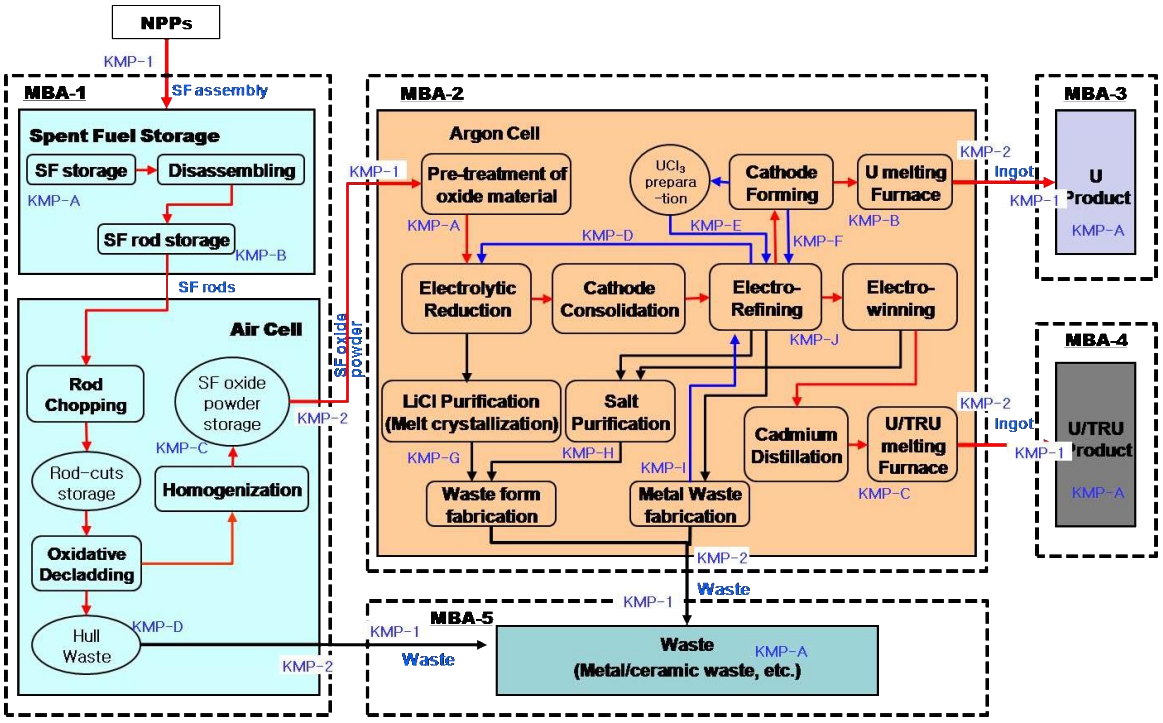

Figure 3.1. Material Balance Area and Key Measurement Points for Reference Pyroprocessing Facility.

Reproduced from [35].

Although KMP's have been identified by Han *et al.* (in Figure 3.1), Lee *et al.* have provided a more comprehensive set of KMPs following the Pu mass balance throughout a conceptually designed pilot-scale plant – the Korean Advanced Processing Facility (KAPF) – for an annual throughput of 100 tHM/yr (Table 3.2). Furthermore, Cipiti *et al.* have identified the key measurements (summarized in Table 3.3) that must be taken to verify material balance of Pu (and track Pu movement) during pyroprocessing [3].

Table 3.2. Characteristics of KMPs for Material Accountancy at the KAPF.

KMP[b]	Material Form[b]	Total Element Actinides (kg)[b]	Total Pu (kg)[b]	Pu Fraction[b]
1	Spent Fuel Feed (UO_2)	11,904.76	138.29	
2	U-Metal Product (most U)	11,637.74		
3	TRU-Metal Product (most TRU)	155.05	135.24	
4	Waste Output	111.97		
A	Spent Fuel Storage	100.00	1.16	0.0116
B	Oxide Powder Storage (UO_2)	99.90	1.16	0.0116
C	Oxide Powder Storage (U_3O_8)	99.90	1.16	0.0116
D	Uranium Metal Chunks (U/TRU)	99.40	1.15	0.0116
E	Uranium Metal Ingots	97.76	0.00	
F	TRU Metal Ingots	1.30	1.14	0.8723
G	Cladding Hull Waste[a]	11.91	0.14	0.0116
H	Magnesia Filter Waste[a]	23.79	0.27	0.00625

Table 3.2. Continued.

I	Reproduction Salt Waste[a]	335.68	0.42	0.004
J	Graphite Cathode Waste[a]	11.91		
K	Refining/Winning Salt Waste[a]	16.79	0.19	0.195g/item
L	Cadmium Cathode Waste[a]	11.91	2.12	0.356g/item

[a] *Reproduced from [14]*.

[b] For 1 material balance period.

Table 3.3. Measurement locations and uncertainties for plutonium in pyroprocess.

Measurement Location	Target Uncertainty
Input SNF Measurement	1%
Electrorefiner Salt Sampling	1%
U Product Assay	1%
U/TRU Product Assay	1%
Metal Waste Assay	10%
U/TRU Recovery Salt Sampling	10%
Fission Product Drawdown Confirmatory	10%
Oxidant Production Confirmatory	10%
Fission Product Waste Assay	10%

Reproduced from [3].

3.1.4 Alternative Nuclear Materials

The irradiation of nuclear fuel in reactors produces other fissile isotopes in addition to Pu, including ^{237}Np, ^{241}Am and ^{243}Cm. Since 1993, the IAEA has considered these isotopes as potential material to fabricate nuclear explosives. Under safeguards considerations, the IAEA has labeled them as "alternate nuclear materials" (ANM) [36]. Although ^{237}Np and ^{241}Am could be misused for military purposes**, t**he presence of ^{244}Cm introduces orders-of-magnitude higher spontaneous fission rates, making ^{243}Cm ill-suited for military purposes [6]. Thus safeguarding the pyroprocess focuses on the actinides U, Pu, Np, and Am.

3.1.4.1 Neptunium

The isotope ^{237}Np is fissile and, while not defined by the IAEA as source or special material, Np is monitored under voluntary protocols as ANM [37]. This nuclide is isotopically pure, as the other Np isotopes with comparatively shorter half-lives have decayed. Above an energy threshold of ~500 keV, the fission cross section ^{237}Np undergoes a sharp increase. Although the fission cross section at thermal energies is low (making it difficult to burn in LWRs), ^{237}Np shows a fission cross-section above 500 keV similar to ^{235}U. In principle, with a purported critical mass around 56 kg and a spontaneous fission rate comparable to ^{235}U, ^{237}Np could have the same utility as highly enriched uranium [6]. As Np is separated in the electrorefiner with the U/TRU product in quantities higher than customary of aqueous facilities, it is of interest to include Np in developing pyroprocessing safeguards.

3.1.4.2 Americium

Americium also is a product formed in UNF either by the decay of ^{241}Pu or via neutron capture. Although the IAEA has not defined Am as source or special material, information related to Am is collected by the IAEA under voluntary safeguards

agreements as ANM [37]. Compared to Np, ^{241}Am is more compressible despite a higher critical mass of 59 kg [6] making it potentially appealing as a material that could be misused for military purposes.

3.2 Motivations for Safeguards

Since as of yet no commercial pyroprocessing plants operate, the Republic of Korea has taken advantage of advanced planning on safeguards for pyroprocessing facilities to allow for the option of a safeguards-by-design approach for construction of new facilities [31]. Safeguards-by-design requires a structured approach to ensure the timely, efficient and cost effective integration of international and national safeguards, physical security and potentially other nonproliferation objectives into the overall design process for a nuclear facility, from initial planning through design, construction and operation [38]. This approach may facilitate research and development of direct measurement technologies capable of quantifying the element/isotopes of interest and applicable to the harsh sampling environment characterizing pyroprocessing.

Several circumstances are behind the IAEA's push to develop safeguards approaches to pyroprocessing plants. Discussion between the ROK and the IAEA on their interest in indigenous fuel cycle development has propelled the need to develop a safeguards approach for the ROK's planned facilities. This has prompted the United States and the Republic of Korea to conduct a joint-fuel cycle study to assess pyroprocessing as a reprocessing technology [39]. Ongoing research in Russia at the Research Institute of Atomic Reactors (RIAR) on an oxide fuel input pyroprocess is advancing as well [40]. It is possible that upon completion of research and development, it may be coupled with fast reactor development as a complete fuel cycle package and made available for other interested countries. Since facility layout is increasingly being fixed at an early stage, the advanced planning of the IAEA for such circumstances may accommodate planning and

installing safeguards alongside functioning operations for the fuel cycle facility, reducing costs associated with delayed safeguards and security application and mitigate hours of labor associated with altering the current design of a facility for safeguards retrofits.

3.2.1 Why Are Safeguards Technologies Needed?

Due to limited experience with pyroprocessing and since such experience has been limited to laboratory or pilot-scale unit operations, the requirements for nuclear material safeguarding at such facilities are uncertain. As with the PUREX cycle, the materials accountancy primarily concerns Pu, and to a lesser extent U, Np and Am. The IAEA timeliness detection goal for safeguards verification of Pu is a detected diversion of one significant quantity (SQ; 8 kg) within 1 month at a 95% detection probability [41]. The traditional combination of nuclear material accountancy, containment and surveillance, and physical protection continue to provide the basis of a safeguards approach for pyroprocessing facilities in order to detect and deter diversion. As a result, intrinsic and extrinsic measures are required throughout the entire cycle of the pyroprocess to ensure sufficient safeguards barriers are in place to detect and deter misuse or diversion.

3.2.2 IAEA Safeguard Goals

The IAEA Department of Safeguards plans in the next decade to prepare to safeguard new, more advanced types of nuclear installations, such as pyroprocessing plants [42]. Within these plans are proposals to develop generic safeguards approaches, in conjunction with development of tools and techniques to characterize the fissile content of process materials containing actinides during pyroprocessing [42]. These plans have been raised to Medium on a scale of urgency that includes Low and High options as well, with the goal of developing a safeguards approach and supporting measures for a specific pyroprocessing facility with a target completion date in 2015 [43]. Metal mixtures containing Np, Am, and Cm during pyroprocessing are emphasized as the items requiring

development of characterization techniques. The summation of the current plans will be a Safeguards Technical Report highlighting generic safeguards strategies for pyroprocessing plants [43]. This approach will allow the agency to attain the near-term milestones it set out to achieve within the next decade.

3.3 Challenges to Safeguards

3.3.1 Electrorefiner In-Process Inventory Assay

Unlike aqueous reprocessing, there is no equivalent of an input accountancy tank within the pyroprocesses. Pyroprocessing was not designed with a front-end tank due to the nature of the process with the coupled nature of the dissolution/extraction of the actinides and fission products during electrorefining. Without an accountancy tank, key measurement points at the electrorefiner inputs and outputs have been proposed and the material balance may rely on the inventory difference between these measurements [14]. However, it is anticipated that TRU material in the electrorefining vessel will not be removed with each batch, as it takes time for it to accumulate within the vessel, and many assemblies worth of TRU may be required before U/TRU extraction begins [3]. The procedure of allowing TRU to accumulate in the vessel is an important design feature since it makes removal of the TRU from the eutectic salt possible [3]. Therefore, a safeguards technique is required to monitor the eutectic salt of the electrorefiner to ensure diversion of the TRU out of the salt does not take place within the diversion scenario timeframe required by IAEA regulations.

This requirement complicates the proposed safeguards approach of accounting only for inputs and outputs from the electrorefiner. While measurements of the plants inputs and outputs can be planned, there is no current method for determining the buildup within the processing vessels. Thus there is an inefficiency in Pu inventory monitoring as a function

of time resulting in the need for a flush out, an approach that has been utilized to determine the hold-up material for PUREX plants. However, it is known that flushing out a pyroprocessing plant hinders the extraction of the U/TRU product from the electrorefiner [3]. If in-process measurements can be used to determine the complete plant in process inventory, it may be possible to eliminate the need for plant flush outs.

Process monitoring or inventory measurements may provide details on the hold-up material as it accumulates in process vessels. A large number of simple low cost sensors could be used to complement the possible non-destructive assay (NDA) approach for safeguards of pyroprocessing inventories, gathering additional information about the fissile material flows in process as well as reducing the reliance on input and output measurements for complete mass tracking [44]. Otherwise a dedicated inventory measurement tool may be applied to sampling and measuring the TRU buildup in electrorefiner salt. These strategies should allow for near-real time accountability of fissile materials and are expected to minimize the financial impact on a facilities safeguards cost structure.

3.3.2 Limited Knowledge of Process Materials

Sample measurements on new material processing regimes such as pyroprocessing will need to accommodate much higher concentrations of minor actinides in comparison to aqueous reprocessing material streams. In addition to the new range of actinide ratios expected, the material forms will be both physically and chemically different from well-known aqueous forms. As fissile material travels throughout each subsystem, the material forms will shift between item and bulk forms, necessitating a diverse range of measurement techniques for material tracking measurements. Evaluation of the performance of safeguards measurements on unknown molten salt samples will be

needed to demonstrate the robust performance of current accounting methods or highlight the demand for innovative technologies to handle the new sampling parameters.

3.3.3 Reliance on Destructive Assay or Burnup Simulations

For pyroprocessing plants, the goal of detecting the loss of one significant quantity of plutonium in one month will begin as soon as the used nuclear fuel assemblies arrive on site. Currently, there is no established non-destructive assay technique to obtain the quantity of plutonium from the used fuel by any direct means, so quick analysis of used fuel assemblies or rods may have no other option other than indirect measurement techniques or simulation software such as ORIGEN-S [35]. It is expected that input nuclear material accountancy of plutonium in pyroprocessing could also be obtained through a reliance on destructive analysis (DA), though this technique occurs over a much longer timeframe. But obtaining the fissile material content of used nuclear fuel elements via these methods may not be practical given the timeliness, uncertainty, and workload required.

3.3.3.1 Burnup Simulations

An effective burnup calculation must minimize the uncertainty of the isotopes of primary importance to safeguards monitoring plans in order to be properly utilized as a safeguards parameter. Determining the nuclear data induced uncertainty in burnup calculations may need further analysis before such simulations may be practically relied upon. Special care may need to be taken when identifying the axial changes in isotopic composition of the used fuel assembly, since some burnup simulation techniques are not able to simulate an axial profile [45]. However, this method is neither a direct nor independent means of quantifying special nuclear material content. The challenge to verify the input fuel fissile material balance into the electrorefiner is made difficult by the high uncertainties from

simulated burnup and the dependence on operator data on assembly exposure time and location in the reactor core.

3.3.3.2 Destructive Assay

Because the materials in pyroprocessing undergo significant changes in composition and form, the special nuclear material content may need to be verified by destructive analysis for each input into the electrorefiner to allow for a high degree of certainty when applying this value to the plutonium outputs. Detracting from this approach is the increased reliance on destructive analysis, demanding a larger workforce for wet work and a higher cost structure for safeguards measurements. Additional time spent on DA compared to NDA based strategies confines the results obtained to apply only for final dispositive accuracy and complete reliance on this strategy will not allow new pyroprocessing facilities to determine plutonium with near-real time accountancy. Sample homogeneity is another necessity required for DA to be an effective representation. The need exists to ensure proper homogeneity from all input materials streams from which samples are chosen. Since some state that the materials in each subsystem of pyroprocessing are inhomogeneous [24, 46], further experimental studies will be needed to define if uniformity exists for all measurement events occurring at different locations throughout the monitored facility.

3.3.4 Reliance on Neutron Counters

Some material accountancy proposals plan to administer safeguards on plutonium inventory using neutron counting to perform accountability measurements and track plutonium movements [3, 14, 24, 31, 46]. Though such detectors are routinely used for safeguards and operational measurements in nuclear facilities throughout the world, one deficiency in using neutron counters in safeguards is the lack of a means of direct verification of the element/isotopes of interest. Direct measurements are preferred over

indirect since they are less susceptible to spoofing. Additionally, this accountancy technology is challenged by several factors unique to pyroprocessing:

- the assumption of continuous association of Pu and Cm might not be applicable for the pyroprocessing cycle and reliance on their ratio as a means of monitoring plutonium may not retain continuity of knowledge for accountancy and control purposes,
- the separation process of actinides from the used fuel elements comingles several neutron sources with the plutonium product, which makes the inclusion of additional neutron emitters or neutron absorbers to the plutonium product difficult to detect and poses a challenge for accountancy techniques based solely on measuring neutron emission,
- the neutron production from the target materials for plutonium detection measurements is dominated by the emission from ^{244}Cm and, with the high neutron multiplication of the target material, determining the Cm mass in the plutonium product may be difficult.

Total neutron counting employing curium has been proposed as part of a holistic neutron balance scheme [3, 14, 16]. Neutron measurements have been proposed at each of the fuel pin, electrorefiner, waste stream and uranium products during the pyroprocess. Indirect verification of the plutonium in used nuclear fuel is possible through evaluation of the Cm neutrons. Plutonium and curium behave similarly during the partitioning steps at reprocessing, forming an argument for plutonium-curium association. This argument assumes that ^{244}Cm is an overwhelmingly prevalent neutron emitter – after a sufficient cooling period for the decay of ^{242}Cm, and that it remains unseparated from the plutonium throughout the reprocessing process. Originally sought to provide plutonium estimates in reprocessing waste streams, this approach discriminates against the

extremely strong gamma radiation accompanying fission products by measuring the spontaneous fission neutrons from the transuranic elements in spent fuel. Using the known spontaneous fission yields and multiplicity distributions for the neutron emitting elements, the mass of plutonium and its associated error can be calculated through direct measurement of samples in well-type coincidence counters.

However, the effective mass of plutonium may be obtained directly only when the relative strength of neutron emissions from curium are of roughly equal or less prevalence than that of plutonium. This relative neutron range is rare, only occurring in spent fuel originating in the radial blanket of fast reactors. For all other cases, curium neutrons dominate as the main source of neutrons, making the direct determination of plutonium mass inadequate since it would be saddled with high values of uncertainty. Thus a supplemental DA or NDA measurement to quantify the plutonium-to-curium ratio is needed for plutonium verification in all other spent fuel origins; to this end, a combination of the hybrid K-edge densitometer instrument and a well-type neutron counter has been used effectively to verify the plutonium content [47]. The Pu:Cm ratio has also been determined with DA methods. Although this method purports to maintain continuity of knowledge for Pu:Cm, it does not measure Pu directly and assumes that the ratio of ^{244}Cm and Pu is fixed. Using this method, 30kg of Pu holdup was not found to be directly verifiable in one study [3].

Additionally, the assumption that the ^{242}Cm ($t_{1/2}$ = 163 days) has decayed away leaving the main contribution of neutron response to ^{244}Cm may become invalid as new fuel cycles approach shorter periods between removing fuel from the reactor and reprocessing it, taking advantage of on-site reprocessing as seen in the design of fast reactor facilities. It also should be noted that continuous association of Pu with Cm might not be applicable for the pyroprocessing cycle since residual amounts of Pu and Cm remaining in the

eutectic salt will mix with new material added to the process vessel. The current accountancy technology is challenged by the assumption of continuous association of Pu and Cm, thus work to expand the capabilities of the monitoring devices for a full range of identification and quantification of heavy elements is needed.

3.3.4.1 Reliance on Pu:Cm Ratio

3.3.4.1.1 Pu:Cm Inseparability Argument

The plutonium-curium inseparability argument states that the actinides plutonium and curium will be transported together at a fixed ratio throughout an entire process and thus the quantity of one can be used to indicate the quantity of the other. For a single used fuel item input into a reprocessing system with a known mass ratio of plutonium to curium, the Pu content of the refined output may be determined from the Cm mass, which may be measured via neutron counting of ^{244}Cm isotope. The application of this argument as a measure for safeguards was developed to indirectly determine the plutonium content from aqueous reprocessing outputs at Rokkasho [47]. This principle has been successfully applied to the nuclear material accountancy for reprocessing facilities [48, 49] and has been proposed by some researchers as the base of the plutonium inventory monitoring plan for pyroprocessing facilities [14, 31, 35, 46]. Current plans to monitor the plutonium inventory are reliant on the validation of this Pu:Cm inseparability assumption for the pyroprocess. However, the plutonium to curium ratio of the used nuclear fuel elements input into the electrorefining process may not be directly correlated to the ratio in the metal ingot product outputs.

Continuous association of Pu with Cm might not be applicable for the pyroprocessing cycle since residual amounts of Pu and Cm remaining in the eutectic salt will mix with new material added to the process vessel. In addition, preferential separation of one over

the other based on the differences in Gibbs free energy further complicate this approach. It is important to retain continuity of knowledge for accountancy and control purposes, but reprocessing in the electrorefiner is dependent on a small but ever present inventory, nominally six weight percent, of heavy metal chlorides to facilitate electrotransport leading to a batch-to-batch variability of the heavy metal inventory in the eutectic salt [50, 51]. Consequently, alternative NDA technology may need to be explored to meet the need to safeguard Pu during pyroprocessing. This work has already been done at a preliminary stage at the Institute for Transuranium Elements (ITU) at the European Commission's Joint Research Center at Karlsruhe, applying non-destructive technology to the analysis of process samples taken from a pyrochemical test facility [52].

3.3.4.1.2 Separation Factors

The Pu:Cm ratio for the metal product outputs is determined by the electrochemistry of the salt solution, and the driving force of the reduction reaction onto the electrorefiner cathodes is the difference in the Gibbs free energies. The higher stability, in Gibbs free energy, of the dissolved transuranic and rare earth chlorides prevents them from reducing to metals on the solid cathode. The alteration of the free energy relationships occurs with the introduction of the liquid cadmium cathode (LCC). The degrees of separation, or separation factors, for transuranic elements between chloride and metal form have been measured and tabulated in the chemical literature [53-55].

The majority of these values are tabulated at equilibrium, and analysis has shown the ratio of plutonium to curium in the LCC will be 1.87 times their ratio in the electrolyte. This value is obtained from the ratio of the plutonium and curium separation factors from Koyama [53]. The plutonium compounds are preferentially electrotransported to the LCC over the curium compounds because curium trichloride is a more stable compound than plutonium trichloride due to its larger free energy of chloride formation. Since at

equilibrium, the plutonium preferentially separates out of the electrolyte almost twice as much with respect to curium, the use of the input ratios obtained before administering the used nuclear fuel elements into the electrorefiner may be underestimating the amount of plutonium in the U/TRU product. The Pu:Cm ratio may not allow definitive safeguards conclusions to be drawn because the Pu material unaccounted for (MUF) may exceed the significant quantity of 8 kg.

The changing concentrations of the actinides during the run of an electrorefiner affect the limits of TRU deposition on the LCC at the end of the run. As TRU concentration in the salt decreases, smaller and smaller amounts of TRU are drawn from the salt solution. At a fixed rate of deposition, eventually the amount of TRU product will build up to the point that more uranium than is acceptable begins to deposit on the LCC. As operation of the LCC proceeds, the ratio of uranium to transuranic elements in the salt will increase to a point where the ratio is too high to efficiently obtain a significant TRU deposit on the cathode [56].

It is clear that the current LCC design cannot completely remove all transuranic masses from the salt. The LCC is best suited to skim some of the TRU out of the salt periodically when TRU concentrations are relatively high [56]. It is expected that due to operational considerations, the LCC will be used as a method of periodically removing TRU from the salt mixture as the TRU concentration rises within a certain band of concentrations. It is anticipated that this operation would decouple the input and output Pu:Cm ratios, making the use of neutron counting for plutonium mass monitoring prone to error.

Attempting to drive the TRU concentration to zero may be attainable through electrowinning, using lithium dissolved in the LCC to reduce the TRU. But since the TRU product is the item containing almost all of the processed plutonium, a high

accuracy for measuring this item is necessary. As the buildup of TRU takes many batches of input material to accumulate before it is possible to remove from the electrorefiner, the approach of removing all TRU at once multiplies the measurement uncertainties involved in obtaining the Pu:Cm ratio of each input fuel batch together. Options will need to be considered to reduce the uncertainty involved with such measurements and may include process monitoring or inventory assessments of the electrorefiner prior to TRU withdrawal.

3.3.4.1.3 Changes to Separation Factors

Work to quantify the degree of separation of transuranic elements under varying operating conditions has been performed showing the dynamic changes in separation factors that can occur under operation away from equilibrium [57]. During the process of electrorefining, electric current flows from one electrode to another driving the system away from its equilibrium state. Reduction of the applied voltage on the electrorefiner to larger and larger overpotentials has been determined to decrease the degree of separation of Pu and Am between the salt and the LCC [58]. This decrease is due to the shift towards more attractive separation efficiencies, or separation factors away from equilibrium [57].

Due to the dependence of separation factors on the applied overpotential, a change in the operating conditions while electrorefining will directly impact the Pu:Cm ratio in the U/TRU ingot, decoupling the Pu:Cm ratio between inputs and outputs. Since operation under different applied voltages will change the ratio of Pu:Cm in the U/TRU product, the overpotentials supplied to the electrical refiner will need to be actively monitored. Assuming that Cm and Am will act similarly electrochemically, the decrease in the degree of separation of Pu and Cm may drive the Pu:Cm ratio of the metal product towards the Pu:Cm ratio in the salt. But recent published data on the Cm Gibbs free

energy show that it may be separating from Pu more than originally thought [59]. Additional research along this direction may prove that Cm will not follow Pu during the separation process. However, operation in this regime of increasing overpotential becomes undesirable as a massive contamination of the U/TRU product with rare earth elements occurs.

3.3.4.2 Limitations of Neutron Counting

A neutron measurement of the U/TRU product from pyroprocessing will measure the intense neutron emission rate from curium which will dominate over all other pyroprocess neutron sources. However, neutron counting systems have limited capability to distinguish between neutrons emitted from different elements/isotopes. The potential for adding neutron sources into the outputs of the cadmium processing exists, creating a false positive for the plutonium product streams. The addition of neutron emitters or neutron absorbers to the plutonium product may be difficult to detect as the separation process of actinides from the used fuel elements comingles several neutron sources with the plutonium product. This highlights the difficulty in obtaining measurements meant to not only prove the existence of a stream of special nuclear material but also quantify the amounts for accountancy requirements and highlights the desirability for direct measurements of Pu. Material accountancy strategies employed in pyroprocessing will need to validate the systems employed on these measurements to provide continuity of knowledge of the plutonium content through the various processing stages.

3.3.4.3 Difficulties with Cm Measurement

A fundamental principle behind neutron counting LWR fuel is that the dominant neutron source being counted is due to the spontaneous fissions of ^{244}Cm isotopes. It is common to allow used fuel assemblies at least three years of cooling before reprocessing, so the only curium isotope of importance is ^{244}Cm. But before cooling, the most dominant

neutron emitting isotopes of curium are ^{244}Cm and ^{242}Cm with the half-lives of 18.1 years and 162.8 days, respectively. Since the process occurs under high-temperature conditions, pyroprocessing used fuel assemblies may be done with much shorter cooling times after removal from the reactor. Now with near-direct transfer of used fuel elements from reactor to pyroprocessing possible, the strong neutron emission from ^{242}Cm may need to be considered in neutron counting measurements.

The excessive neutron emission rate from ^{244}Cm will be added to by the neutrons from ^{242}Cm. Thus the neutron emission rate of pyroprocessing materials will be proportional to the decay of the ^{242}Cm and thereby challenge any safeguards measurement dependent on a static rate of neutron emission. Because the neutron emission rate is very high and the neutron multiplication is estimated to be over two [60], direct application of neutron coincidence counting for curium mass quantification may not be prudent until the technique has been tested against the various kinds of materials expected in the back-end of the pyroprocessing fuel cycle. The assessment of a material balance plan may need to consider new requirements such as these identified for measurements of back-end advanced fuel cycle processes via pyrochemical processing.

Obtaining a constant Pu:Cm ratio may prove difficult as well. One serious deficiency in using Cm in safeguards is the lack of certified reference standards [61], negatively impacting any type of destructive assay analysis and resulting in a larger uncertainty. Additionally, chemical analysis of spent fuel samples from fast and light water reactor assemblies have been done to assess the presence of ^{244}Cm and establish if its ratio to Pu over the sample set is constant [62]. Though the results did not refute the use of the Pu:Cm ratio for plutonium monitoring, they did reveal the extreme difficulty involved with quantifying ^{244}Cm content from fast reactor fuel as well as maintaining a constant Pu:Cm ratio when electrorefining light water reactor fuel.

CHAPTER 4

HYBRID K-EDGE DENSITOMETER FOR SAFEGUARDING PYROPROCESSING ACTIVITIES

The Hybrid K-Edge Densitometer (HKED) system was originally designed for use with solutions where plutonium (Pu) was a minor constituent with 1% of the uranium (U) concentration (i.e. U:Pu of 100:1) and containing trace amounts of other minor actinides such as americium (Am) and neptunium (Np), representative of light water reactor (LWR) spent fuel [63]. Newer Generation IV material processing regimes have necessitated development of analytical methods and instruments to accommodate mixed oxide fuel (MOX) with higher levels of plutonium, where the ratio of the concentrations of uranium and plutonium (U:Pu) approach 1:1. These new processes subsequently result in higher concentrations of minor actinides such as Am and Np. With the International Atomic Energy Agency's (IAEA) increased interest in tracking Am and Np [6, 64, 65] and with the development of new spent fuel processing technologies, tracking uranium with higher concentrations of plutonium, americium, and neptunium has sparked renewed interest in the HKED technique, on its algorithms and on better understanding of first principles modeling. High concentration MOX solutions, used for calibration, rapidly degrade and ways to calibrate and maintain calibration is also of prime interest.

Oak Ridge National Laboratory (ORNL) recently installed the only domestic, commercial HKED measurement system – as employed by the IAEA – in the Radiochemical Engineering Development Complex (REDC). This system is intended to be a test bed for new HKED applications. Given its access to an array of stock U, Pu, Np, Am and curium (Cm) solutions, ORNL is uniquely capable of developing new reference standards and is well positioned to test software algorithms necessary to expand HKED

capabilities for a full range of actinide ratios representative of current and next-generation fuel cycles. In addition, testing with ORNL's HKED system permits investigating its potential for online process monitoring.

Another technology being developed globally is electrochemical reprocessing (pyroprocessing). Pyroprocessing is an electrochemical method for recovering actinides from both oxide and metallic used nuclear fuel for further use as burnable fuel in Gen IV fast reactor design concepts [1, 2]. There is a clear need for a direct measurement technique for safeguards on pyroprocessing in order to develop an effective plutonium monitoring plan. One option worthy of investigation has been to adapt a mature material control and accountability plan based on existing technology that operators of reprocessing plants already have experience.

Safeguards validation measurements using the HKED system have been integrated into the commercial Plutonium URanium EXtraction (PUREX) operations for recycling used nuclear fuel for some time [36, 66]. However, the HKED system has not yet been integrated into the pyroprocessing scheme, as pyroprocessing exists only on a pilot scale. The feasibility and role of HKED is not yet established, and several technological and practical challenges need to be addressed. The potential for HKED to be integrated into a larger safeguards-by-design pyroprocessing concept exists once system capabilities have been expanded to account for higher actinide concentrations. Developing and testing standards and software for the HKED system is essential to meeting the need for analytical capabilities for timely on-site safeguards accountancy verification during pyroprocessing operations.

The HKED was chosen due to its high precision assay which is designed to simultaneously identify and quantify heavy elements, such as U and Pu, within a limited

time scale. Because of the inability to flush out the pyroprocessing plant to close material inventory balance, this leads to reliance on near real time accountancy, providing a strong need for rapid onsite accountancy verification. The HKED provides analytical measurement capabilities for timely on-site input accountancy verification. Compared to the current reliance on inductively coupled plasma – mass spectrometry (ICP-MS) or isotope dilution mass spectrometry (IDMS) to obtain input plutonium amounts, HKED can be installed onsite under a safeguards plan to validate physical inventory without being subject to material transfer off site or costly time delays. It has proven to give equivalent measurement precision as expensive destructive chemical analysis methods, yet is much simpler and faster to use. The HKED has been already been applied to the analysis of process samples at pyroprocessing test facilities once in solution, and real-time monitoring of primarily the molten salts may be possible with the HKED monitoring system [52].

4.1 Hybrid K-Edge Densitometry

The introduction of the HKED system represented a milestone in the independent safeguards verification capabilities onsite at reprocessing facilities. The HKED design was originally investigated in 1985 at ITU [66]. The first instance of the HKED instrument being installed at a reprocessing facility was at France's La Hague plant of COGEMA in 1989, followed by the United Kingdom's Thermal Oxide Reprocessing Plant (THORP) at Sellafield in 1993. At present, HKED systems are installed at reprocessing facilities in La Hague, Sellafield, Rokkasho-mura (Japan), Lanzhou (China), and Mayak (Russia) [63]. Given absence of commercial reprocessing in the United States, domestic experience with the HKED has been limited.

The HKED combines the use of x-ray fluorescence (XRF) spectrometry and K-edge densitometry (KED) for identifying and quantifying heavy metal actinide elements, such

as uranium and plutonium. The system is capable of assaying highly radioactive samples in homogeneous solid or liquid forms, making it well-suited for its existing operations in aqueous recycling facilities. Even in this medium, the HKED is able to determine the U and Pu concentrations simultaneously. Compared to traditional destructive assay (DA) techniques, such as IDMS, the HKED requires minimal sample preparation but delivers comparable accuracy with a faster turnaround time [67]. The reporting turnaround time for HKED at Rokkasho reprocessing plant is 1-3 days compared to 10 days for IDMS [27]. The HKED has been employed for aqueous reprocessing facilities where it has been used adjacent to hot cells to take routine verification measurements from the input and output accountability tanks, as well as to perform interim inventory verification [27].

4.1.1 K-Edge Densitometry

K-edge densitometry is one of the two techniques employed by the HKED for elemental concentrations of the major (uranium) constituent by determining the optical transmission of the sample being assayed. An x-ray tube is used to produce a continuum of photons with a maximum energy usually of 150 keV. The x-ray spectrum is transmitted through the sample, which liberates K-shell electrons by absorbing x-rays. The absorption by the sample appears as a drop in the intensity of the x-ray spectrum. The transmission difference between a spectrum of a known sample obtained during calibration and the uncharacterized sample is used to determine the elemental concentration(s) of the unknown sample. The energy at which the KED absorption occurs is characteristic of the element present, and the magnitude of the K-edge drop in the transmission spectrum is proportional to the concentration of the constituent element(s). In the case of U, the K-edge absorption occurs at 115.606 keV (Figure 4.1). The KED method is best suited for determining the concentration of the major constituent element in high concentration solutions (> 20g/L for 1-4 cm vials). In the purview of material accountancy in reprocessing facility, KED is capable of determining the concentration in solutions of

high U content, such as from samples in the dissolver solution of an aqueous facility [68]. The KED can be run for single element samples (like U or Pu) and dual pairs (U/Pu). The optimum concentration of K-edge densitometry is between 50-350 g/L of the major constituent being assayed [63] [36].

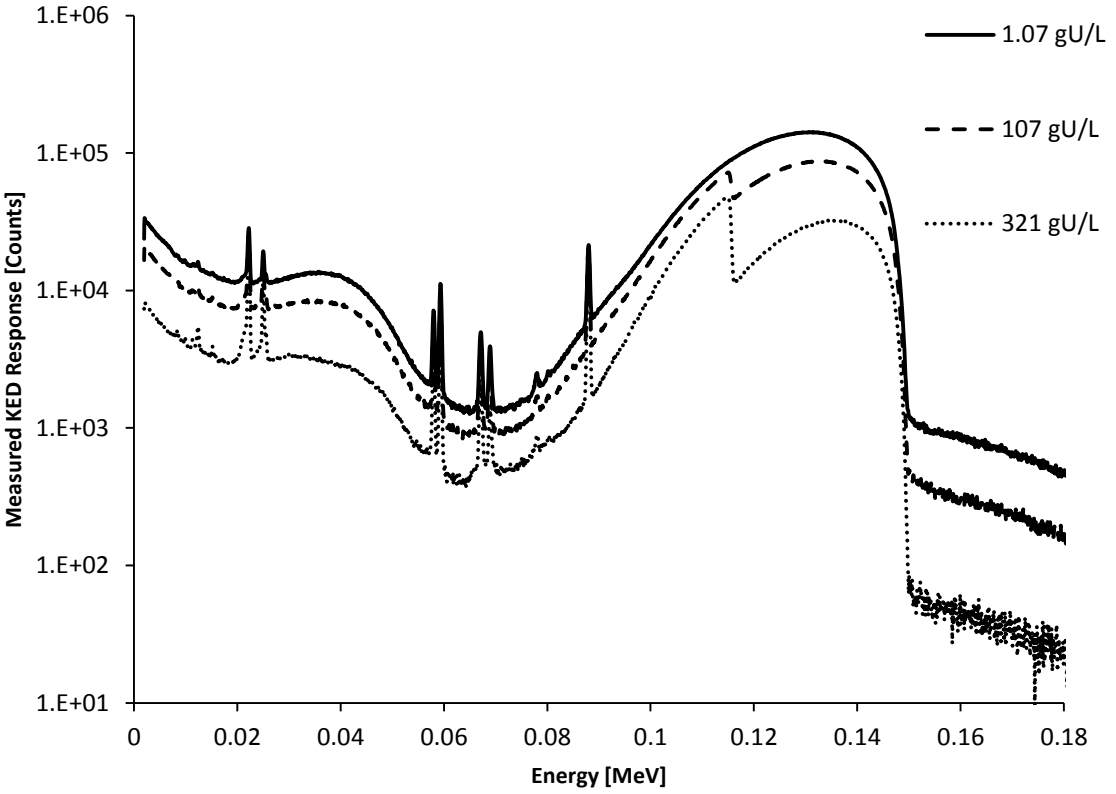

Figure 4.1. K-edge transmission spectra for various uranium solution concentrations in 3M nitric acid matrices. Solution concentrations range from 1.07-321 g U/L. The K-absorption edge for uranium occurs at 115.6 keV.

The calibration of the KED spectral response relies in part to the tungsten x-rays generated by interaction with the tungsten shielding and collimation material within the system, but primarily on the cadmium-109 gamma source located roughly 2 cm away from the face of the high purity germanium (HPGe) detector. The tungsten Kα and Kβ

peaks are located in the energy regions around 58 keV and 68 keV, respectively, and the cadmium-109 gamma energy is 88.08 keV.

4.1.2 X-Ray Fluorescence Spectroscopy

The XRF technique is the second technique employed by HKED and is capable of determining the ratio of elements present. XRF uses a bremsstrahlung beam to excite orbital electrons to create a vacancy, which de-excites through the emission of a characteristic x-ray. The energy of each x-ray is collected via a high-resolution gamma-ray detector, producing a spectrum characteristic of a specific element's known emission energies. Based on this spectrum, the elemental ratios can be determined. However, XRF is not as straight forward as KED, since the technique must account for matrix effects. Standalone XRF is employed within the HKED instrument for very low concentrations ranging from 0.5-40 g/L [69]. The XRF technique approaches uncertainty values better than 1% for concentrations approximately 1 g/L, but only 10% at 0.05 g/L. A reported detection limit using XRF is 0.01 g/L with a 20 minute count time [70]. In current implementation, it is assumed that the solution is U only, Pu only, or that the minor element is present at a low level (1-2%) of the major element. Figure 4.2 shows a typical XRF response from the HKED, where each of the spectra is offset by a factor of 10 to be able to visualize the individual actinide x-ray peaks.

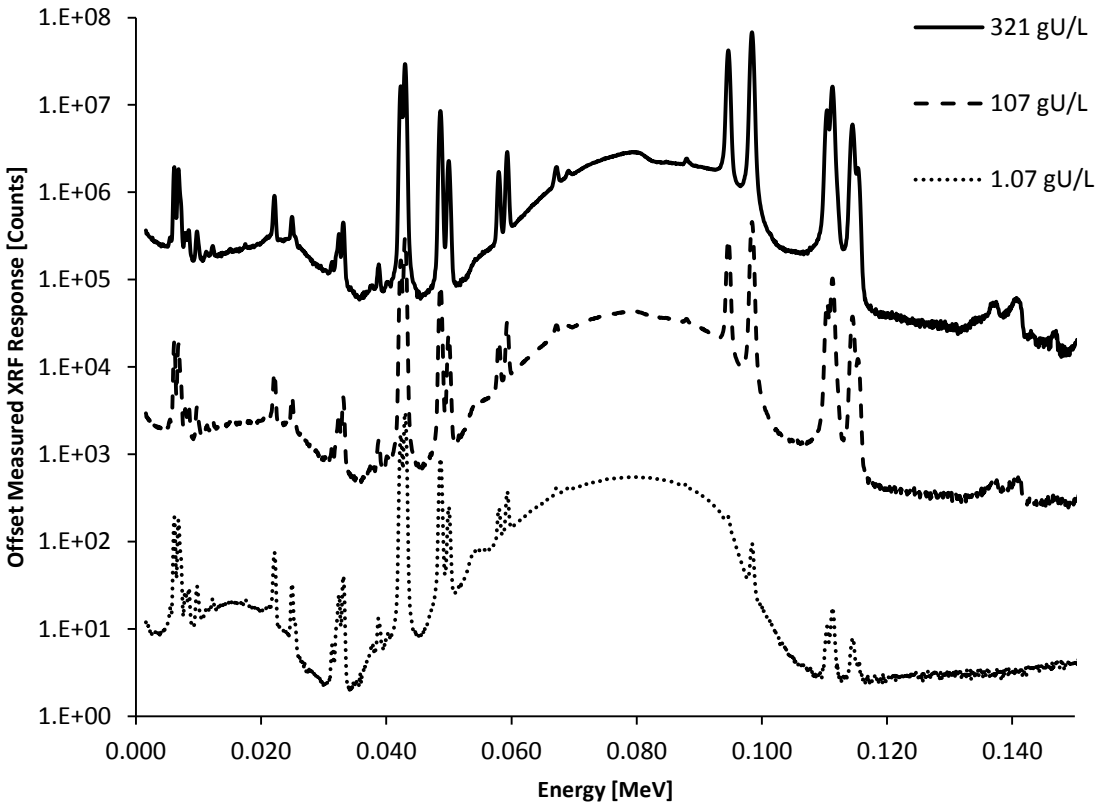

Figure 4.2. X-ray fluorescence spectra for various uranium solution concentrations in 3M nitric acid matrices. Solution concentrations range from 1.07-321 g U/L.

The calibration of the XRF spectral response relies in part on the x-rays generated by interaction with the shielding and collimation material within the system, but primarily on the cadmium-109 gamma source located roughly 2 cm away from the face of the HPGe detector. Additionally, a gadolinium beam monitor is installed as part of the ORNL REDC HKED. The stability of the x-ray tube spectrum is observed through the variation in the gadolinium x-ray peaks. The gadolinium Kα and Kβ peaks are located in the energy regions around 42 keV and 49 keV, respectively.

4.1.3 Hybrid K-Edge Technique

The HKED system combines the KED and XRF techniques to establish the reference basis for determining the elemental composition of an input sample. The HKED can be

used to determine concentrations of elements in UNF (U/Pu and potentially Np, Am) simultaneously. Since HKED relies solely on x-ray phenomena, results are limited to elemental analysis. However, the system is capable of elemental analysis in the presence of high-activity fission products.

In the HKED, depicted in Figure 4.3, a filtered x-ray beam of 150 keV end point energy is used for both absorption and fluorescence measurements. The beam passes through a solution of defined path length and the transmission is measured near the U/Pu K-edge absorption energy. This KED measurement obtained with a high-resolution gamma-ray detector, such as a high purity germanium (HPGe) detector, to determine the U concentration. Next, a second HPGe located at a backward angle of 150 degrees relative to the x-ray beam measures the $K\alpha_1$ x-rays from U and Pu to determine the ratio of the elements. Finally, the concentration of Pu is determined by the ratio (U:Pu) obtained from the XRF measurements relative to the absolute concentration measurement of the U obtained from the KED measurement. The reference basis of the absolute concentration of the major constituent (i.e. U) is determined using KED, where the XRF determines the elemental ratios of the sample constituent (i.e. U:Pu). With both KED and XRF employed together, the HKED system is calibrated for identifying sample elemental constituents (U and/or Pu) at concentrations ranging from 0.5-400 g/L [69]. Since the HKED is employed for verification measurements at reprocessing facilities, for typical application, the system usually is attached to a glove box or hot cell.

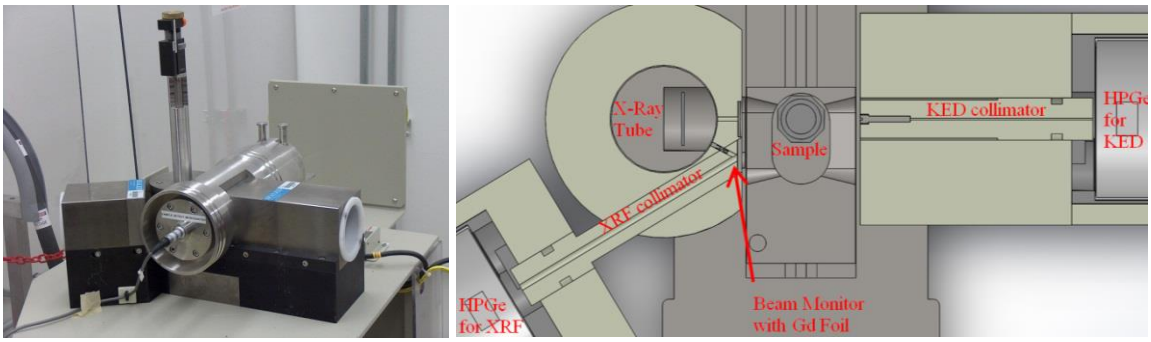

a. **b.**

Figure 4.3. Hybrid K-Edge Densitometer shown in (a) installed at Oak Ridge National Laboratory and as (b) a top-plane cross-sectional view of a CAD design in SolidWorks.

4.1.4 Hybrid K-Edge Accuracy

In judging the reliability of analytical techniques for a particular application, HKED is held to the same IAEA International Target Values (ITV) – or the uncertainties to be considered – as the destructive assay tool IDMS. Both IDMS and HKED are characterized by an ITV of 0.28 % uncertainty for uranium concentration measurements though the HKED has a higher uncertainty tolerance for plutonium concentration [71].

When compared HKED to traditional DA techniques, the HKED at Rokkasho reprocessing plant accuracy has ~ <1% uncertainty in Pu concentration for HKED versus 0.3-0.5% for IDMS [27]. The concentrations have even been reported to an accuracy of 0.5% Pu and 0.1% U for HKED [36, 67]. The accuracy of the system is dependent on calibration with characterized reference standards and pertinent software algorithms. The calibration curve required for the KED component requires a series of carefully characterized (by IDMS) U and Pu solutions.

However, the accuracy of the system is contingent upon not only calibration, but also on the elemental concentrations in the samples and the subsequent detection counting times of the system. For a 1000 second count, it has been reported that U (or the major element) can be identified with 0.2% uncertainty (better than one sigma at 0.5%) at 180 g/L and Pu (or the minor element) with 0.7% uncertainty – representative of a sample taken from a dissolver solution in an aqueous reprocessing facility [36] [68]. In verification activities, input accountability tank in aqueous reprocessing facilities have been measured with uncertainties of 0.6% U and 1.0% Pu, where verification measurements from the output accountability tank approaches 0.3% U and 0.9% Pu [69]. In addition to LWR fuel (ratios of U:Pu approaching 100:1), MOX fuel (ratios approaching 1:1) can also be assayed with the HKED for a product sample containing 90-95% U and 1-5% Pu [36], with an associated uncertainty 0.2% and 0.3%, respectively [63].

4.2 Hybrid K-Edge Applicability in Pyroprocessing

The robust nature of the HKED system makes it attractive to apply to pyroprocessing safeguards measurements. Independent, onsite, safeguards verification measurements of pyroprocessing facilities may be routinely achieved with precision approaching that of traditional destructive assay, but turnaround that, notably, is much faster. The safeguards approach for the bulk nuclear material in pyroprocessing will need to employ extensive process monitoring and extensive containment and surveillance measures to complement material accountancy and control regulations to meet IAEA requirements. This is complicated by a deficiency in developing quantitative analytical methods for determining actinide content at several stages of the pyrochemical partitioning process. No single analytical technique is capable of covering the entire range of safeguards measurements required.

If a safeguards technique is required to monitor the eutectic salt in the electrorefiner, it is possible to use the HKED to determine the transuranic buildup in the process vessels. Furthermore, the applicability of the HKED system may be extended to metal or powder sampling and measurement or include quantification of alternative nuclear materials such as Np and Am through dilution of the expected high density samples. Previous HKED measurements have been performed on actinides in solution, primarily nitrate solutions, even though the technology has been tested for solid samples. New applications of HKED may be expanded for oxide powders, metal chunks, or actinides in molten salt solution. Thus work must be performed to expand the capabilities of the HKED for a full range of material accountancy and process monitoring measurements for pyroprocessing safeguards.

The HKED has been applied to the analysis of pyroprocessing samples at test facilities once in solution [16], and real-time monitoring of primarily the molten salts may be possible with the HKED monitoring system. But the other types of material handled within a pyroprocessing facility, especially the relevant material at the head end of the reprocessing stream, must be measured and analyzed in accordance with current safeguards strategies dependence on input and output measurements along with periodic inventory measurements of all process vessels. A secondary alternative material form of potential interest is UNF powder. After the voloxidation stage for used nuclear fuel from light water reactors, but before oxide reduction the material form is a homogenized oxide powder. Quantification of the fissile content of this oxide powder is an attractive option due to its homogenized quality which provides the ability to obtain Pu composition and Pu:Cm ratio data from samples representative of the overall input fuel constitution for Pu accountability. Sampling primarily of the electrolyte salt and secondarily of the UNF powder are two products from pyroprocessing that are of interest for use with the HKED.

4.2.1 Sampling Eutectic Salt in the Electrorefiner

A key challenge to implementing the HKED for quantifying nuclear material in pyroprocessing will be sampling the eutectic salt. To ensure diversion of the TRU out of the salt does not take place, a safeguards technique is needed to monitor the eutectic salt of the electrorefiner (ER). TRU accumulates in the process vessel over a series of input used fuel batches and is not removed with the frequency of the pure uranium product [3]. The procedure of allowing TRU to accumulate in the vessel is an important design feature since it makes removal of the TRU from the eutectic salt possible [3]. As of yet, there is no agreed upon monitoring approach to safeguard the fissile material in solution with the molten salt.

4.2.1.1 Salt Removal

Sampling of the eutectic salt may be possible by removing a small quantity of the salt for quantification measurements. This approach is challenged by the high temperature and potential corrosive nature of the salt as well as the need to retain the inert atmosphere inside of the electrorefining vessel. Small samples may be obtained from the vessel through the same process as the removal of the eutectic salt for distillation, in most cases a gravity driven drain, or otherwise isolated and removed from the electrorefiner. For a HKED to quantify the U and Pu in the cooling salt sample, the sample carrier would need to be designed to accommodate (i) the potentially high temperature and radiation, currently done through a shielded carrier for PUREX measurements, as well as (ii) the potentially corrosive nature of the salt being investigated. As the salt cools once outside of the vessel, the changes in density or the formation of cracks or voids as the sample hardens will complicate analysis, but may be mitigated by dissolution of samples in nitric acid [52]. Pre-treatment processes such as dissolution of samples in nitric acid before analysis may need to be further investigated to validate HKED quantification of actinide-

salt samples, although pre-treatment would rather be avoided to reduce sample handling and the preparation time that would be necessary before obtaining assay results.

4.2.1.2 *In-situ* Salt Measurement

Real-time monitoring of molten salts also may be possible when the HKED monitoring system is used. Since the radiometric analysis of samples is of key importance for enabling effective safeguarding of pyroprocessing, proposals for design changes to the electrorefining vessel to incorporate safeguards monitoring devices may be viewed favorably. One such change may include a heated accountancy tube designed as an attachment to the ER vessel wherein a small sample of the electrolyte could be isolated and moved to a position where it may be measured. Isolated electrolyte samples could be brought into a carefully designed HKED installation, retaining the sample in an enclosed geometry to avoid the difficulties of handling or removing a molten salt. The x-ray tube of the HKED should be able to measure through the materials of the accountancy tube and may be capable of quantifying U and Pu and potentially Np and Am at this specific phase. This approach to real-time monitoring would avoid potential difficulties with extreme temperature, corrosive material, and inert atmosphere – which must not be altered inside the electrorefining vessel. Such a design change to the vessel would take advantage of the fact that pyroprocessing is still in the prototype stage. Thus no costly retrofits will be required to update any currently operating pyroprocessing plants.

4.2.1.3 Salt Standards

Creation of salt-based actinide standards will be required to gain insight into responses from sample materials with non-standard matrices. Reference samples reflecting the cooled form of the eutectic salt should be investigated for HKED validation as a quantitative analytical method. These and other potential approaches to process monitoring of the eutectic salt must be developed and demonstrated by experiment and

testing. Additionally, experimental standards and simulation development should focus on demonstrating the performance of this approach under a full dynamic range of actinide concentrations of interest.

4.2.2 Sampling Alternatives

Some proposed safeguards plans anticipate largely relying on destructive analysis or burnup calculations to quantify special nuclear material, potentially including alternative nuclear material [14, 35]. However, additional time spent on destructive assay compared to nondestructive assay based strategies confines the results obtained to apply only for final dispositive accuracy and places temporal strains on the material balance plan. Reliance on burnup calculations to quantify special nuclear material is known to have a large uncertainty. However, these impediments may be alleviated through operation of a HKED system designed to accommodate the sampling forms and environment of the pyroprocess.

4.2.2.1 Assaying Metal Deposits

The uranium and transuranic products removed from the back end of the process undergo plating or dendritic deposition onto a cathode and are removed as metal chunks. These metal chunks exhibit much higher densities than the solutions typically monitored with the HKED. The K-edge modality, used for primary constituents, may not be applicable for the other stages in the pyrochemical process, due to the expected high densities of the samples. However the energy dispersive XRF may have applications for quick elemental analysis. Sample pre-treatment such as dissolution in nitric acid would be necessary; an additional step to alter the form of the sample to be measured could be added to allow for timely actinide quantification with HKED. Such updates to the pyroprocess safeguards scheme would potentially enable the use of HKED to assay the uranium deposit on the cathode or the TRU deposit following electrowinning.

4.2.2.2 Assaying Voloxidation Powder

A secondary alternative material form for which HKED-based assay may be possible is the used nuclear fuel voloxidized oxide powder. After the voloxidation stage for used nuclear fuel from light water reactors, but before oxide reduction the material form is assumed to be a homogenized mixture of oxide powder [14]. Quantification of the fissile content of this oxide powder is an attractive option due to its homogenized quality which provides the ability to obtain Pu composition and Pu:Cm ratio data from samples representative of the overall input fuel constitution for Pu accountability. Still, sample pre-treatment would be necessary to accommodate the expected high density of such samples.

4.2.2.3 Assaying Alternative Nuclear Material

Recent increased emphasis in tracking Am and Np coupled with the increase in the Pu amounts relative to U in proposed processing solutions has required validation of HKED software for these applications [72]. Recent studies have investigated the ability of HKED to conduct simultaneous elemental analysis for minor actinides in eutectic salt sample through liquid-liquid extraction in the electrorefiner [52]. These studies have shown that the HKED is capable of assaying Np, Am, and Cm at minimum detection quantities of 50 μg, 70 μg, and 100 μg, respectively, for measurement precision approaching 5% [52]. Further study in this area is critical to continuing development of a HKED based monitoring plan for minor actinides.

4.3 Requirements for Enhanced Development

The feasibility and role of HKED for pyroprocessing measurements is not yet established, and several technological and practical challenges need to be addressed. The reason why it is being considered as a monitoring tool at proposed pyroprocessing facilities is because the system is a powerful tool widely used at reprocessing sites

worldwide, enabling determination of elemental uranium and plutonium with a single measurement and offering onsite, relatively fast quantification compared to other options of similar precision and accuracy. It may become capable of overcoming the sampling challenges inherent to pyroprocessing.

Adapting to the sampling needs characterizing pyroprocessing will require sampling and measurement capabilities for high density, corrosive, high temperature samples with new forms or surrounding material matrices that have yet to be established as viable for the measurement range of the HKED. The system may need to be tested against possible non-homogeneities of samples [46], high concentrations of heavy metals [73], and higher actinide concentrations expected of the safeguards measurements. To accommodate the vastly different actinide concentrations and ratios encountered with pyroprocessing sampling, both new reference materials (standards) and algorithms will be needed. Extending the HKED system beyond its current applications should include simulation developments to encompass the expected materials and concentrations which are beyond the range of existing representative standards.

A key challenge to implementing HKED for quantifying nuclear material in pyroprocessing will be sampling the eutectic salt. Material balances found in the literature have made it possible to analyze the concentrations of uranium- and plutonium-chlorides in LiCl-KCl eutectic salt of the electrorefiner [50, 74]. However, the importance of determining the input material form and composition is highlighted by the difference between the work by Vaden and the work by Mariani, where Vaden shows the weight percentage of uranium in the salt at less than 1.0% while Mariani publishes greater than 10.0% [50, 51]. Thus, at this time, there is a broad range of design basis for pyroprocessing against which to create an analytical capability. With no standardization in the field of pyroprocessing for expected actinide concentrations sampled out of the

electrorefiner, the difficulty of creating a comprehensive set of calibration standards to evaluate on the HKED system is apparent. Efforts to determine the best range of acceptable standards should be made to reduce the disparity between analyses and come closer to an agreed upon range of actinide concentrations existing within the electrorefiner.

4.3.1 Standards Development

Creation of salt-based actinide standards are required to gain insight into responses from sample materials with non-standard matrices. For the expected operating materials, concentrations, and ratios, a set of complex solution standards may be produced providing an extension on the existing standards limitations. The total number of standards should encompass the expected concentrations ranging from 0 to 200 grams per liter of uranium and plutonium with a modest increment of intermediate values (e.g., 50 g/L increments). A subset of these standards also should contain the amounts of minor actinides present in order to allow the HKED system to analyze process samples and validate multi-elemental analysis software, which then can be used to evaluate and refine the current algorithms. Based on UNF actinide contents in Table 4.1 and the dynamic chemical equilibrium in electrorefining and electrowinning summarized in Table 4.2, standards with appropriate concentration ranges for Np, Am, and Cm could be prepared. Tables 4.1 and 4.2 summarize the actinide inventory of the spent fuel from a typical light water reactor and the actinide inventory of the electrolyte salt, respectively, evaluated by the Nuclear Energy Agency for the Japanese Central Research Institute of the Electric Power Industry's (CRIEPI) pyrochemical process [75]. Higher relative concentration standards also may be created in complex salt solutions reflecting the expected electrolyte weight percentages and densities under measurement conditions.

Table 4.1. Typical Actinide Composition of a LWR Spent Nuclear Fuel Assembly.

Element	5 Years Cooling Time		30 Years Cooling Time	
	Burnup, 45 GWd/t kg/t	**Burnup, 60 GWd/t kg/t**	**Burnup, 45 GWd/t kg/t**	**Burnup, 60 GWd/t kg/t**
U	941	923	941	923
Pu	11.2	12.6	10.2	11.5
Np	0.57	0.78	0.57	0.78
Am	0.51	0.74	1.38	1.78
Cm	0.033	0.113	0.014	0.0497
Total TRUs	12.3	14.2	12.2	14.1

Reproduced from [75].

Table 4.2. Equilibrium Composition of LiCl-KCl Salt Bath for LWR UO_2 and MOX fuel.[a]

Element	UO_2		MOX	
	Burnup, 45 GWd/t kg	**Burnup, 60 GWd/t kg**	**Burnup, 45 GWd/t kg**	**Burnup, 60 GWd/t kg**
U	67	67	67	67
Pu	100	100	100	100
Np	5.1	3.7	6.1	3.6
Am	4.5	6.3	*5.8*	7.5
Cm	0.3	1.0	0.9	1.9
Rare Earth	125.5	44.5	146.2	63.4
I	0.1	0.1	0.3	0.2
Cs, Sr, Ba	41.7	15.6	48.1	22.1

Data obtained from [75].

[a]Normalized for 1000 kg UNF.

4.3.2 Algorithm Development

New software has been introduced to the HKED system updating the data acquisition and analysis routines (built on VAX/VMS® platform) to Windows® platform, thereby accommodating modern PC users [70, 76]. Strategies using the new platform must accommodate higher levels of U/TRU, where the concentrations of uranium and plutonium approach 1:1. This has necessitated the validation of HKED system software through more complex representative material standards. Additionally, HKED's multi-elemental analysis approach may expandable beyond the current region of interest (ROI)

based analysis. New algorithms currently under development will accommodate the more complex solutions of pyroprocessing by using a spectral fitting routine allowing for simultaneous calculation of uranium and plutonium with suitable means of disregarding the responses from other actinides [77, 78]. Potential additions may account for influences of temperature, density and structural changes that will need to be taken into account when analyzing a cooling or cold form of the molten salt.

4.3.3 Simulation Development

Transition to using the HKED will depend on simulations that could assist in the extension of this assay method to predict the detector response to the new sample types and configurations. The limited availability of representative solution standards expected from pyroprocessing molten salts have spurred efforts to develop Monte Carlo models to facilitate algorithm development and optimization of the measurement configuration of the HKED system. Simulations will be needed to accommodate the expected different actinide concentrations and ratios encountered with pyroprocessing sampling and to assess the capabilities and limitations of such an approach. It is expected that a realistic HKED model will reflect any potential alterations to the HKED system, allowing for a reduction in the calibration efforts, an extension of the applicability of the method, and an inclusion of an extensive range of system effects influencing the measurements.

CHAPTER 5

SIMULATION TECHNIQUE

5.1 Representation of the Hybrid K-Edge Densitometer in MCNP

The goal of this work was to develop Monte Carlo simulations to extend the hybrid K-edge densitometry system to pyroprocessing safeguards measurements. The simulation tool was to be used to interpret the expected results from known samples, examine the response of the HKED system to more complex sample types, and develop new algorithms. In order to do this, a computer model was created for use with the Monte Carlo N-Particle (MCNP) radiation transport code to produce a faithful representation of the resultant spectra of nitric acid based uranium and plutonium standards when compared to experimental spectral results derived from the Oak Ridge National Laboratory (ORNL) Radiochemical Engineering Development Complex (REDC) Hybrid K-Edge Densitometry (HKED) measurement system.

Monte Carlo simulation is a common computational approach for modeling radiation transport. MCNP was chosen as it offers capabilities to simulate and interpret the spectral data and is straightforward to implement [79]. The approach for developing the model's geometry in SolidWorks before transitioning the dimensions into the MCNP model resulted in high confidence that the simulated HKED was an accurate representation of the realistic system. A precisely defined geometry derived from the manufacturer's drawings of the HKED allowed for exact dimensions to be modeled. With both a precisely defined geometry and an accurate source term for the representation of the interrogating x-ray tube spectra, a faithful representation of the HKED spectra can be simulated.

The objective was then to apply the validated model to simulate the XRF and KED spectral shape from salt samples representative of those expected from the pyroprocessing electrorefining vessel. The research endeavors included determining how well the underlying Monte Carlo physics models and associated data libraries represent the realistic atomic relaxation processes of the actinide fluorescence systems and the mass attenuation coefficients of the elements being examined. This was assessed by generating spectral results of K-edge and x-ray fluorescence modalities from Monte Carlo simulations of the performance of the HKED under different conditions (i.e. the ability of the model to efficiently reproduce the x-ray radiation transport as well as accurately generate characteristic actinide x-ray intensities and branching ratios). Deviations were examined to determine any necessary corrective actions.

The most recent version of MCNP, MCNP6.1, was used in the simulations to take advantage of recent developments in photon transport models [80]. The x-ray peaks and the K-edge magnitudes were smoothed with the Gaussian energy broadening function within MCNP to simulate the detector resolution. Various variance reduction techniques were applied to the MCNP model in order to develop a computationally efficient simulation. Spectral results of the MCNP model were obtained from pulse-height tallies over the active regions of the detector crystals to determine the pulse-height spectra.

5.1.1 Simulation Geometry

In order to create a highly detailed and accurate representation of the HKED in MCNP, the geometry of the HKED was first constructed in SolidWorks. The geometric configuration and the physical characteristics of the ORNL REDC HKED system are seen in Figure 5.1. Development of the model included a detailed physical description of the measurement geometry of the HKED to minimize interferences from radiation sources within the sample with the interrogating x-ray generator's bremsstrahlung

spectrum. From the precise CAD model, MCNP simulations of both the KED and XRF modalities were carried out to establish a calibration approach for both branches of the system, shown in Figure 5.2.

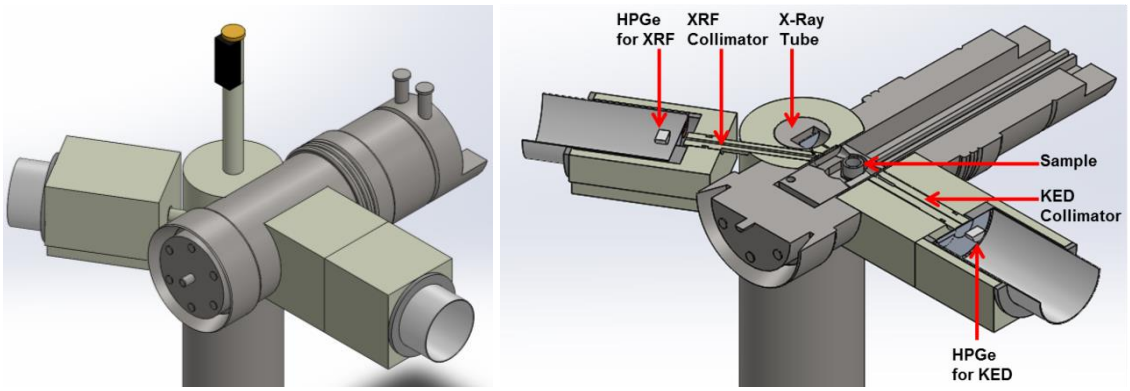

a. **b.**

Figure 5.1. CAD-based model representative of the detailed model of the ORNL REDC HKED with (a) an isomeric view of the HKED and (b) an isomeric top-view cross section of the CAD model.

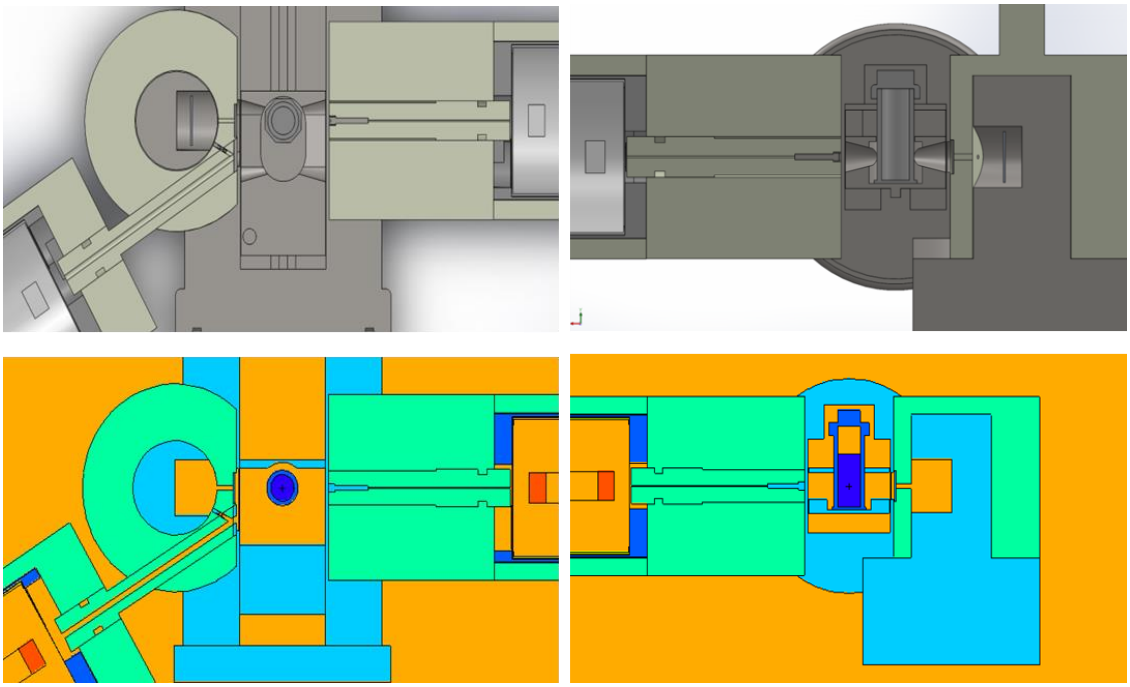

a. **b.**

Figure 5.2. Translation of the CAD-based model of the ORNL REDC HKED (Top Row) into the Visual Editor program for visualization of MCNP input files (Bottom Row) for (a) a top-view cross section and (b) a side-view cross section of the KED collimation line.

The HKED system response is very sensitive to the attenuators in the radiation transmission pathways and the structural surface angles that contribute scattered radiation to the spectral response. In order to have high confidence that the system dimensions were accurately translated into the simulation model, three approaches were used. First, engineering drawings from Canberra, the manufacturer of the ORNL REDC HKED, were analyzed for all pertinent details regarding the interior system dimensions. However the available drawings were created for use by customers installing the HKED system and thus mostly dealt with the exterior dimensions and shielding of the HKED system. The lack of precise details of the interior attenuators and radiation pathways necessitated a second approach to determining the system details.

The ORNL REDC HKED was systematically taken apart piece by piece and each of the components was photographed and measured, recording the dimensions to four significant digits (e.g. 14.17 mm). This approach proved to be the most useful for obtaining the precisely detailed geometry of the entire system. A sample of one of the sets of photos is shown in Figure 5.3. Crucial components such as the XRF collimator, the KED stainless steel beam filter, and the x-ray tube cadmium filter were isolated and measured.

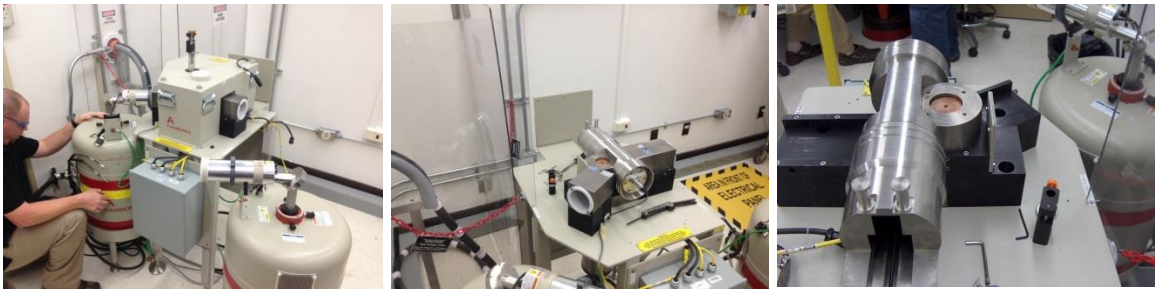

a. **b.** **c.**

Figure 5.3. Sampling from the set of deconstruction photos taken of the ORNL REDC HKED showing (a) the system with the lead outer shield, (b) the system with the outer shield removed and x-ray tube shield open, and (c) the system further deconstructed so individual components can be isolated and measured.

The final approach to determining the HKED dimensions was through a literature review of the documents pertaining to the use and application of the HKED. Several documents provided insight into the inner dimensions and angles of the HKED [69, 81, 82]. Such sources were only used to get rough ideas on system dimensions since there are multiple HKED system designs and updates that have come since the original system was created. Thus this approach was the least useful as none of the public literature was representative of the exact ORNL REDC HKED system.

5.1.1.1 XRF Pathway

Attenuator thickness along the XRF pathway includes 0.95 mm of beryllium (from 0.8 mm x-ray tube filter and 0.15 mm germanium detector endcap thickness), 1.05 mm cadmium (from the x-ray tube filter), 0.2854 mm stainless steel (from two passes through 0.13 mm of stainless steel milled out window of the sample transfer tube, and 0.0254 mm of the stainless steel XRF filter), and 0.0254 mm gadolinium (from the gadolinium XRF beam monitor). The XRF pathway is defined as the x-ray tube radiation attenuated along a single 31^0 backscatter within the sample vial between the x-ray tube source emission point and the front face of the XRF low-energy germanium (LEGe) detector. The tungsten collimator inner diameter for the XRF pathway is 3.0 mm.

5.1.1.2 KED Pathway

The KED pathway includes the 0.95 mm of beryllium (from 0.8 mm x-ray tube filter and 0.15 mm germanium detector endcap thickness) and 1.05 mm cadmium (from the x-ray tube filter), in addition to a total stainless steel thickness of 25.8 mm (from the 0.13 mm milled out window of the sample transfer tube, the 1.99 mm wall of the opposite side of the sample transfer tube, and the 23.58 mm length of the KED beam filter). The KED pathway is defined as the x-ray tube radiation transmitted through the sample and stainless steel KED beam filter, along the KED collimator, to the surface of the KED LEGe detector. The tungsten collimator inner diameter is 0.8 mm for the KED pathway.

5.1.1.3 Sample Vial

The high density polyethylene sample vial has inner and outer diameters of 14.18 mm and 18.96 mm, respectively.

5.1.1.4 Beam Monitor and Calibration Source

To maximize the flexibility of the simulation to take modifications of the HKED system into account, both the beam monitor and cadmium calibration source were separately

modeled. The beam monitor port provides a real-time parameter to monitor the x-ray tube operation and the cadmium calibration source is used to determine energy calibration and detector resolution as well as account for any temporal drift of the calibration [81]. Including these sources had a minimal impact on the photon energies above the K-absorption edge of the lowest atomic weight actinides. Though this provided measurement responses mostly below the range of the photon energies used to determine actinide concentrations, the transport of the low-energy photons was included in the model to ensure a realistic response. This allowed for the model to reflect changes to the spectrum caused by any structural or geometrical adjustments made to the HKED system to accommodate the new sampling environment of pyroprocessing.

5.1.1.5 Final Dimensions

Final dimensions of the HKED simulation can be found in the sample MCNP input file in Appendix B. Once developed, the computational model played an important role in helping identify attenuator thicknesses for those dimensions difficult to measure by hand. In one case, comparing the model predictions to observed responses from the ORNL REDC HKED was used to discover an inaccuracy in one of the manufacturer's defined dimensions documented in the Hardware Reference Manual, a proprietary document which only comes with the purchase of the Canberra HKED. The milled out window of stainless steel in the sample transfer tube between the x-ray tube and XRF detector and the sample chamber was published to be 0.5 mm but determined through simulation to be in fact approximately 0.13 mm.

5.1.2 Source Term Definition

The MCNP code has proven well suited for simulating the spectral distribution of x-ray tube radiation [83, 84]. Semi-empirical models and analytical functions have also been used to generate x-ray tube spectra [85, 86]. In order to obtain a source profile for the

highly intense bremsstrahlung spectra generated by the x-ray tube employed by the HKED, the SpekCalc program was utilized for calculation of the x-ray spectra from the tungsten anode x-ray tube [87]. SpekCalc was chosen as a convenient means of generating the x-ray source spectral profile that could easily be formatted into the MCNP source term definition. Comparison of the SpekCalc generated x-ray tube source term with MCNP generated results, analytical functions, and the semi-empirical models can be found in Appendix D.

To model the tungsten anode x-ray spectra using SpekCalc, the following parameters for the operating conditions were required to be input: peak energy [keV], theta [degrees] (the takeoff angle from the anode), and attenuator thicknesses [mm] (including air, beryllium, aluminum, copper, tin, tungsten, tantalum, and water). Figure 5.4 shows an example of the graphical user interface of the SpekCalc software. The *Nf* and *P* parameters in Figure 5.4 are normalization factors for the bremsstrahlung and the characteristic radiation, and were unchanged from the default values.

Only a small portion of the HKED sample vial is irradiated by the x-ray tube due to the tungsten shield collimation window, a rectangle roughly 2 mm wide and 3 mm tall. A significant emphasis is placed on determining the volume of the active interrogation region within the sample in order to accurately relate the actinide content of the sample to the actinide content of the bulk material from which the sample was taken. Thus the location on the sample vial where the x-ray tube source photons enter was determined through the use of x-ray photo paper. Photo paper was wrapped around a sample vial and irradiated, as shown in Figure 5.5. This analysis confirmed the active irradiation region on the vial and defined the size of the irradiation window of the sample for the simulation.

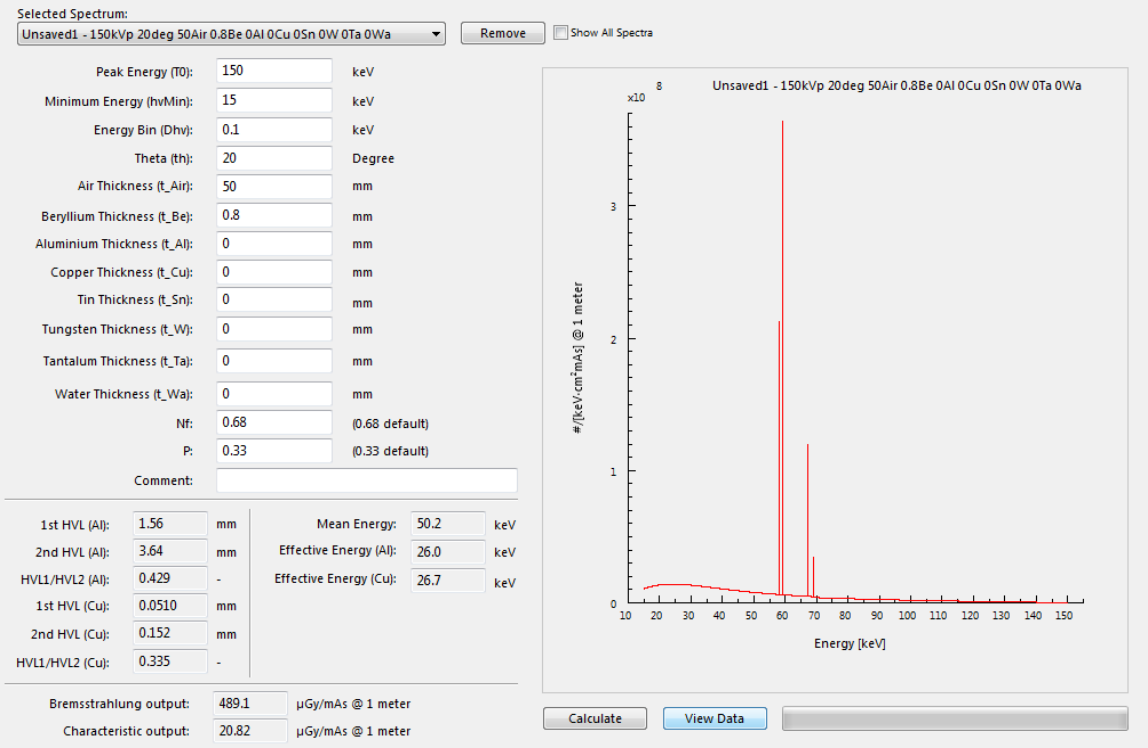

Figure 5.4. Graphical user interface for SpekCalc showing the generation of tungsten anode source spectra for a set of input operating conditions (150 keV peak energy, 0.1 keV bin size, 20 degree takeoff angle, 50 mm of air, 0.8 mm beryllium).

Figure 5.5. Sample container wrapped in photo paper to determine the active area of the irradiating x-rays from the x-ray tube.

5.1.3 MCNP Data Libraries

Recent developments [88] in photon transport models have moved past the simplified treatment of the Kβ-series fluorescence x-rays [89] to improve the quality of the photoatomic data by providing more detailed atomic relaxation processes. This has led to refined fluorescence systems in which analog sampling of the relaxation cascade is available. Previously, fluorescence systems had been weighted averages grouped into only two electron shells, K and L. Since the simulation accuracy strongly depends on the underlying physics models organized in the MCNP photoatomic data libraries, the inclusion of new data for electron subshells removes the bias in the peak intensities and spectral shapes. Hence, the most recent version of MCNP (MCNP6.1) was used along with an updated photoatomic data library (eprdata12) to allow the HKED model to include the effects of the new set of photoatomic data. One drawback of using this updated version, however, is the approximately 0.5 keV offset in the energies of the x-rays to higher values which was not present in some earlier versions. A post-processing routine was needed to reshape the simulated results into agreement with the generally accepted values. Alternatively, the database could be corrected [90]; however this task was outside the scope of this work.

5.1.4 MCNP Tallies

MCNP pulse-height tallies can be used to represent the spectral responses of multichannel energy deposition detectors such as the LEGe detectors used within the HKED system. Pulse-height tallies count the number of pulses of differing amounts of energy deposited in a crystal detector and bin the results according to the energy of the incident particle [79]. These tallies have been widely used for the simulation of detectors in the field of nondestructive analysis, nuclear safeguards, and homeland security. Coupled with an appropriate detector response function, such as a Gaussian broadening

function, the pulse-height tally can be used effectively to reproduce the spectral responses of nuclear detection devices.

Pulse-height tallies were performed over the active region of both the XRF and KED detector crystals to simulate the pulse-height spectrum of the bremsstrahlung and characteristic x-rays scattering and being transported within the HKED system. The generated spectra represent the responses from an ideal detector with optimal resolution, so the spectrums were convoluted with detector response functions to reproduce a typical observed pulse height spectrum from the LEGe detectors. In order to compare the simulation with experimental data, the same energy per channel was mirrored for the simulation spectra to match the calibration of the experimental data.

A separate experiment tracking the K-edge vacancy production within the sample vial was accomplished using a combination of a different tally and a new tally collection tool available in MCNP6.1. The K-shell vacancy production experiment, discussed in Section 7.1.2, employed a cell flux tally for each cell within a discretized mesh over the sample vial. The collection tool, called tally tagging, allows the user to separate the tally into the components of interest. The tally can be specified only to be populated with particles fitting a list of designations, such as only particles that have undergone incoherent scattering or all particles that are uncollided. For example, the tool can be used to tally particles as specific as the deexcitation gammas from the spallation of ^{56}Fe into ^{52}Cr [80]. The designations for which particles are tallied extends to the photon description of K-shell x-rays or even fluorescence x-rays from a specific element. The new tally collection tool was applied to only populate the cell flux tally with those K-shell fluorescence photons from uranium.

5.1.5 Gaussian Broadening

The Gaussian Energy Broadening (GEB) function in MCNP was used to simulate the detector resolution, based on the full-width-at-half-maximum (FWHM) data. This smoothing function broadens the pulse-height tally results in order to represent the electronic effects of the detector response functions. According to Canberra, their low energy germanium detector with 200 mm^2 surface area has 170 and 520 eV resolution at 5.9 and 122 keV, respectively [91]. The required parameters for the GEB function were fit to the Equation 5.1 to obtain the GEB parameters where a and b are the fitting parameters and E is the energy in units of MeV [92]. The fitting parameters were determined to be: a =7.13335E-05 and b = 1.28453E-03 and the fitted function can be seen in Figure 5.6. Both the HKED XRF and KED modalities were broadened using the GEB function, however a further modification of the XRF x-rays for the higher atomic number elements was necessary to include a Voigt profile to account for the natural line width of the x-ray lines.

$$FWHM = a + b\sqrt{E} \quad [92] \qquad \text{Equation 5.1}$$

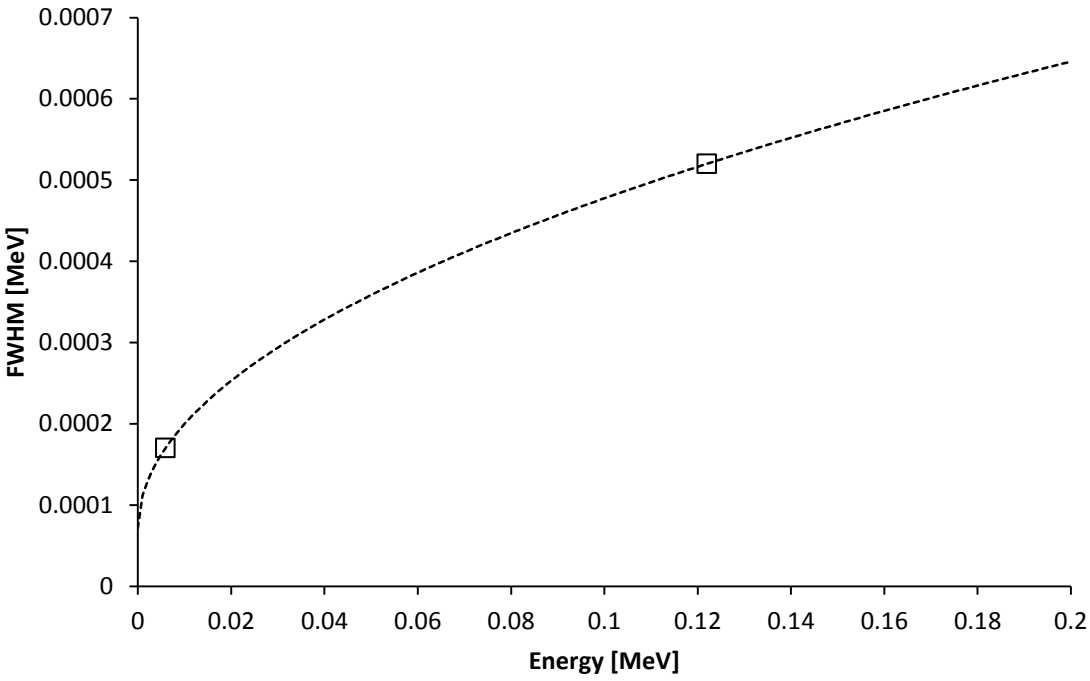

Figure 5.6. Fit of the FWHM for the HKED LEGe detectors as a function of energy to obtain the Gaussian energy broadening parameters.

5.1.6 Variance Reduction Approaches

To increase the efficiency of execution of the model, intrinsic optimization techniques within the MCNP code were applied to minimize the model run time. The computation speed of the simulation was optimized via the use of variance reduction techniques. While this was helpful to increase the computational efficiency of the KED branch simulation, the use of variance reduction methods was implicitly required for the XRF branch model in order for the simulation to converge within a practical timeframe. From running analog simulations of the XRF branch, it was determined that around 10^9 simulated source photons emitted from the x-ray tube are needed to get one fluorescent K x-ray at the surface of the XRF detector. Simulation of a full 1000 second XRF spectrum, which accumulates between 10^7 to $4*10^7$ counts, would require around 10^{16} source

photons and necessitate an infeasible amount of processing hours to calculate. This constituted a computational challenge to reproduce the simulation of the XRF modality in an accurate while computationally efficient way. Thus, a range of variance reduction techniques featured within MCNP were analyzed: (i) geometry splitting and Russian roulette, (ii) weight windows, (iii) DXTRAN spheres, (iv) point detector (next-event estimator) scoring and ring detector scoring, (v) source biasing, (vi) forced collisions in the sample, (vii) and exponential transform [80].

5.1.6.1 Geometry Splitting, Russian Roulette, and Weight Windows

Geometry splitting, Russian roulette, and weight windows can all be used to increase the number of particles within the important regions of the simulation and reduce or remove particles from unimportant regions [79]. To ensure the problem does not become distorted, the increased number of particles in the important region has a corresponding decrease in the weight, or importance for each of the particles. Russian roulette refers to the process of removing particles from the simulation once their weight has decreased below an imposed limit. Geometry splitting allows the particles entering specific cells to be expanded in number of particles but with reduced weights, while weight windows can be applied as a mesh that can be placed throughout a geometry and alter particle importance at the boundaries of the mesh. While these techniques are important for other simulations, such as deep penetration problems, they were not applicable in simulation of the HKED. These approaches do not adequately reduce the variance of a simulation with narrow and highly collimated regions of importance, such as the HKED system. Thus the importance of each particle within the geometry was kept constant and neither geometry splitting, Russian roulette, nor weight windows were employed.

5.1.6.2 DXTRAN and Point Detectors

The narrow and highly collimated region of the HKED system, specifically the XRF branch, requires a unique approach to transport particles from the area of interest within the sample vial to the XRF detector. Since the fluorescent x-ray current at the face of the XRF detector is approximately 10^9 times smaller than the photon current exiting the x-ray tube, the probability for each simulated particle to interact within the sample vial and be then transported to the detector is vanishingly small. This great difference is due in part to the narrow collimation to the XRF detector to limit the backscatter from the incoherently scattered x-ray tube bremsstrahlung and limit the detection of fission product gamma-rays. For the case of tallying x-rays generated within the sample vial, it is also due to the probabilities of a particle remaining attenuated along the pathways between the x-ray tube and the XRF detector combined with the probability of interaction with a x-ray generating element in the sample and that x-ray being transported in the correct solid angle towards the XRF detector. This likelihood is increased when considering the multiple scatterings particles undergo within the system, but by a negligible amount.

In cases such as this, pseudoparticles [79] can be generated at all collision and interaction points in the system and then transported with attenuation through space to the detector region where the probability of transmission is very low. Both point detectors [79] and DXTRAN spheres [79] can be used to generate and transport these pseudoparticles. The difference is the DXTRAN sphere forms a region in space, instead of a point, where the particles can be deterministically transported and then allowed to scatter and be tallied within the volume of the sphere. Additionally, in simulations with symmetrical geometry about the axis, ring detectors can be used instead of point detectors to enhance the efficiency of the calculation.

Both point and DXTRAN based techniques were investigated. It was discovered that due to the logic of the pulse-height tally variance reduction processes, the combination of the new MCNP data tables with the updated fluorescence libraries with the DXTRAN sphere and the pulse height tally was incompatible. Thus, the point detector, also called the next event estimator, was chosen to reproduce the XRF branch spectral response. The downside to using the point detector tally for variance reduction was that the simulation was then separated into two parts, increasing the computation time needed to produce results. The first part utilized the point detector tally for particle transport to the detector and the second simulated the detector response with the pulse height tally. Of all the variance reduction techniques applied to the simulation of the HKED, the use of the point detector for variance reduction resulted in the largest reduction of computational time required for simulation convergence.

This two-part variance reduction technique was only applied to the XRF branch simulation. The first part tallied the data of the x-ray generation and transportation to the XRF detector and the second part simulated the scattering of along the collimation pathway and the detector response. The starting point for the new source term of the second part was placed at the entrance to the XRF collimator to ensure that the simulated particles were not attenuated more than once for each material along the transmission pathway. Since the HKED system is rotationally symmetric, we were able to utilize a ring detector to efficiently attenuate and transport the pseudoparticles to the face of the XRF detector. A consequence of this variance reduction technique approach is that there is a small probability of a simulated particle being transported to the XRF detector while tallying pseudoparticles. This results in a large error due to the abrupt difference in weight of the pseudo- and nonpseudoparticles. A radius of exclusion was set around the ring detector to prevent this occurrence.

5.1.6.3 Source Biasing

The second largest reduction in computational time required for the simulation to converge came from application of source biasing. In practice, the x-ray tube generates x-rays within a cone of emission much larger than the solid angle subtended by the KED collimation. Much of this radiation results in capture within the tungsten x-ray tube shielding. In order to avoid using computational time to simulate this process, the source term for the x-ray tube simulation was directionally biased to have a two order of magnitude higher probability of being emitted within a 1° cone of emission. This biasing results in a very small overlap of the emitted source particles with the collimation exit of the x-ray tube shield. In this way, the correct representation of the interaction area within the sample vial was obtained while minimizing tracking of source particles not likely to contribute to the tallies of interest.

5.1.6.4 Forced Collisions

The forced collision variance reduction technique imposes a requirement that all particles entering a cell must interact within the cell [79]. This technique was utilized to increase the interaction rate in the sample vial in the case of the XRF branch simulation.

5.1.6.5 Exponential Transform

The exponential transform method stretches the path length between collisions in a preferred direction to limit the amount of captured particles passing through a cell [79]. The x-ray tube photons must pass through a cadmium filter before they can interact with the sample and similarly the photons transmitting through the sample must pass through a stainless steel filter before reaching the KED detector. These filters are used to remove many of the unimportant low energy x-rays that will not contribute to the XRF or KED detector response. However, simulated particles absorbed by these filters represent wasted computation time as they do not contribute to the detector response. Thus, the

exponential transform was applied to these filters, effectively reducing the total cross section by a set input value. A range of values between 0 and 1 were analyzed for use as the stretching parameter to control for any potential biases from this variance reduction technique. A value of 0.9 was used for both filters, limiting the capture of radiation within the filters to a maximum of ninety percent of the theoretical value while retaining the attenuation effects of the material on the transmitted photons. As this artificial increase in the path length between collisions is correspondingly offset by a decrease in the weight of the uncollided particles, the application of the exponential transform does not skew the distribution of transmitted particles.

5.2 Detector Responses of the Hybrid K-Edge Densitometer in MCNP

To validate the developed MCNP models, experimental data from two sets of uranium nitrate and uranium-plutonium nitrate standards were used to ensure the modeled system matched experimental results. Samples containing mixtures of actinides matching those analyzed on the ORNL REDC HKED system [93] were simulated and the resultant spectra were compared to the measured spectra. The capability of the MCNP simulation to accurately reproduce the measured spectra was verified. Simulation of the XRF and KED modalities were found to be in good agreement with the experimental data except for several systematic issues. Those issues included: (i) an energy offset for the fluorescent x-rays in the MCNP database, (ii) insufficient simulation of the scattering effects in the system, (iii) unavailable broadening parameters within MCNP for representing the the spectral profile of fluorescent x-rays, and (iv) no representation for the pulse-pileup effects in the simulated detector. Several post-processing methods were needed to adjust the MCNP spectral results in order to correctly represent the realistic parameters and processes.

5.2.1 X-Ray Fluorescent Responses

The use of MCNP to provide realistic XRF assay results was examined and found to be able to acceptably reproduce the x-ray bremsstrahlung spectrum scattering, interaction, and transmission. However, the MCNP code was found to be severely deficient in reproducing fluorescent x-rays energies and peak profiles. There is a lack of fidelity between the MCNP photoatomic data in comparison to the generally accepted theoretical values published by the National Institute of Standards and Technology (NIST) [94]. An approximately 0.5 keV offset is present between the energies of the actinide x-rays and the generally accepted energies. This offset presented a challenge when comparing the experimental and simulated detectors with the same channel to channel energy variation. Moreover the offset was present for the x-rays of all elements and it increased with increasing atomic number as shown in Figure 5.7. The $K\alpha_1$ and $K\alpha_2$ x-rays of the elements plutonium, uranium, lead, tungsten, gadolinium, and xenon are shown follow a quadratic fit with a low residual. However, the offset between each element's $K\alpha_1$ and $K\alpha_2$ x-rays is shown to increase towards higher atomic numbers, suggesting a more fundamental reason behind the origin of the energy offset.

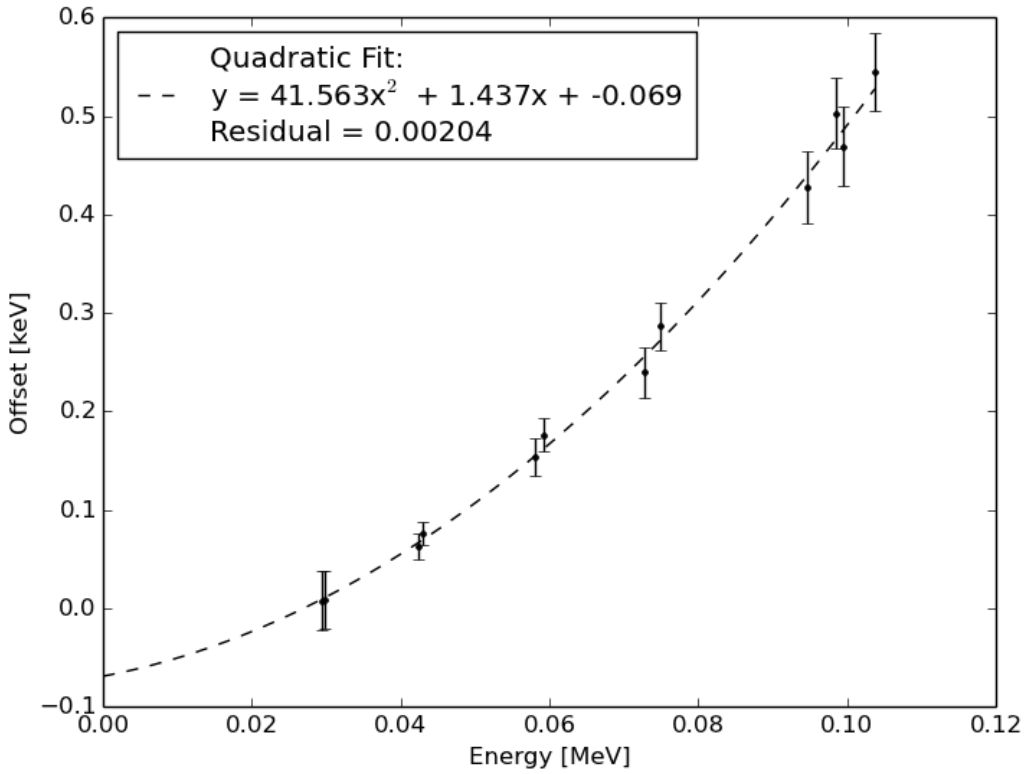

Figure 5.7. The increasing offset between x-ray energies in the MCNP photoatomic datatables and the x-ray energies published by NIST [94].

In addition to the energy offset, MCNP does not fully reproduce peak shapes for x-rays from large atomic weight elements. The only available function available for representation of the detector response functions in MCNP is the Gaussian energy broadening function [80]. However, the characteristic x-rays have a natural Lorentzian distribution [95]. In most cases, this natural line width is only a few eV, and is not distinguishable from the Gaussian detector response in x-ray spectra measured with high-quality semiconductor devices. However, for elements with atomic number above 50, this width begins to exceed 10 eV and a Gauss function is no longer an adequate approximation of the peak profile. Treatment of the peak profile then requires a convolution of the Gaussian and Lorentzian peak profiles, resulting in a Voigt profile

which must replace the Gaussian shape. This Voigt treatment is not available in MCNP, detracting from the usefulness of MCNP for simulating the correct peak profiles of x-rays.

Design of a HKED simulation model without an accurate means of simulating the x-ray peak areas would have no application in the development of the HKED for safeguarding pyroprocessing facilities. This is because the x-ray peak areas are the primary source of information for the XRF measurement to determine the relative concentrations of the actinides being assayed. Thus, this deficiency discussed above constitutes an important drawback for the application of MCNP simulations to faithfully represent the XRF spectra of the HKED. Figures 5.8 and 5.9 depict the unprocessed results from MCNP of the HKED system for the XRF branch. As seen in Figure 5.8 and zoomed in on Figure 5.9, the incorrect peak shape and location for the uranium and plutonium samples is highlighted by the large residual in the region corresponding to the x-ray peaks. The residual for both plots is in terms of the standard deviation (σ). Both plots are compared by normalizing the maximum value of the bremsstrahlung spectra, located around approximately 80 keV, to a normalization factor of 1E3.

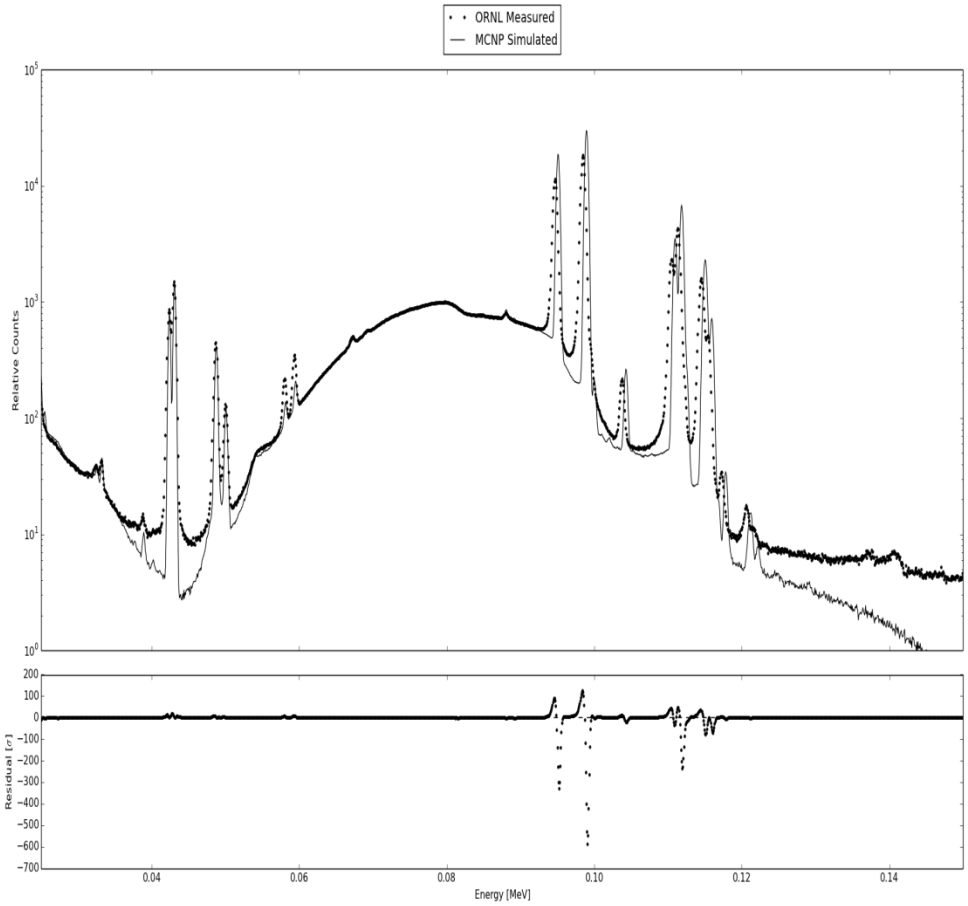

Figure 5.8. Modeled and measured XRF responses of the continuum and the x-ray peaks for a uranium-plutonium nitrite sample with approximately 243 g U/L and 2.93 g Pu/L with the residual shown in terms of sigma.

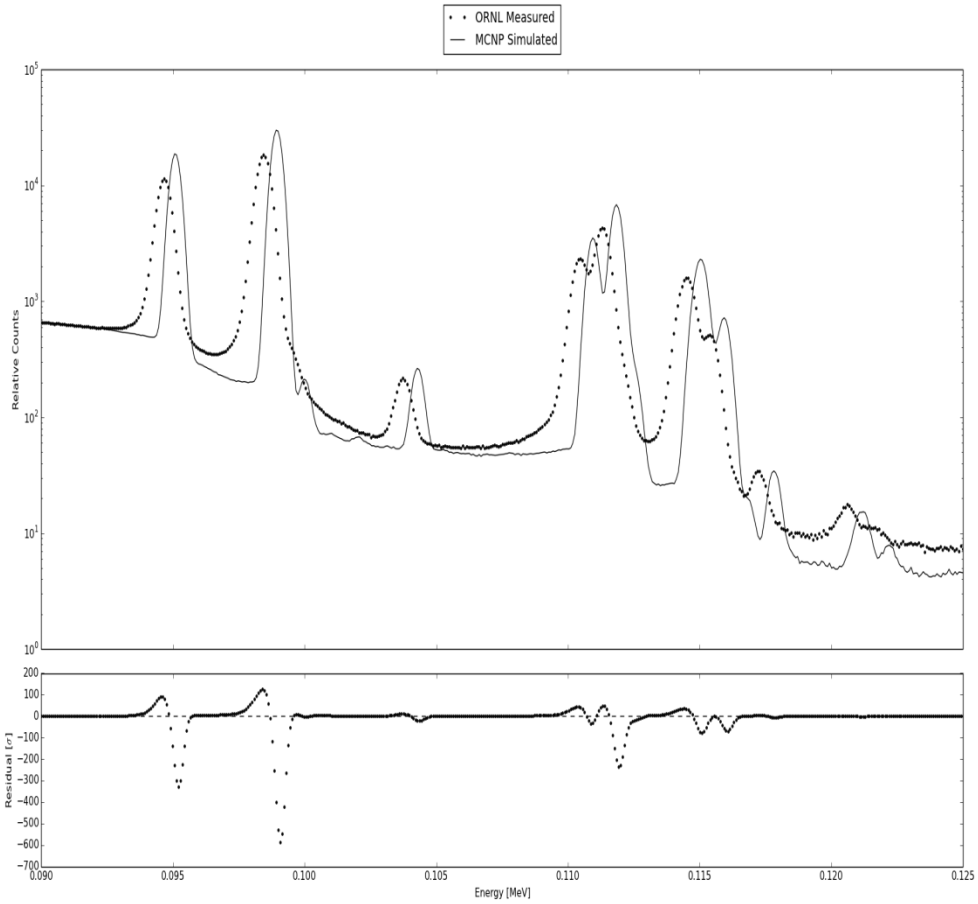

Figure 5.9. Modeled and measured XRF responses of the Kα and Kβ x-ray peaks for a uranium-plutonium nitrite sample with approximately 243 g U/L and 2.93 g Pu/L with the residual shown in terms of sigma. The differences between the measured and simulated responses illustrates the deficiencies of MCNP for the simulation of XRF spectra.

Shown in Figure 5.8, the scattered radiation around the gadolinium peaks near 42 keV was not matched by the simulation, although this deviation is also due in part to the lack of Lorentzian broadening of the gadolinium x-ray peaks. The scattered radiation from the beam monitor and the cadmium calibration source were modeled separately from the radiation incident on the XRF detector from the sample vial. The counts from the

separate runs were normalized to match the correct peak location and combined in post-processing to form the XRF spectral results shown in Figures 5.8 and 5.9. Both the gadolinium beam filter and cadmium calibration source were modeled and were not optimized to precisely match the resultant XRF spectrum since neither dramatically impacts the areas of high importance, namely the energy region containing the actinide Kα and Kβ x-rays. Thus the scattering in the XRF collimator and the correct tailing of the peak profiles around the gadolinium peaks was not accurately reflected in the preliminary results.

The impact of pulse pileup in nuclear detector systems accounts for the deviation between the simulation and the experimental results towards the highest energy values shown in Figure 5.8. The pulse-height tally in MCNP does not simulate the effects from pulse-pileup as this effect is due to multiple particles arriving to the detector within the detector resolving time and in simulation the particles are tracked individually. The lack of simulated pulse pile up affected the spectral responses of both the XRF and the KED modalities, and a post-processing routine was necessary to account for the effects of pulse pileup.

5.2.2 K-Edge Densitometry Responses

The bremsstrahlung shape and the KED magnitude from experimental measurements from the ORNL REDC HKED KED detector were compared to simulated results to analyze the capability of the MCNP model to replicate the spectra of the KED branch. At this stage, the general robustness of the simulation technique was confirmed in its capability to accurately reproduce the KED magnitude, but several components of the bremsstrahlung shape were inadequately reproduced. Figure 5.10 shows the unprocessed results from the MCNP simulation directly compared with experimentally measured results for a uranium standard in a nitric acid matrix and Figure 5.11 shows an expanded

view of the K-edge transition energy region. Both experimentally measured and simulated spectra are normalized to an arbitrary normalization parameter chosen to be 1E3. The spectra can be scrutinized by viewing the residual difference in terms of the standard deviation (σ) located below the spectral graph.

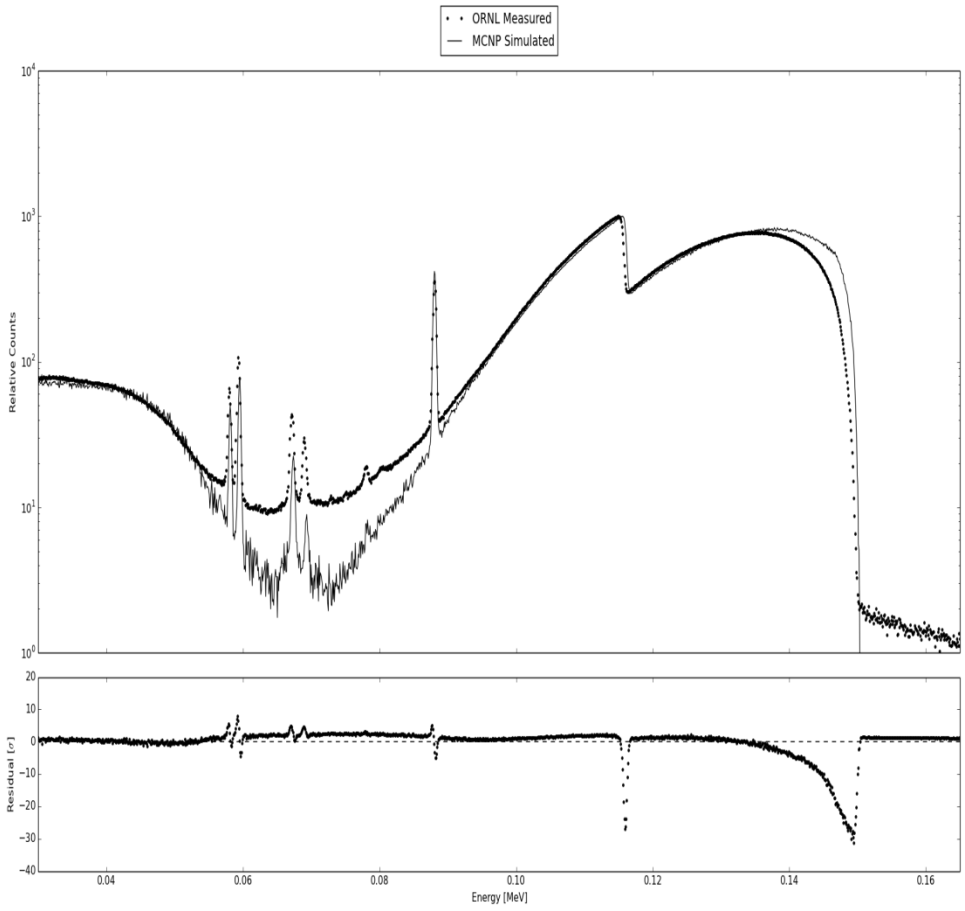

Figure 5.10. Modeled and measured KED responses of the continuum and the K-edge magnitude for a uranium nitrite sample with approximately 268 g U/L with the residual shown in terms of sigma.

The uranium K-edge magnitude, while the appropriate size in structure, does not match the energy of the measured uranium K-edge. The transmission simulation of the KED

detector response placed the uranium K-edge at approximately 1.1611E-01 MeV, 0.5019 keV offset from the published NIST value of the uranium K-edge at 1.15608E-01 MeV [94].

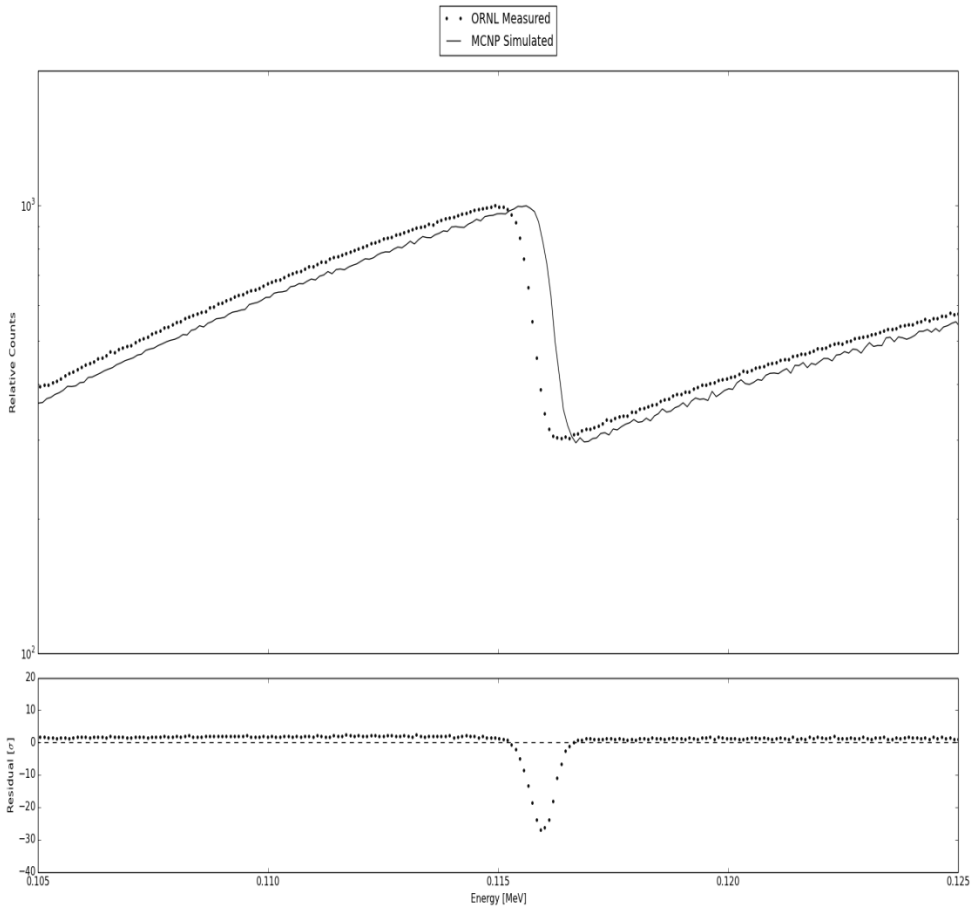

Figure 5.11. Modeled and measured KED responses of K-edge magnitude for a uranium nitrite sample with approximately 268 g U/L with the residual shown in terms of sigma.

The initial results from the MCNP models highlighted the fact that the same offset in the photoatomic datatables for representing the x-ray fluorescence peak energies is present in the K-edge energies. This offset alters the mass attenuation coefficients of the simulation,

affecting the required energy for the liberation of the inner atomic shell electrons. As the incident x-ray tube energies are in a continuous spectrum, the offset of the x-ray production rates can be quantified by the relative difference in the flux of x-ray tube radiation between the incorrect simulated threshold for K-edge fluorescence and the energy threshold published by NIST. This offset has a small but not negligible impact in the x-ray fluorescence rate, and the bias it introduces into the results must be quantified in order to correctly reproduce the x-ray peak profiles. The offset of the K-edge represents a significant degradation in the accuracy of the MCNP simulation to reproduce the correct x-ray yields.

5.3 Post Processing Methods

Fundamentally, MCNP has been proven to produce a faithful representation of the spectral responses from the HKED, but not to the degree necessary to allow for simulation results to be used as a guide to design for future development. Variations between the simulated peak shapes and energies and the theoretical x-ray and K-edge values provided insight into the applicability of the simulated results for model validation.

Considering the drawbacks in simulating x-ray fluorescence in MCNP, a set of requirements was drafted that had to be met in order for the MCNP results to be applicable in matching experimental results. The necessary requirements include making changes and adjustments to the simulated spectral results to reflect the generally accepted theoretical x-ray and K-edge energies. Additional changes to the simulated results would need to incorporate the experimental effects from the electronic detection system such as pulse pileup. In anticipation of the effects from the Lorentzian broadening of the natural x-ray line widths on the Gaussian detector response, a processing routine to convolute the

Gaussian and Lorentzian peak profiles would need to be generated to account for the Voigt shape of the actinide x-ray peak profiles.

The need for the MCNP simulated results to match the correct energy values was handled independently for the XRF and KED results. The corrective actions were first focused on the matching the XRF response over the KED response as the residual difference between the simulated and experimentally measured XRF results was far greater than those for the KED response. A separate program was needed to adjust the simulated results to fit the necessary requirements to allow for matching of the simulated results with the experimental data. This program needed to be malleable and easily updated in order to be applicable to adjusting the wide range of simulated results for separate concentrations and elements being assayed by the HKED. Therefore, the MCNP tally output was written into the programming language Python [96] to post-process the results. Python was chosen as an easy and flexible language with a large store of pre-written libraries for data analysis and presentation.

5.3.1 XRF Post Processing

The XRF spectra from the assayed sample, the cadmium-109 calibration source, and the gadolinium beam filter were each modeled separately, so the individual spectra were combined together using normalization factors to combine the cadmium and gadolinium data to match the assayed sample counts. The first aim in processing the simulated XRF spectrum was to reduce the noise and locate the x-ray peaks. The reduced noise data, obtained via a smoothing filter, were used to help in determining the peak locations. The noise reduction proved useful in the quantitative analysis of the XRF spectra but did not play a role in the quantitative spectrum evaluation. The smoothed data were not evaluated to obtain any peak or continuum information, in order to ensure the evaluation of the peak information was not biased by the smoothing algorithms.

5.3.1.1 Smoothing and Peak Search Methods

A Savitzky–Golay filter and a subroutine to locate the x-ray peak maximums were included in the post-processing of the modeled data. A Savitzky–Golay filter applies an adjustable order polynomial to a sufficiently small interval of the data to obtain smoothed values of the spectrum [97]. Such filters are less effective in removing noise but have the advantage of causing less peak distortion than other filters. In the case of the HKED spectral results, it was acceptable to obtain less noise removal in place of removing the potential for peak distortion as the percent change in peak height needed to be kept to a minimum. This filter was found to be ineffective for smoothing un-broadened MCNP spectral results, as the zero width x-ray peak lines became large oscillations at the peak edges when smoothed. Thus the smoothing filter was only applied on MCNP results that were already broadened employing the Gaussian energy broadening function [80].

Many peak search algorithms focus on the use of the first and second derivative of the smoothed data or some correlation technique which emphasizes the peak, making it more easily separated from the continuum [95]. In this case, peak locations were determined using an iterative procedure that sweeps across the spectral values applying an adjustable parameter for determination of peaks within statistical significance. This approach employs a peak search method based on the relative change in the spectral intensity if the preceding channel value was lower by an input parameter *delta*. This algorithm can be viewed in Appendix C.

Although tabulated input of the known peak locations for the elements simulated in the XRF spectrum remains the best way to identify peak locations, an iterative peak search algorithm was employed in the post-processing of the simulated HKED XRF data to ensure that diverse changes in the sample elemental compositions resulting in a wide range of possible x-ray peaks would be able to be processed by the post-processing

algorithm. A downside to using this approach for peak search is that the adjustable parameter must be changed while processing the data if the peaks due to fission product contamination or small weight percent elements are to be located, making the application of this peak search method more complex. The filtering and peak search routines were employed on a simulated HKED XRF spectra for an approximately 243 g U/L and 2.93 g Pu/L standard in a nitric acid matrix and the results are shown in Figure 5.12 and zoomed in on the uranium and plutonium Kα peaks in Figure 5.13.

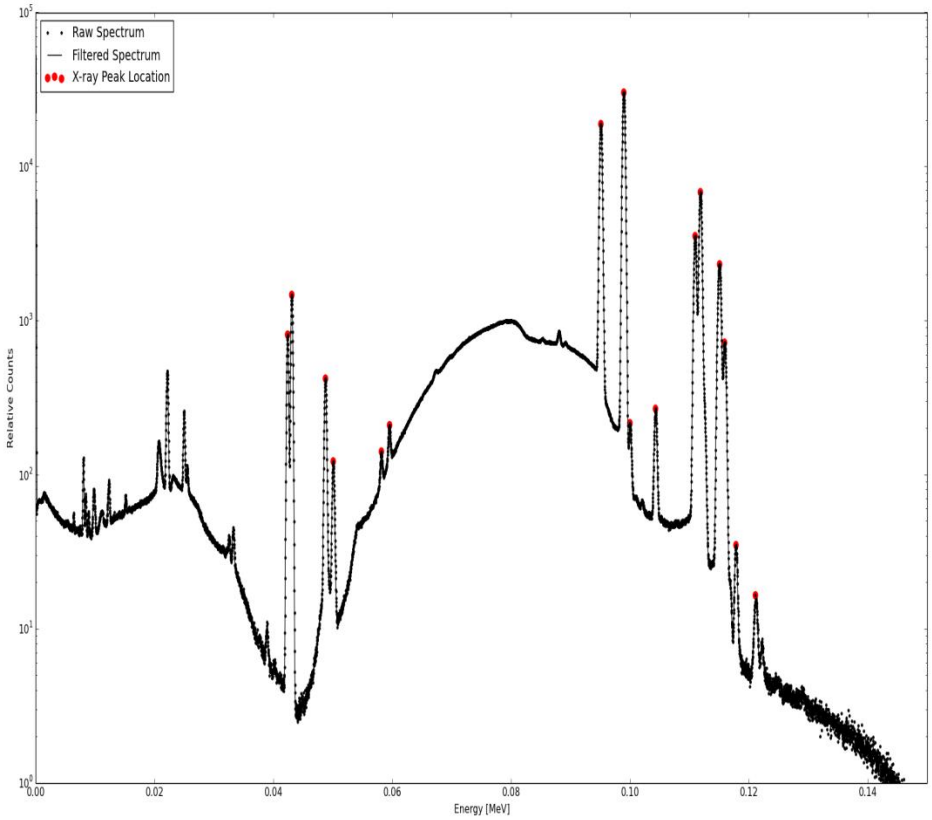

Figure 5.12. Modeled XRF response of the continuum and the x-ray peaks for a uranium-plutonium nitrite sample with approximately 243 g U/L and 2.93 g Pu/L with the filtered spectrum shown and the peak maxima highlighted.

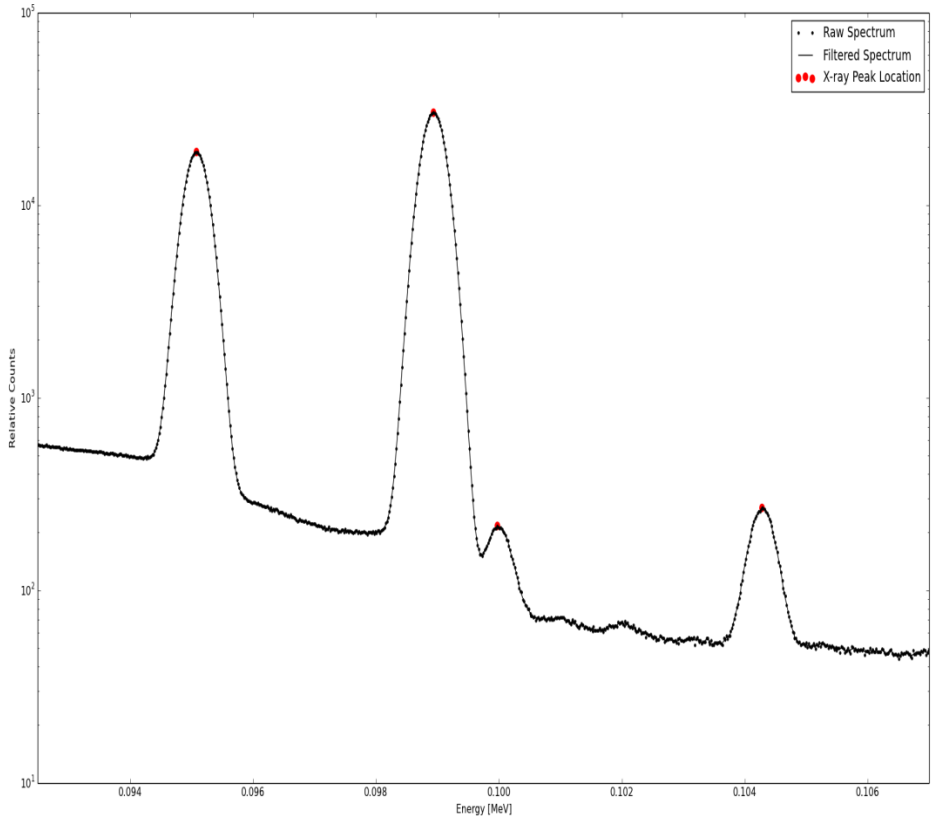

Figure 5.13. Modeled XRF response of the Kα x-ray peaks for a uranium-plutonium nitrite sample with approximately 243 g U/L and 2.93 g Pu/L with the filtered spectrum shown and the peak maxima highlighted.

5.3.1.2 Continuum Estimation Method

Once the peak maximum is approximately located in the filtered spectrum, the next aim for adjusting the simulated XRF responses is to separate the bremsstrahlung spectra from the inaccurate peak locations and profiles. The bremsstrahlung continuum observed in the x-ray spectrum arises from the scattering, attenuation, and slowing down of electrons and photons in the HKED system. The shape can be very complex and the presence of

characteristic x-ray peaks further complicates the analysis of XRF results, thus it is difficult to discriminate between peaks and continuum. Therefore, a method based on the removal of rapidly varying structures in the spectral data was chosen to separate the relevant analytical information in the net peak areas from the continuum. The continuum estimate algorithm uses a statistical nonlinear iterative peak stripping method and is shown in detail in Appendix C.

By comparing individual channels with surrounding channels, and repeatedly replacing the central channel with the mean of its direct neighbors, the peaks can be iteratively stripped from the spectrum. To reduce the number of iterations required, a square root transformation of the data was performed prior to stripping, and an inverse transformation returned the continuum to the original shape afterwards. One disadvantage of this approach to continuum estimation is that broad peaks are formed in the stripped spectrum in the energy regions near overlapping peaks in the spectrum. Thus the continuum spectrum was instead obtained by applying the peak stripping method on the non-Gaussian broadened simulated XRF results. As the continuum shape was confirmed to be the same before and after the application of the Gaussian broadening function to the simulated data, this approach proved to be adequate in separating the peaks in the spectrum from the continuum.

The peak stripping method was selectively applied to the energy region of importance for determining the peaks and their areas for the actinide x-rays. In Figure 5.14 and Figure 5.15, the red line representing the continuum follows the original shape of the XRF spectrum until roughly 90 keV, where the spectrum is replaced by the peak stripped continuum values. This approach to the continuum estimation was used since the adjustments on the XRF spectra were only necessary for an area of importance defined as the energy region surrounding the actinide x-ray peaks, approximately between 90 keV

and 125 keV. While this approach was limited to the area of importance, the peak stripping method could be easily changed to cover the entire spectrum making it more applicable for wider uses.

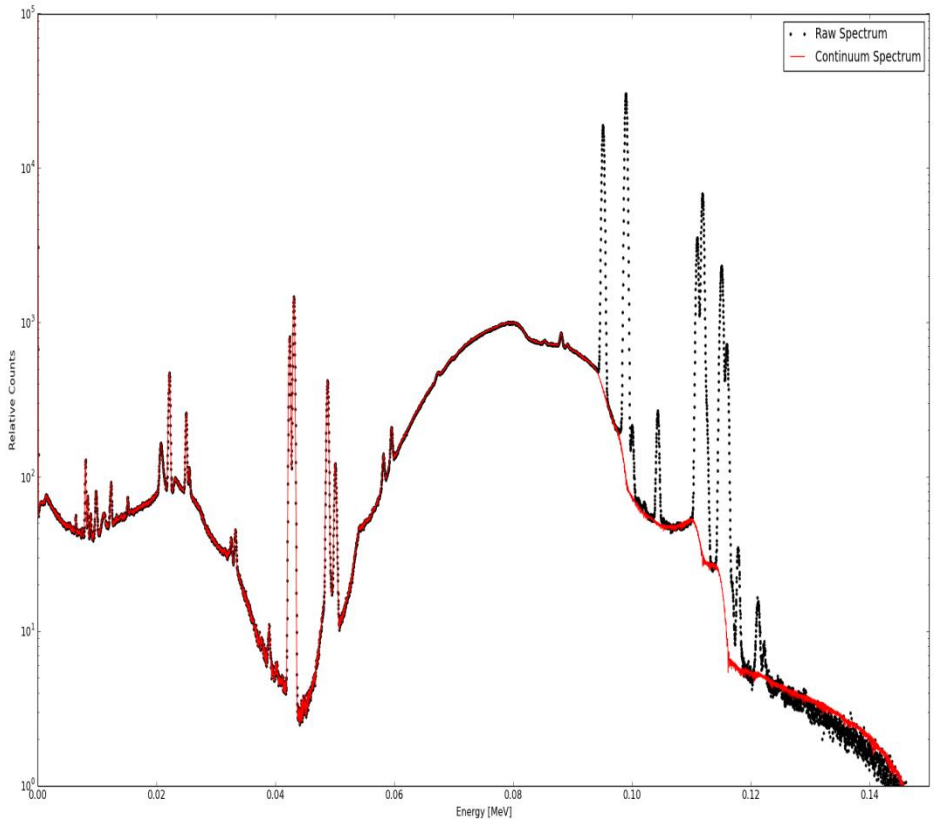

Figure 5.14. Modeled XRF responses for a uranium-plutonium nitrite sample with approximately 243 g U/L and 2.93 g Pu/L with the spectrum and the continuum separated from each other beginning at 90 keV and continuing to 150 keV. The continuum estimation is shown as a red line to ensure it is clearly visible around the actinide x-ray peaks.

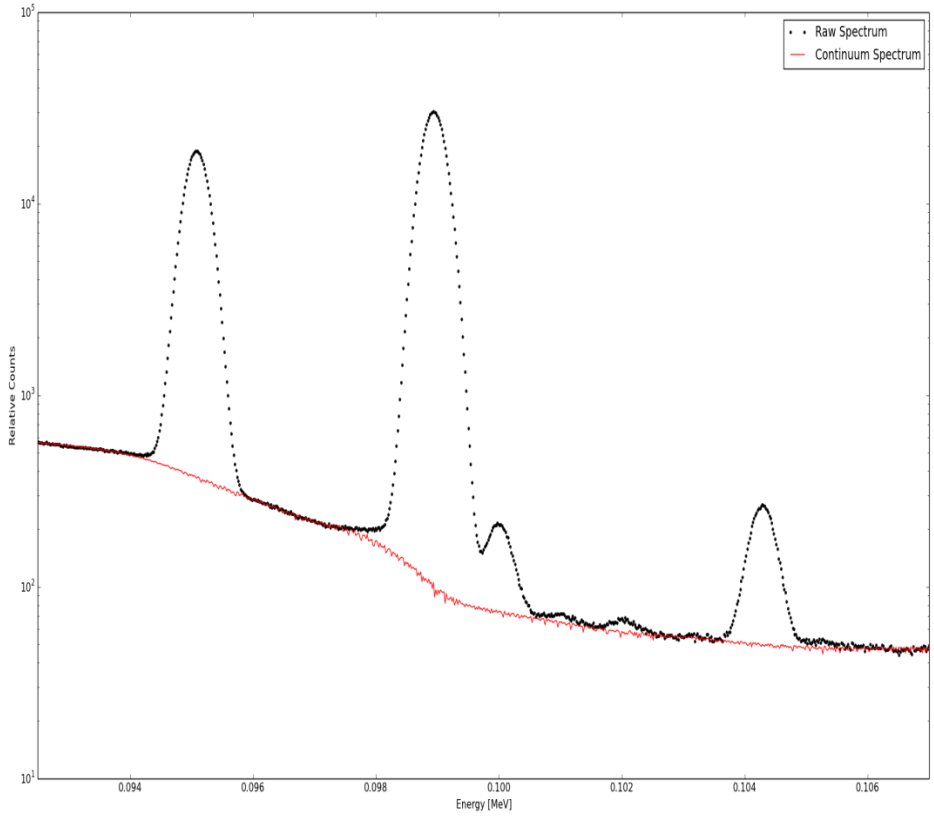

Figure 5.15. Modeled XRF responses for the Kα x-ray peaks for a uranium-plutonium nitrite sample with approximately 243 g U/L and 2.93 g Pu/L with the spectrum and the continuum separated.

5.3.1.3 Offset Energy Correction

After smoothing the modeled results, the energy of the local maxima from the smoothed data was verified and any offset from the generally accepted energies for the x-ray peak locations was corrected [94]. A two-fold correction employing least-squares fitting and tabulated values was used to optimize the corrected values of the actinide peaks. The first approach to the energy offset correction was fitting linear and quadratic curves to the offset values as a function of the x-ray energies, as is shown in Figures 5.16 and 5.17,

respectively. The energy values on the x-axis refer to the MCNP energy of a set of fluorescent x-rays from the elements plutonium, uranium, lead, tungsten, gadolinium, and xenon. The offset values on the y-axis correspond to the size of the shift in keV necessary to adjust the MCNP x-ray energy values to the generally accepted energies for the x-ray locations published by NIST [94].

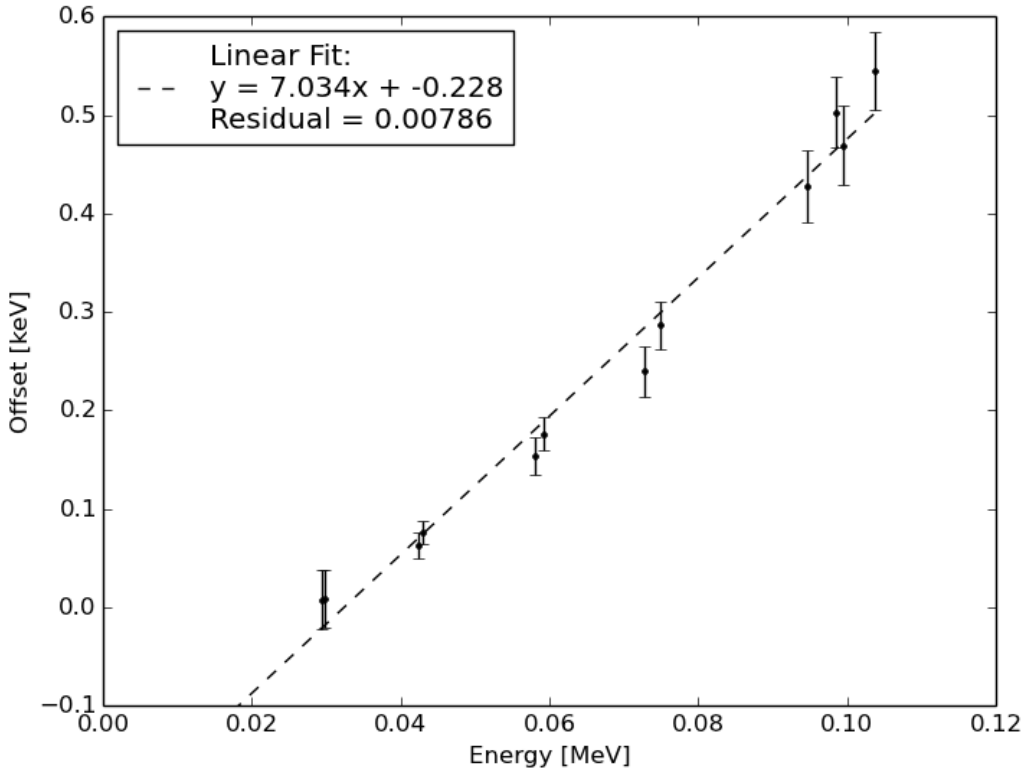

Figure 5.16. Linear least squares fitting curve applied to the offset from the generally accepted x-ray energies for the modeled x-ray peak energies in MCNP.

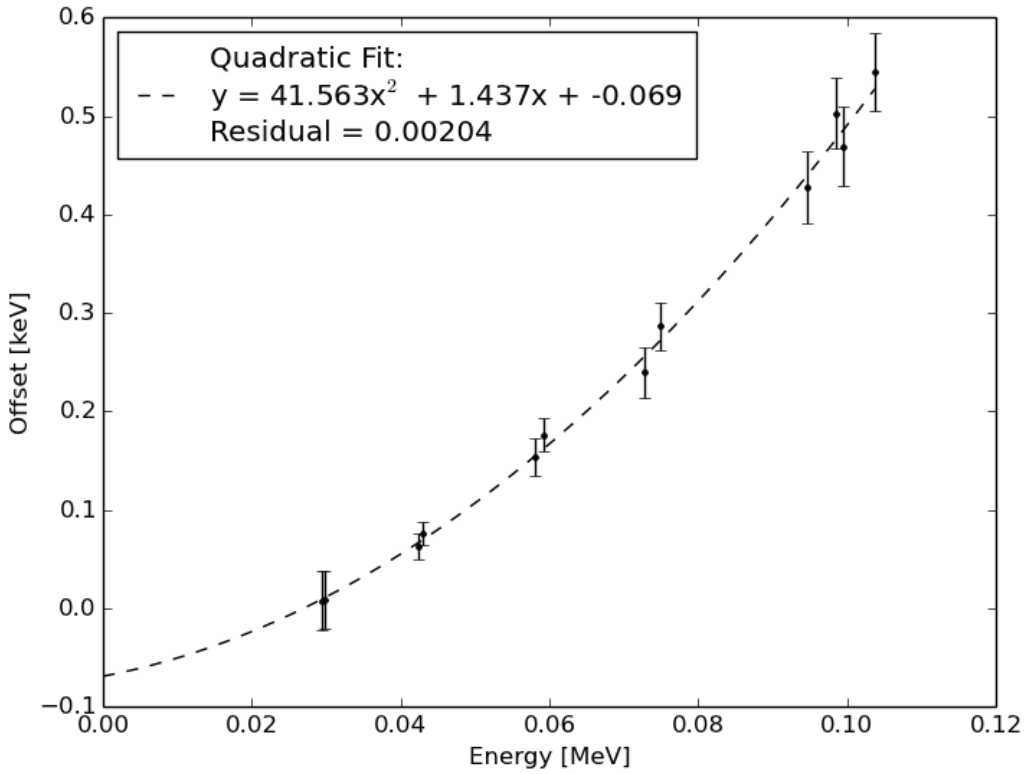

Figure 5.17. Quadratic least squares fitting curve applied to the offset from the generally accepted x-ray energies for the modeled x-ray peak energies in MCNP.

The fitted functions were applied to shift the MCNP x-ray peak locations and the results were compared to the measured XRF peak locations from the ORNL REDC HKED spectra. While the linear fitting matched the experimentally measured x-ray locations closely when comparing the entire range of energies, the application of the quadratic fit matched the uranium and plutonium x-ray peak locations more accurately. Thus the quadratic fit was used to adjust the offset x-ray values from the MCNP x-ray energy locations to the correct values. However, the two least-squares fitting approaches both still resulted in roughly 30 and 20 eV offsets for the linear and quadratic fits, respectively, between the modeled and measured uranium $K\alpha_1$ peak location, thus another approach was applied specifically for the uranium and plutonium x-rays.

As both the theoretical energies and the MCNP generated energies of the x-ray values are known and constant, an adjustment was made to fit the individual K uranium and plutonium peaks precisely to the energy locations published by NIST [94]. Using the iterative peak search method, the maxima for the MCNP x-rays were adjusted to the published x-ray values specifically for the uranium $K\alpha_1$ peak and the plutonium $K\alpha_1$ peak. These peaks are the most important for determining the relative concentration of the uranium and plutonium for sample assay with the HKED. It is possible for this application of precise adjustments to be made for the entire spectrum, but analysis was limited to the uranium and plutonium peaks to refine the scope of the post-processing for the simulated XRF spectra.

5.3.1.4 Voigt Fitting Using Lorentzian Widths

In analyzing the components of an actinide x-ray spectrum with semiconductor devices, peak profiles are observed as a convolution of the particular x-ray lines' Lorentzian distribution with the Gaussian detector response function. This convolution of Gaussian and Lorentzian broadening is due to the influence of the strong interaction close to the nuclear surface causing dramatic broadening of the lowest electron orbital levels [98], giving rise to a Voigt profile. The Voigt function is shown in Equation 5.2, where Γ stands for the Lorentzian full width at half maximum, x_o is the position of the x-ray peak maxima, and σ is the width of the Gaussian.

$$V(x) = \int_{-\infty}^{\infty} e^{-u^2} \frac{du}{(\frac{1}{2}\Gamma)^2+[(x-x_0)^2-\sqrt{2}\sigma u]^2} \qquad \text{Equation 5.2}$$

Voigt profiles can be calculated using numerical approximations [99], but since it was preferred to avoid numerical integration in the analysis of the simulated HKED spectral

results, a unified analytical approximation [98] has been applied to realistically represent the peak profiles of the actinide x-ray peaks.

The known Gaussian and Lorentzian peak parameters have been convoluted to produce the Voigt peak profile for the actinides being assayed in the HKED as shown in Figure 5.18 and expanded upon in Figure 5.19. The Gaussian width is related to full width at half maximum of the LEGe detector response functions by the factor $2\sqrt{2\ln(2)}$ or FWHM(Gaussian) = 2.35σ. Referring to the published values for the natural Lorentzian full width at half maximums for the actinides [100], then linearly extrapolating the published values towards the higher atomic numbers of the transuranic elements [101], an empirical approach for determining the natural Lorentzian line widths of the TRU element x-rays has been applied.

The x-ray peaks generated through convolution to produce the Voigt profile were normalized to the simulated peak heights using a peak fitting normalization parameter and a peak broadening parameter was included to reproduce the detector response to the now Voigtian broadened x-ray peaks. The Voigt profiles are shown compared to the MCNP simulated x-ray peaks, where the differences using the corrected energy offset and the accurate peak profile is clearly distinguishable.

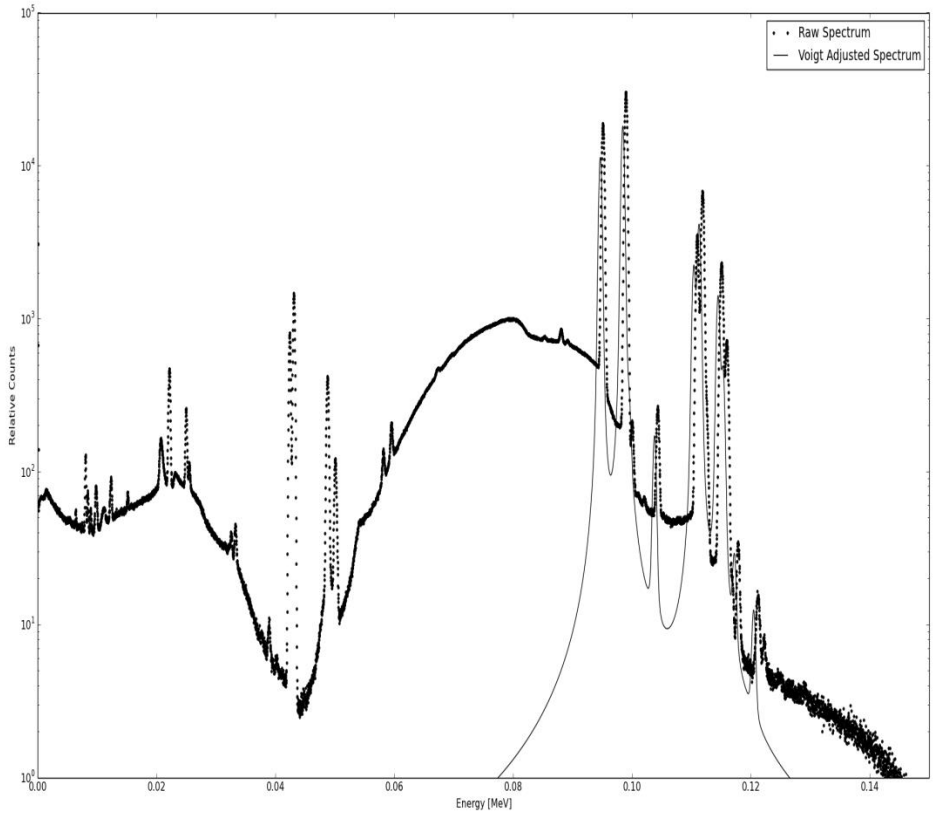

Figure 5.18. Raw modeled XRF response for a uranium-plutonium nitrite sample with approximately 243 g U/L and 2.93 g Pu/L is compared with the offset energy corrected x-ray peak shapes replaced with Voigt profiles.

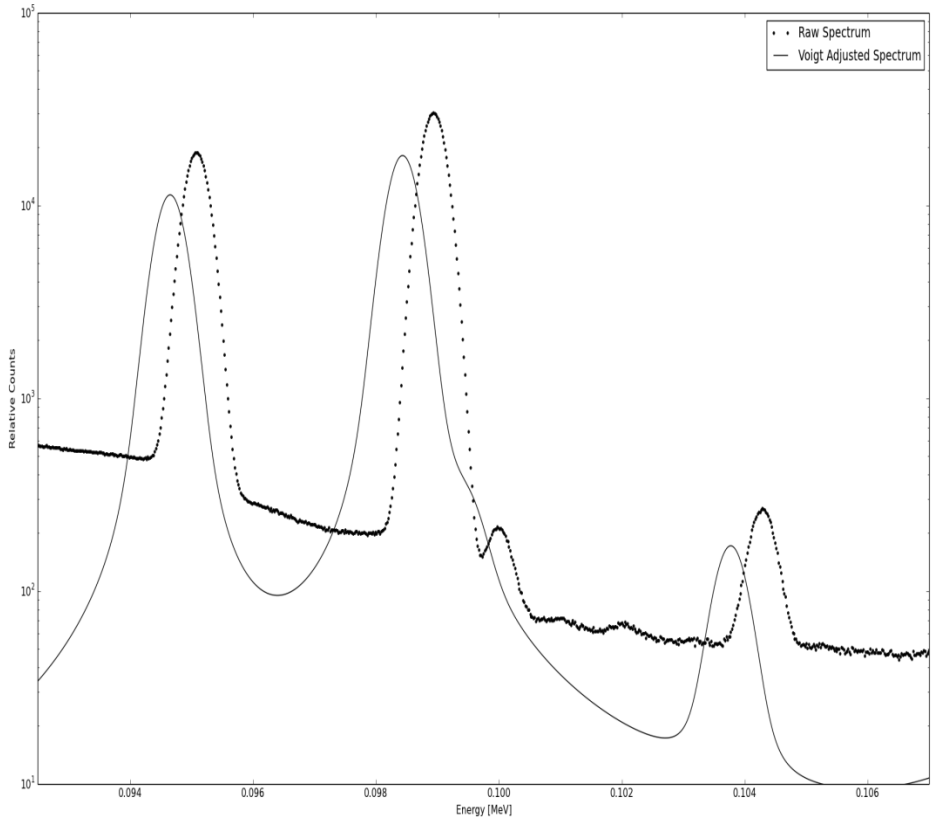

Figure 5.19. Raw modeled XRF response for the Kα x-ray peaks for a uranium-plutonium nitrite sample with approximately 243 g U/L and 2.93 g Pu/L is compared with the offset energy corrected x-ray peak shapes replaced with Voigt profiles.

5.3.1.5 Comparison of Adjusted MCNP XRF Spectra with Measured XRF Spectra

In analyzing the comparison of the measured actinide XRF spectrum with the simulated one, the Voigt broadened peak profiles are combined with the simulated XRF continuum, shown in Figure 5.14, to represent the entire spectrum. The broadened x-ray profiles are shown overlaid on top of the bremsstrahlung continuum in Figure 5.20 and the uranium and plutonium K x-ray region is shown zoomed in Figure 5.21.

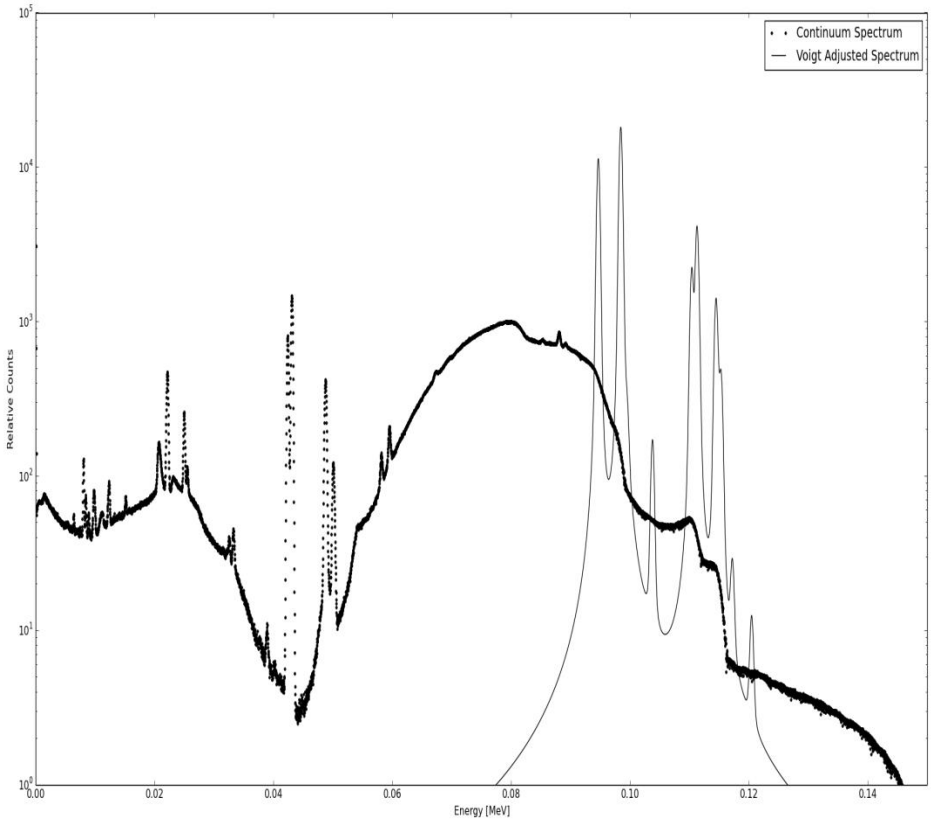

Figure 5.20. Modeled continuum spectrum and the overlaid Voigt broadened x-ray peaks from the XRF response for a uranium-plutonium nitrite sample with approximately 243 g U/L and 2.93 g/L Pu.

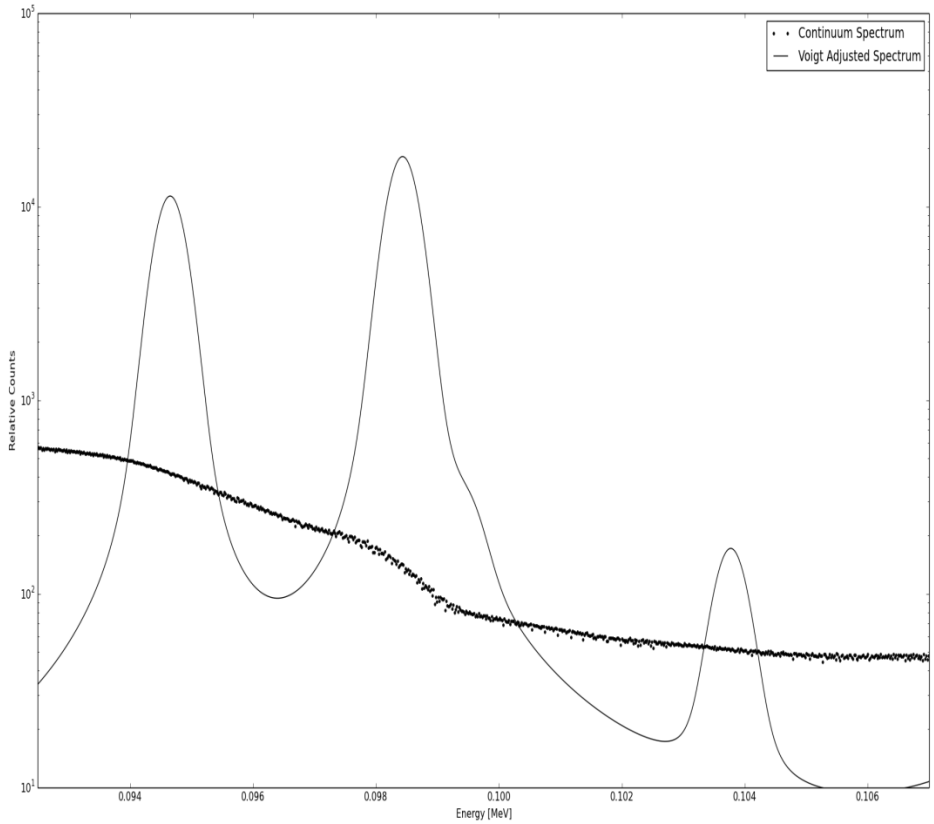

Figure 5.21. Modeled continuum spectrum and the overlaid Voigt broadened x-ray peaks from the XRF response for the Kα x-ray peaks for a uranium-plutonium nitrite sample with approximately 243 g U/L and 2.93 g/L Pu.

A method for reproducing the pulse pileup, found in Appendix C, can be generated from the combined continuum and Voigt peak profiles spectra to complete the list of necessary requirements to be met in order for the MCNP simulation results to be feasibly applicable in validating experimental results. Figure 5.22 shows a comparison between two spectra with and without pulse pileup for the combined contributions from the simulated continuum and the Voigt peak profiles.

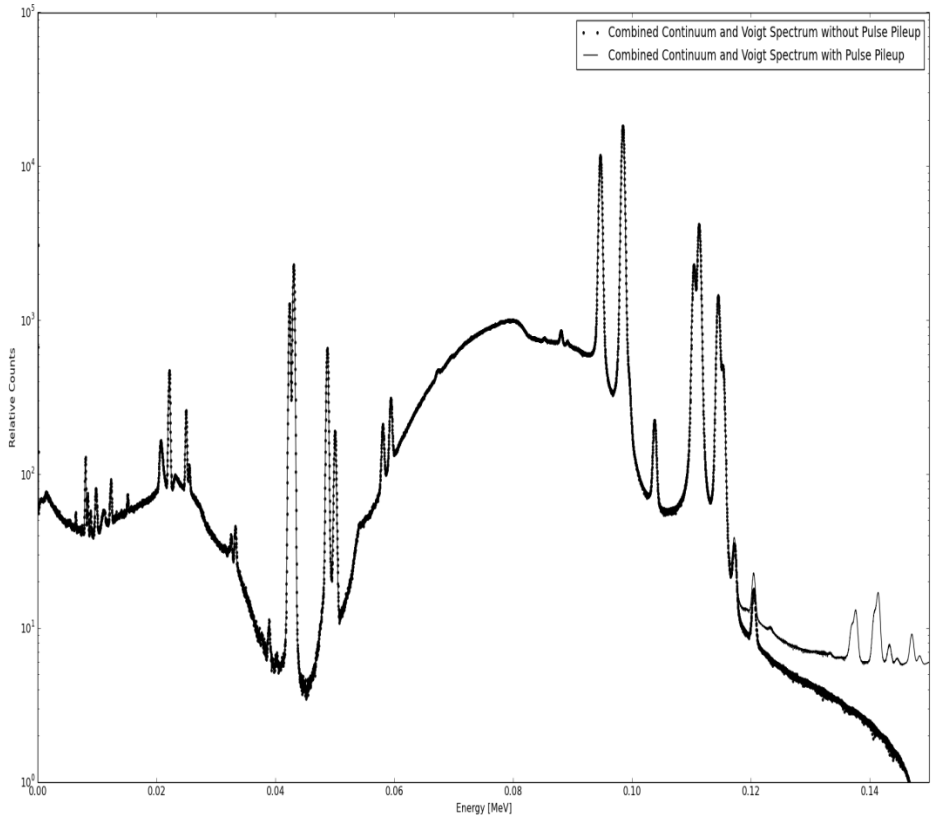

Figure 5.22. Simulated MCNP XRF spectral results for a uranium-plutonium nitrite sample with approximately 243 g U/L and 2.93 g/L Pu. Post processing of the simulated results has adjusted the energy offset of the x-ray peaks, corrected the peak shapes to Voigt profiles, and included the pulse pileup.

Reproducing the pulse pileup in the LEGe detector is useful in demonstrating the energy locations in which pileup peaks may exist. The existence of these peaks must be monitored as they can potentially form interferences with the x-rays within the spectra. However, the pulse pileup estimate does not reproduce the broadened pulse shapes that are characteristic of the overlapping peaks within the detector resolving time. Thus while the locations of the pileup peaks can be determined, the degraded energy resolution of the

peaks is not simulated due to the limitations of the pileup generation method. Moreover, less emphasis was placed on optimizing the simulation to reproduce the scattering due to the x-ray tube spectra interacting with the gadolinium filter as it has a negligible impact on the region of the XRF spectrum that contains the actinide x-ray peaks.

After post processing is completed, the entire simulated XRF spectrum can be compared to measured spectra with the same energy per channel variation and of the same assayed uranium-plutonium sample. Initial observations of the simulated XRF spectra highlight the largest deviations around the gadolinium x-ray peaks near 40 keV and the generated pulse pileup peaks around 140 keV. This is shown in Figure 5.23.

More emphasis was placed on accurately reproducing the peak shapes for the uranium and plutonium Kα x-rays. The energy region of importance is highlighted in Figure 5.24 to show the close fit and the low residual for these peaks. Figures 5.25 and 5.26 isolate the residual differences between the raw unprocessed MCNP XRF results and the post-processed simulated results. As is shown in Figure 5.26, the inverted peak shape of the red line representing the residual of the post processed data shows that the fitting procedure is not precisely reproducing the correct amount of broadening required for the highest possible accuracy fit to the uranium $K\alpha_1$ and $K\alpha_2$ x-ray peaks at energies, 9.84336E-02 MeV and 9.46531E-02 MeV, respectively. This inverse peak shape of the residual around the isolated uranium Kα peaks may be due to several factors: the analytical approximation for the Voigt function employed to represent the x-ray peak profiles may not be accurate enough to represent the x-ray profiles, the exponential tailing components resulting in the asymmetry of the measured x-ray peaks may not be modeled correctly by the fitting routine, or the choice of the peak stripping algorithm to determine the continuum shape around the actinide x-ray peaks may be changing the shapes of the peaks.

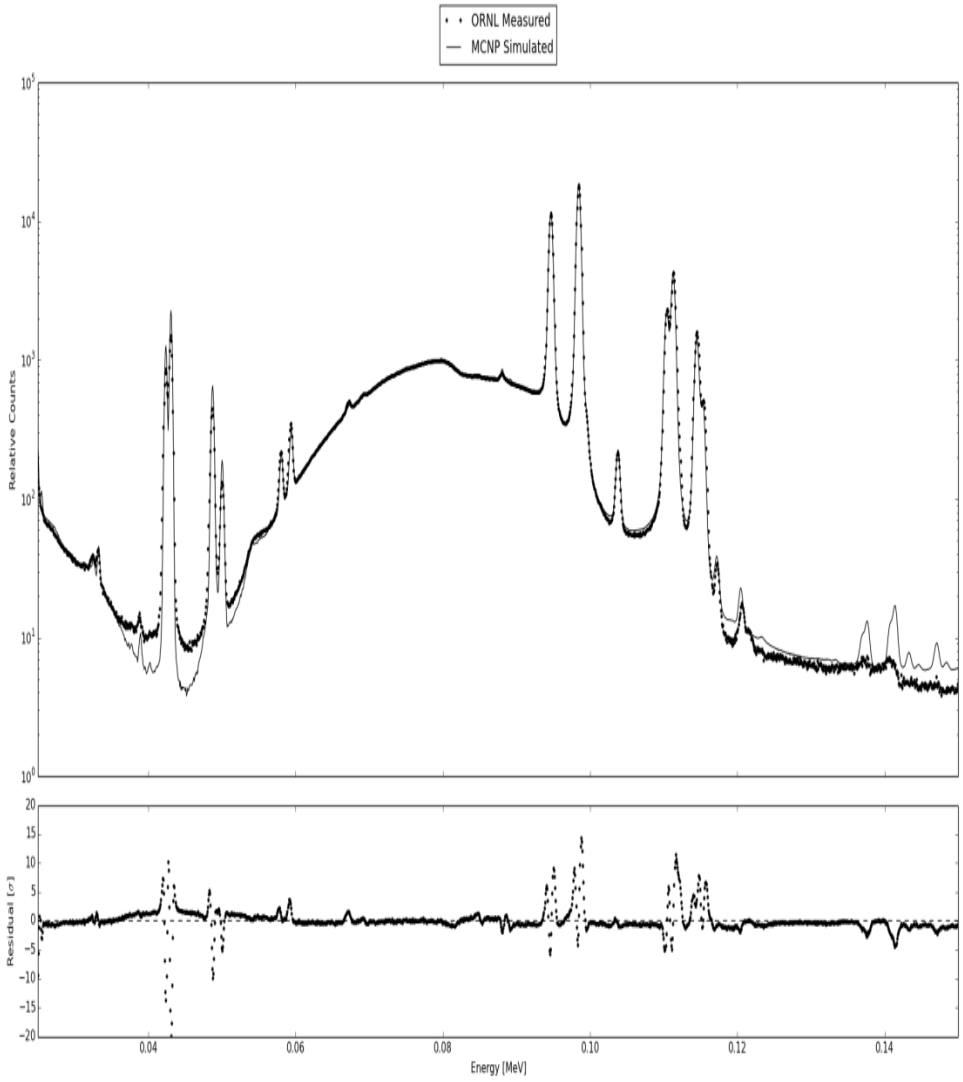

Figure 5.23. Comparison plot between experimental results on the ORNL REDC HKED and the post processed MCNP simulation for approximately 243 g U/L and 2.93 g Pu/L nitric acid based sample. The residual plot is shown in terms of sigma.

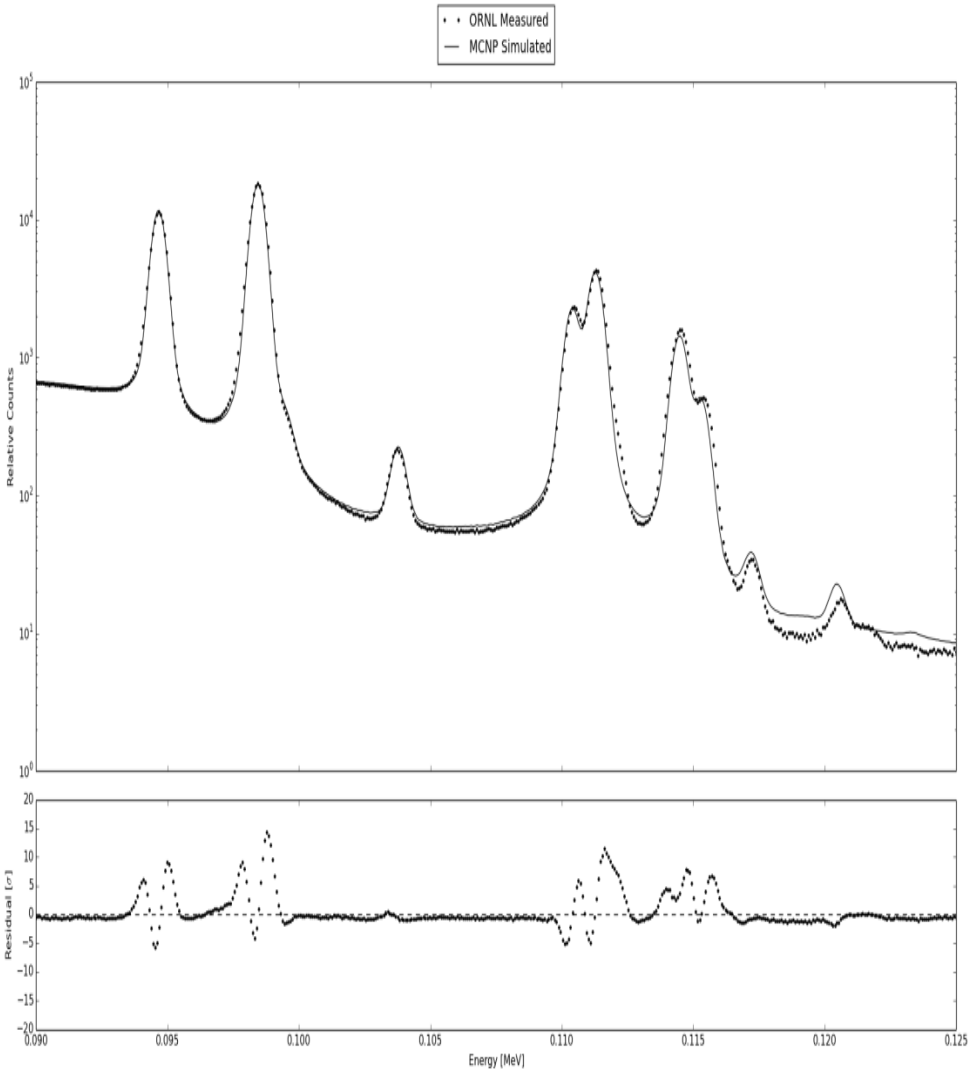

Figure 5.24. Comparison plot between experimental results on the ORNL REDC HKED and the post processed MCNP simulation for approximately 243 g U/L and 2.93 g Pu/L nitric acid based sample showing the residual difference in terms of sigma between the uranium and plutonium Kα and Kβ x-ray peaks.

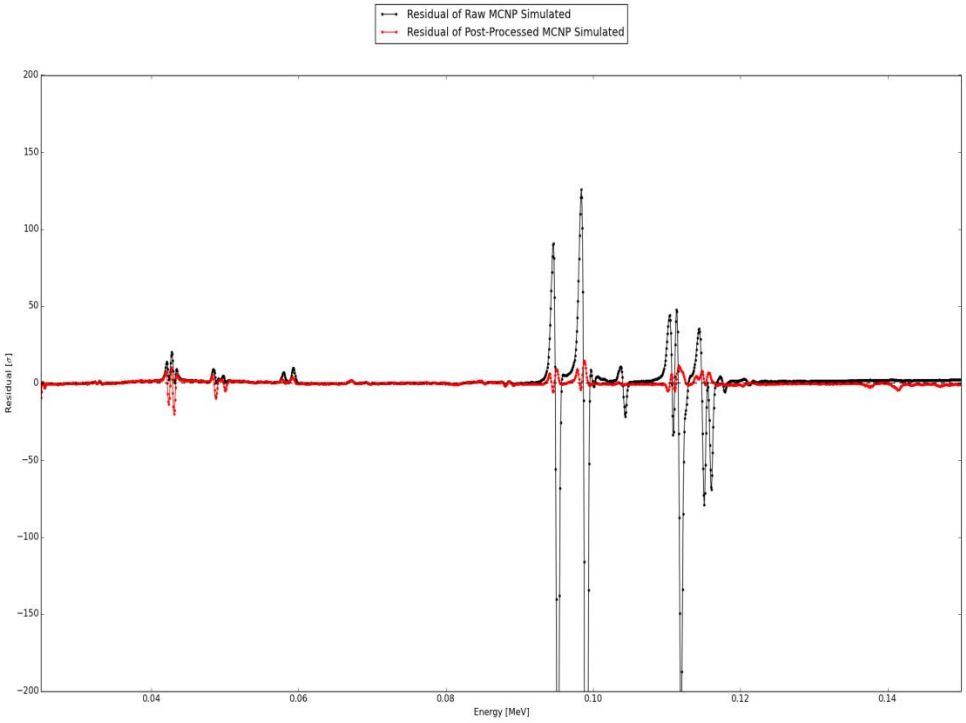

Figure 5.25. Comparison plot between the residual differences between the experimental data and the simulated data before and after the application of post-processing for HKED assay of an approximately 243 g U/L and 2.93 g Pu/L nitric acid based sample.

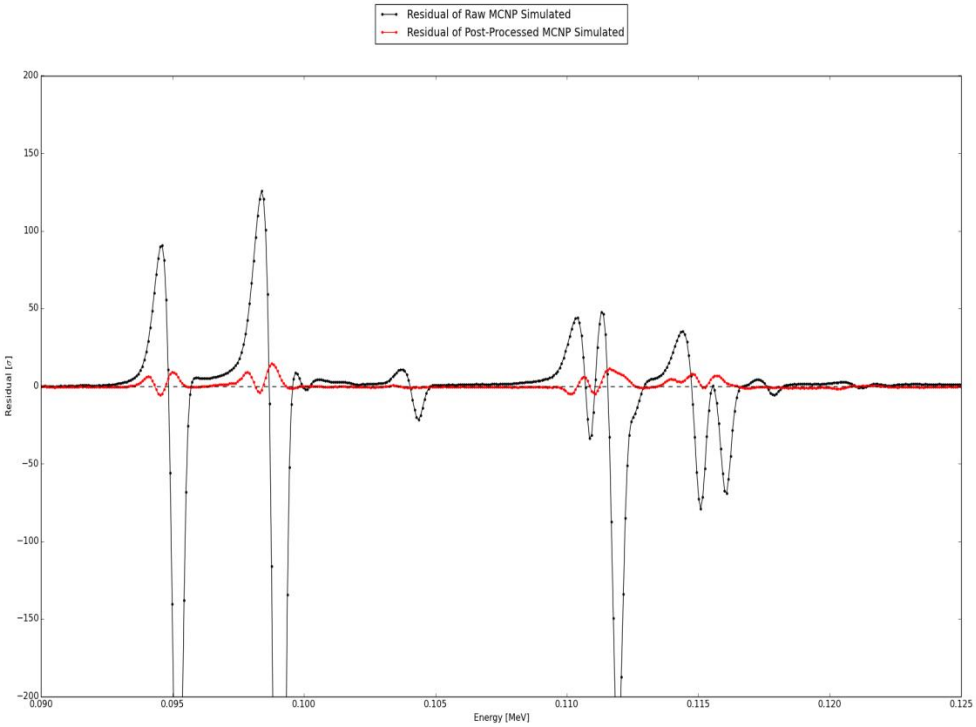

Figure 5.26. Comparison plot between residual difference of the raw, unprocessed MCNP simulated results and the post processed MCNP simulated results, showing the energy range containing the Kα and Kβ x-rays for the uranium and plutonium for HKED assay of an approximately 243 g U/L and 2.93 g Pu/L nitric acid based sample.

The simulations into HKED XRF assay results for the nitric acid based uranium-plutonium samples have verified that MCNP can be used to reproduce faithful representations of the actinide x-ray fluorescence spectra to within ± 2σ for the bremsstrahlung continuum counts. However, the simulated actinide peaks did not retain the same low level of uncertainty, but correction of the energy offset and application of new methods to broadening the peaks has reduced the residual difference for the x-ray peaks by as much as 60 times. Figures of the other samples analyzed can be found in Appendix A.

The peak broadening routine can still be optimized, as is shown through a comparison of the x-ray peak areas for simulated and experimentally measured uranium and plutonium $K\alpha_1$ x-rays. Table 5.1 shows the difference between simulated and experimentally derived peak areas to match well over the range of actinide concentrations typical for nitric acid based standards. An increase in the difference between the simulated and measured peak areas towards lower plutonium concentrations is shown to occur in Table 5.2. This reduction in accuracy for fitting the correct peak shape is most likely due to the effect the increased overlap between the peak broadening components and the background continuum as the concentration of the actinide is reduced. The error associated with each peak measurement is error of the determination of the peak area for the measured peak using the Simpson rule for numerical integration [102].

Table 5.1. Simulated uranium XRF peak areas compared to the ORNL measured XRF peak areas for the uranium $K\alpha_1$ x-ray.

Sample No.		XRF Peak	Simulated	Measured	Difference [%]
U250	268.21 g/L U	U $K\alpha_1$	12.395	12.039	*2.96 ± 0.417*
UPu250	243.26 g U/L	U $K\alpha_1$	11.155	11.069	*0.77 ± 0.484*
U150	160.91 g/L U	U $K\alpha_1$	8.451	8.370	*0.97 ± 0.492*
UPu150	160.91 g/L U	U $K\alpha_1$	7.857	8.185	*4.01 ± 0.461*
UPu100	107.3 g/L U	U $K\alpha_1$	5.650	5.880	*3.90 ± 0.466*
U045	48.273 g/L U	U $K\alpha_1$	2.960	2.955	*0.17 ± 0.824*

Table 5.2. Simulated plutonium XRF peak areas compared to the ORNL measured XRF peak areas for plutonium $K\alpha_1$ x-ray.

Sample No.		XRF Peak	Simulated	Measured	Difference [%]
UPu250	2.932 g/L Pu	Pu $K\alpha_1$	0.168	0.163	*3.35 ± 1.043*
UPu150	1.566 g/L Pu	Pu $K\alpha_1$	0.1138	0.1045	*8.84 ± 1.148*
UPu100	1.041 g Pu/L	Pu $K\alpha_1$	0.0825	0.0749	*10.2 ± 1.202*

5.3.2 KED Post Processing

In order to allow for a detailed comparison of the simulated K-edge magnitude to the experimentally measured K-edge magnitude, the offset of the K-edge energy was adjusted through a shift of the simulated spectra. The raw simulated intensity of the KED detector response was scaled to lower energies by roughly 0.5 keV to line up the energies of the simulated and measured K-edges. This minimal approach proved effective in allowing a comparative study of the KED spectral results for uranium samples and is represented in Figure 5.27. Analysis of the inverted peak of the residual in Figure 5.28 around the uranium K-edge at 115.606 keV shows a twelve times reduction of the residual difference between the unprocessed, simulated K-edge and the shifted, simulated K-edge. Note in Figure 5.28 the scaling of the residual has been decreased from the scale on Figure 5.27 to zoom in on the size of the residual around the uranium K-edge. A comparison of the residuals between the unprocessed MCNP results in Figure 5.10 and the shifted MCNP results in Figure 5.27 is shown in Figure 5.29.

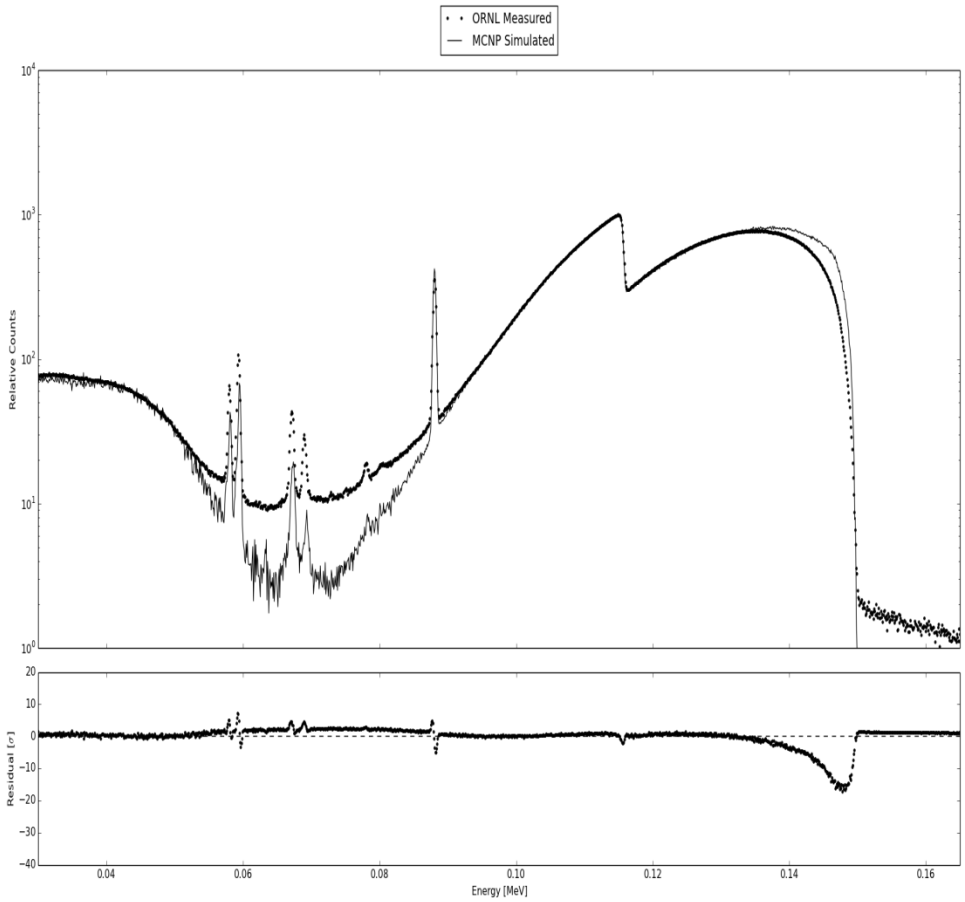

Figure 5.27. Modeled and measured KED responses of the continuum and the KED magnitude for a uranium nitrite sample with approximately 268.21 g U/L with the residual shown in terms of sigma. The simulated results have been shifted by approximately 0.5 keV.

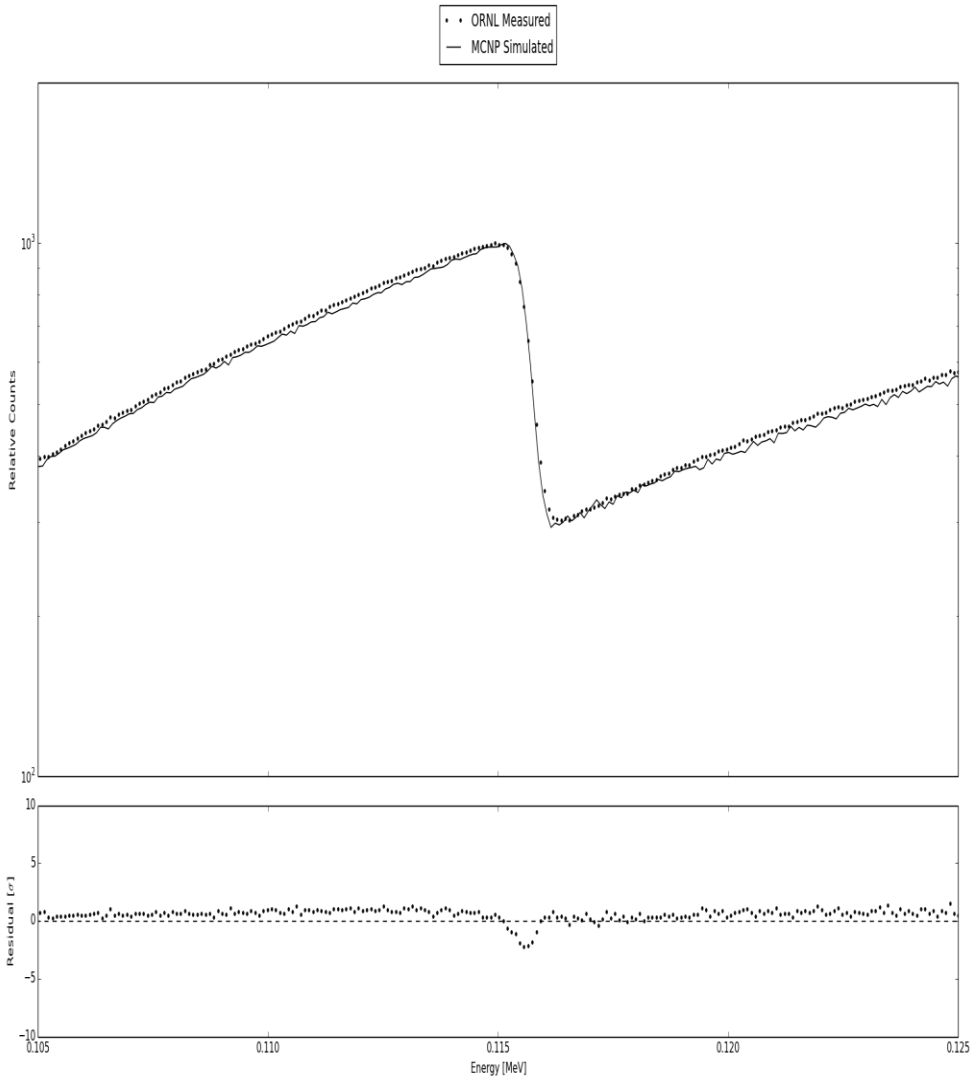

Figure 5.28. Modeled and measured KED responses of the K-edge magnitude for a uranium nitrite sample with approximately 268.21 g U/L with the residual shown in terms of sigma. The simulated results have been shifted by approximately 0.5 keV.

Additionally, there exists a small positive bias in the residual surrounding the uranium K-edge as shown in Figure 5.28. This small bias is thought to correspond to the normalization procedure, where the maximum values of the simulated and experimentally measured uranium K-edges are both normalized to a normalization parameter (1E3).

Thus the small bias is most likely due to the statistical error between the mean value and the maximum value for the relative counts at the uranium K-edge, and as expected, it is shown to be within 2σ.

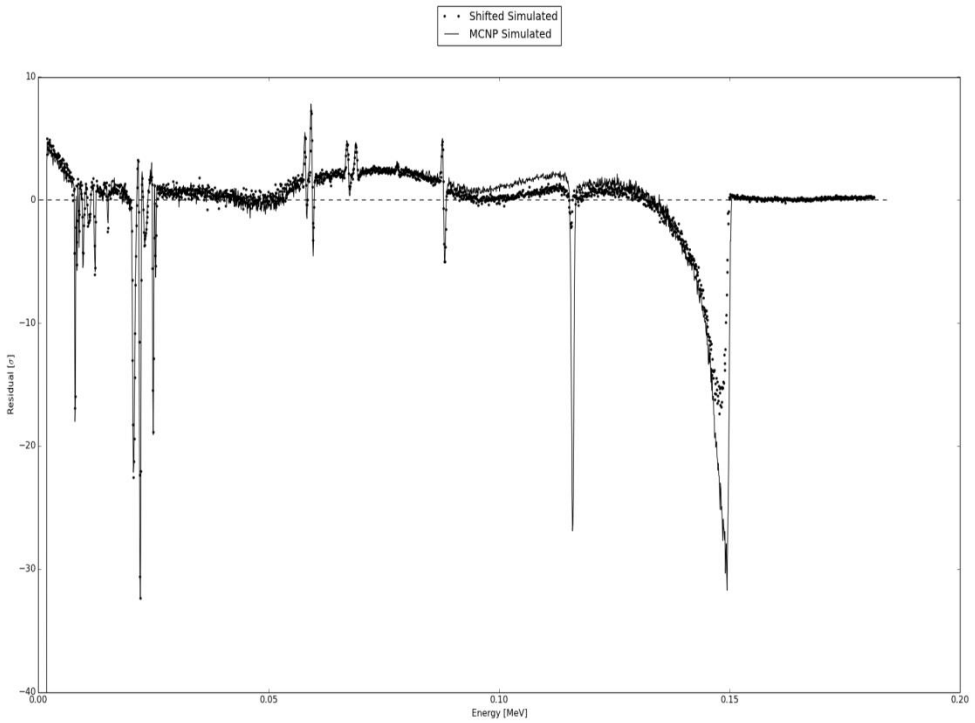

Figure 5.29. A comparison of the modeled and measured KED response residuals for the unprocessed results from MCNP. The shifted response from MCNP is shown for results that have been adjusted to lower energies by approximately 0.5 keV.

The important factor regarding the applicability of the MCNP simulation for reproducing a faithful representation of the measured HKED KED results is the magnitude of the K-edge. Shown in Figure 5.28, the simulation matches the shape and the size of the uranium K-edge well. An analysis of the summed intensity of the data points surrounding the K-edge on the high and low side determined the difference between the simulated and

experimental magnitude to be 0.01302 or 1.30% for the assay of the uranium nitrite sample containing approximately 268 g/L uranium.

This approach combined five channel intensities directly above and below the uranium K-edge and compared the calculated magnitude from the simulation to the experiment. The maximum and minimum locations surrounding the K-edge were determined from the relative counts as shown in Figure 5.28 using the same peak search algorithm as used to determine the XRF peak maximums, but optimized to find local minima as well. A Savitzky-Golay smoothing function was applied to the simulated KED results to ensure that counting statistical variations around the K-edge did not offset the location of the K-edge maxima and minima. However, the smoothed results were not used in determining the K-edge magnitude, only in determining the channel location of the K-edge maximum and minimum. Table 5.3 shows the comparison of simulated to ORNL measured uranium K-edge magnitudes for the nitric acid based samples with varying compositions of actinides. The error was determined based on the counting error and included the propagation of error for subtracting two terms to determine the difference. Figures of the other uranium concentrations can be found in Appendix A.

Table 5.3. Simulated uranium K-edge magnitudes compared to the ORNL measured uranium K-edge magnitudes.

Sample Actinide Composition	Simulated	Measure	Difference [%]
321.91 g/L U	726.09	752.35	*3.49 ± 0.342*
268.21 g U/L	678.59	669.75	*1.30 ± 0.372*
243.26 g/L U; 2.932 g/L Pu	623.15	644.45	*3.31 ± 0.396*
160.91 g/L U; 1.566 g/L Pu	471.86	484.57	*2.62 ± 0.523*
160.91 g U/L	479.15	483.25	*0.84 ± 0.520*
107.3 g/L U; 1.041 g/L Pu	321.49	337.20	*4.66 ± 0.735*
48.273 g U/L	133.58	133.20	*0.29 ± 1.792*
16.119 g/L U	5.5588	5.3439	*3.87 ± 11.99*

In addition to the offset energies in the MCNP datatables, the simulation of the KED spectral response highlighted two deviations between the simulation and the experimentally measured results. In the energy region between 60 and 80 keV surrounding the tungsten x-rays, the depression in the simulated relative counts is most likely due to the lack of simulated scattering in the KED collimator. The forward peaked transmission spectra passing through the sample is attenuated within the stainless steel KED beam filter and may then scatter off the tungsten KED collimator before impinging on the detector. The scattering interactions within the tungsten KED collimator were not sampled sufficiently in the simulation to match the relative intensity of the counts.

Additionally, the simulated relative counts at the high energy region around 150 keV has not been shown to match the ORNL measured relative counts. The alternate bremsstrahlung shape at high energies around 150 keV is thought to be due to the incorrect sampling of the x-ray tube energy via the SpekCalc x-ray tube energy distribution and to a lesser extent some energy jitter of the maximum energy of the

bremsstrahlung spectra over the timespan of the experiment. The simulated source term for the x-ray tube is derived from the software SpekCalc for tungsten anode x-ray tube spectra and does not account for the variation of the energy spectra over time. Neither are the systematic differences between the theoretical input parameter for the maximum x-ray tube energy and the actual maximum energy output from the x-ray tube correctly represented by the SpekCalc program. Thus the large residual shown for Figure 5.27 at the highest energies most likely arises from ineffective simulation of the irradiating x-ray tube energy spectra. Additionally, the pulse pileup is generated for the KED spectra using the same method employed for the XRF spectra, and the post processed KED spectra with the pulse pileup included is shown in Figure 5.30.

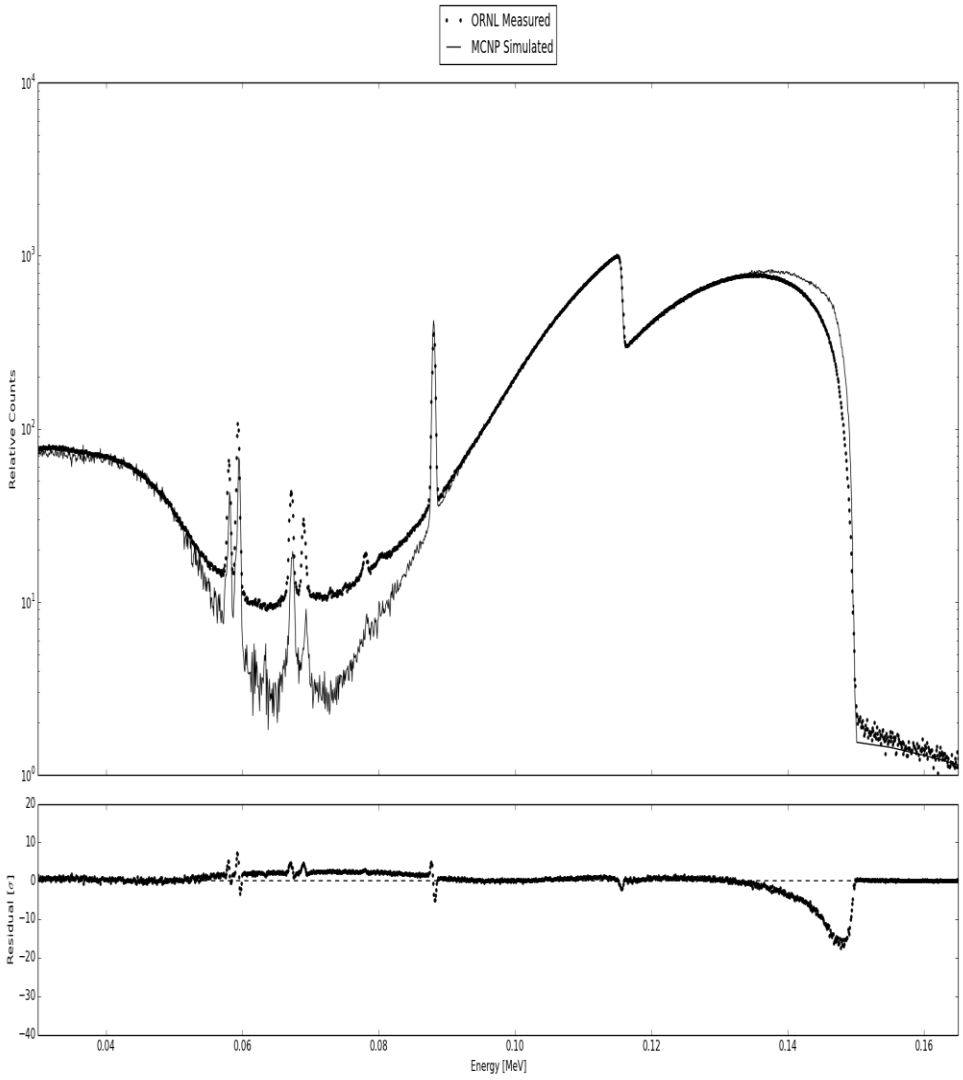

Figure 5.30. ORNL measured KED responses of the continuum and the KED magnitude for a uranium nitrite sample with approximately 268.21 g U/L are compared to the post processed MCNP KED spectra with the pulse pileup included.

CHAPTER 6

SENSITIVITY STUDY

To demonstrate the robustness of the Monte Carlo models developed herein, detailed uncertainty and sensitivity analyses were performed. A significant emphasis has been placed on reducing and quantifying the amount of error or uncertainty that is associated with the results of the computer simulation. Quantifying the amount of error or uncertainty in such responses has been approached through an analysis of the reducible and irreducible error. To account for the need to produce realistic results, the fluorescence data tables used in the simulation were analyzed to observe their impact on the simulated x-ray predictions. New empirical algorithm development has been supplemented through an in-depth analysis of the origin of each component of the HKED spectral responses. Furthermore, a sensitivity study was performed to ensure spectral interferences such as absorption and enhancement from matrix effects were correctly modeled. In aiming to ensure the fundamental simulation parameters are correct, sample matrices themselves were simulated and compared to experimentally measured assay results to allow for a detailed analysis of the results without the spectral components due to the actinides.

6.1 Estimation of Uncertainty

The estimation of the uncertainty in the simulation of the HKED with MCNP requires an analysis of both the random and systematic error. Random error is the inherent variation of the physical phenomena under consideration and can be evaluated through statistical analysis and reduced by increased sampling methods, such as Monte Carlo sampling. Monte Carlo sampling is useful for random uncertainty quantification since the sampling from random processes to solve deterministic problems can be controlled by choosing the

number of histories that need to be generated. This control over the statistical fluctuations of the results allows for the simulation to be run at any length to produce the desired counting statistics.

Systematic error is introduced in any phase of the modeling process from incorrect assumptions, deficiencies in the underlying physics models in MCNP, lack of accurate fundamental data, or human error. The errors in MCNP simulation work usually come from errors in the input parameters or incorrect use of the simulation, but can also come from unexpected deviations between the data being used in the simulation and the generally accepted data values of the physical phenomena being simulated.

6.1.1 Simulation Uncertainty

Given an x-ray tube excitation spectrum and a highly detailed geometry, the transmission of the photons within a system and their probability of interaction can be accurately reproduced with a Monte Carlo simulation. The capability of a model to provide realistic assay results and a faithful representation of the spectral shape of the x-ray transmission rates and XRF production rates from the ORNL HKED was tested for uranium and uranium-plutonium samples in nitric acid matrices. The obtained spectra represent the response from an ideal detector with optimum resolution, and must be convoluted with detector response functions to reproduce a typical observed pulse height spectrum from a real detector. In order to compare the simulation with experimental data, the same energy per channel was mirrored for the simulation spectra to match the calibration of the experimental data.

6.1.1.1 Random Uncertainty

The simulated spectra from MCNP were collected into user defined tallies, and MCNP tally results were printed with the uncertainty, or statistical precision, of the tally

corresponding to one estimated standard deviation. The uncertainty estimate of the tally is derived from the tally and its second moment in forming confidence intervals for the Monte Carlo results. This uncertainty estimate will be reduced as the computational time, and consequently the number of particles in the sample, is increased for the simulation. By increasing the number of particles simulated in a single MCNP run, the associated uncertainty with the tally can thereby be reduced to the desired level. However, another approach to reduce the uncertainty of the tally is to create multiple, identical MCNP runs each seeded with a different starting random number and combine them.

In the case of recording *N* multiple independent runs, a simple approach is taken to find the expected error for the sum of the runs. Treating the runs as a single combined run, the multiple counts are summed together, shown in Equation 6.1. From application of the error propagation formula, Equation 6.2, it is determined that the sum of the squared standard deviations for each run is equal to the squared standard deviation for the combination of all runs, shown in Equation 6.3. This is because the partial derivatives in Equation 6.2 are all equal to one. If each of the independent runs did not have nearly the same associated precision, a more complex approach involving weighting factors would be needed for combination of the runs with unequal errors [92].

$$\boldsymbol{M = x_1 + x_2 + \cdots + x_N} \qquad \text{Equation 6.1}$$

$$\boldsymbol{\sigma_M^2 = \left(\frac{\partial M}{\partial x_1}\right)^2 \sigma_{x_1}^2 + \left(\frac{\partial M}{\partial x_2}\right)^2 \sigma_{x_2}^2 + \cdots} \qquad \text{Equation 6.2}$$

$$\boldsymbol{\sigma_M^2 = \sigma_{x_1}^2 + \sigma_{x_2}^2 + \cdots + \sigma_{x_N}^2} \qquad \text{Equation 6.3}$$

The calculation of the mean value *A* from the independent runs can now be determined straightforwardly, and as dividing a value by a constant does not change its relative error, the expected standard deviation of the mean value *A* from a set of independent runs is established and shown in Equation 6.4.

$$\boldsymbol{\sigma_A = \frac{\sigma_M}{N}} \qquad \text{Equation 6.4}$$

The aim of determining the expected standard deviation from a set of independent runs is so the random uncertainty requirement for the combination of the simulated data tallies can be met. Two different tallies were utilized in this research, a next event estimator point detector tally and a pulse height distribution tally. For a single run, to obtain a high quality pulse-height distribution tally with confidence intervals that are generally reliable, the statistical precision should be set to less than 0.10 [79]. However, point detector results tend to have larger third and fourth moments of the individual tally distributions, so a smaller value of the statistical precision, < 0.05, is required to produce generally reliable confidence intervals [79].

To ensure adequate counting statistics from the simulations of the HKED, the tally results were required to obtain statistical uncertainty below the value of 0.05 before convergence was obtained. The decision subsequently was made to require the statistical precision for the XRF branch to be an order of magnitude more precise than this, to a value of 0.005. The purpose of holding the statistical precision of the simulation results to such a degree was decided in order to ensure the simulation results were kept consistent with the statistical precision of the experimental results. Furthermore, the statistical precision for the KED branch was set to a value of 0.0025 similarly to match the random uncertainty in the experimental data. These uncertainty requirements were placed over an energy region in the XRF and KED spectra with low relative count rates, between 0.120 and 0.130 keV

and 0.05 and 0.06 keV respectively, to ensure the uncertainty would be less than the values chosen for all energy regions with higher relative count rates in the spectra.

If these uncertainty requirements are applied to a set of multiple independent tallies, the cumulative uncertainty for the set is known, and the uncertainty for each run can be determined using Equation 6.4. Requiring the precision of specific tallies to be met before convergence was possible by introducing the precision cutoff STOP card [80]to the MCNP simulation input files. This card allows for the termination of calculations based on the desired precision for a specific tally, ending the run when the tally fluctuation chart of the specified tally has a relative error less than the input control value. Thus a minimum uncertainty was set for the random uncertainty of the simulation to match the experimental error.

6.1.1.2 Systematic Uncertainty

A potential source of systematic error is the application of variance reduction techniques to reduce the computational time needed to resolve the simulation with a required precision. In order to produce a computationally efficient simulation model of the x-ray generation and transmission within the sample vial, several approaches to reduce the variance of the simulation are offered by the MCNP code. The drawback of the application of these techniques is the potential bias brought into the results, arising from the nonanalog Monte Carlo sampling affecting the natural probabilities of the various interactions occurring. Biasing the x-ray tube source term, an exponential transform, forced collisions, and point detectors were all employed to control and optimize the performance of the simulations. The simulation results were compared to analog models to ensure the introduced bias was within a negligible range. The analog comparison can be found in Appendix D. The improvement in the computational efficiency from each

successive application of a variance reduction technique is shown as a cumulative result in Figure 6.1 for a single MCNP XRF tally.

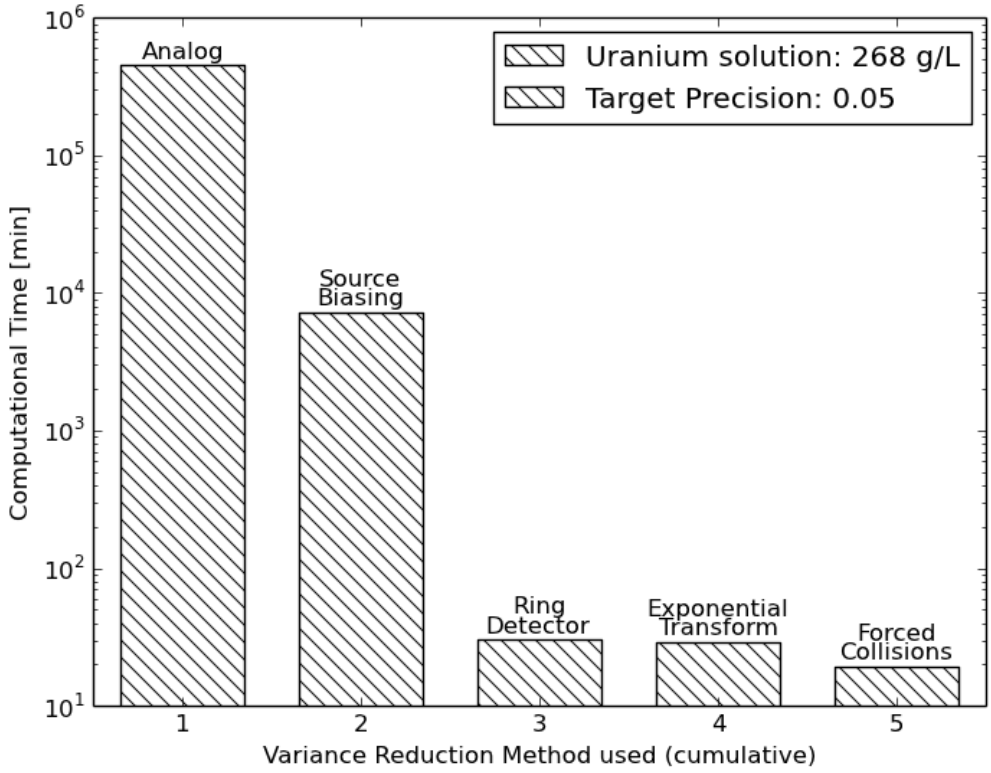

Figure 6.1. Calculation time required to achieve 0.05 statistical precision for a single XRF branch tally with the annotated type of variance reduction applied cumulatively.

Another source of irreducible error in the simulation was quantified and found to have a measureable impact on the accuracy of the simulation results. The ability to simulate x-ray spectra that agree very well with real measured spectra is hindered by an energy offset in the MCNP fluorescence data tables. A closer look was made into the origin of this offset within the MCNP data file *eprdata12*, named so by the code developers to avoid confusion with earlier data libraries in the *mcnplib* series. If the data tables in *eprdata12* are parsed into four columns, then starting on row 1791116, the uranium K-

edge value is shown to be set at 1.1611E-1 MeV. This value is 0.5019 keV and 0.434 % offset from the generally accepted theoretical value of the uranium K-edge published by the National Institute of Standards and Technology (NIST), 1.156081E-1 MeV [94]. A sample set of the offset and generally accepted values is shown below in Table 6.1 for the associated fluorescence x-rays for uranium and plutonium and their K-edges.

Table 6.1. K-edge and x-ray offsets from the MCNP data library.

	MCNP Energy [MeV]	NIST Energy [94] [MeV]	Offset [keV]
Uranium K-edge	1.1611E-01	1.15608E-01	0.5019
Uranium Kα1	9.8928E-02	9.84336E-02	0.4944
Uranium Kα2	9.5066E-02	9.46531E-02	0.4129
Plutonium K-edge	1.2235E-01	1.21795E-01	0.5546
Plutonium Kα1	1.0428E-01	1.03735E-01	0.5436
Plutonium Kα2	9.9979E-02	9.95260E-01	0.4530

6.2 Full Spectral Definition

6.2.1 X-Ray Fluorescence Definition

A highly detailed analysis of the energy range between 30 and 120 keV was undertaken for the XRF branch of the HKED in order to determine the origin of each component of the spectral response. This analysis is required to improve the performance of empirical spectral fitting algorithms. The majority of the XRF spectrum counts originate from elastic or inelastic scattering of the interrogating x-ray tube source at a backwards angle of roughly 150° from the incident beam on the sample. The peaks throughout the spectra mostly come from the K- and L-edge fluorescence from the actinides and structural material as well as pulse pile up within the detector. Figure 6.2 shows a typical uranium-

nitric acid sample output from MCNP. The top of graph displays the output from the simulation for a detector with optimum energy resolution. The bottom graph depicts the experimental results from the ORNL HKED overlaid with the MCNP results once convoluted with a detailed detector response.

Peaks from the cadmium-109 calibration check source as well as the gadolinium beam monitor are identifiable due to their characteristic energies. However, there were several discernable anomalies within the XRF spectra whose origin needed to be understood before a complete understanding of the various contributors to the resultant XRF spectrum could be obtained. An examination of the broadened hump around 55 keV and the broadened edge beginning at 80 keV was done to determine the origin of each anomaly through conservation of energy and then checked via dedicated simulation runs.

It was assumed that the broadened hump at 55 keV was associated with x-rays generated due to the existence of trace metals within the structural material or the sample being investigated. In fact, it is due to the inelastic scattering of x-rays from the x-ray tube source. The x-ray tube uses a tungsten anode for generating a broad bremsstrahlung spectra and emitting a series of characteristic K x-rays at 59.318 and 57.981 keV and L x-rays at 69.102 and 67.245 keV. By application of the simultaneous equations for the conservation of energy and momentum, the energy of the scattered characteristic K and L x-rays at an angle of 150° was calculated to be roughly 49 and 55 keV. Removal of the spectral contributions from the gadolinium beam monitor through dedicated simulation runs displays a corresponding peak to the Compton scattered K x-rays. The origin of the broadened hump at 55 keV was confirmed by simulating the x-ray tube source sans the characteristic peaks from the tungsten anode, resulting in a noticeable absence of any anomaly.

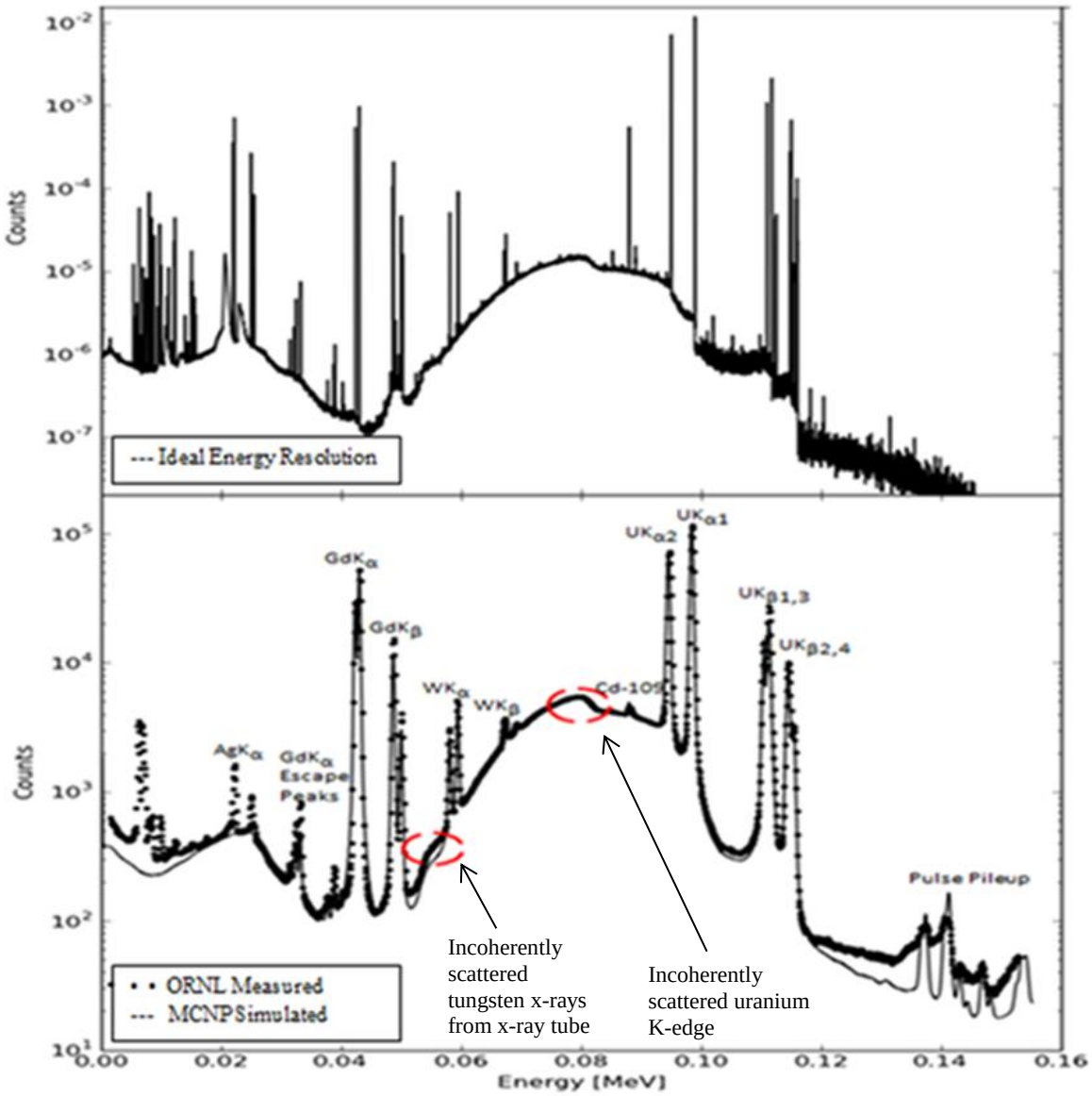

Figure 6.2. MCNP simulation of the HKED XRF spectral data from an approximately 268 g/L uranium sample in nitric acid matrix. Anomalies in XRF spectra are highlighted by dashed circles.

The broadened edge after 80 keV in the XRF spectra was found to be due to the Compton scattered photons from the x-ray tube counts around the uranium K-edge. XRF spectra from the HKED with a 5 g/L of uranium sample was found to have no noticeable change of shape at 80 keV, but the 80 keV edge would begin to resolve as the concentration of

uranium in the sample was increased. Again using the application of conservation of energy and momentum, theoretically the 150° backscatter of a 115.6 keV photon from the uranium K-edge results in an energy of 81.3 keV. In order to determine that the edge was originating from the backscattered K-edge photons, samples containing elements with different K-edges were simulated and compared to the spectra containing uranium. As expected, the edge was shifted to lower energies for lower atomic number elements and higher energies for those elements of greater atomic weight than uranium.

6.2.2 K-Edge Definition

While a full spectral definition of the KED was not required, as the spectral contributors are easy to recognize and fairly straightforward, there was an aspect of the measured KED response where the origin was not initially clear. In the region surrounding 90-110 keV of the HKED KED response, a change in the shape of the spectrum not due to the incident attenuated transmission through the sample was noted. Analysis of the broad change in the shape of the spectrum, as well as the location between 90-110 keV suggested that the origin of the change in the spectrum shape was due to the transmission spectrum passing through the entirety of the KED LEGe detector and Compton scattering off the copper cooling rod immediately behind the detector, then returning to the detector volume. Theoretically, an interaction such as this to a 150 keV photon undergoing a backwards directed scatter between 130° and 160° would result in a broad energy deposition in the detector between 95 and 100 keV.

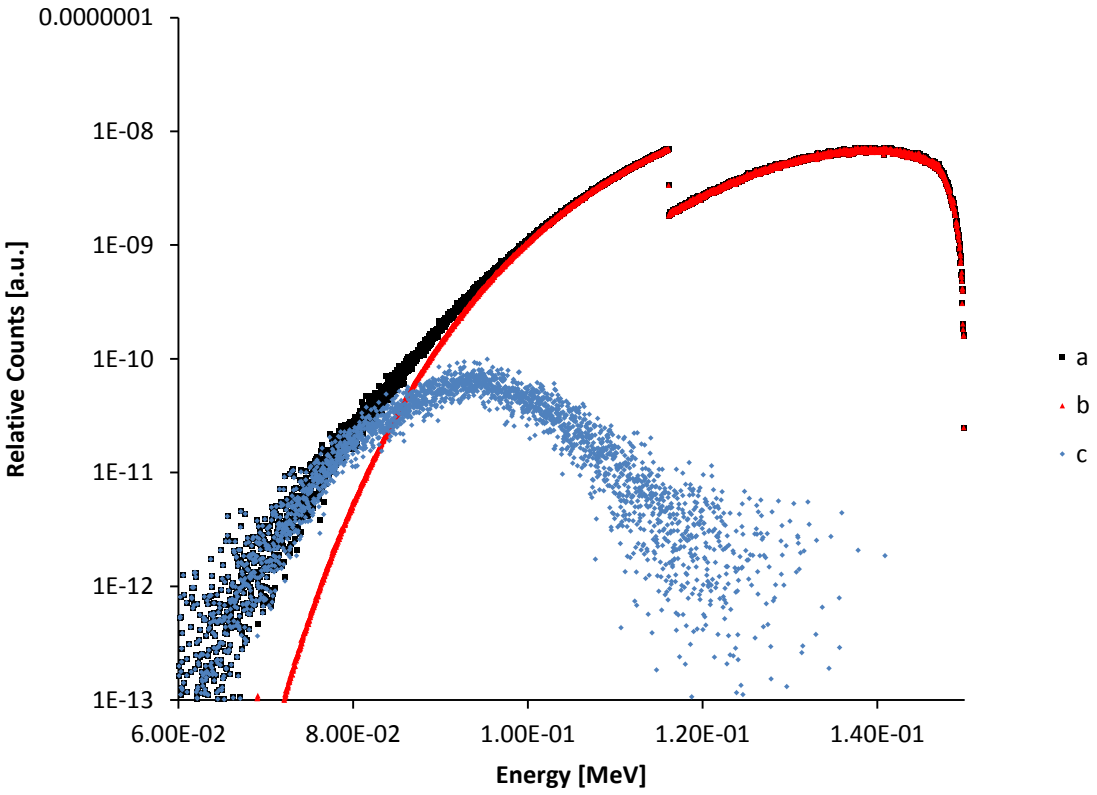

Figure 6.3. MCNP tally tagging simulation of the HKED KED spectral data from an approximately 268 g/L uranium sample in nitric acid matrix. The difference between (a) all scattered particles interacting in the KED LEGe detector and (b) only the uncollided source x-rays from the x-ray tube was shown to be due to (c) the backscatter of the transmitted photons past the KED LEGe detector and reflecting off the copper cooling rod. This is the cause of the change in shape of the KED continuum around 90 – 110 keV

In order to confirm this through simulation, a new tally collection tool was applied to populate the tally with only the photons depositing energy in the detector that have first undergone an interaction with the copper cooling rod behind the detector. The collection tool, called tally tagging, allowed the analysis of the separated components of interest from a single tally. As the tally collection tool is incompatible with the pulse height tally,

the information obtained was not applicable for reproducing the detector response, but only to validate the hypothesis that the collimated KED beam was transmitting through the KED LEGe detector and interacting with the copper base. Thus, a cell flux tally within the detector volume was set up to be separately populated with (a) all scattered particles interacting within the detector, (b) only the uncollided source x-rays from the x-ray tube, and (c) only the particles that have interacted with the copper cooling rod, and the results are shown in Figure 6.3. The change in shape is highlighted by the difference between the black (a) counts and the red (b) counts, where an increase in the relative counts in the overall spectra is shown to be due to the backscattering of transmitted particles through the LEGe detector.

Additional benefits from simulating the KED response included an ability to deduce the HKED system structural materials attenuation thicknesses and material compositions. Due to the fact that MCNP simulation of the HKED has been shown to create a faithful representation of the bremsstrahlung continuum, optimization of the KED response allowed to the correct window thickness of the stainless steel sample transfer tube to be determined. Also an analysis of the simulation results was able to confirm that a component of the HKED system was manufactured out of cadmium, instead of stainless steel as originally thought.

6.3 X-Ray Production

6.3.1 Spectral Interferences in K-Edge Vacancy Production

A full spectral definition of the simulated HKED response is incomplete without ensuring the realistic interference processes are being modeled. In fact, matrix effects are one of the major sources of error when using the measured fluorescent intensities from the actinides in the sample to determine their concentration [95]. The spectral interferences

from matrix effects such as absorption and enhancement were analyzed through an analysis of the K-edge vacancy production rates for actinides. In an effort to determine that the MCNP simulation model of the HKED system accurately reproduces these effects, a dedicated analysis of several different binary actinide sample compositions was performed. Shown in Figure 6.4, to provide a basis of comparison, the matrix effects in XRF spectrometry including absorption (Curve B), enhancement (Curve C), and negative absorption (Curve D) were compared to the results of an existing study observing the matrix effects between samples containing differing weight fractions of iron combined with either manganese, chromium, or nickel [103].

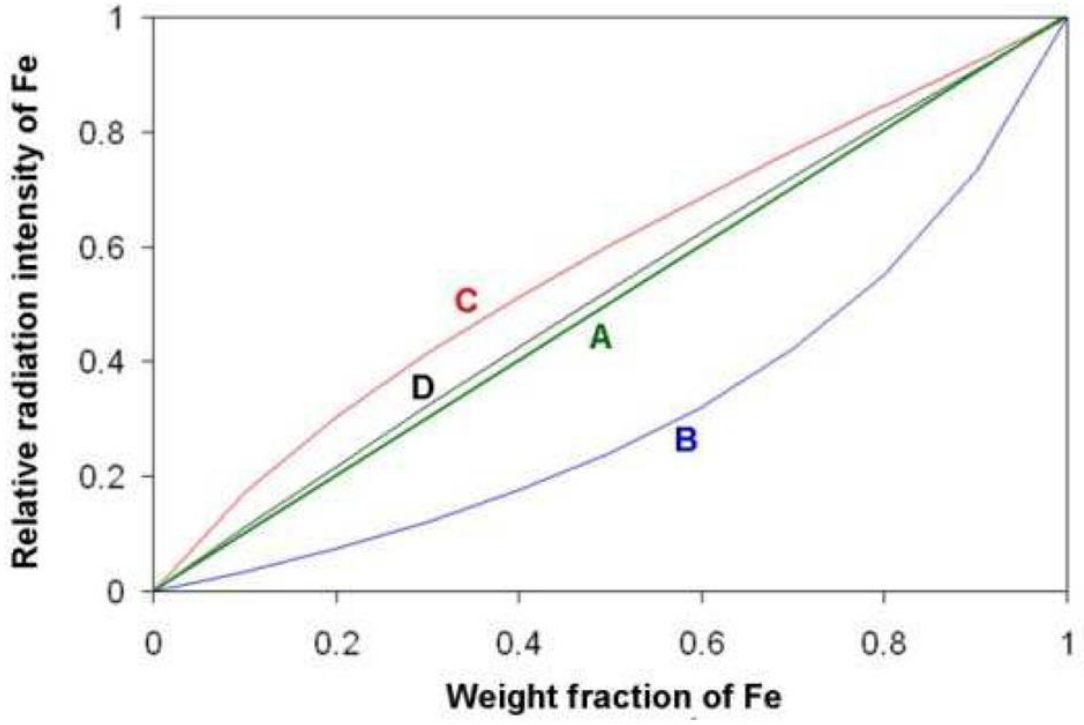

Figure 6.4. Relationship between radiation intensity of Fe and weight fraction of Fe for several examples of matrix effects due to spectral interferences: Curve A – matrix effects are negligible, Curve B – FeCr, Curve C – FeNi, Curve D – FeMn.

Reproduced from [103].

A sensitivity study on each of the binary actinide sample compositions (UBi, UPu, PuRn, and PuCm pure metal binaries) proved that MCNP was accurately reproducing the expected matrix effects affecting the results of the HKED quantitative XRF analysis. This analysis is entirely based on simulation and does not have experimental work other than the relationships shown in Figure 6.4 to confirm the presence of, or magnitude of the spectral interferences.

Absorption effects are observed when the uranium sample contains an element such as bismuth that has an absorption edge of slightly lower energy that of the uranium and thus can absorb the uranium characteristic radiation. As the energy of the plutonium K-edge exceeds the uranium K-edge, the uranium $K\alpha_1$ x-rays relative intensity can be enhanced by the presence of plutonium, due to the plutonium Kβ x-rays ability to liberate K-shell electrons in uranium.

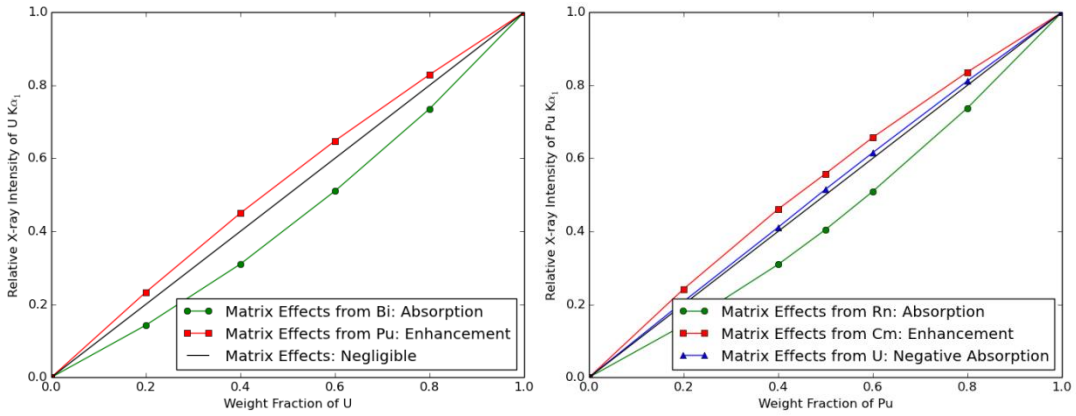

Figure 6.5. Left: matrix effects of absorption and enhancement on the relative intensity of the uranium $K\alpha_1$ x-rays as the weight fraction of the uranium is changed. Right: matrix effects of absorption, negative absorption, and enhancement on the relative intensity of the plutonium $K\alpha_1$ x-rays as the weight fraction of the plutonium is changed. Both sample compositions are pure metal binaries using binaries (UBi, UPu, PuRn, and PuCm).

Figure 6.5 shows the spectral interference from uranium- and plutonium-based binary samples where the uncertainty in the data was less than 0.2% for all data points. This work on spectral interference from matrix effects has made an important distinction for actinide samples containing uranium and plutonium. As uranium has an absorption edge of slightly lower energy than that of plutonium, it is expected that this would result in the absorption of plutonium K x-rays and correspondingly lower their spectral intensity. In reality a negative absorption effect occurs where the uranium in the sample absorbs the plutonium radiation to a lesser degree than had the sample contained plutonium alone. This results in a small but measurable enhancement in the intensity of the plutonium K x-rays in the presence of uranium. Both this enhancement and the enhancement effects the presence of plutonium has on uranium K x-ray intensity counts are important distinctions that must be made in order for the correct concentration of plutonium to be calculated when performing safeguard measurements.

As the weight fraction of uranium to plutonium in a sample reaches unity, this enhancement effect can enhance the amount of the x-ray intensity by up to 10%. This enhancement is determined from first principles analysis of pure metal binary samples and would not be expected to be as large for the solution-based samples used for the HKED XRF analysis. However, such enhancement from matrix effects must be taken into account regardless as it is not a negligible increase.

6.3.1.1 Spectral Interferences on HKED Sample

As shown in Figure 6.6, the spectral effects of absorption and enhancement are muted when a sample typical to a HKED assay is examined, where a 3M nitric acid based sample is combined with a range of uranium and plutonium weight fractions. This analysis used a sample with a maximum of 18.24% mass uranium at 1.0 weight fraction

uranium or 18.24% mass plutonium at 0.0 weight fraction uranium. While the pure metal analysis noted a 10% enhancement at equal uranium and plutonium weight fractions, the HKED sample is shown to have a maximum enhancement of the relative uranium K intensity of 4% as the uranium and plutonium weight fractions become equal. This enhancement of the uranium K intensity will need to be confirmed through experimental analysis.

The importance of monitoring the matrix effects in HKED responses has been previously noted [104], and will only become more important especially when assaying samples where the weight fractions between actinides are close to equal. These matrix effects produced by the Monte Carlo code are necessary in order to allow for the correction of the representative peak height intensities for the actinides.

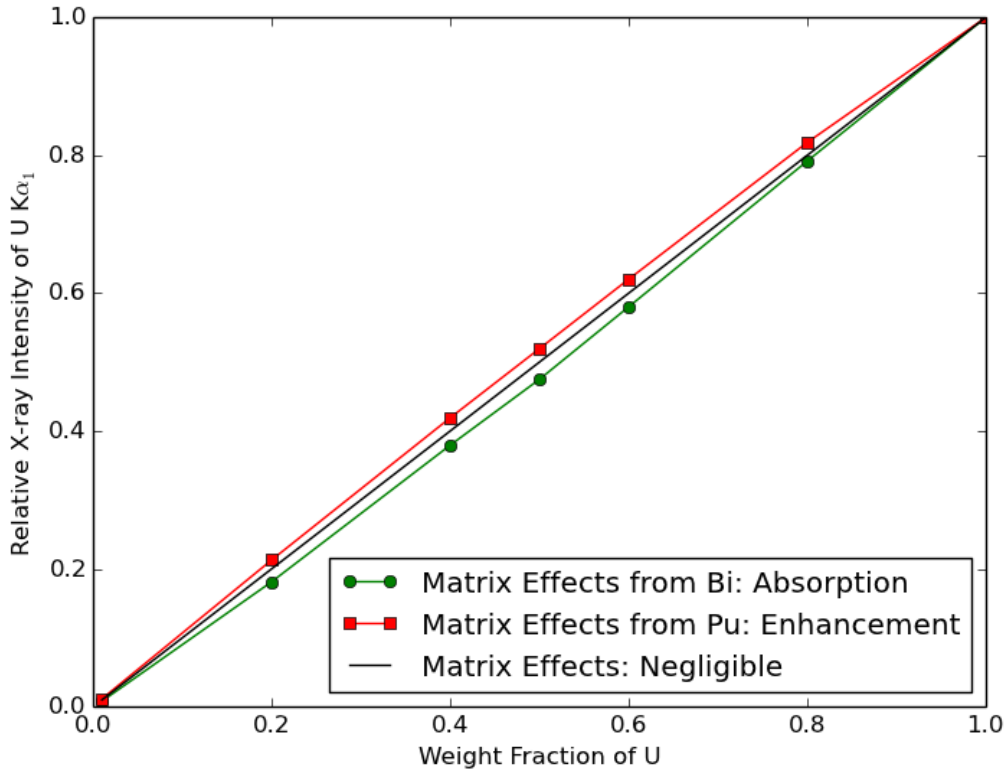

Figure 6.6. Matrix effects of absorption and enhancement on the relative intensity of the uranium $K\alpha_1$ x-rays as the weight fraction of the uranium is changed for a uranium-plutonium based sample in a 3M nitric acid mixture. The sample has a maximum of 18.24% mass uranium at 1.0 weight fraction uranium or 18.24% mass plutonium at 0.0 weight fraction uranium.

6.3.2 Branching Ratios for X-Rays

As a means of developing confidence that the simulation inaccuracies, such as the energy offset in the MCNP fluorescent data tables, do not extend to the branching ratios for generation of x-rays, an analysis was administered on the simulated ratio between the uranium $UK\alpha_1$ and $UK\alpha_2$ x-ray peaks. This work was done to complement the analysis of the peak areas between simulated and experimentally measured results found in Table

5.1. Because the peak area analysis took into account the various broadening parameters from the post processing, a separate analysis was investigated to be solely dependent on the data and the transmission processes within the MCNP simulation code. The ratio, defined as the UKα_1 x-ray peak magnitude divided by the UKα_2 peak magnitude, was compared to the measured ratio for a range of sample concentrations. Table 6.2 shows the difference between the simulated and measured peak ratios and the uncertainty shows the propagation of error when taking the difference, and the ratio, of the counts for the range of concentrations analyzed. The results show the simulated and experimentally measured ratios match up well within the error bounds for each of the samples analyzed. The error analysis shows the propagation of error when taking the difference, or the ratio, of the measured counts for the range concentrations analyzed.

Table 6.2. Peak Maxima Ratio for Comparison of Branching Ratios from MCNP.

Actinide Ratio	**Concentration [g/L]**	**Simulated Ratio UKα_1/ UKα_2**	**Measured Ratio UKα_1/ UKα_2**	**Difference [%]**
100:1	107.3 g U/L	1.55309	1.55847	*0.35 ± 1.615*
100:1	160.91 g U/L	1.57719	1.58597	*0.55 ± 1.377*
100:1	243.26 g U/L	1.60042	1.59945	*0.06 ± 1.191*

6.4 Sample Matrices

To ensure the fidelity of the MCNP model, the model was validated against experimental data of representative samples with traditional sample matrices. The capability of the model to provide realistic assay results was tested for a water filled vial and a 3M nitric acid filled vial. Each represented sample matrix was analyzed to match the fundamental properties of the experimental assay and then overlaid on top of experimental data to

visualize a direct comparison. The direct comparison was made difficult as the experimental sample matrix data analyzed herein was obtained without calibration. This meant that without the same energy per channel variation between simulation and experimental results, a direct comparison would only be useful to visualize the general spectrum shapes and more specifically, plots of the residual differences would be unhelpful. For this reason, the sample matrices spectra plots were binned in channel numbers instead of energies.

In analyzing the fundamental components of the sample matrix spectrum, the experimental results for each of the assayed samples were plotted together to understand the substantial differences between spectra. Figure 6.7 shows that the difference in the experimental results when changing the sample matrix between water and nitric acid are negligible, only visible as a slight increase in overall counts for the nitric acid sample due to the increased number of electrons from the heavier molecule causing slightly more interactions. This slight increase in overall counts is reflected in the simulation of the sample matrices, as shown in Figure 6.8.

The primary differences between simulation and measured results are the lack of a cadmium-109 check source, the higher intensity counts from the simulation in the channel region between 600 and 1000, and a lack of scattering around the gadolinium peaks near channel 600. The first two differences originated from the difficulties in obtaining the same energy per channel between the spectra and the other difference is due to a combined aspect of the lack of appropriate broadening for the simulated x-ray peaks and the insufficient simulation of scattering events in the XRF collimator.

However, the important characteristic of the sample matrices that is shown to compare well with this analysis approach is in the energy region containing the actinide x-ray

peaks. The broad energy distribution of the x-ray tube causes a large background from the inelastic scattering with the sample material, and the accurate simulation of this background shape is important to reproducing the correct peak areas for the actinides being assayed. In order to compare the shapes of the simulated and experimentally measured sample matrices, the two spectra are overlaid on top of each other. Figures 6.9 and 6.10 show the simulated and measured water and nitric acid sample matrix spectral shapes to match up well, respectively.

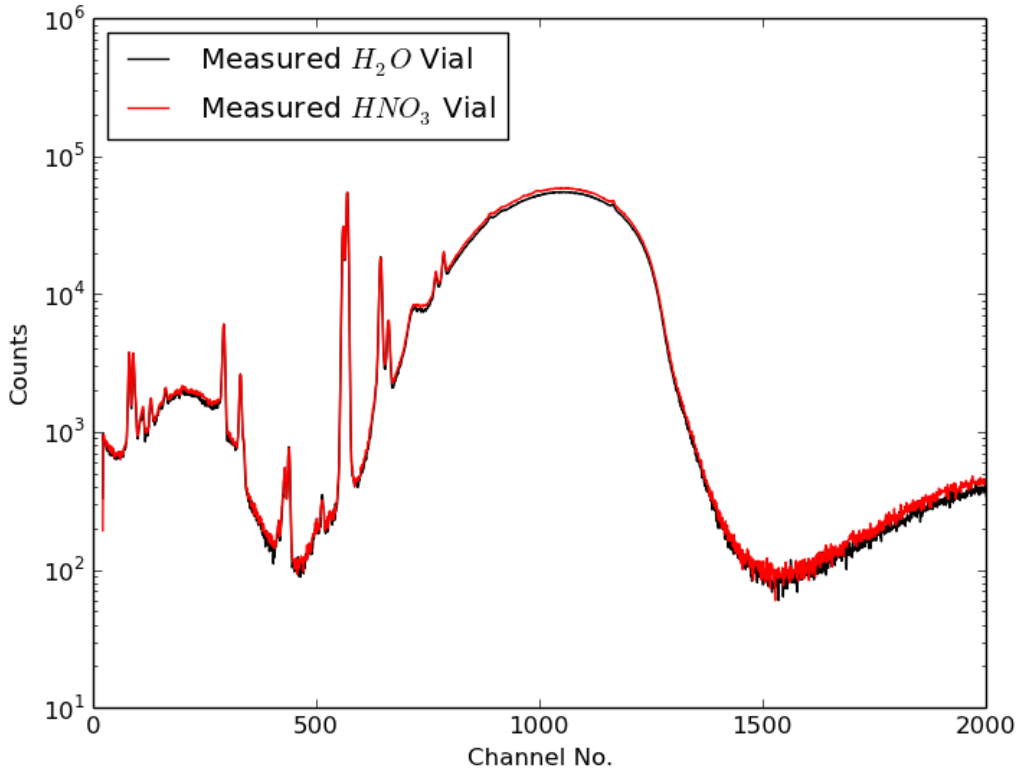

Figure 6.7. Comparison of experimental XRF assay results from water and 3M nitric acid mixture sample matrices.

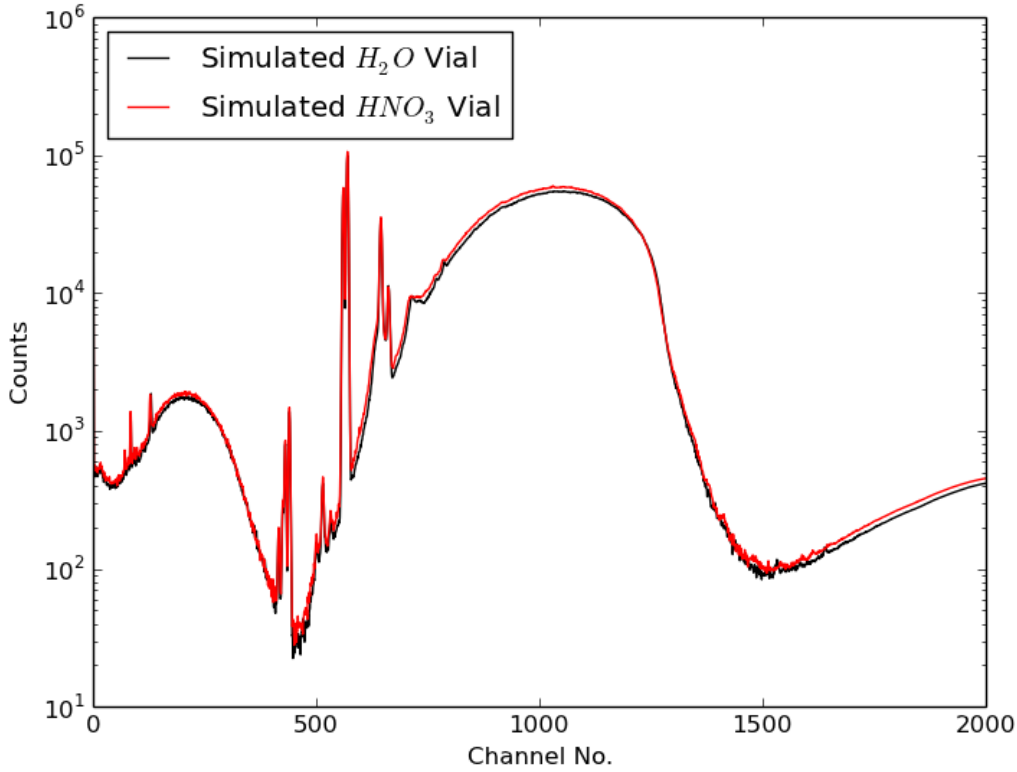

Figure 6.8. Comparison of simulated XRF assay results from water and 3M nitric acid mixture sample matrices.

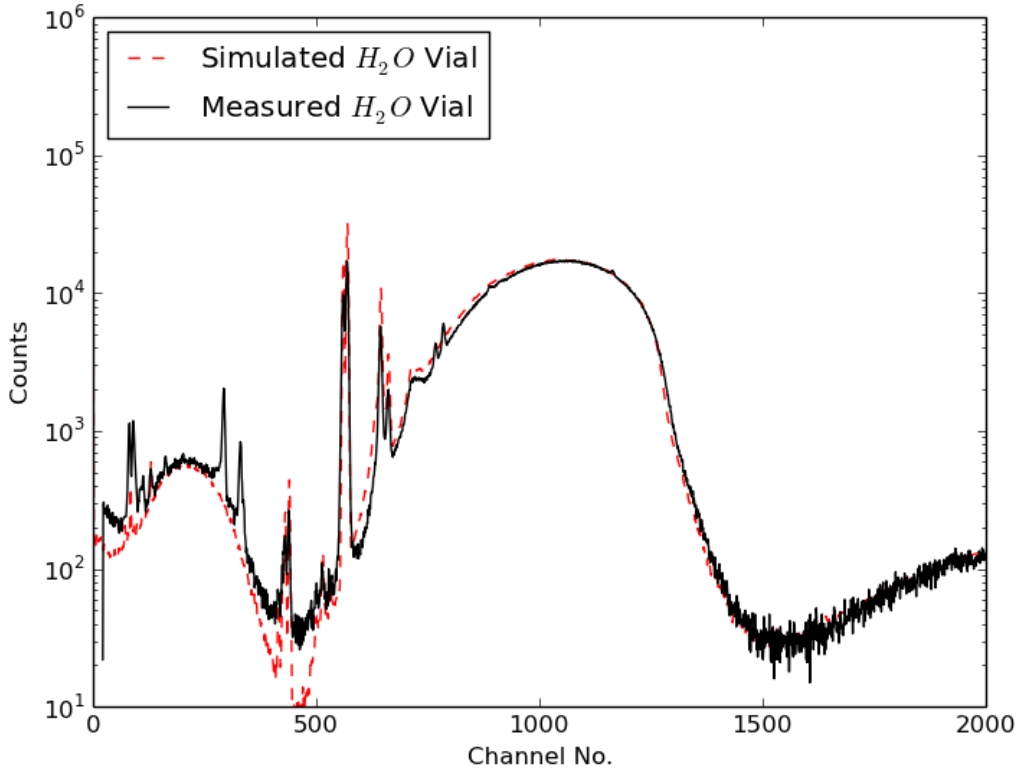

Figure 6.9. Comparison of the measured and simulated XRF assay results from water filled sample vial.

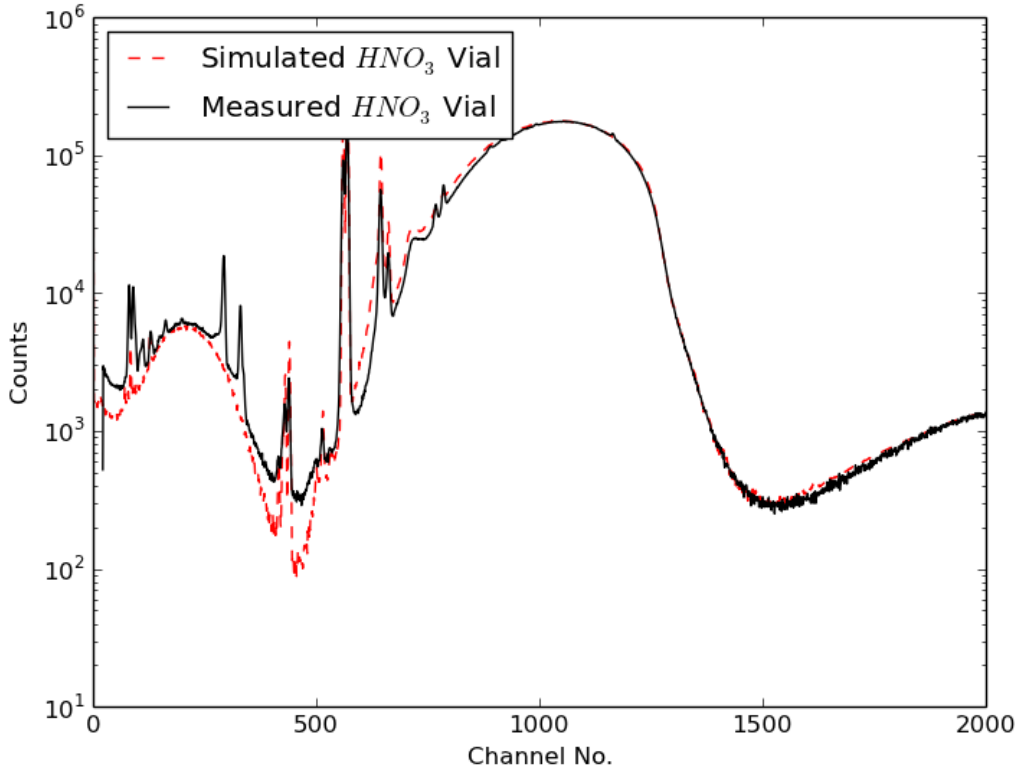

Figure 6.10. Comparison of the measured and simulated XRF assay results from 3M nitric acid mixture filled sample vial.

CHAPTER 7

OPTIMIZATION FOR PYROPROCESSING

The proposed research endeavors seek to evaluate a technical basis for the safeguarding of nuclear material from a pyroprocessing facility at the electrorefining processing step. The feasibility of implementation of a dedicated HKED system into safeguards measurements on pyroprocessing will depend on the accuracy, capabilities, and applicability limitations determined through experimentation and model validation of the expected pyroprocessing samples. In order to extend the HKED system beyond its current applications, this research included simulation developments to encompass the expected materials and concentrations which are beyond the range of existing representative standards.

To support this effort, Monte Carlo simulations of the ORNL HKED have been designed for extending the HKED system beyond solutions for aqueous systems with uranium and plutonium ratios of 100:1 to include additional minor actinides (neptunium/americium) in spent fuel and where uranium and plutonium ratios approach 1:1. The HKED sampling and measurement system will need to be optimized to allow for the system to assay actinide content with a smaller sample volume. The simulation will take into account variables such as possible non-homogeneities of samples, non-traditional isotopic mixtures, and higher actinide concentrations

7.1 System Optimization

7.1.1 Higher Actinide Concentrations

MCNP has been shown to be good at reproducing most parts of the XRF and KED spectra, but some post processing is necessary for the simulated spectra to surpass the

requirements set in Section 5.3 to allow for a faithful spectral representations. However, with a modeling system created and tested on standards representative of traditional reprocessing samples, concerns for introducing biases with the processed results are expected when transferring the modeling system onto an analysis of samples outside of the calibration regime. Therefore, a simulation study has been undertaken using commercial reprocessing plant HKED XRF spectra with higher plutonium values to validate the accuracy of the simulation for samples more closely representative of the samples expected from pyroprocessing, specifically matching the higher actinide concentrations anticipated for pyroprocessing based samples.

The experimental results are obtained from a set of nitric acid based sample matrices with uranium to plutonium ratios in the range of 1:1. As the spectral results were supplied without precise details as to the complete sample compositions, x-ray tube operating conditions, or the geometry and dimensions of the structural materials of the HKED system used to obtain them, the sample compositions and structural makeup of the ORNL REDC HKED system remained the foundation for the simulation analysis. This limited the accuracy of the results, as aspects of the simulated spectra did not match up with the experimental data due to lack of sufficient information for determining the modeling conditions. To offset the difficulties of modeling with insufficient information, a normalization parameter was added to the post processing of the simulated results to ensure the XRF peak area comparison reflected the difference between the experimental measured and simulated results.

The comparison results for one of the three high actinide concentration samples analyzed is shown in Figure 7.1, with the remaining two samples located in Appendix A. The large deviations between experimentally measured and MCNP simulated are thought to be due to the structural system differences between the experimental HKED system and the

simulated system. Specifically, the presence of the gadolinium foil in the ORNL REDC HKED system results in the x-ray peaks around 45 and 50 keV for the simulated results while the measured data was obtained on a system without a gadolinium beam monitor and thus no peaks are present. Additional alterations in the bremsstrahlung spectra may be due to sample composition differences between measured and simulated. Figure 7.2 shows a zoomed in view of the energy region containing the actinide peaks. The MCNP simulation of the 1:1 uranium plutonium sample is shown to match the actinide peaks well from the residual plotted in terms of sigma. The residual difference is on the same order of magnitude as the residual differences from the comparative analysis of 100:1 uranium plutonium samples.

However, there are some differences worth making note of, including the simulations lack of resolving the small peak at 106 keV due to the $K\alpha_1$ x-ray from americium and the shoulder peaks at 112 keV and 117 keV due to the $K\beta_5$ x-rays of uranium and plutonium. These differences are due to the nature of the peak search algorithm dependency on using the Gaussian broadened simulated spectra to determine the peak locations. This may be updated for future versions of the simulation in order to refine the post-processing analysis to include the smaller and overlapping peaks.

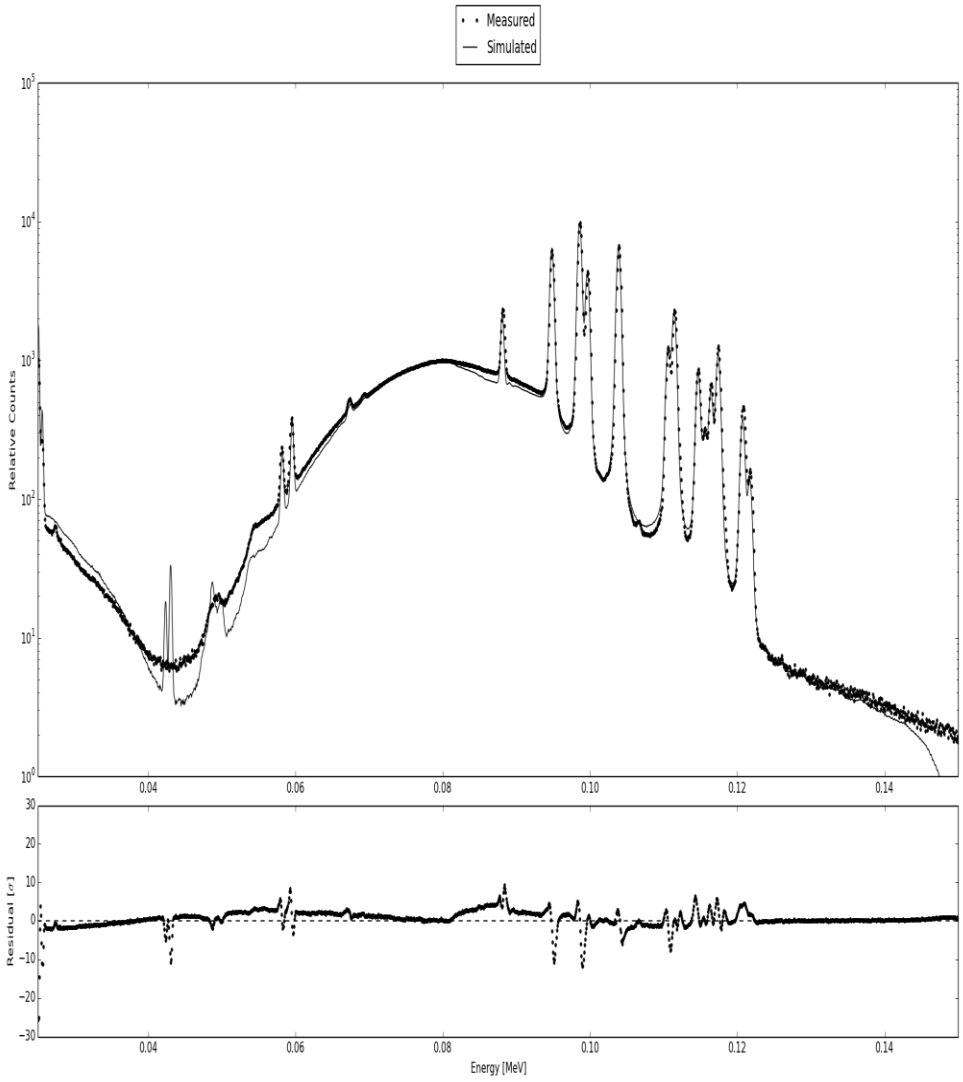

Figure 7.1. Comparison plot between experimental HKED XRF results from a sample with a 1:1 U:Pu ratio and the corresponding MCNP simulation of a similar HKED system XRF results from a sample with 1:1 U:Pu ratio. Both results are generated using a sample with approximately 152.23 g U/L and 159.47 g Pu/L in nitric acid based matrix.

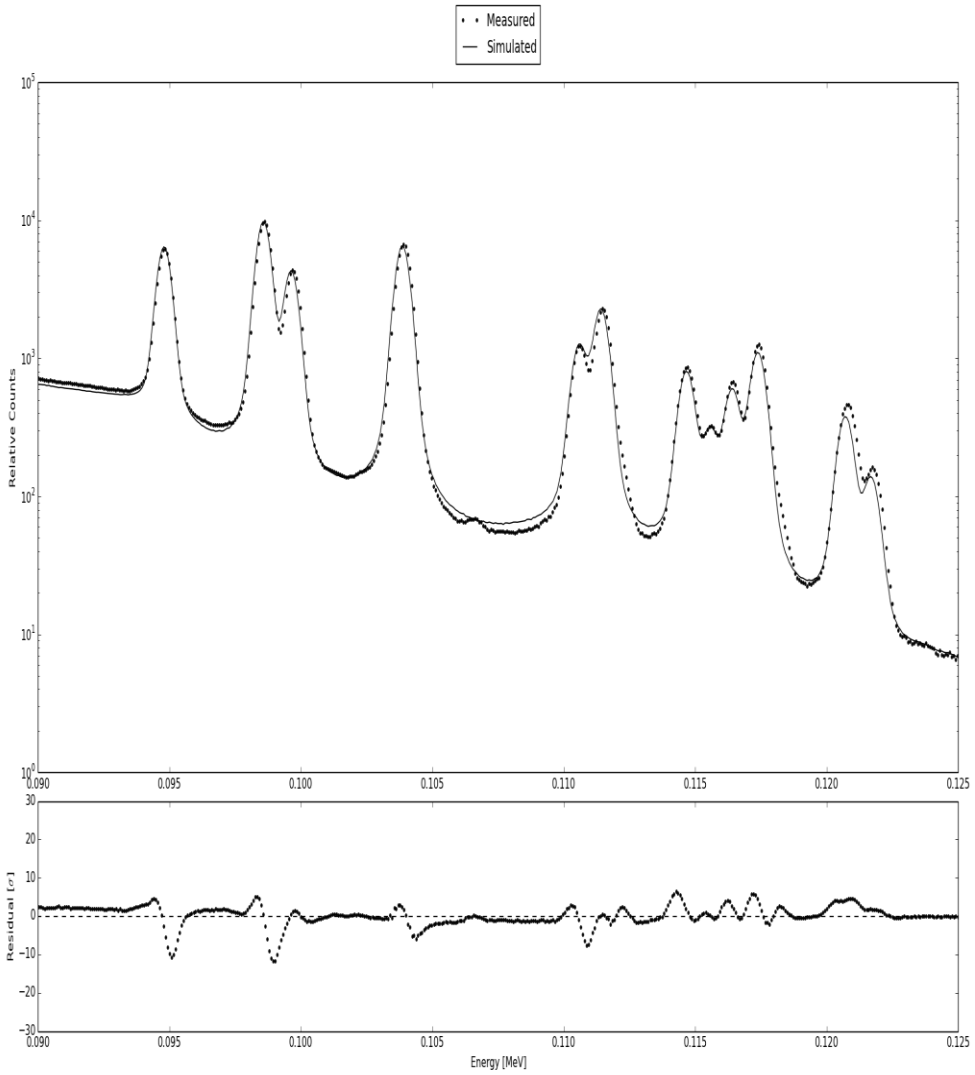

Figure 7.2. Comparison plot between experimental HKED XRF results from a sample with a 1:1 U:Pu ratio and the corresponding MCNP simulation of a similar HKED system XRF results from a sample with 1:1 U:Pu ratio showing the energy range containing the Kα and Kβ peaks for the actinides. Both results are generated using a sample with approximately 152.23 g U/L and 159.47 g Pu/L in nitric acid based matrix.

An in depth look into the peak areas and branching ratios for the actinide elements between simulation and measurement was completed to investigate the limitations of the post processing algorithms and review the fundamental MCNP data to ensure it simulated the correct x-ray branching ratios. Shown in Table 7.1, the difference in the peak areas between simulated and measured peaks was analyzed for the uranium $K\alpha_2$ peak in order to approach the analysis of single isolated peak areas instead of the overlapping peaks formed between the uranium $K\alpha_1$ and the plutonium $K\alpha_2$. The error is the uncertainty involved in the approach to determine the measured peak area. The percent difference between simulated and measured peaks is within the same range for samples with 1:1 uranium to plutonium samples as it was for 100:1 uranium to plutonium samples.

Table 7.1. Simulated uranium XRF peak areas compared to the ORNL measured XRF peak areas for the uranium $K\alpha_2$ and plutonium $K\alpha_1$.

	Sample No.	XRF Peak	Simulated	Measured	Difference [%]
2	127.29 g/L U	U $K\alpha_2$	3.601	3.465	*3.93 ± 0.606*
	140.99 g/L Pu	Pu $K\alpha_1$	3.698	3.732	*0.91 ± 0.723*
3	152.23 g/L U	U $K\alpha_2$	4.003	3.710	*7.90 ± 0.620*
	159.47 g/L Pu	Pu $K\alpha_1$	3.952	3.820	*3.48 ± 0.754*
6	191.08 g/L U	U $K\alpha_2$	4.609	4.349	*5.97 ± 0.598*
	182.29 g/L Pu	Pu $K\alpha_1$	4.437	4.444	*0.15 ± 0.484*

The peak area results highlight the fact that the MCNP simulation of the actinide x-ray peaks do not vary over a large range of actinide concentrations when coupled with the post processing routine for applying the corrective energy shift and Voigt peak profiles. This is a promising result considering the calibration range of pyroprocessing samples will most likely include much higher concentration ratios than the typical HKED standards currently contain.

A separate study into the branching ratios of the simulated x-rays was done in order to discover if higher actinide concentrations may result in a bias in the relative x-ray production rates. The maximum values for the simulated peaks were combined to analyze the fundamental MCNP outputs independent of the post-processing broadening effects. Shown in Table 7.2, the simulated and measured ratio of the $UK\alpha_1$ and $UK\alpha_2$ peaks was analyzed for the 1:1 uranium to plutonium nitric acid samples. Similarly in Table 7.3, the analysis was done for the ratios of the $PuK\alpha_1$ and $PuK\alpha_2$ peaks. The error analysis shows the propagation of error when taking the difference, and the ratio, of the counts for the range concentrations analyzed.

Table 7.2. Peak Maxima Ratio for Comparison of Uranium Branching Ratios from MCNP for Higher Actinide Concentrations .

Actinide Ratio	Concentration [g/L]	Simulated Ratio $UK\alpha_1/ UK\alpha_2$	Measured Ratio $UK\alpha_1/ UK\alpha_2$	Difference [%]
1:1	127.29 g/L U	1.58587	1.58996	*0.25 ± 1.662*
1:1	152.23 g/L U	1.58728	1.58190	*0.34 ± 1.620*
1:1	191.08 g/L U	1.61040	1.58996	*1.28 ± 1.507*

The results show a increase in the difference for the simulated and measured ratios of both actinide x-ray pairs towards higher actinide concentrations. This trend was not present for the 100:1 uranium to plutonium ratio samples. It is possible that the difference between simulated and measured x-ray branching ratios is due to the spectral interferences not being sample appropriately in the simulation, but the trend may also be due to the incorrect x-ray data in the MCNP fluorescent data tables.

Table 7.3. Peak Maxima Ratio for Comparison of Plutonium Branching Ratios from MCNP for Higher Actinide Concentrations.

Actinide Ratio	Concentration [g/L]	Simulated Ratio $PuK\alpha_1$/ $PuK\alpha_2$	Measured Ratio $PuK\alpha_1$/ $PuK\alpha_2$	Difference [%]
1:1	140.99 g/L U	1.58209	1.54442	*2.44 ± 1.974*
1:1	159.47 g/L U	1.58953	1.54852	*2.64 ± 1.946*
1:1	182.29 g/L U	1.60514	1.54442	*3.93 ± 1.880*

7.1.2 K-Edge Vacancy Study

In implementing safeguards in future pyroprocessing facilities, the HKED must be used to correlate the amount of special nuclear material in an examined sample to the amount of material in the container from which the sample was taken. For existing HKED devices only a small portion of the entire sample is actively interrogated, so reconstruction of the amount of material in the container from which the sample was taken requires a precise understanding of the amount of material being irradiated. This places a significant emphasis on an accurate determination of the size and shape of the material within the sample that is being actively assayed by the HKED x-ray tube. Additional information from the system geometry and the expected attenuators along the XRF pathway are needed as well in order to understand not only how much of the sample is being irradiated, but also what percentage of the irradiated portion actively contributes to the output XRF spectra.

Currently techniques such as L-edge technology are being pursed to get to a smaller sample size for reprocessing safeguards measurements. There is an interest in reducing the volume of the sample needed for the assay in order to reduce the radiation dose to operators. In pursuing optimization of the HKED for pyroprocessing, an analysis of the

size of the sample vial necessary to reproduce sufficient results with the HKED was undertaken with emphasis on determining if a smaller vial could be appropriately used for the ORNL REDC HKED.

It is known that determination of the special nuclear material concentration will be dependent on the actual physical area of the sample where the K-edge vacancy production of x-rays is occurring. Assuming that the cross sectional area of the entire sample being irradiated is contributing to the XRF output will result in an error. Thus in order to refine the analysis, the location of the uranium $K\alpha_1$ x-rays generated within the sample was determined relative to a cross sectional area being irradiated by the HKED x-ray tube. MCNP parameter dependent tallies were used to tag specific photons and accumulate data specific to those particles generated by K-edge vacancy production from uranium nuclei. Shown in Figure 7.3, a K-edge vacancy production plot was superimposed on top of a cross sectional view of a CAD-based HKED model, where the production normalized to the overall production is seen to be heavily shifted towards the entry point for the interrogating x-ray tube x-rays.

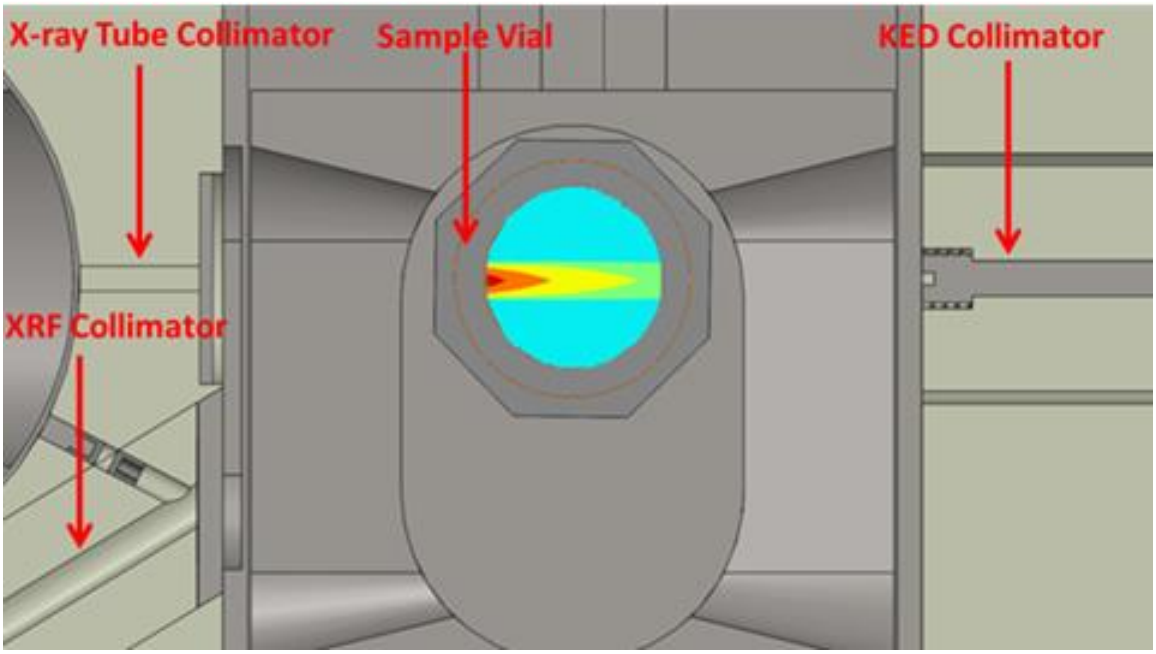

Figure 7.3. Overview of the K-edge vacancy production within a sample containing approximately 268 g/L of uranium, depicted as a top-view cross sectional cut across a CAD-based computer model of the HKED.

This analysis on the location within the sample where the K-edge x-rays are generated has been further refined to show the change in intensity throughout the sample vial. It was refined by discretizing the sample vial in a fine mesh in two dimensions across a specified height of the sample vial corresponding to the intersection of the centerline of the x-ray tube irradiation pathway. A fine mesh of ten thousand cells was overlaid through the center of the sample vial and highly detailed plots of the K-edge vacancy production were created. Such an analysis of narrow and wide collimation of the x-ray tube radiation provides insight into the relationship between intensity of the generated x-rays and the corresponding location within the sample vial.

7.1.2.1 Narrow Irradiation Pathway

Figures 7.4, 7.5, and 7.6 show the area of uranium K-edge x-ray generation from a 3M nitric acid sample with approximately 243 g/L uranium and 2.93 g/L plutonium on a

logarithmic scale with the intensities normalized to the maximum intensity. Note the difference in the scaling between the figures – as the minimum scaling parameter is changed from 1E-02 to 1E-08, the x-ray generation going on within the entire sample is not changed, but the less intense x-rays can be visualized. An important takeaway from this analysis though is that the x-rays generated outside of the central irradiation pathway contribute a negligible amount to the overall intensity of the x-rays.

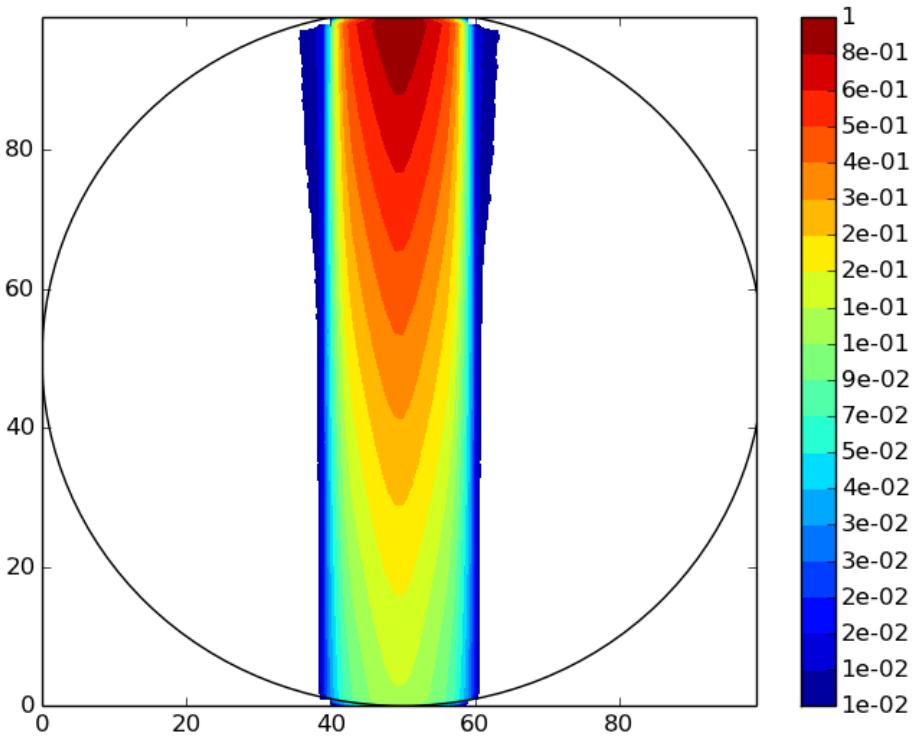

Figure 7.4. Overview of the uranium K-edge vacancy production within a sample containing approximately 243 g/L uranium and 2.93 g/L plutonium, depicted as a top-view cross sectional cut across the height of the vial corresponding to the intersection of the centerline of the x-ray tube irradiation beam.

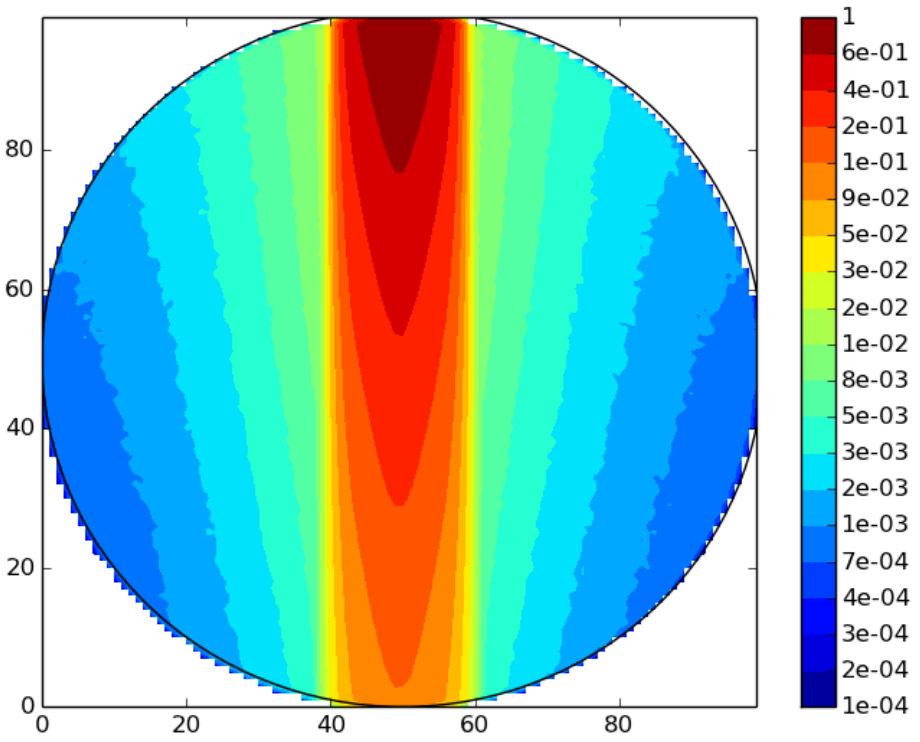

Figure 7.5. Overview of the uranium K-edge vacancy production within a sample containing approximately 243 g/L uranium and 2.93 g/L plutonium, depicted as a top-view cross sectional cut across the height of the vial corresponding to the intersection of the centerline of the x-ray tube irradiation beam, with increased scaling to 1E-04.

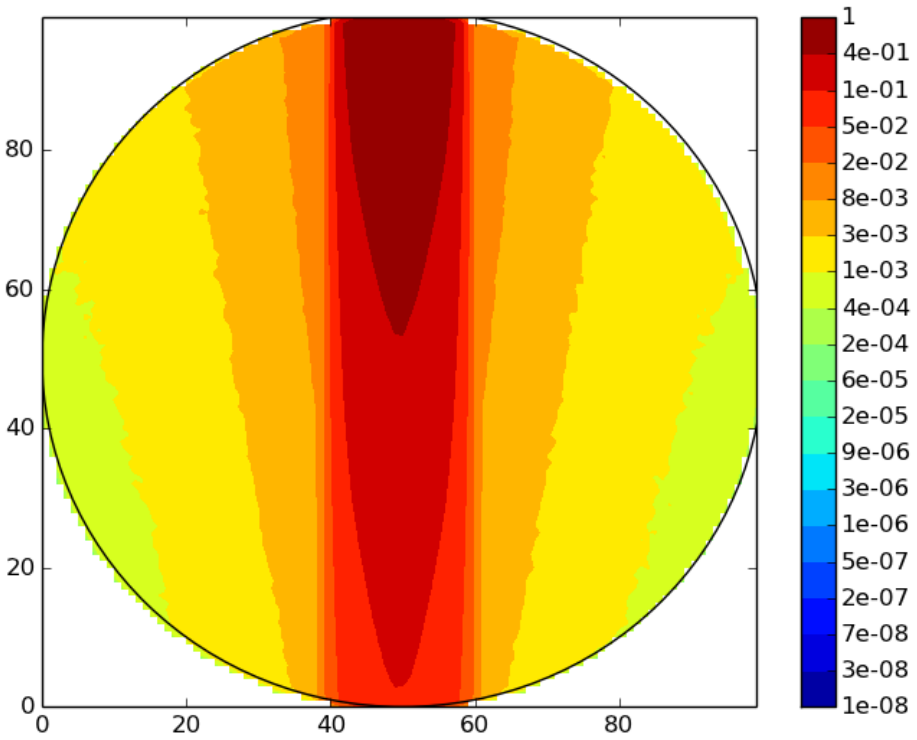

Figure 7.6. Overview of the uranium K-edge vacancy production within a sample containing approximately 243 g/L uranium and 2.93 g/L plutonium, depicted as a top-view cross sectional cut across the height of the vial corresponding to the intersection of the centerline of the x-ray tube irradiation beam, with increased scaling to 1E-08.

Additionally, the uranium $K\alpha_1$ x-rays must be transmitted through a narrow XRF collimator to the XRF detector to be measured. This limits the area of x-ray contribution to the XRF detector response, since the effects of attenuation, solid angle for collimation, and spectral interference will be included in the results for K-edge vacancy production. Using the process of acquiring the K-edge vacancy production depicted in Figures 7.4, 7.5, and 7.6, combined with the probabilities of interaction, attenuation, and transmission towards the XRF detector, the locations and the overall area within the sample from

contributing x-rays detected by the XRF detector can be determined and is shown in Figures 7.7, 7.8, and 7.9.

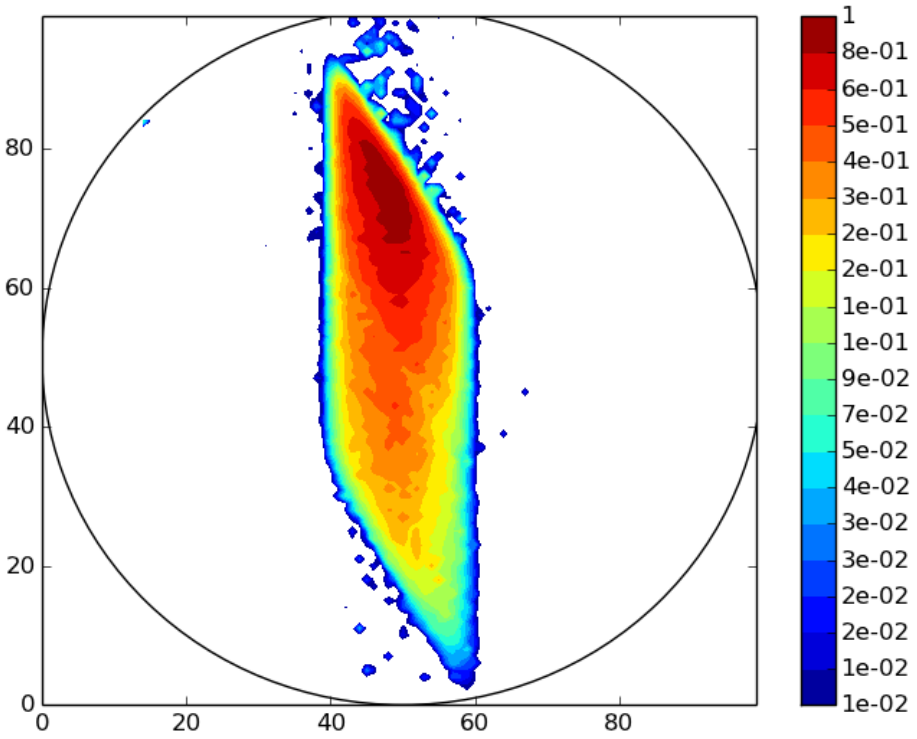

Figure 7.7. Overview of the uranium K-edge vacancy production intensity combined with the probability of impinging on the XRF detector within a sample containing approximately 243 g/L uranium and 2.93 g/L plutonium, depicted as a top-view cross sectional cut across the height of the vial corresponding to the intersection of the centerline of the x-ray tube irradiation beam.

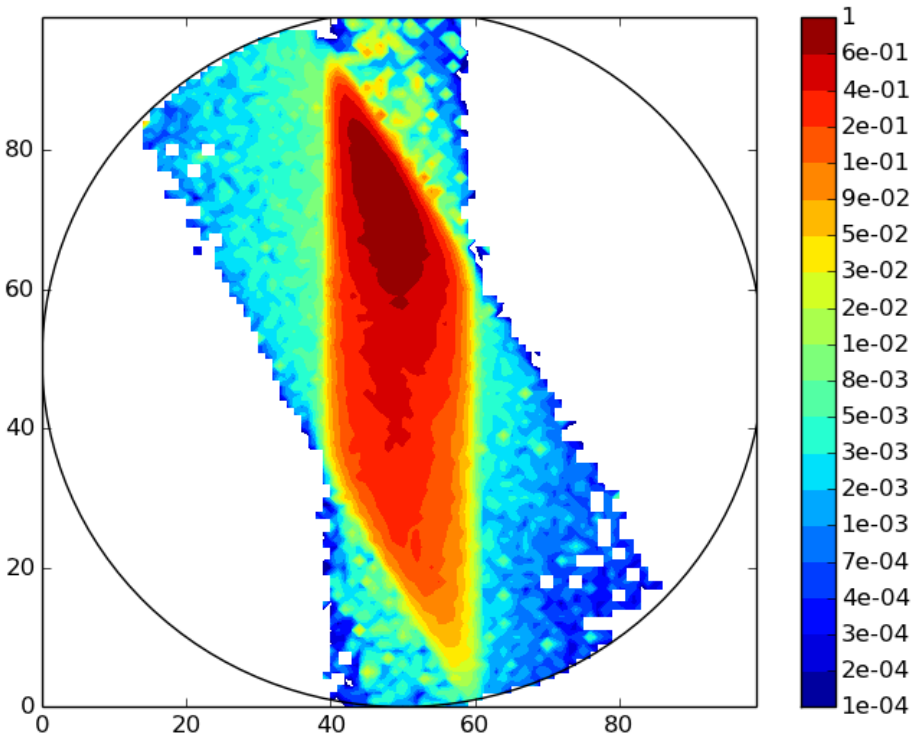

Figure 7.8. Overview of the uranium K-edge vacancy production intensity combined with the probability of impinging on the XRF detector within a sample containing approximately 243 g/L uranium and 2.93 g/L plutonium, depicted as a top-view cross sectional cut across the height of the vial corresponding to the intersection of the centerline of the x-ray tube irradiation beam, with increased scaling to 1E-04.

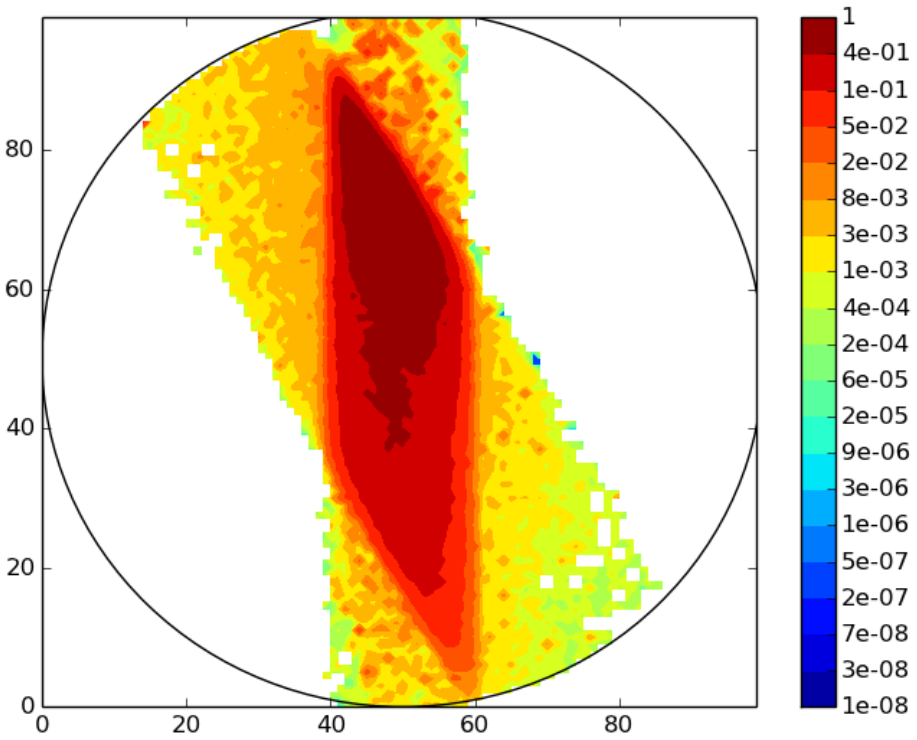

Figure 7.9. Overview of the uranium K-edge vacancy production intensity combined with the probability of impinging on the XRF detector within a sample containing approximately 243 g/L uranium and 2.93 g/L plutonium, depicted as a top-view cross sectional cut across the height of the vial corresponding to the intersection of the centerline of the x-ray tube irradiation beam, with increased scaling to 1E-08.

Figures 7.7, 7.8, and 7.9 were created to show the uranium K x-ray contribution normalized to the maximum intensity within a cross sectional area of the sample container located down the center line of the interrogating x-ray tube spectral pathway. These figures take into account the K-edge vacancy production due to the probabilities of generation of uranium $K\alpha_1$ x-rays, the solid angle transmission towards the detector, attenuation from sample materials and system structures, and the spectral interferences from matrix effects in the sample. The relative contribution to the XRF detector is shown

to be heavily weighted towards the top of each sample container, as this is the closest point to the entrance of the irradiating x-ray beam which is shown passing straight down through the sample. The solid angle for transmission through the XRF collimator to the detector, or the collimation effect, is shown as the roughly thirty degree rotation of the centerline column of the K-edge vacancy production that is nor shown for scaling of 1E-2 but resolves for scaling of 1E-4 and 1E-8.

As the uranium concentration within the sample vial is reduced, a larger percent of the x-ray contribution to the XRF spectrum comes from further down into the sample. This is because the irradiating x-ray tube beam and the generated x-rays are less attenuated by the sample materials and the reduced concentration of uranium dilutes the potential x-ray generation locations within the sample. This is shown in Figures 7.10, 7.11, and 7.12. As the collimation effect becomes more resolved towards higher uranium concentrations, the contribution of the x-rays coming from the scattering of photons outside the centerline irradiation column on the resultant spectra is shown to be a negligible amount of less than 0.1 %.

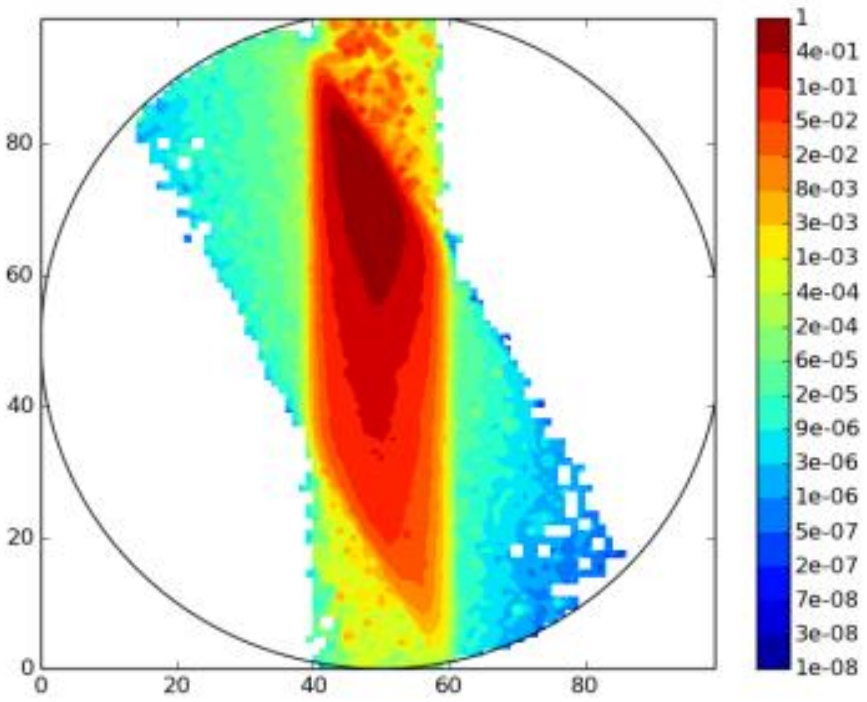

Figure 7.10. Uranium K x-ray contribution depicted on a logarithmic scale, relative to the total contribution for a sample with a uranium concentration of approximately 268 g/L in a nitric acid matrix.

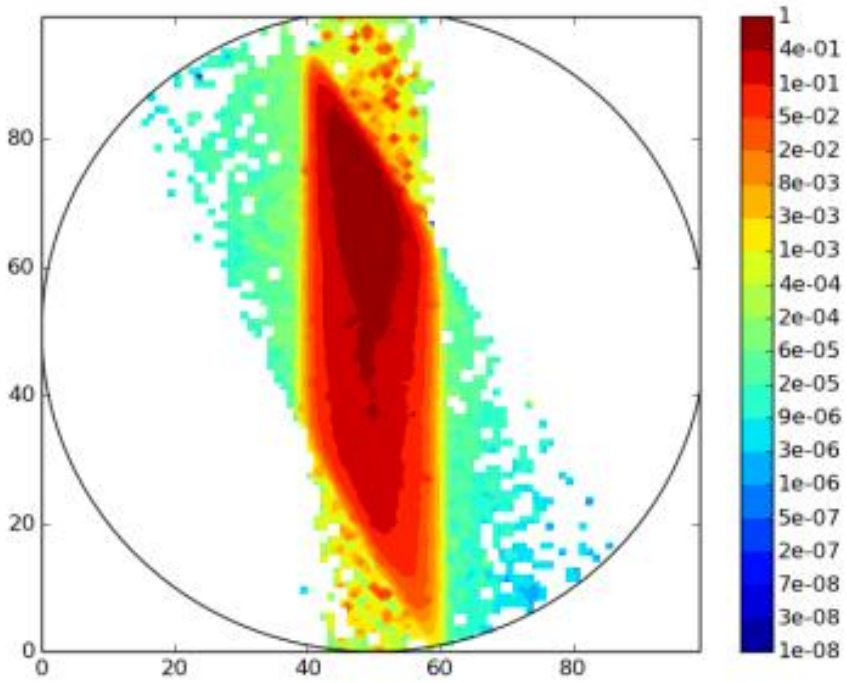

Figure 7.11. Uranium K x-ray contribution depicted on a logarithmic scale, relative to the total contribution for a sample with a uranium concentration of approximately 107 g/L in a nitric acid matrix.

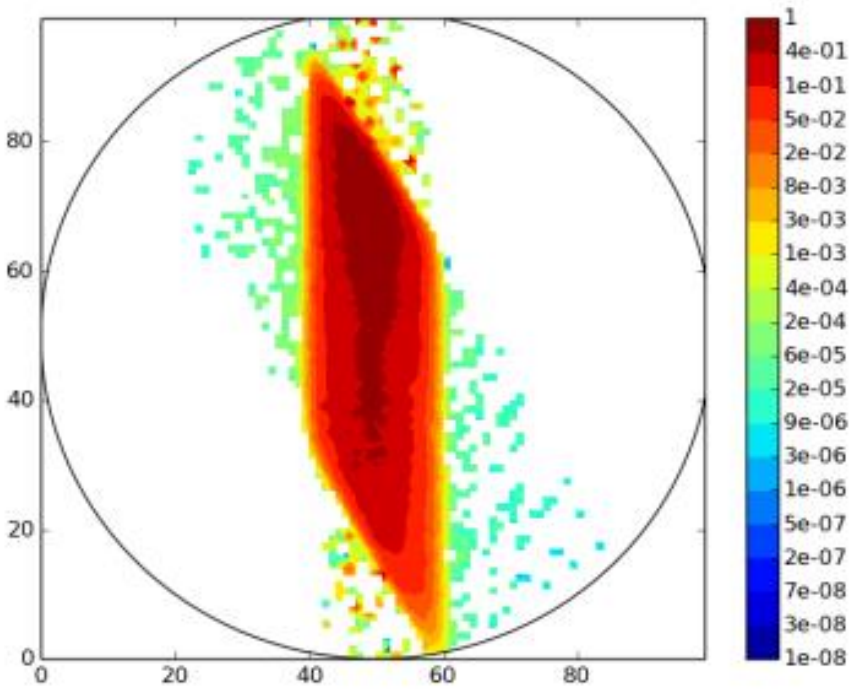

Figure 7.12. Uranium K x-ray contribution depicted on a logarithmic scale, relative to the total contribution for a sample with a uranium concentration of approximately 48 g/L in a nitric acid matrix.

7.1.2.2 Three Dimensional Analysis

The analysis of the K-edge vacancy production was separately visualized by a three dimensional model of the discretized sample vial to identify the volume within the vial where the generated x-rays that impinge on the XRF detector were being created. Figure 7.13 shows the 3D model of the sample vial viewed directly down the XRF collimation axis towards the sample and Figure 7.14 shows the model viewed off axis, with the grey circle in the lower right corner representing the entrance to the XRF collimation pathway for perspective.

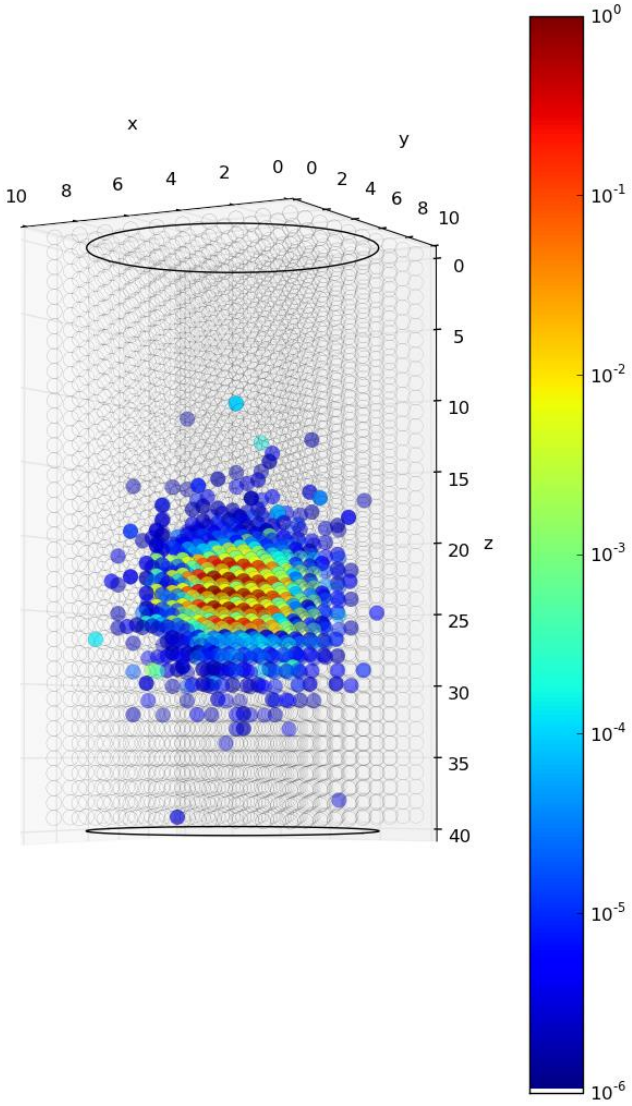

Figure 7.13. Three dimensional inline view from the entrance of the XRF collimation pathway towards the sample vial of the K-edge vacancy production from a sample containing approximately 268 g/L of uranium in a 3M nitric acid mixture.

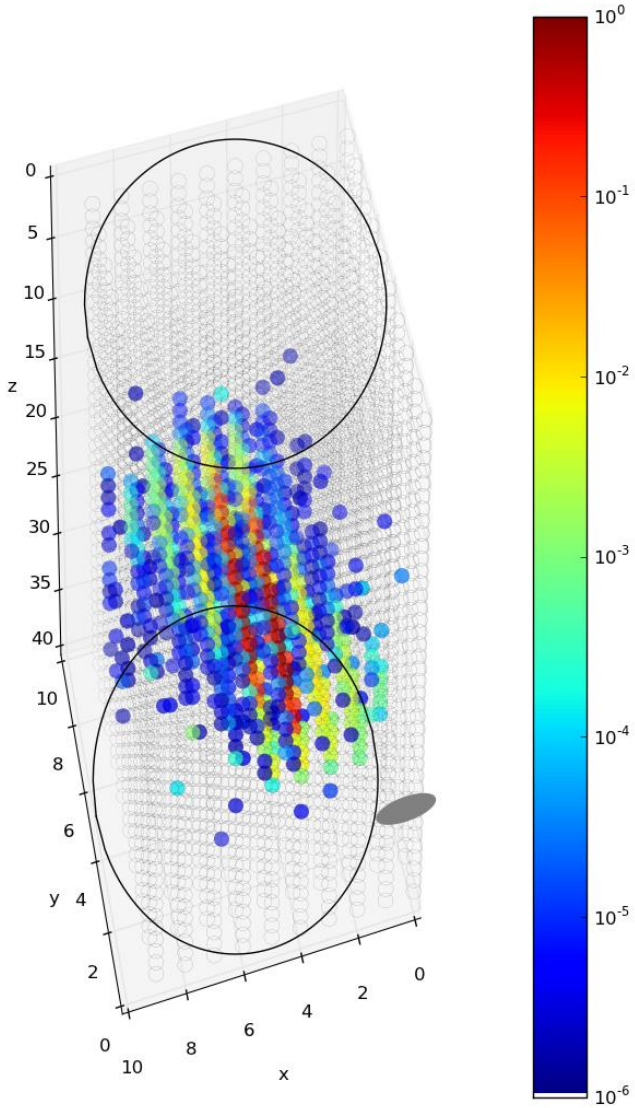

Figure 7.14. Three dimensional off axis view of the K-edge vacancy production from a sample vial containing approximately 268 g/L of uranium in a 3M nitric acid mixture, where the grey circle in the lower right corner represents the entrance to the XRF collimation pathway.

Though the three dimensional views of the K-edge vacancy production proved difficult to visualize the interactions locations, it did provide meaningful information about the intensity change as a function of volume. This new approach to visualizing the data allowed for the total size of the region contributing K-edge x-rays to the XRF detector to be determined.

In the case of optimizing the HKED for pyroprocessing samples, this evidence of K-edge production and transmission within the sample suggests that the sample size needed to determine the special nuclear material concentration can be greatly reduced. Reduction to a much smaller sample vial may in fact mitigate some of the sampling challenges for pyroprocessing as well as reduce the overall dose rate from samples to the near-by operators of the HKED system. Integration of this approach to design future sample sizes and even sample geometries can allow for system optimization and can consequently lead to a more efficient and cost-effective safeguards approach in future pyroprocessing facilities.

7.1.2.3 Wide Irradiation Pathway

A separate analysis was undertaken to investigate if sample sizes for wide aperture irradiation from the x-ray tube can also be minimized. The wide aperture is currently employed for some operating HKED systems to greatly expand the volume of the sample vial being irradiated and can be used to for systems employing separate sample vials for the XRF and KED modalities. In this case, the single vial system of the ORNL REDC HKED was simulated to be irradiated by the same x-ray beam spread in the vertical direction, but the 2 mm rectangular collimation in the horizontal direction was increased to a 24 mm width. The 3 mm tungsten anode of the x-ray tube was simulated to emit x-rays in a cone directed towards the sample vial with a 20° spread. The resulting K-edge vacancy production from a 3M nitric acid sample matrix with approximately 243 g/L

uranium and 2.93 g/L plutonium is shown with the uranium K-edge x-ray intensity plotted on a logarithmic scale in Figures 7.15, 7.16 and 7.17.

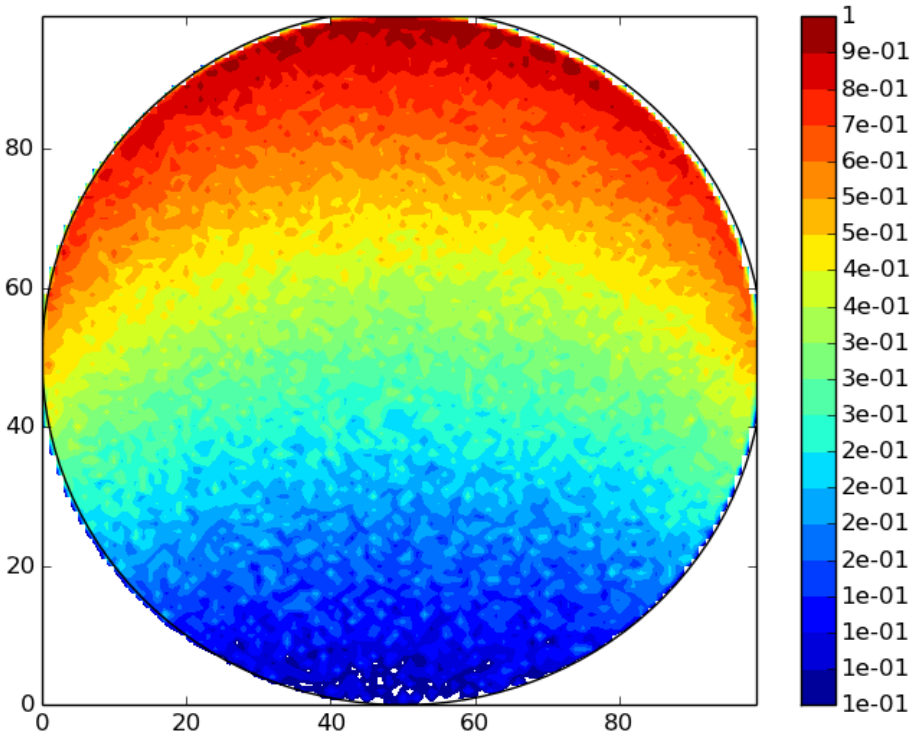

Figure 7.15. Overview of the wide aperture irradiation for uranium K-edge vacancy production within a sample containing approximately 243 g/L uranium and 2.93 g/L plutonium, depicted as a top-view cross sectional cut across the height of the vial corresponding to the intersection of the centerline of the x-ray tube irradiation beam.

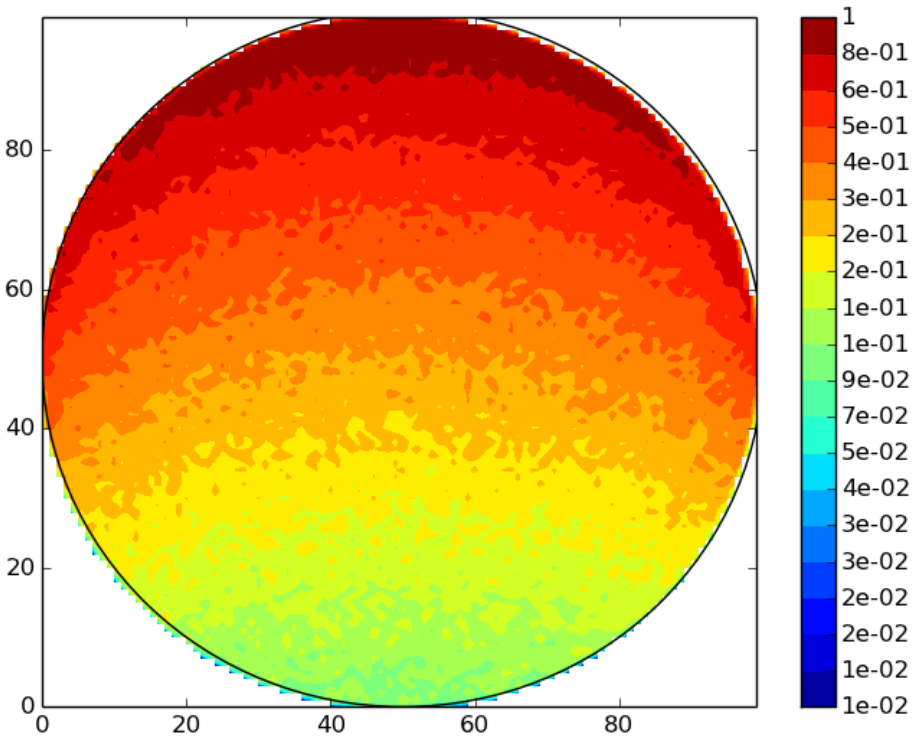

Figure 7.16. Overview of the wide aperture irradiation for uranium K-edge vacancy production within a sample containing approximately 243 g/L uranium and 2.93 g/L plutonium, depicted as a top-view cross sectional cut across the height of the vial corresponding to the intersection of the centerline of the x-ray tube irradiation beam, with increased scaling to 1E-02.

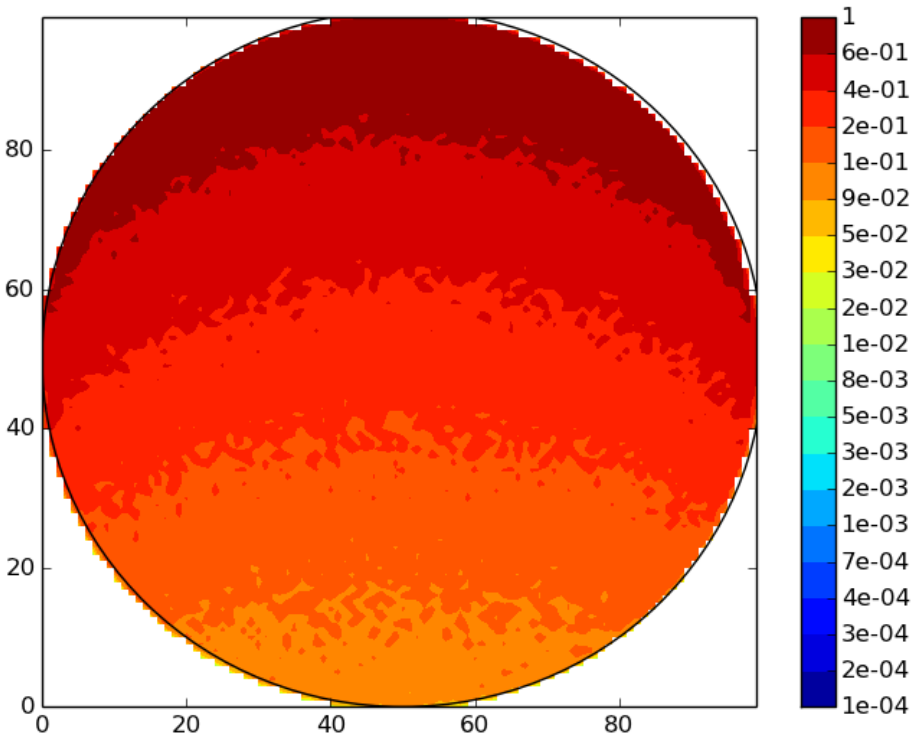

Figure 7.17. Overview of the wide aperture irradiation for uranium K-edge vacancy production within a sample containing approximately 243 g/L uranium and 2.93 g/L plutonium, depicted as a top-view cross sectional cut across the height of the vial corresponding to the intersection of the centerline of the x-ray tube irradiation beam, with increased scaling to 1E-04.

As the uranium $K\alpha_1$ x-rays must still be transmitted through a narrow XRF collimator to the XRF detector to be measured, the combined probabilities of generation and transmission towards the XRF detector were simulated and the results are shown in Figures 7.18, 7.19, and 7.20. The results highlight the area of highest importance for x-ray contribution to the XRF detector to be at the edge closest to the XRF collimation entrance within the sample vial and following the direction of the XRF collimation pathway into the sample. It is also noted that the importance of x-rays generated within

the collimation pathway decreases rapidly the further away from the entrance to the XRF collimation pathway that the x-rays are generated. This rapid decrease in intensity is due to the attenuation of the x-rays further within the sample vial by the sample material.

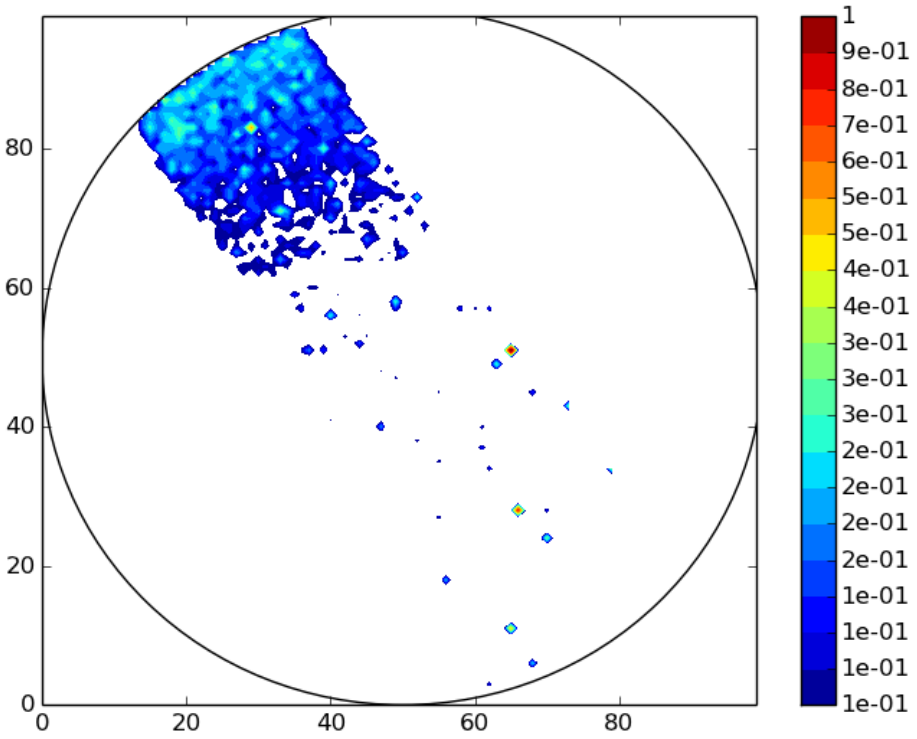

Figure 7.18. Overview of the uranium K-edge vacancy production intensity combined with the probability of impinging on the XRF detector within a sample containing approximately 243 g/L uranium and 2.93 g/L plutonium, depicted as a top-view cross sectional cut across the height of the vial corresponding to the intersection of the centerline of the x-ray tube irradiation beam.

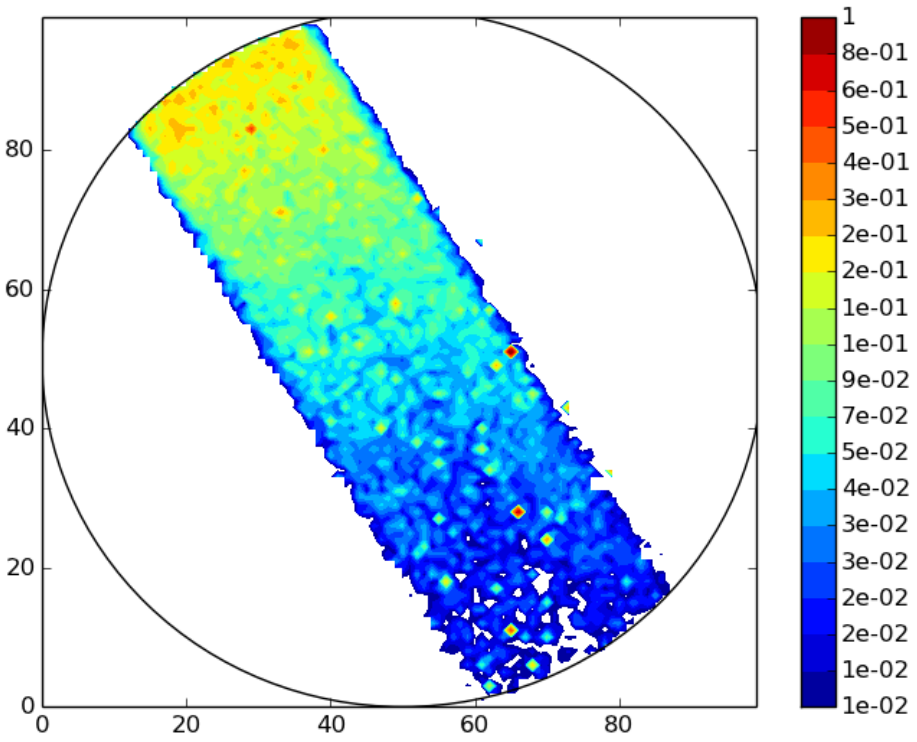

Figure 7.19. Overview of the uranium K-edge vacancy production intensity combined with the probability of impinging on the XRF detector within a sample containing approximately 243 g/L uranium and 2.93 g/L plutonium, depicted as a top-view cross sectional cut across the height of the vial corresponding to the intersection of the centerline of the x-ray tube irradiation beam, with increased scaling to 1E-04.

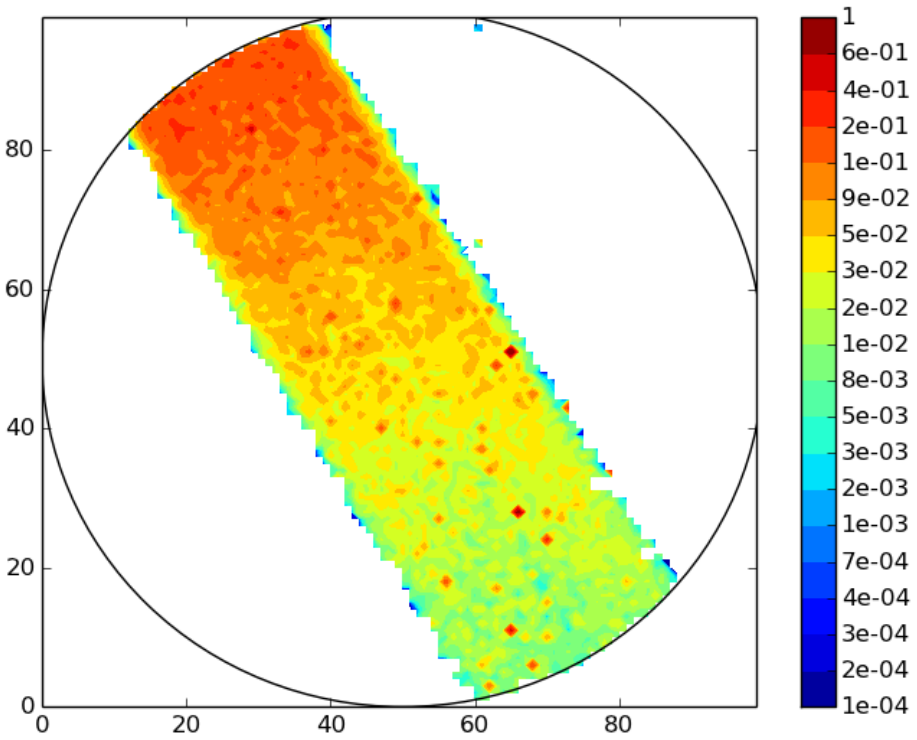

Figure 7.20. Overview of the uranium K-edge vacancy production intensity combined with the probability of impinging on the XRF detector within a sample containing approximately 243 g/L uranium and 2.93 g/L plutonium, depicted as a top-view cross sectional cut across the height of the vial corresponding to the intersection of the centerline of the x-ray tube irradiation beam, with increased scaling to 1E-08.

Another note is made that the areas of the sample outside of the XRF collimation pathway solid angle contribute almost nothing to the XRF detector response, suggesting that the x-ray scattering within the sample vial has a negligible impact on the spectral response compared to the x-rays generated within the solid angle of the XRF collimation pathway. Each of these observations from the wide aperture irradiation of the HKED sample vial suggest that the amount of material required for the XRF response is much

smaller than is currently used. The 5 mL sample vial volume may be greatly reduced without dramatically influencing the XRF spectral response.

7.2 Salt Samples

To this point, the HKED simulated detector responses for nitric acid based samples have been modeled and analyzed in order to view the applicability of the simulated spectra for validating experimental results. However, the applicability of the work presented herein is predicated on the simulation's ability to faithfully reproduce the spectral results of samples expected from pyroprocessing. To this end, the MCNP model was applied first to a salt based standard containing no actinides to analyze the difference between simulation and experimentally measured results for altered sample matrices. Then the composition from the processed fuel and salt from the Idaho National Laboratory Mark V electrorefiner was input into the MCNP simulation as the closest possible representative sample to the output expected from pyroprocessing used nuclear fuel [74]. Finally, analysis of the Mark V salt samples were altered to examine the impact of changes to the sample from the cooling or cooled form of the salt, specifically by modeling cracks and voids formed inside the salt sample.

7.2.1 ORNL Salt Standard

A salt standard created at ORNL was assayed with the ORNL REDC HKED. The salt sample was created from a dry slurry of potassium chloride. Spectral results for XRF measurement are shown compared with the simulated salt standard in Figure 7.21 with slight offsets around channel 500 and 1125. The overall differences between the simulated and measured spectrum are the same as expected from the analysis in Section 6.4 of the nitric acid and water based samples.

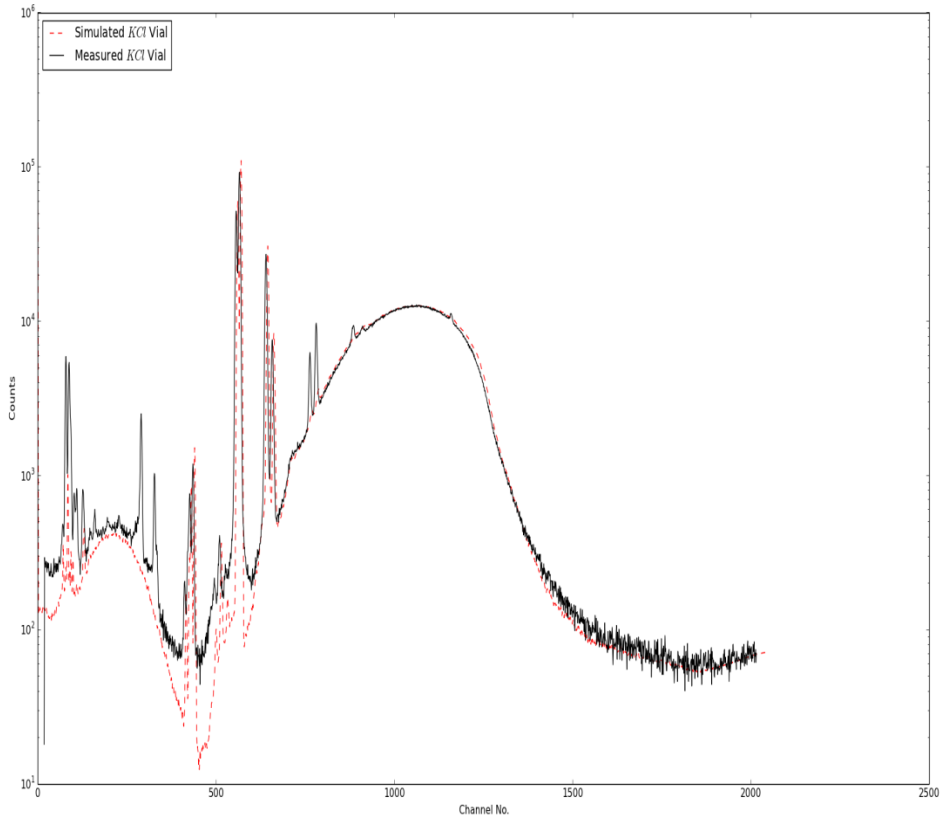

Figure 7.21. Comparison of experimental XRF assay results with simulated results for a potassium chloride sample matrix.

Figure 7.21 shows a small difference between the experimental results and those simulated, which is seen as a slight offset immediately after the cadmium-109 peak located roughly at channel 1125. A close inspection of the gadolinium x-ray peaks around channel 600 shows they are shifted slightly to higher channel numbers than the measured spectral peaks as well. This slight offset is most likely due to the difference in the energy per channel variation between the simulated and measured results. This difference is due to the fact that the measured results were obtained as an uncalibrated spectrum. However,

even considering the offset from the lack of similar energy binning, the two spectra match up well when compared against one another.

7.2.2 Mark V Salt

The processed salt mix, analyzed as the expected form of pyroprocessing samples, was generated during operation of the Experimental Breeder Reactor – II at Idaho National Laboratory [74]. The Mark V salt is composed of a LiCl-KCl eutectic interspersed predominantly with uranium trichloride and plutonium trichloride in a roughly 1:2 ratio, respectively, and to a lesser extent various rare earth fission product and minor actinide chlorides. The concentrations of uranium and plutonium for the Mark V salt at room temperature density of 1.995 g/mL are 43.59 g U/mL and 79.35 g Pu/mL. The elemental composition and mass fractions of the Mark V salt mix are shown in the input file shown in Appendix B. No gamma-rays from the decay of actinides or fission products were included in the source term, so the results were confined to the interrogating x-ray tube spectra, the cadmium-109 calibration source, the gadolinium beam filter, and the resulting fluorescent x-rays generated from the actinides and fission products in the salt.

7.2.2.1 Spectral Interferences

By simulating spectra of the HKED assay results with differing amounts of uranium-plutonium and uranium-bismuth salt mixtures from pyroprocessing samples, it was possible for not only the scattering and transmission of primary radiation to be observed but also the higher order effects from the enhancement or absorption of fluorescent lines by secondary radiation. The spectral effects of absorption and enhancement are muted when the Mark V salt sample that has a LiCl-KCl based sample matrix is compared to a pure metal sample.

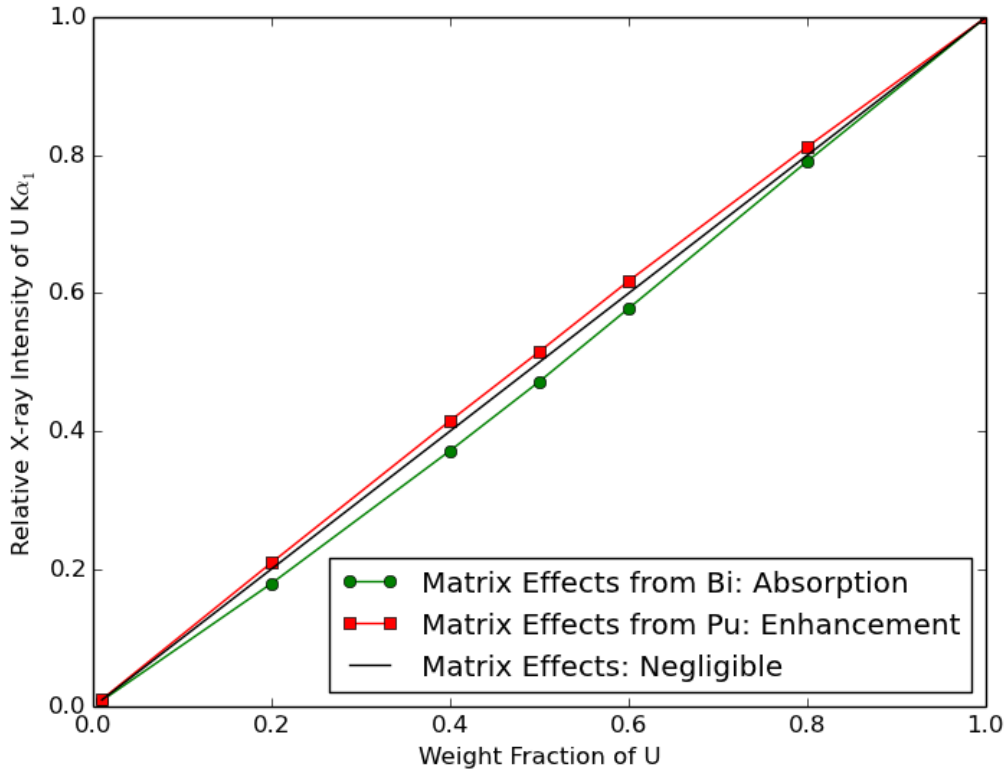

Figure 7.22. Matrix effects of absorption and enhancement on the relative intensity of the uranium Kα_1 x-rays as the weight fraction of the uranium is changed for a uranium-plutonium based sample in the Mark V salt mixture. The concentrations of uranium and plutonium for the Mark V salt at room temperature density of 1.995 g/mL are 43.59 g U/mL and 79.35 g Pu/mL.

A significant advantage of monitoring the matrix effects through Monte Carlo code simulation is that it allows for the correction of these absorption and enhancement effects on the representative peak height intensities for the actinides. As shown in Figure 7.22, this correction will only become more important when assaying salt samples where the weight fractions between actinides are close to equal as this location results in the highest deviation from the peak height intensity with negligible matrix effects. While the pure

metal analysis noted a 10% enhancement at equal uranium and plutonium weight fractions, the Mark V sample is shown to have a maximum enhancement of the relative uranium K shell peak intensity of 3% as the uranium and plutonium weight fractions become equal.

7.2.2.2 XRF Detector Responses

Both room temperature and molten temperatures were analyzed for the Mark V salt mix. Since the differences between the XRF spectra are very slight, the cooled form and molten form of the salt mix were simulated and shown separately in Figures 7.23 and 7.24. Under close examination, the overall counts for the cooled and denser sample are slightly higher at higher energies and slightly lower at lower energies with the intersection point roughly at 70 keV.

Figure 7.25 shows a zoomed in graph including both room temperature and molten salt x-ray peaks. As the salt cools, simulated XRF assay results show an overall increase in the uranium $K\alpha_2$ x-ray peak area and the plutonium $K\alpha_1$ peak area of approximately 0.25 %, and 0.88 % respectively. The uranium $K\alpha_2$ peak was analyzed instead of the $K\alpha_1$ to avoid determination of the peak area of the doublet peaks formed by the overlapping uranium $K\alpha_1$ and plutonium $K\alpha_2$. This observation of the difference between analyzing the cooled or molten form of the salt is another of the innovative ways that Monte Carlo simulation can help plan out safeguards measurements of the electrorefiner for pyroprocessing.

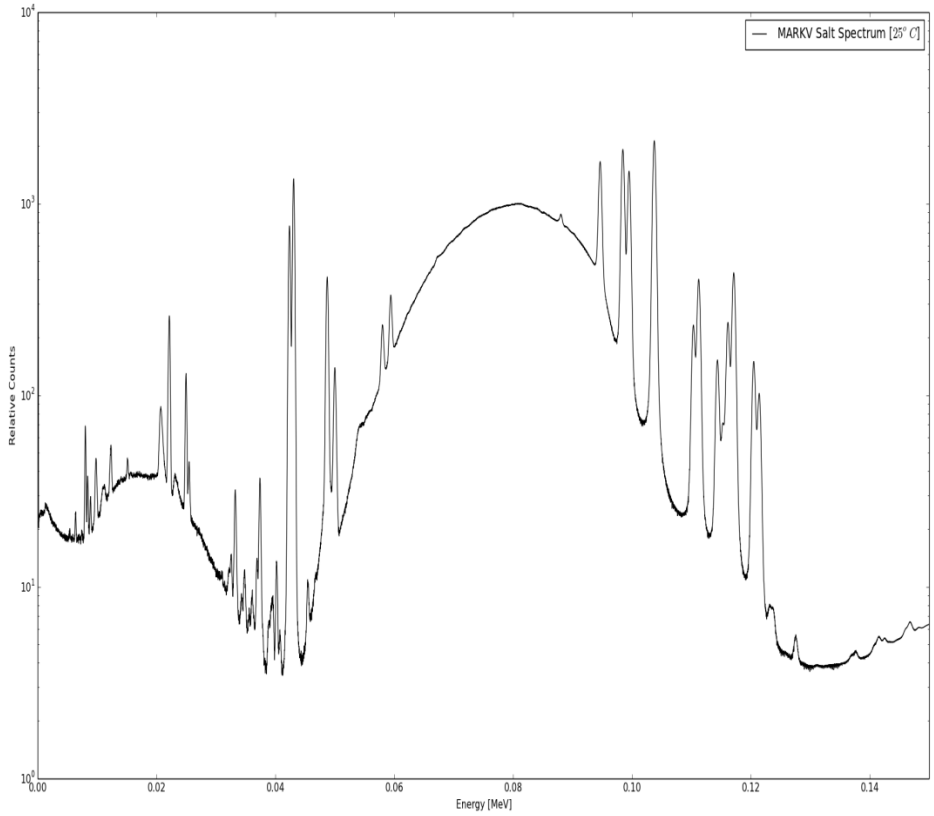

Figure 7.23. Simulated XRF spectra of the Mark V actinide salt mix from a sample with an approximately 1:2 U:Pu ratio at room temperature.

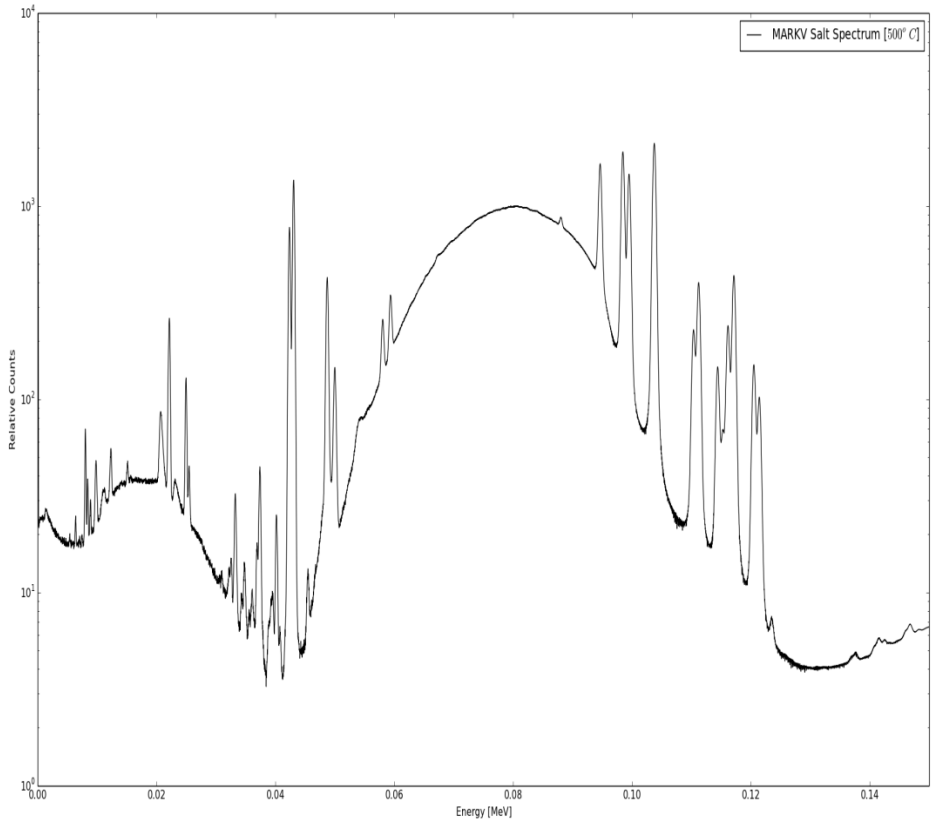

Figure 7.24. Simulated XRF spectra of the Mark V actinide salt mix from a sample with an approximately 1:2 U:Pu ratio at molten temperature.

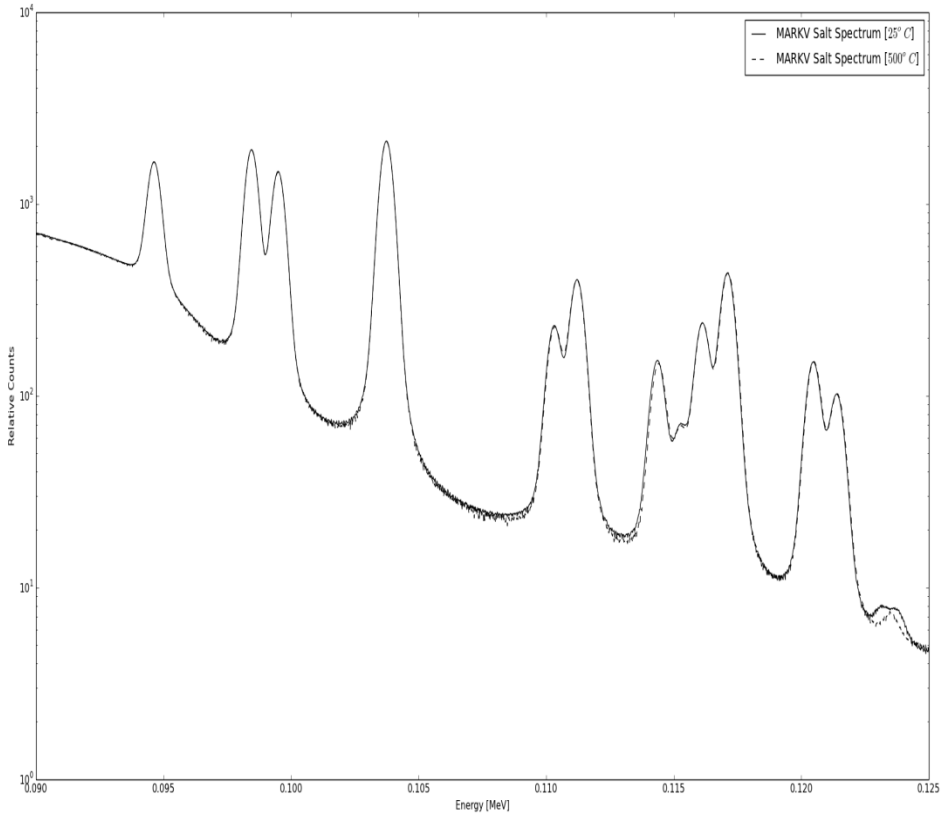

Figure 7.25. Simulated XRF spectra of the Mark V actinide salt mix from a sample with an approximately 1:2 U:Pu ratio at room temperature and molten temperature shown for the energy region of the actinide Kα and Kβ x-ray peaks.

Due to the higher counts from the cooled salt, some of the high energy, low intensity peaks above 120 keV were resolved by the post processing routine for the room temperature salt but were not resolved for the analysis of the molten salt. Due to the nature of the peak search algorithm dependency on using the Gaussian broadened simulated spectra to determine the peak locations, some of the lower intensity peaks and the overlapping peaks in the simulated spectra are not located and broadened in the final simulated results.

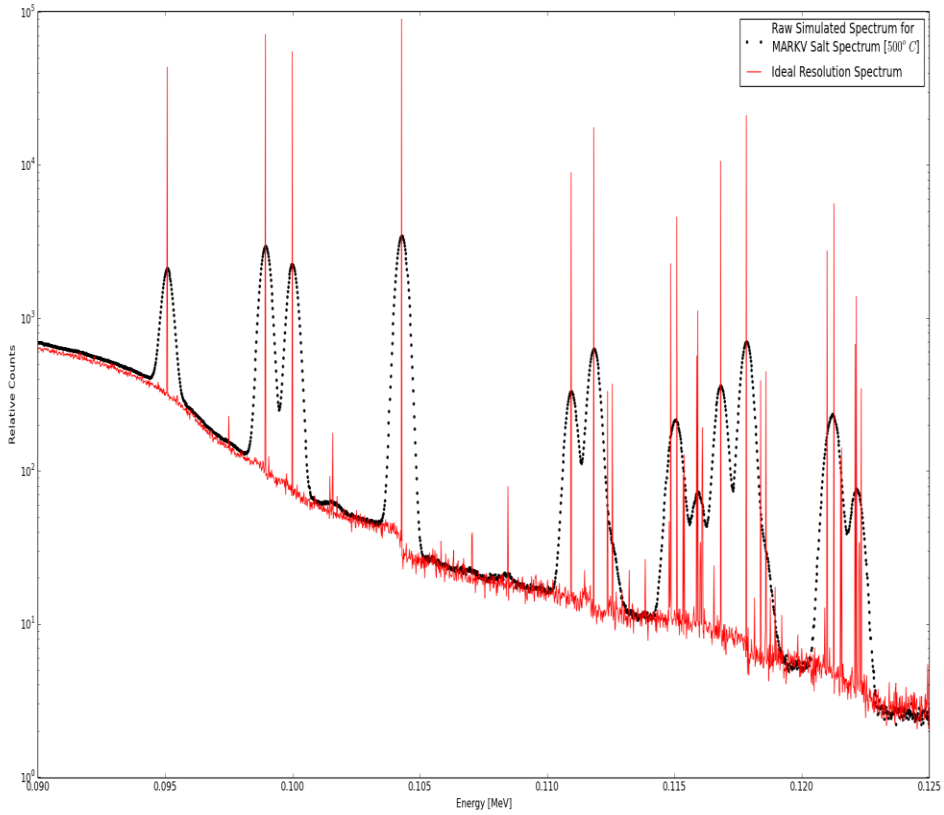

Figure 7.26. Simulated XRF spectra of the Mark V actinide salt mix from a sample with an approximately 1:2 U:Pu ratio at molten temperature shown for the energy region of the actinide Kα and Kβ x-ray peaks and overlaid with the optimal detector resolution simulated XRF spectra for simplified peak identification.

Specifically, the post processed results for the Mark V salt do not include the small x-ray peaks due to the presence of americium or the $K\beta_5$ peaks from uranium or plutonium. This approach may be updated for future versions of the simulation in order to refine the post-processing analysis to include the smaller and overlapping peaks by refining the simulated data which the algorithm uses to determine the energy locations of the x-ray peaks. With this correction, the ideal detector resolution results from simulation may be

processed, as shown in Figure 7.26, to obtain a precise understanding of the peak location and information. With this fine amount of detail of the peak locations, every peak contributing to the simulated XRF results can be broadened and included in the final results.

7.2.2.3 KED Detector Responses

Three density points were investigated for the actinide salt mixture. The points corresponded to the densities of the actinide salt mixture at room temperature, the actinide salt mixture at molten temperature, and only the salt mixture at molten temperature, respectively. The density for the processing salt at room temperature was calculated to be 1.997 g/mL, given the combination of the individual salt compound densities, while the density for the molten processing salt was determined based on the calculation derived by Mariani [50] using values for KCl and LiCl at 500° C and combining them to obtain the value of 1.620 g/mL. This density value was determined solely for the eutectic salt, essentially forming a lower bound for the possible density of the molten salt mixture, so an additional density was analyzed. A density in between two endpoints was calculated to be 1.836 g/mL, considering the densities of the salt as well as the associated actinides.

Figures 7.27, 7.28, and 7.29 show the results of the simulated KED responses to the Mark V salt mixture at these distinct densities, respectively. Table 7.4 shows the difference between the uranium and plutonium K-edges as the density of the sample is decreased. The error was determined based on the counting error and included the propagation of error for subtracting two terms to determine the difference.

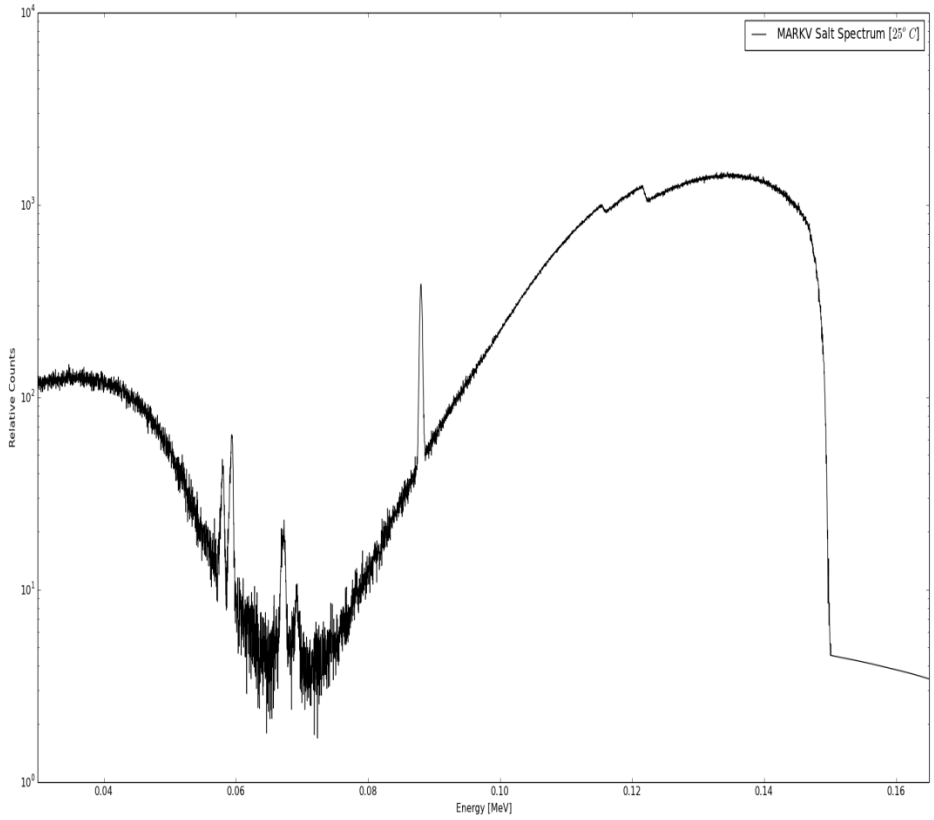

Figure 7.27. Simulated KED spectra of the Mark V actinide salt mix from a sample with an approximately 1:2 U:Pu ratio at a density of 1.997 g/mL corresponding to room temperature. The concentrations of uranium and plutonium for the Mark V salt at room temperature density of 1.995 g/mL are 43.59 g U/mL and 79.35 g Pu/mL.

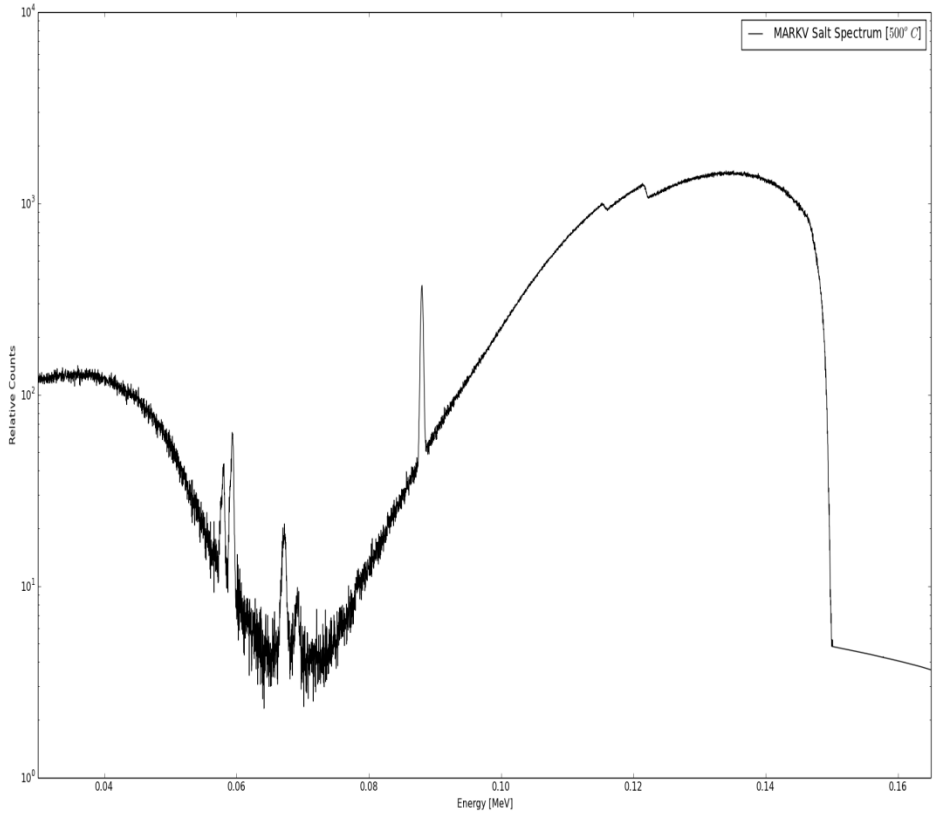

Figure 7.28. Simulated KED spectra of the Mark V actinide salt mix from a sample with an approximately 1:2 U:Pu ratio at a density of 1.836 g/mL corresponding to the molten temperature of both the salt and the actinides.

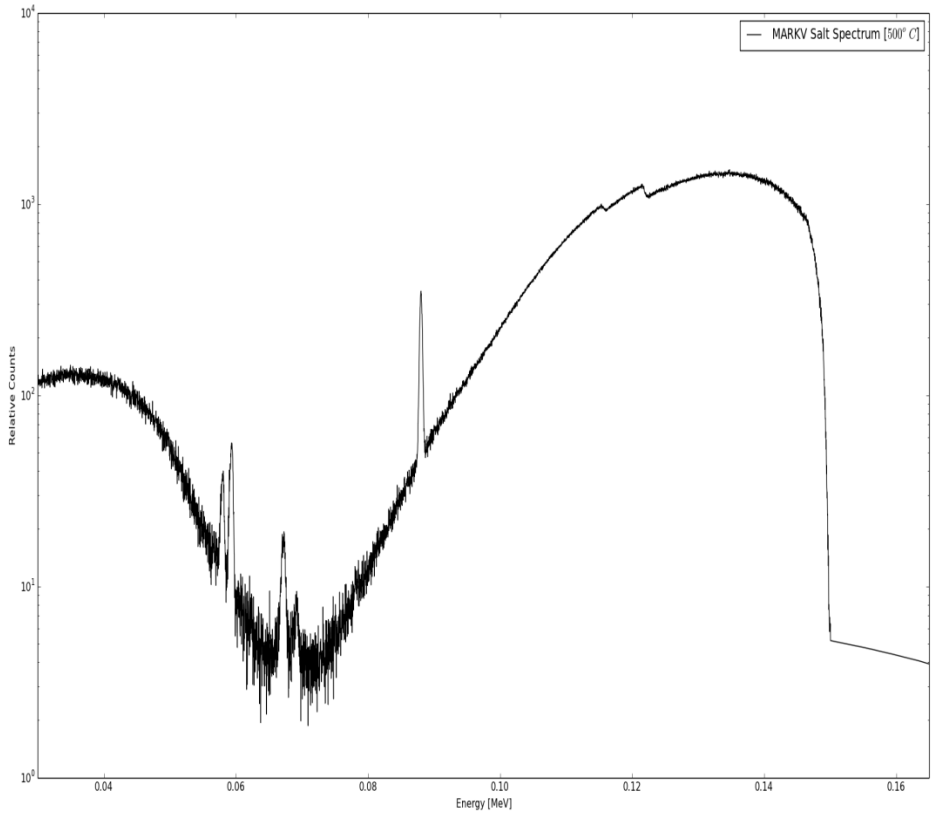

Figure 7.29. Simulated KED spectra of the Mark V actinide salt mix from a sample with an approximately 1:2 U:Pu ratio at a density of 1.620 g/mL corresponding to the molten temperature of only the salt.

Table 7.4. Simulated uranium and plutonium K-edge magnitudes compared to the 25 °C sample constitution while changing sample constitution of the MARK V salt. The difference for the 25 °C sample is left blank.

Sample Constitution	K-edge	Simulated	Difference from 25° C [%]
25° C, ρ = 1.997	U	94.024	- ± *4.784*
	Pu	225.209	- ± *2.378*
500° C, ρ = 1.836	U	86.433	*8.073* ± *4.590*
	Pu	206.896	*8.132* ± *2.276*
500° C, ρ = 1.620	U	84.45	*10.183* ± *5.162*
	Pu	198.227	*11.981* ± *2.606*

Figure 7.30 shows the comparison of the two simulated density spectra of 1.620 g/mL and 1.997 g/mL, showing the decreased counts representing an increase in the magnitude of the uranium and plutonium K-edges after cooling the salt sample. An decrease in overall counts is seen to occur for the normalized KED branch spectra between the molten and cooled samples. The relative counts change results in uranium and plutonium K-edge magnitudes increasing by 37.5 % and 34.3 %, respectively. This increase constitutes an exceptional variation between the forms of the salt being assayed. It will be important to ensure either the sample densification for cooled salt or the corresponding system materials expansion when assaying the molten form of the salt is included in the calibration methods.

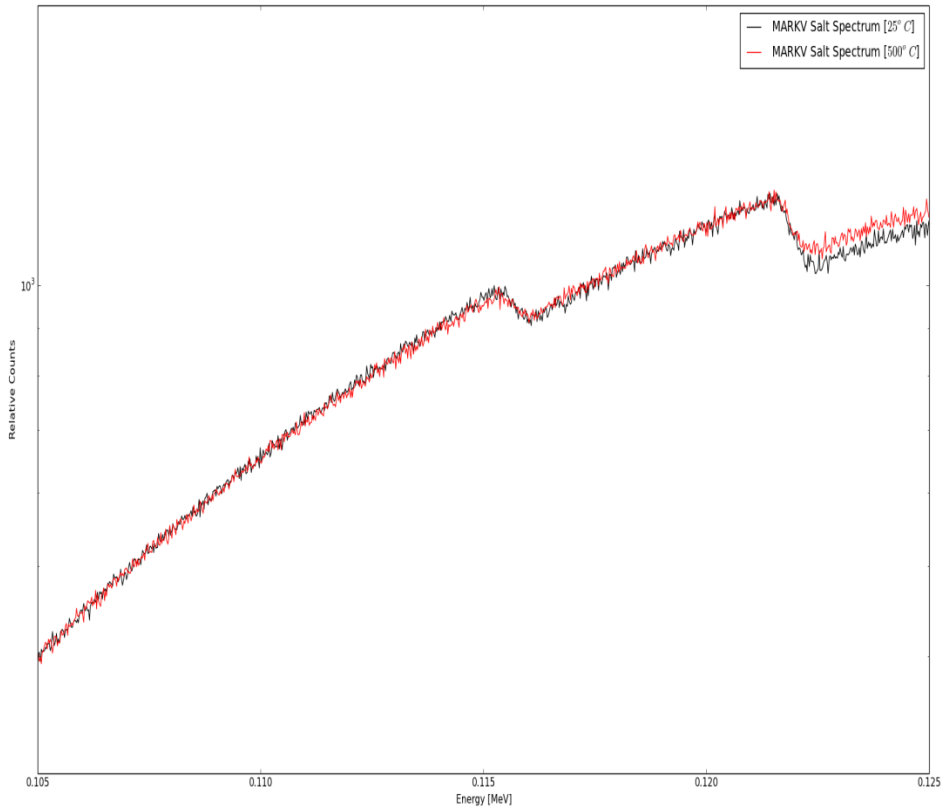

Figure 7.30. Simulated KED spectra of the Mark V actinide salt mix from a sample with an approximately 1:2 U:Pu ratio showing the decrease in counts representing an increase in the uranium and plutonium K-edge magnitudes when cooling the sample from molten temperature to room temperature.

7.2.3 Mark V Salt with Non-Homogeneities

Characterization of the non-homogeneities created within the cooled form of the sampled electrorefiner salt will be crucial to determining the range of applicability of the HKED system on pyroprocessing safeguards. Non-homogeneities such as temperature gradients or stratification of the sample, where heavy elements drift towards the bottom and form distinct layers of elemental composition throughout the sample, will pose a direct

challenge to the HKED quantification approach. Cracks and voids within the cooled sample will have significant impacts on the HKED analysis by altering the optical path length seen by the x-ray tube source x-rays. Analysis of the cooled form of the electrorefiner salt will need to determine if these non-homogeneities will occur, and if so, accommodate for the expected effects on the assay spectra.

It is expected that the existence of these types of non-homogeneities will have a noticeable effect on the XRF and KED results, so the Mark V sample was simulated under several expected circumstances. As the salt samples cools from its molten temperature, cracks and voids may be created within the sample vial. So three separate thin, cylindrical cracks within the sample material were modeled to determine their impact on the spectral results: a crack through the entire sample diameter in line with the KED branch collimation centerline, a crack through the entire sample diameter in line with the XRF branch collimation centerline, and a crack in the same plane as the first two but off axis from both collimation centerlines. Each crack was simulated with a diameter of approximately half the diameter of the KED collimation pathway diameter, approximately 0.4 mm. An example of the off axis crack is shown in Figure 7.31.

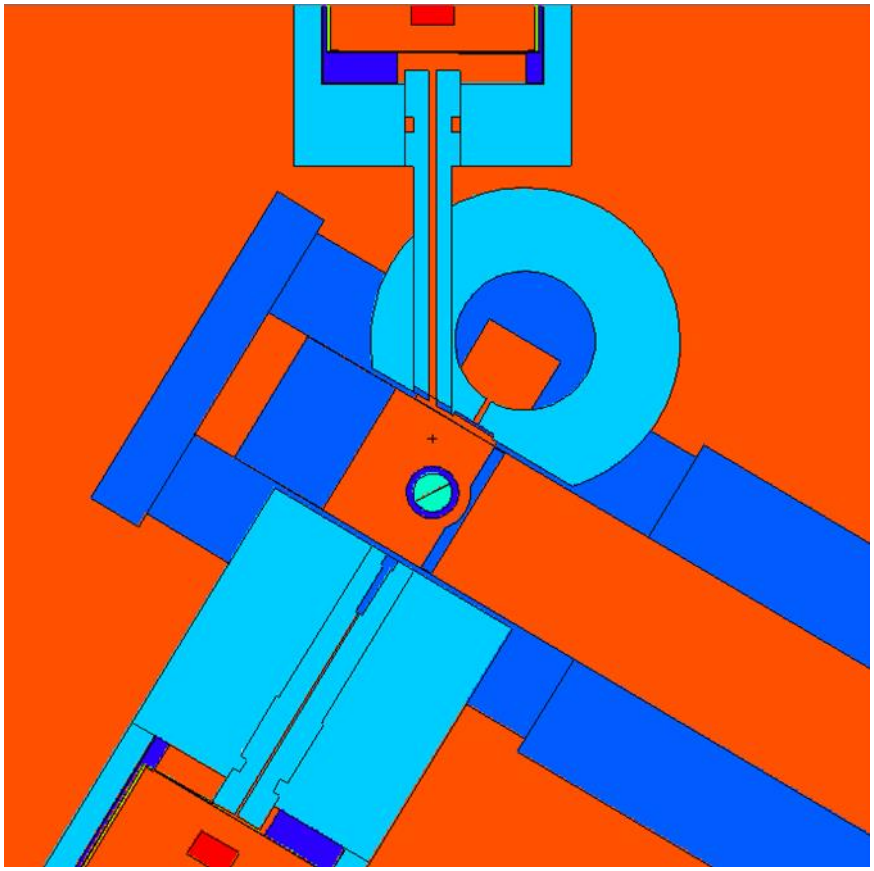

Figure 7.31. Top view cross section of the simulated HKED system with Visual Editor showing the sample material with an off-axis crack through the entire sample diameter. The cylindrical crack has a diameter of 0.4 mm.

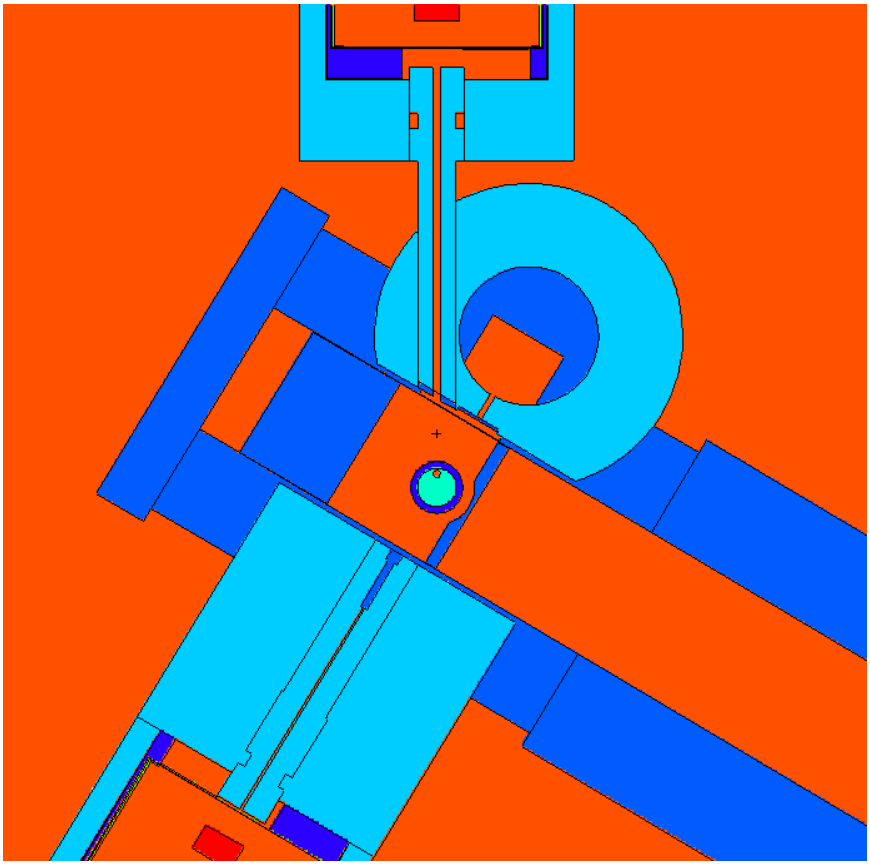

Figure 7.32. Top view cross section of the simulated HKED system with Visual Editor showing the sample material with a void formed in the region closest to the entrance to the XRF collimation pathway. The spherical void has a diameter of 0.00263 m.

Additionally, bubbles or voids may form in the cooling salt. Bubble distribution and size in LiCl-KCl eutectic salt at molten temperature of 500°C has been investigated and recorded bubble properties have been published for bubbles ranging from 0.00263 m to 0.00407 m [105]. Due to the fact that the inner diameter of the sample vial itself is only 0.01418 m, it is unlikely that many voids will form within the sample. Thus a single spherical void with a diameter equal to 0.00263 m was simulated at the center of the sample vial, at the vertical location in line with the collimation centerlines for the KED and XRF branches. Another void was separately simulated within the sample volume

nearest to the entrance of the XRF collimation pathway to determine adverse effects on the resulting XRF response. An example of the void formation near the XRF collimation entrance is shown in Figure 7.32.

7.2.3.1 XRF Detector Response to Salt Mix with Non-Homogeneities

The results of the cracking and voiding simulations can be seen in Tables 7.5 and 7.6 where the difference between the base case of room temperature Mark V salt and the updated sample constitutions are analyzed. The simulated XRF peak areas and K-edge magnitudes for uranium and plutonium of the normalized spectra are measured for each subsequent change to the sample, and the differences between the results are presented. Due to the highly localized K-edge vacancy production detailed in Section 7.1.2, it was expected that the cracking simulations would not cause large changes to the XRF responses. Table 7.5 shows that for every crack studied, the change to the simulated uranium and plutonium peak areas is negligible and does not exceed the error bounds.

However, this is not the case for the voids formed at the center of the vial and in close proximity to the XRF collimation pathway entrance. A decrease in the simulated peak areas for the actinide x-rays was expected due to the presence of a void in the center of the sample vial. Instead the change in the simulated peak area showed a slight increase of 0.69 % and 0.63 % for the uranium and plutonium peaks, respectively, from the base case of room temperature salt. Additionally, the approximately 1.6 % and 2.3 % peak area decrease for the uranium and plutonium peaks, respectively, from the base case of room temperature salt represent a unexpected decrease from the presence of a void directly in the area of the highest attenuation within the sample for x-ray counts contributing to the XRF detector response. As this region of the sample adds a negligible amount of x-rays to the detector response and serves primarily to attenuate the actinide x-rays generated in

the central collimation region, it was expected for the peak areas to increase under the circumstance of a void in this region.

Table 7.5. Simulated uranium XRF peak areas are shown for the uranium $K\alpha_1$ and plutonium $K\alpha_1$ peaks compared to the peak area of the 25 °C sample constitution while changing sample constitution of the MARK V salt. The difference for the 25 °C sample is left blank.

Sample Constitution	XRF Peak	Simulated Peak Area	Difference from 25° C [%]
25° C	U $K\alpha_2$	1.1502	- ± *0.907*
	Pu $K\alpha_1$	1.3469	- ± *0.513*
500° C	U $K\alpha_2$	1.1473	*0.25213* ± *0.910*
	Pu $K\alpha_1$	1.3350	*0.88351* ± *0.513*
25° C with CL KED Crack	U $K\alpha_2$	1.1526	*0.20518* ± *0.914*
	Pu $K\alpha_1$	1.3451	*0.13461* ± *0.514*
25° C with CL XRF Crack	U $K\alpha_2$	1.1580	*0.66997* ± *0.920*
	Pu $K\alpha_1$	1.3454	*0.11426* ± *0.514*
25° C with Off Axis Crack	U $K\alpha_2$	1.1565	*0.54557* ± *0.908*
	Pu $K\alpha_1$	1.3572	*0.76636* ± *0.515*
25° C with Void at Center	U $K\alpha_2$	1.1581	*0.69092* ± *0.917*
	Pu $K\alpha_1$	1.3554	*0.62985* ± *0.509*
25° C with Void at XRF Edge	U $K\alpha_2$	1.1319	*1.58939* ± *0.898*
	Pu $K\alpha_1$	1.3163	*2.26738* ± *0.511*

7.2.3.2 KED Detector Response to Salt Mix with Non-Homogeneities

For a KED measurement, simulating the correct amount of attenuating material through which the detected beam passes is crucial to making accurate reproductions of experimental measurements. Changes on the order of tenths of millimeters can have noticeable effects on the resultant spectra. Thus it was expected that the cracking and voiding simulations would greatly affect the K-edge magnitude results. Table 7.6 examines the changes to the relative counts representing the uranium and plutonium K-edge magnitudes for the normalized spectra of the altered sample constitutions.

Large differences of up to 47 % exist for the simulated uranium K-edge of the Mark V salt between the homogeneous room temperature sample and the cracked sample. Of note, the two sample conditions of the centerline XRF crack and the Off Axis crack should have relatively similar effects on the simulated K-edge magnitude as they are symmetric, yet the differences of the simulated K-edges are dissimilar. This belies a potential error in the results, and suggests a topic of investigation for future work.

Even so, the current analysis has determined that cracks and voids directly in line with the KED collimation pathway will alter the results by reducing the magnitude of the step across the K-edges by a maximum of one half, under the current investigation parameters. This difference between homogenous and non-homogeneous samples constitutes a very crucial factor for application of the HKED to determining the major actinide content of pyroprocessing samples. If the cooled form of the eutectic salt is proven to develop cracking and voids, the accurate determination of the K-edge magnitudes for actinides may necessitate large error bounds, greatly reducing the benefits of the HKED when compared to traditional destructive assay methods.

Table 7.6. Simulated uranium K-edge magnitudes compared to the simulated K-edge magnitude for the 25 °C sample constitution while changing sample constitution of the MARK V salt. The difference for the 25 °C sample is left blank.

Sample Constitution	K-edge	Simulated	Difference from 25° C [%]
25° C	U	94.024	- ± *4.784*
	Pu	225.209	- ± *2.378*
25° C with CL KED Crack	U	49.682	*47.160* ± *8.508*
	Pu	118.846	*47.229* ± *4.241*
25° C with CL XRF Crack	U	93.29	*0.781* ± *4.880*
	Pu	233.507	*3.685* ± *2.293*
25° C with Off Axis Crack	U	107.167	*13.978* ± *4.191*
	Pu	209.595	*6.933* ± *2.521*
25° C with Void at Center	U	49.41	*47.45*± *20.826*
	Pu	158.176	*29.765*± *6.830*

CHAPTER 8

CONCLUSIONS

The research endeavors described herein sought to evaluate a technical basis for the safeguarding of nuclear material from a pyroprocessing facility at the electrorefining processing step. As it is susceptible to spoofing and relies on the extension of the plutonium curium inseparability argument to pyroprocessing, a neutron counting method will not provide sufficient confidence to safeguard the pyroprocesses alone. Thus a direct means of actinide assay was selected that will provide independent, onsite, safeguards verification measurements of pyroprocessing facilities with precision approaching that of traditional destructive assay, but turnaround that, notably, is much faster. In order to develop the hybrid K-edge densitometer for pyroprocessing, simulations were required to extend the applicability of the method, facilitate algorithm development, and optimize the measurement system. Thus a computational model was developed to precisely reproduce the spectral response of the HKED and supplement research to extending the applicability of the HKED to safeguarding pyroprocessing activities.

The computer model was created using the Monte Carlo N-Particle code to support the design study of the HKED and provide realistic assay results when examined using current HKED analysis algorithms. Validation of the model has been shown to exhibit satisfactory agreement with the experimentally measured responses from data measured with known sample matrices. The model produced a faithful representation of the XRF and KED branches of the HKED spectral response provided the simulated results were post-processed to account for several issues with the MCNP code. The model has demonstrated the capability to be used as a mechanism to clarify spectral contributions origins and verify the nature of several spectral anomalies. In assessing the ability to

reproduce realistic results, the model proved to be recreating the spectral interferences such as absorption and enhancement within the system. It is posited that models such as the one developed herein are one of most accessible methods to discern the impact that such spectral interferences have on experimental results. These matrix effects become more prevalent as the assayed sample compositions move from primary actinide ratios of 100:1 towards 1:1, so the developed model will be applied in the future to obtain a better understanding of the spectral results under a wider range of sampling situations.

Comparisons to spectral results from samples with actinide ratios of 1:1 from a commercial reprocessing facility were undertaken to asses any relative bias values that may become present as the simulation is extended past the known calibration range. Approximately equal differences were seen when comparing the 100:1 XRF peak areas to the 1:1 peak areas, suggesting that the differences between experimental and simulated peaks are due to systematic errors and can be evaluated and improved in future work. Such evaluations will likely include several changes noted herein, such as including the peak tailing functions to the Voigt broadened peak areas, updating the peak search algorithm to utilize the unbroadened simulated spectra, and expanding the analysis to include additional data points.

In assessing the overall performance of the model, residual plots were generated characterizing the difference between experimentally measured and simulated spectral results with the same energy per channel binning. A roughly sixty time reduction in the residual value surrounding the actinide x-ray peaks was achieved through detailed application of post-processing methods to correct such inaccuracies as the energy offset of the simulated x-ray peaks and the Gaussian broadening of x-ray peak profiles. The remaining relative differences between the simulated and measured spectra have been characterized as most likely due to incorrect simulation of scattering and x-ray tube

energy spectrum for the KED branch as well as lack of peak tailing functions and further optimization of the peak areas for the XRF branch.

This model was developed in order to supplement research on the extension of the HKED to pyroprocessing safeguards. Application of the model has allowed for a detailed determination of the volume of the sample being actively irradiated as well as providing a basis for optimization of the HKED for safeguarding pyroprocessing facilities. Detailed analysis of the simulated results for the HKED assay of an actinide salt mix representative of the samples expected from the electrorefiner during pyroprocessing included several potential sample constitutions. Cracking in the plane of the collimation pathways of the salt sample upon cooling from the molten temperature and the formation of voids within the salt mix were investigated, providing a basis for the measurement results under such circumstances. It was determined that the XRF results are relatively insensitive to such changes, with a maximum difference under 2.5 % for simulated peak areas with the presence of a void within the sample up close to the XRF collimation pathway entrance. However, the KED response was determined to be very sensitive to non-homogeneous samples. As such, future requirements for the extension of the HKED technique to pyroprocessing measurements will need to include a detailed sample analysis in order to determine if cracks and voids in the cooled salt samples will be present or if other non-homogeneities, such as stratification of the sample elements, will occur.

The goal of this work was to apply a computer model capable of reproducing realistic HKED assay results from nitric acid based samples to assess the extension of the HKED technique to the analysis of salt samples representative of those expected from pyroprocessing. This work has been completed, and in accomplishing this goal several other advancements were made to the effort of developing the HKED system for

pyroprocessing. These include creation of a post-processing algorithm to accurately represent the x-ray peak profiles and the x-ray and K-edge energies, development of a simulation approach to determine the effects of spectral interferences on the HKED results, identification of the K-edge vacancy production within samples for system optimization, and investigation into the potential spectral effects of non-homogeneous samples on HKED assay. The underlying Monte Carlo N-Particle code data libraries have been discovered to realistically represent the x-ray branching ratios and K-edge magnitudes for actinides but to lack accurate x-ray energy values and K-edge energy locations. Additionally, research into the application of the HKED to pyroprocessing has unearthed challenges to the current proposed safeguards approaches due to the plutonium curium ratio and the limitations of neutron counters.

This work has served as a means to significantly reduce the calibration and validation efforts behind the design study of the HKED instrument optimized for safeguarding pyroprocessing materials. The simulation tool was developed as an extension to the existing research on the ORNL REDC HKED and has served as crucial component in understanding the radiation transport processes within the measurement system. By demonstrating the expected performance for samples from pyroprocessing, the tool has supplemented the optimization of the HKED instrument for expanded safeguards assay roles. Further developments of the presented modeling approach will include making adjustments for the exponential tails of the x-ray peaks, changes to the peak search algorithms to optimize for small and overlapping peaks, increasing the amount of sample vial shapes, sizes, and materials investigated, and identifying the adequacy of HKED system changes to account for the sampling environment of pyroprocessing.

APPENDIX A

XRF AND KED SIMULATED RESPONSE

This appendix illustrates the XRF and KED responses to the uranium and uranium-plutonium nitric acid based samples for the simulated HKED system for the known calibration range, ranging from around 300 g/L uranium to 50 g/L uranium and 3 g/L plutonium to 1 g/L plutonium.

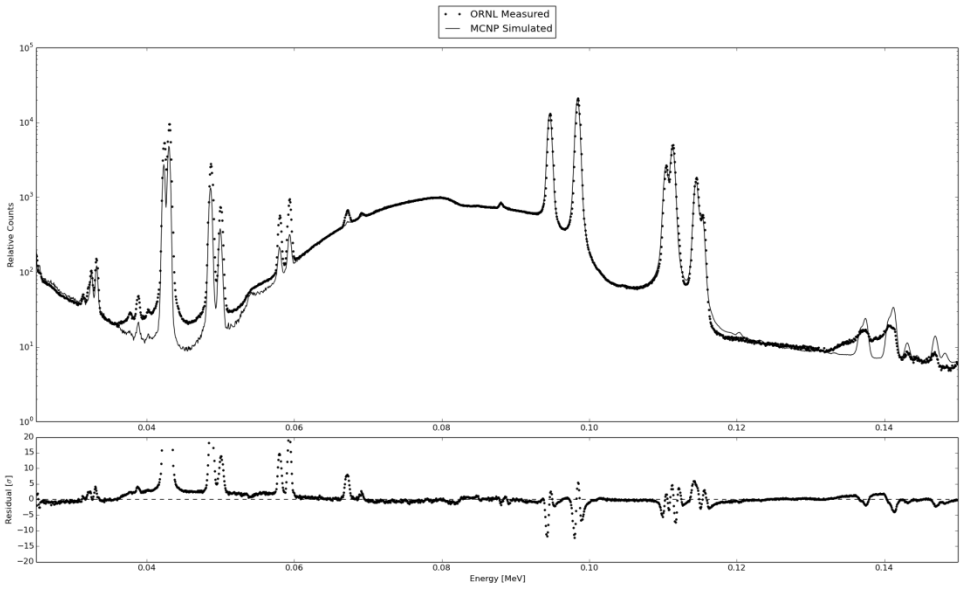

Figure A.1. Comparison plot between experimental results on the ORNL REDC HKED and the post processed MCNP simulation for approximately 268.21 g U/L nitric acid based sample. The residual plot is shown in terms of sigma.

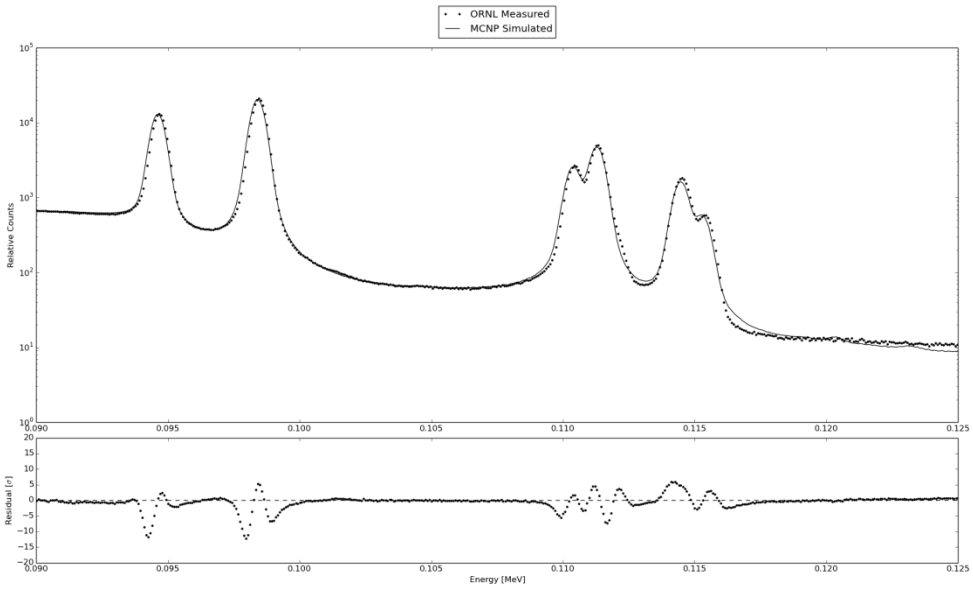

Figure A.2. Comparison plot between experimental results on the ORNL REDC HKED and the post processed MCNP simulation for 268.21 g U/L nitric acid based sample highlighting the residual difference in terms of sigma between the uranium and plutonium K*α* and Kβ x-ray peaks.

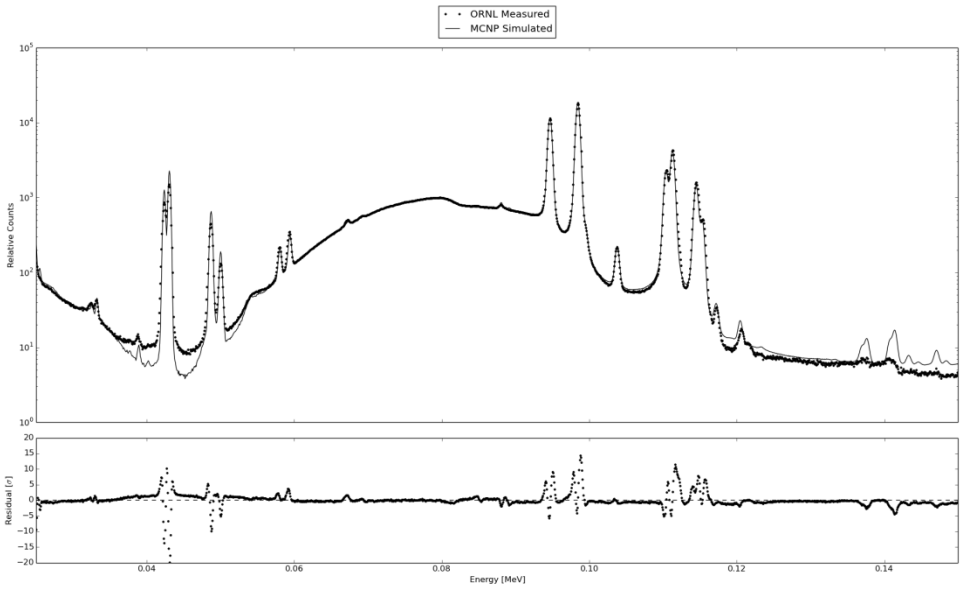

Figure A.3. Comparison plot between experimental results on the ORNL REDC HKED and the post processed MCNP simulation for approximately 243.26 g U/L and 2.93 g Pu/L nitric acid based sample. The residual plot is shown in terms of sigma.

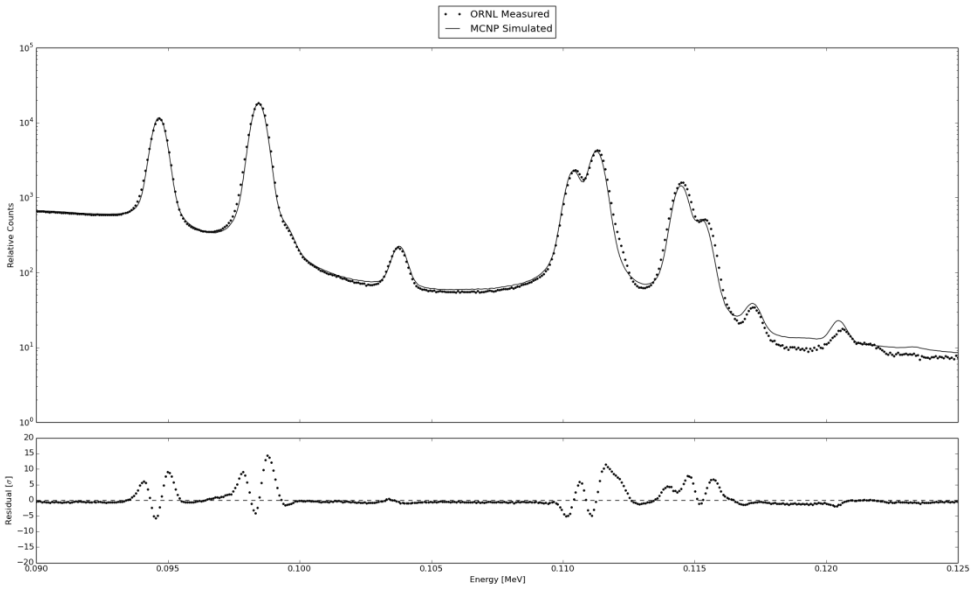

Figure A.4. Comparison plot between experimental results on the ORNL REDC HKED and the post processed MCNP simulation for approximately 243.26 g U/L and 2.93 g Pu/L nitric acid based sample highlighting the residual difference in terms of sigma between the uranium and plutonium Kα and Kβ x-ray peaks.

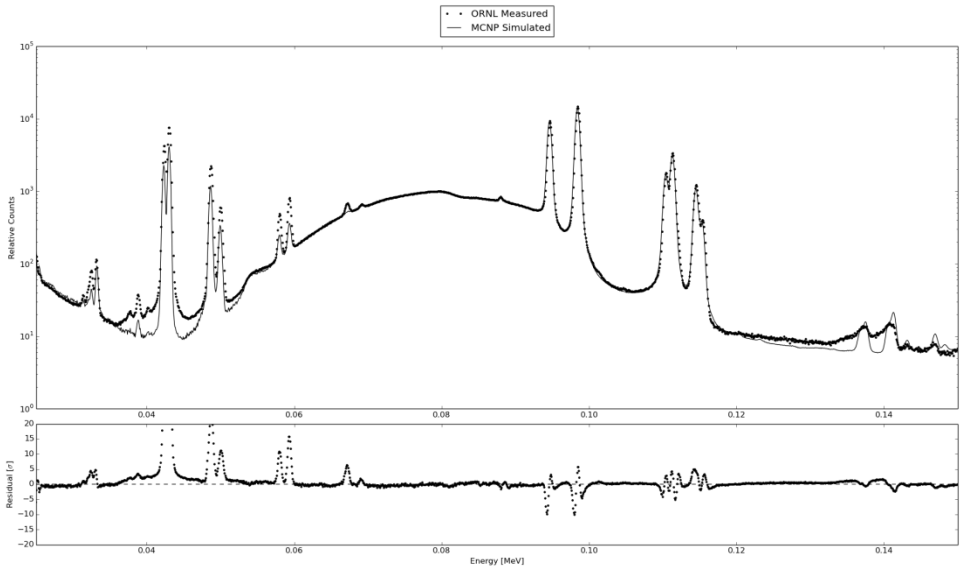

Figure A.5. Comparison plot between experimental results on the ORNL REDC HKED and the post processed MCNP simulation for approximately 160.91 g U/L nitric acid based sample. The residual plot is shown in terms of sigma.

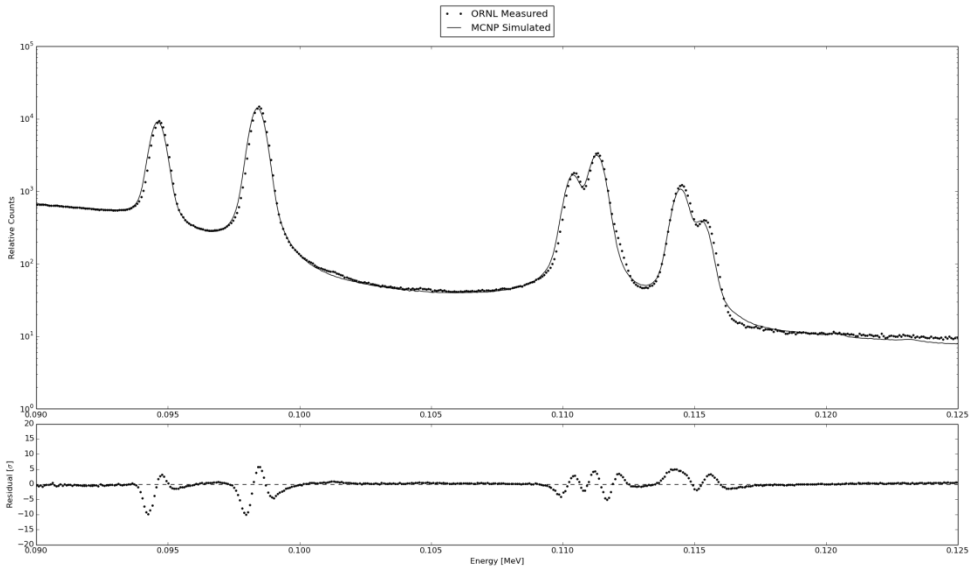

Figure A.6. Comparison plot between experimental results on the ORNL REDC HKED and the post processed MCNP simulation for 160.91 g U/L nitric acid based sample highlighting the residual difference in terms of sigma between the uranium Kα and Kβ x-ray peaks.

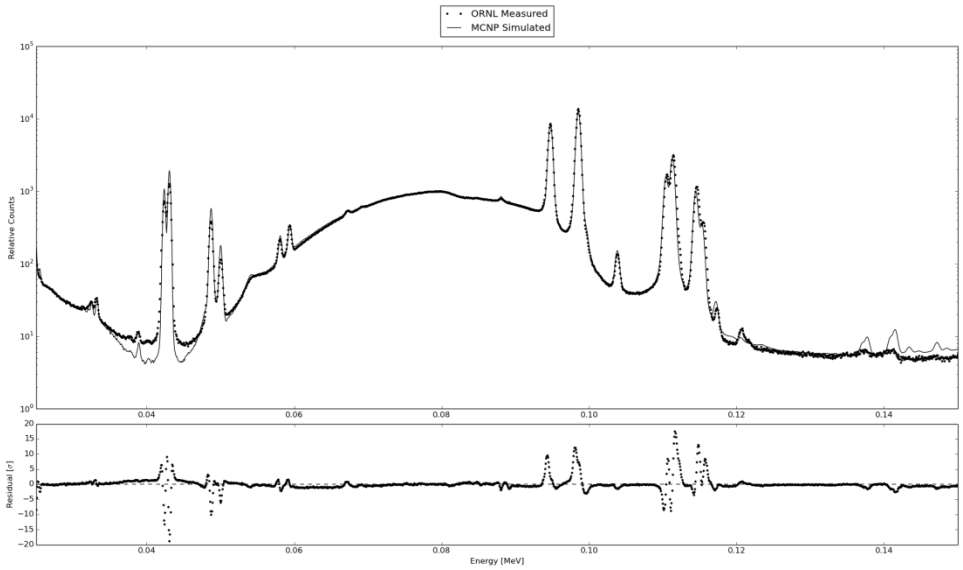

Figure A.7. Comparison plot between experimental results on the ORNL REDC HKED and the post processed MCNP simulation for approximately 160.91 g U/L and 1.566 g Pu/L nitric acid based sample. The residual plot is shown in terms of sigma.

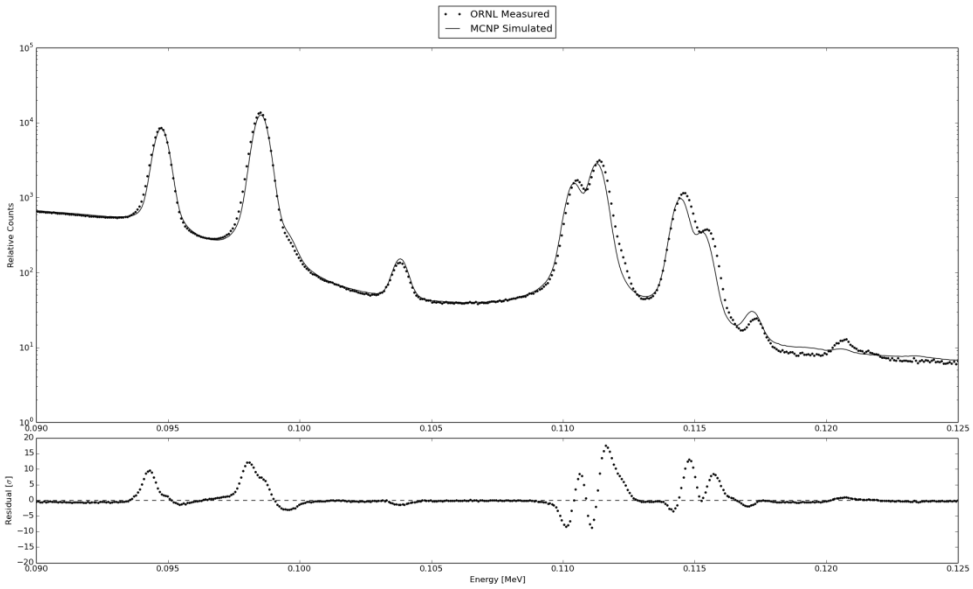

Figure A.8. Comparison plot between experimental results on the ORNL REDC HKED and the post processed MCNP simulation for 160.91 g U/L and 1.566 g Pu/L nitric acid based sample highlighting the residual difference in terms of sigma between the uranium and plutonium K*α* and Kβ x-ray peaks.

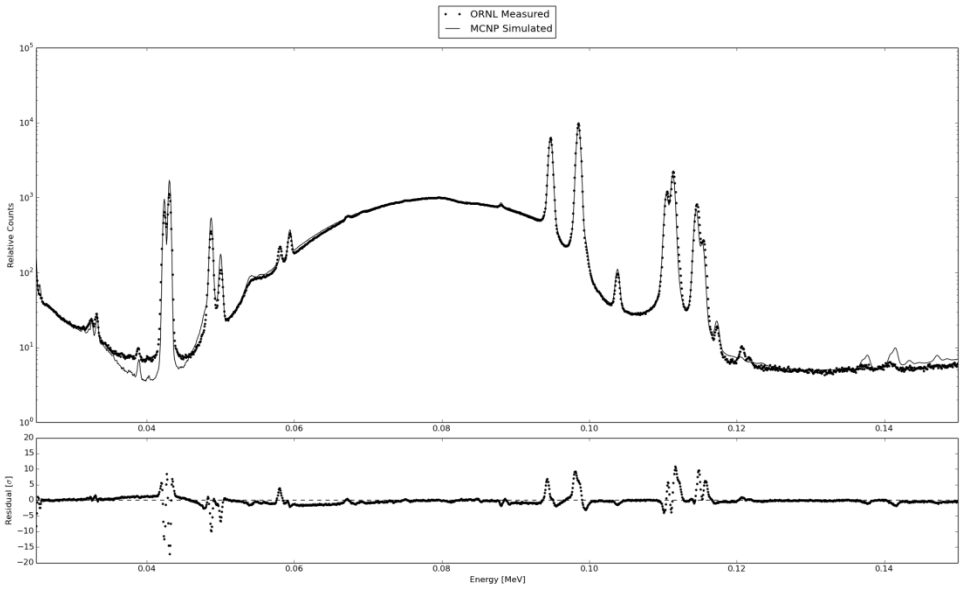

Figure A.9. Comparison plot between experimental results on the ORNL REDC HKED and the post processed MCNP simulation for approximately 107.3 g U/L and 1.041 g Pu/L nitric acid based sample. The residual plot is shown in terms of sigma.

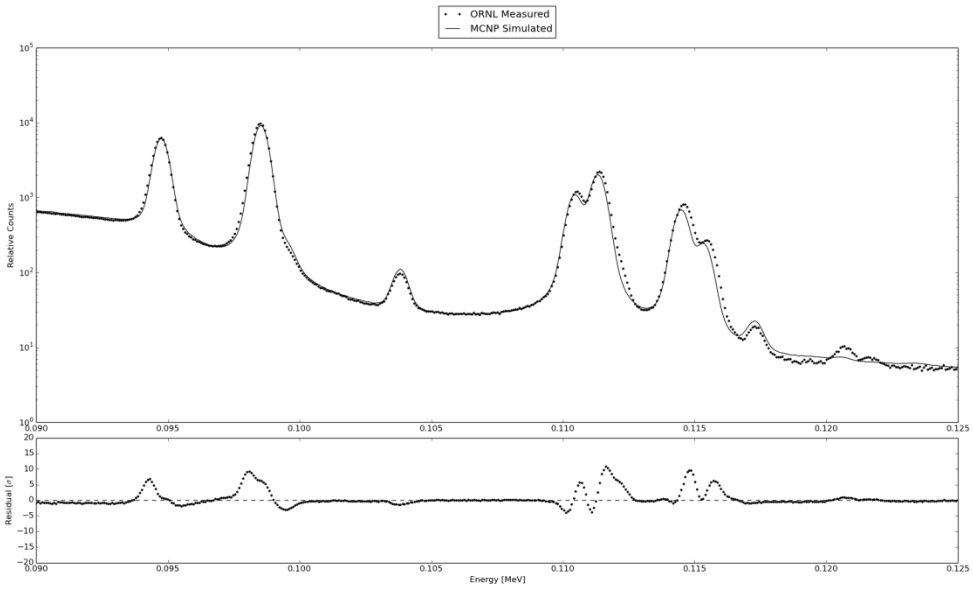

Figure A.10. Comparison plot between experimental results on the ORNL REDC HKED and the post processed MCNP simulation for approximately 107.3 g U/L and 1.041 g Pu/L nitric acid based sample highlighting the residual difference in terms of sigma between the uranium and plutonium Kα and Kβ x-ray peaks.

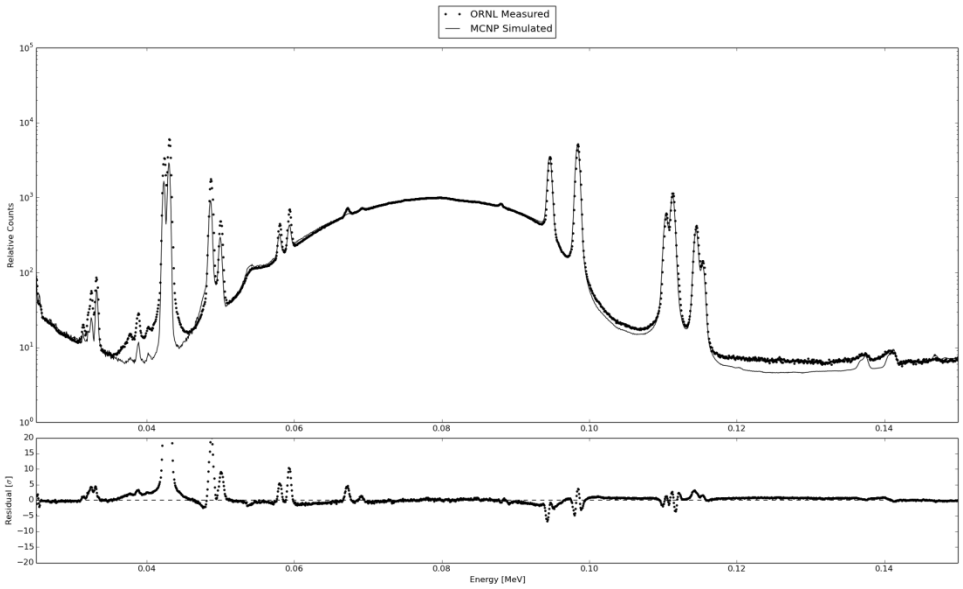

Figure A.11. Comparison plot between experimental results on the ORNL REDC HKED and the post processed MCNP simulation for approximately 48.273 g U/L nitric acid based sample. The residual plot is shown in terms of sigma.

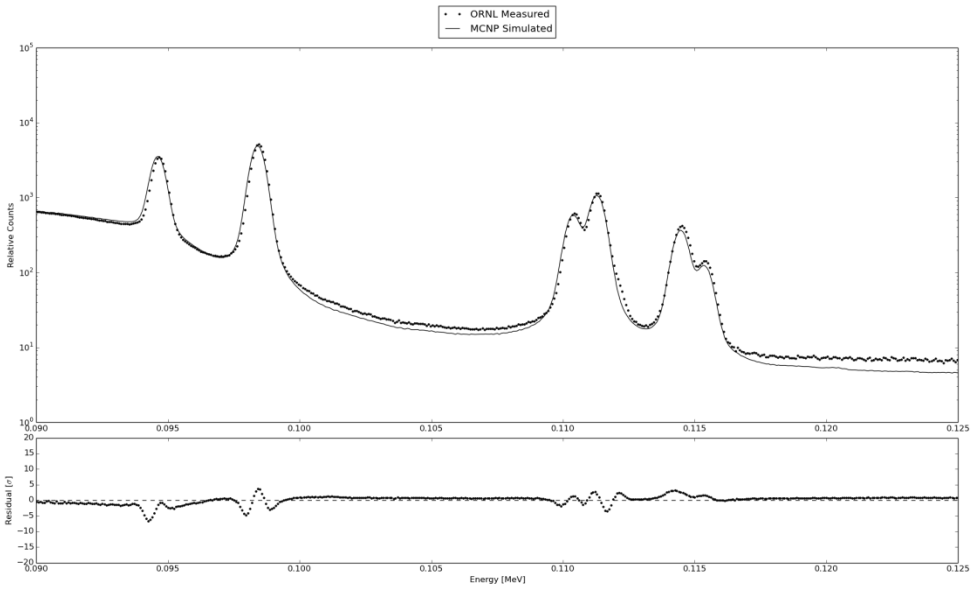

Figure A.12. Comparison plot between experimental results on the ORNL REDC HKED and the post processed MCNP simulation for 48.273 g U/L nitric acid based sample highlighting the residual difference in terms of sigma between the uranium and plutonium K*α* and Kβ x-ray peaks.

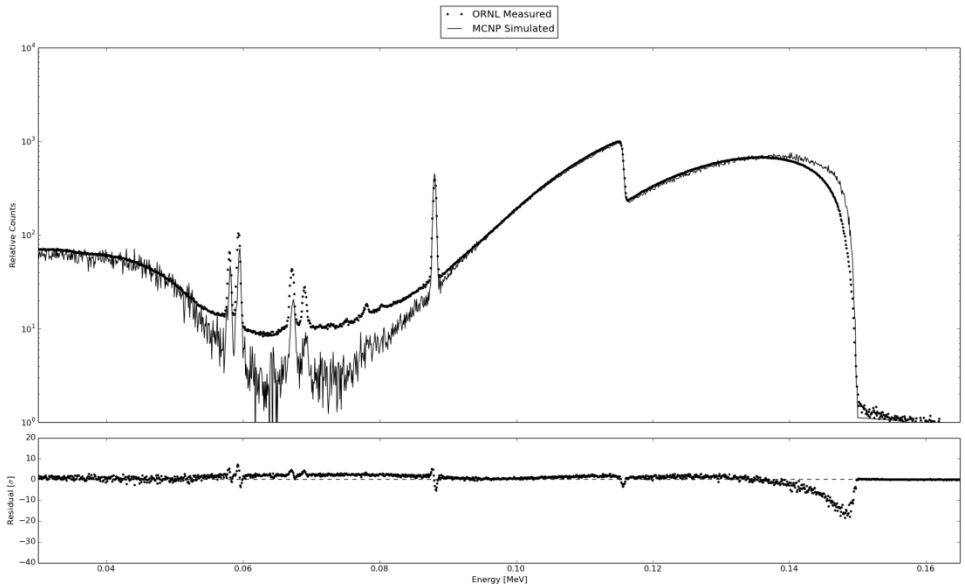

Figure A.13. Modeled and measured KED responses of the continuum and the K-edge magnitude for a uranium nitrite sample with approximately 321.91 g U/L with the residual shown in terms of sigma.

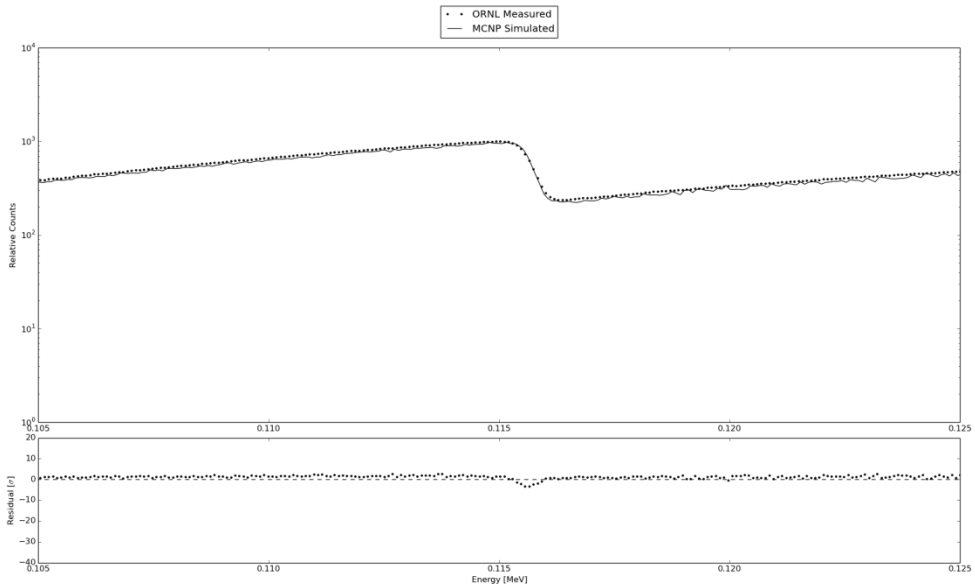

Figure A.14. Modeled and measured KED responses of the uranium K-edge magnitude for a uranium nitrite sample with approximately 321.91 g U/L with the residual shown in terms of sigma.

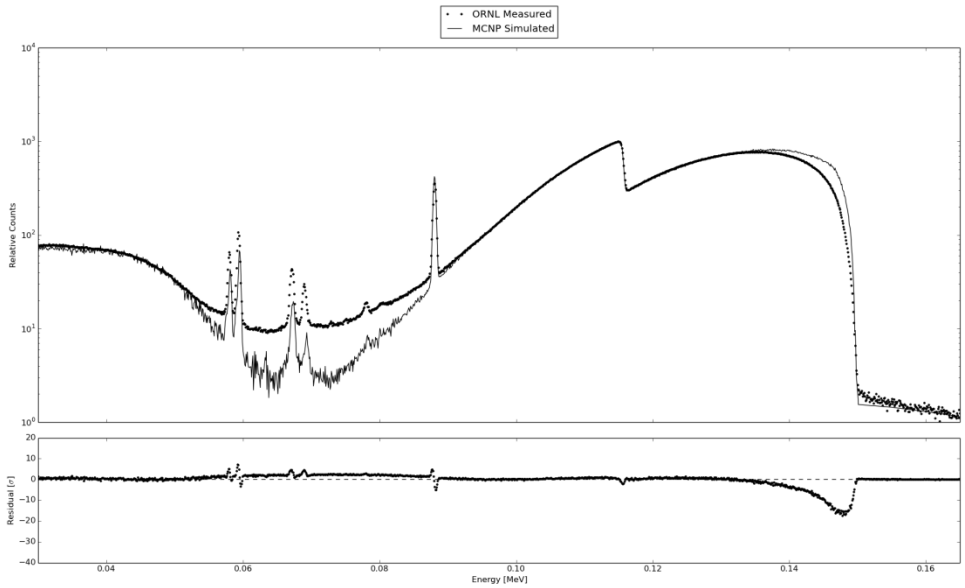

Figure A.15. Modeled and measured KED responses of the continuum and the K-edge magnitude for a uranium nitrite sample with approximately 268.21 g U/L with the residual shown in terms of sigma.

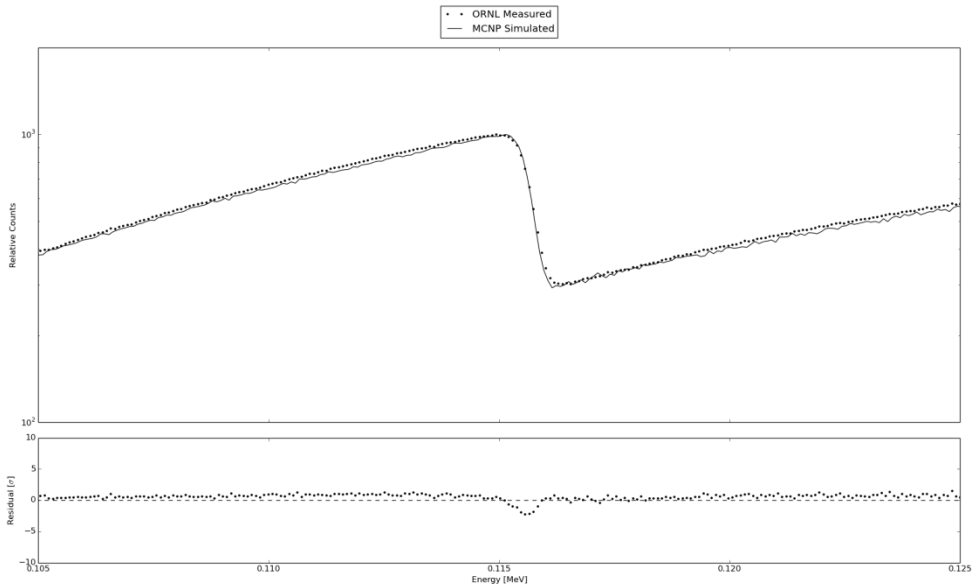

Figure A.16. Modeled and measured KED responses of the uranium K-edge magnitude for a uranium nitrite sample with approximately 268.21 g U/L with the residual shown in terms of sigma.

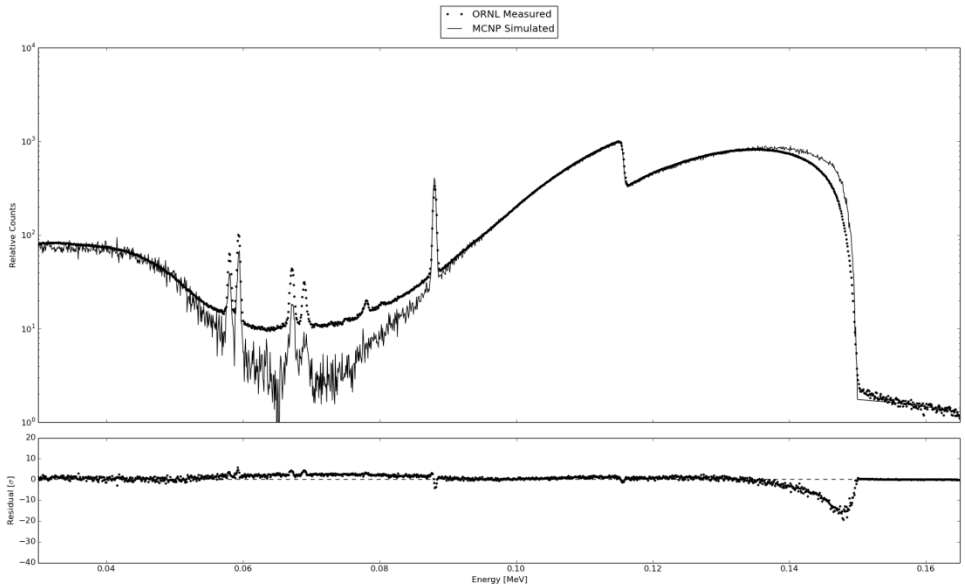

Figure A.17. Modeled and measured KED responses of the continuum and the K-edge magnitude for a uranium nitrite sample with approximately 243.26 g U/L and 2.932 g Pu/L with the residual shown in terms of sigma.

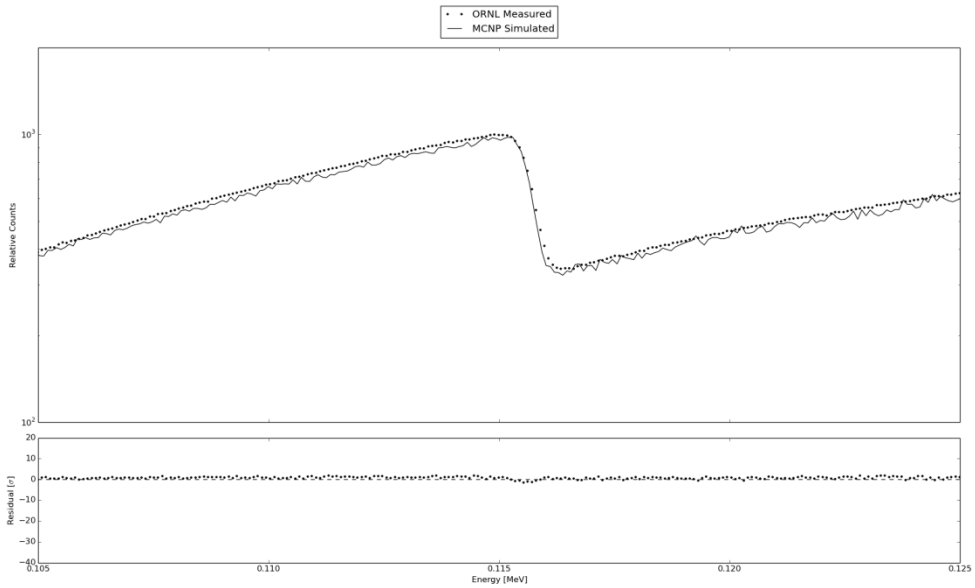

Figure A.18. Modeled and measured KED responses of the uranium K-edge magnitude for a uranium nitrite sample with approximately 243.26 g U/L and 2.932 g Pu/L with the residual shown in terms of sigma.

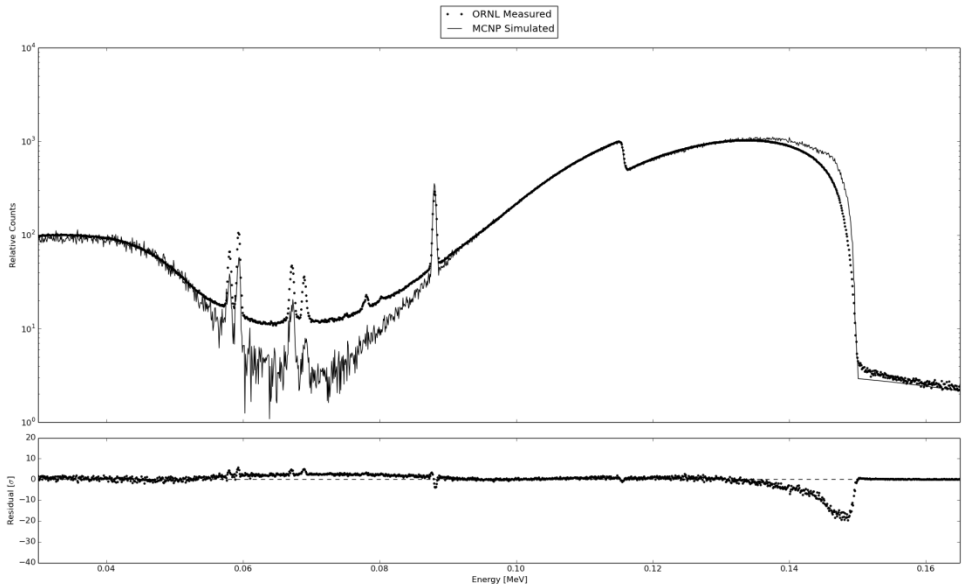

Figure A.19. Modeled and measured KED responses of the continuum and the K-edge magnitude for a uranium nitrite sample with approximately 160.91 g U/L and 1.566 g Pu/L with the residual shown in terms of sigma.

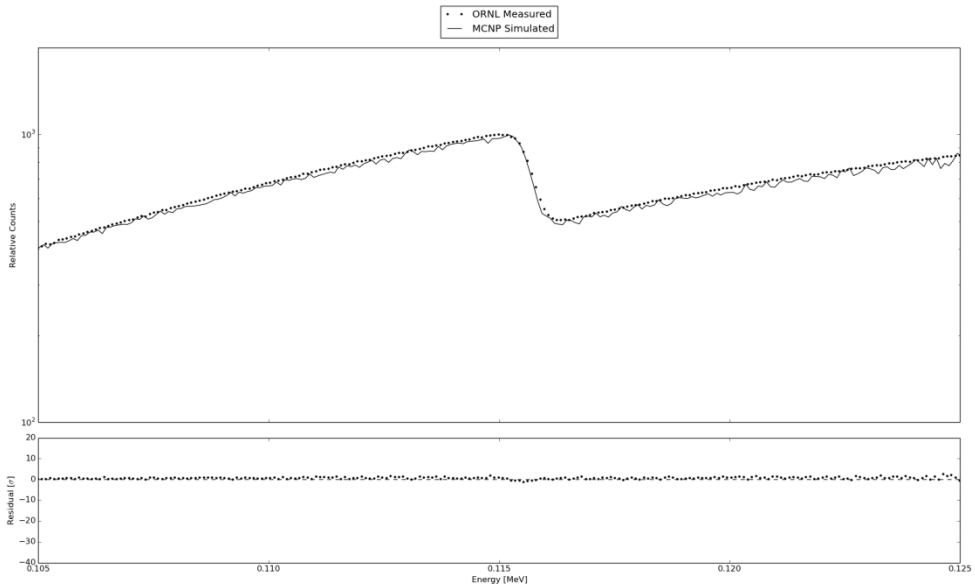

Figure A.20. Modeled and measured KED responses of the uranium K-edge magnitude for a uranium nitrite sample with approximately 160.91 g U/L and 1.566 g Pu/L with the residual shown in terms of sigma.

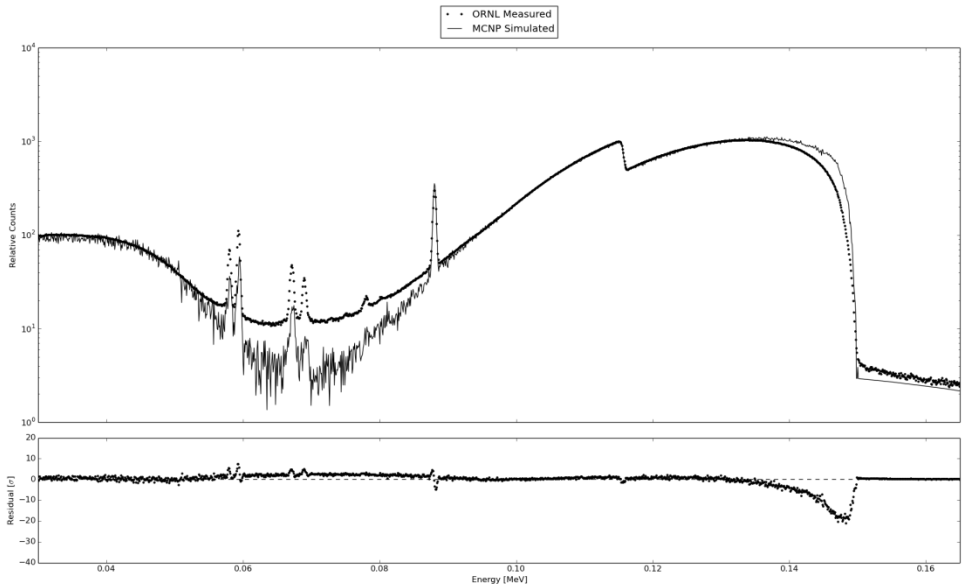

Figure A.21. Modeled and measured KED responses of the continuum and the K-edge magnitude for a uranium nitrite sample with approximately 160.91 g U/L with the residual shown in terms of sigma.

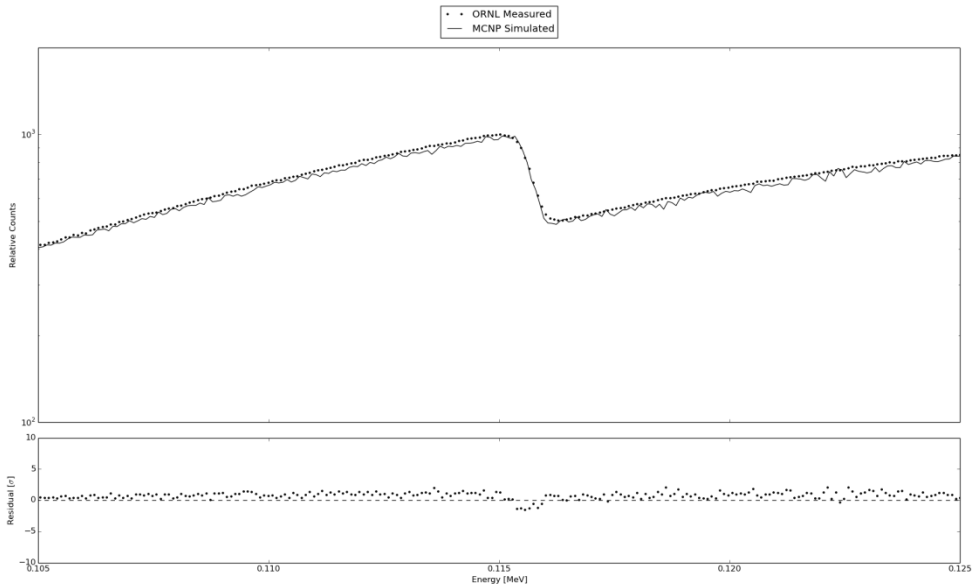

Figure A.22. Modeled and measured KED responses of the uranium K-edge magnitude for a uranium nitrite sample with approximately 160.91 g U/L with the residual shown in terms of sigma.

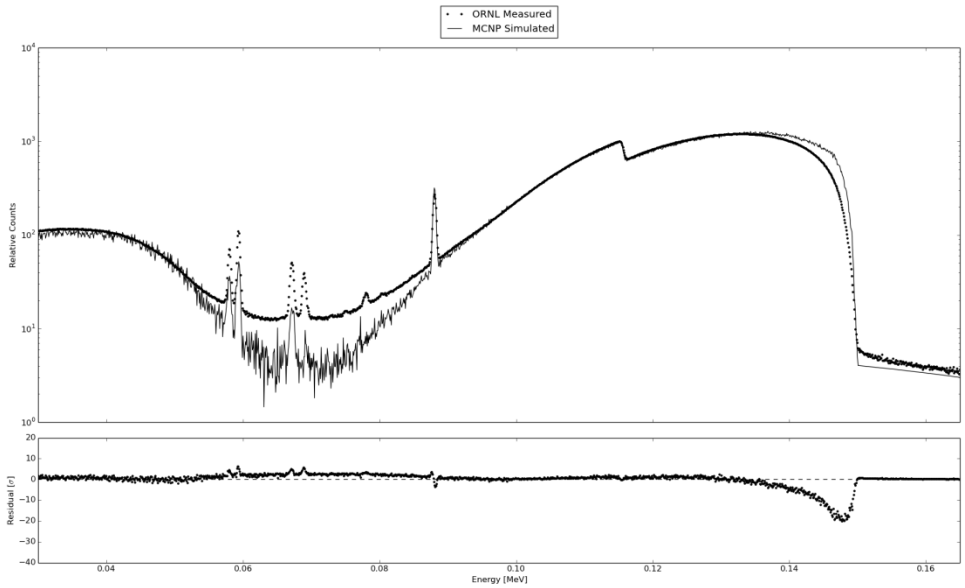

Figure A.23. Modeled and measured KED responses of the continuum and the K-edge magnitude for a uranium nitrite sample with approximately 107.3 g U/L and 1.041 g Pu/L with the residual shown in terms of sigma.

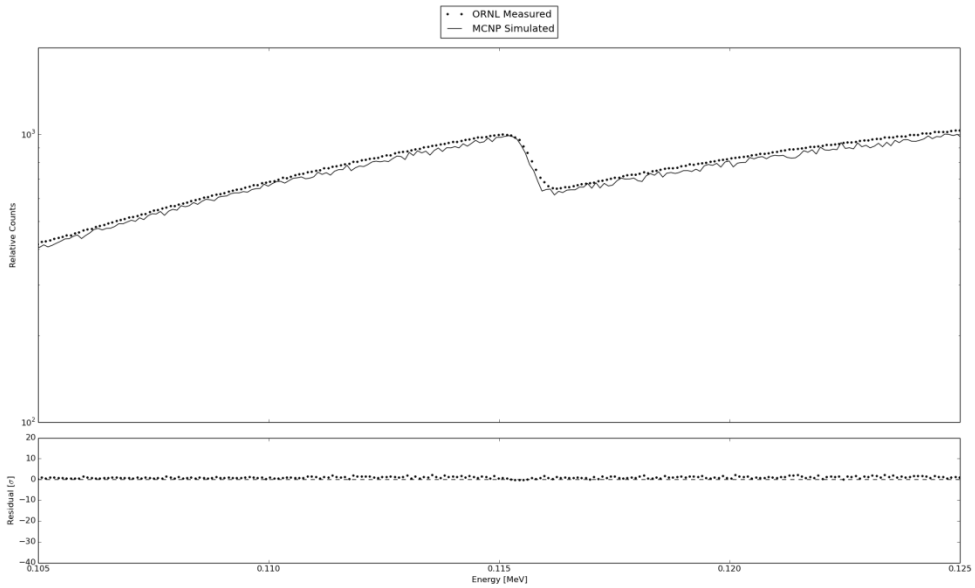

Figure A.24. Modeled and measured KED responses of the uranium K-edge magnitude for a uranium nitrite sample with approximately 107.3 g U/L and 1.041 g Pu/L with the residual shown in terms of sigma.

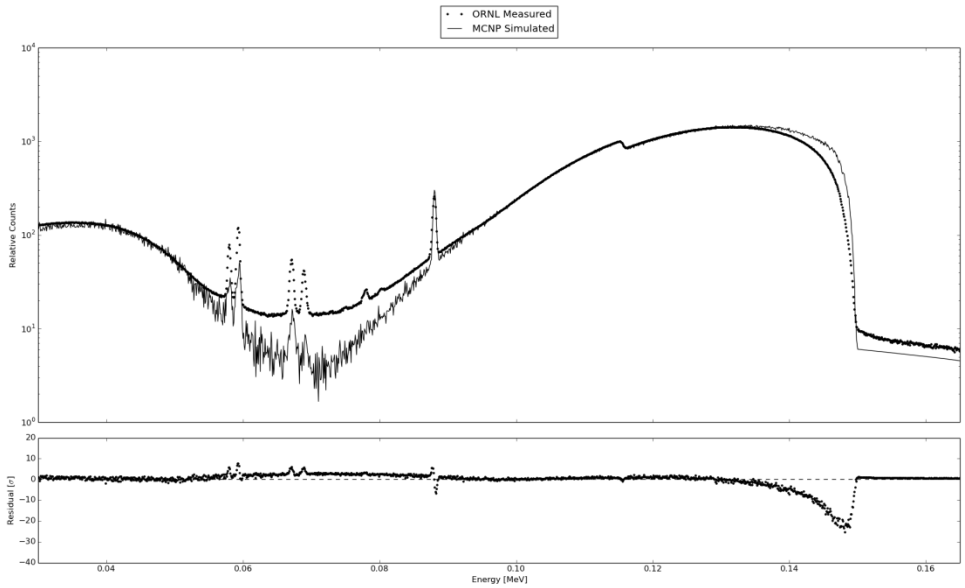

Figure A.25. Modeled and measured KED responses of the continuum and the K-edge magnitude for a uranium nitrite sample with approximately 48.273 g U/L with the residual shown in terms of sigma.

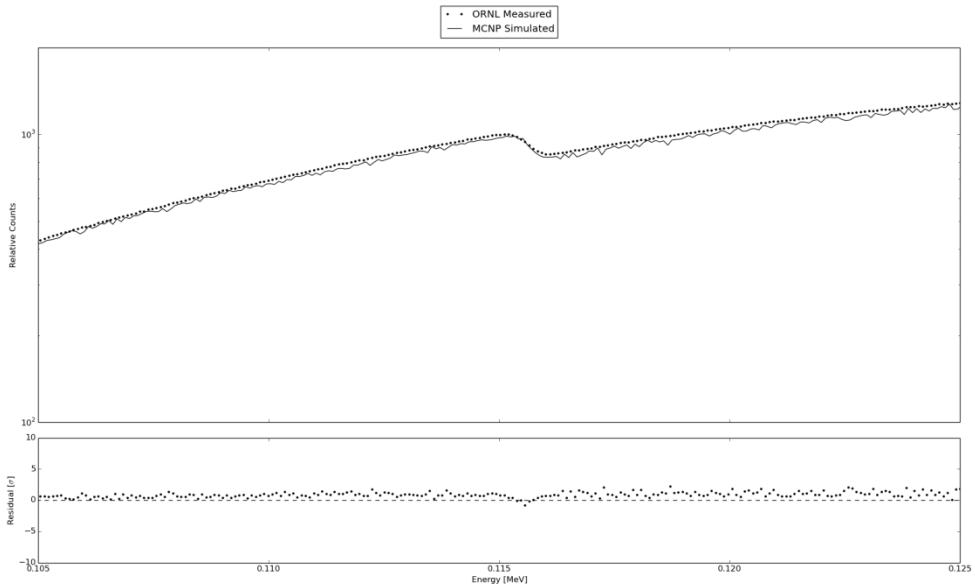

Figure A.26. Modeled and measured KED responses of the uranium K-edge magnitude for a uranium nitrite sample with approximately 48.273 g U/L with the residual shown in terms of sigma.

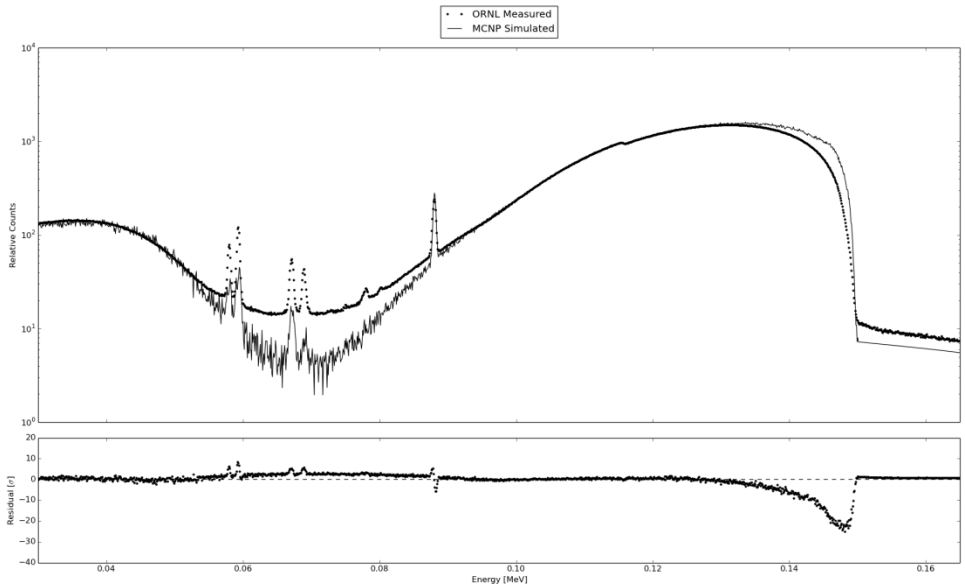

Figure A.27. Modeled and measured KED responses of the continuum and the K-edge magnitude for a uranium nitrite sample with approximately 16.119 g U/L with the residual shown in terms of sigma.

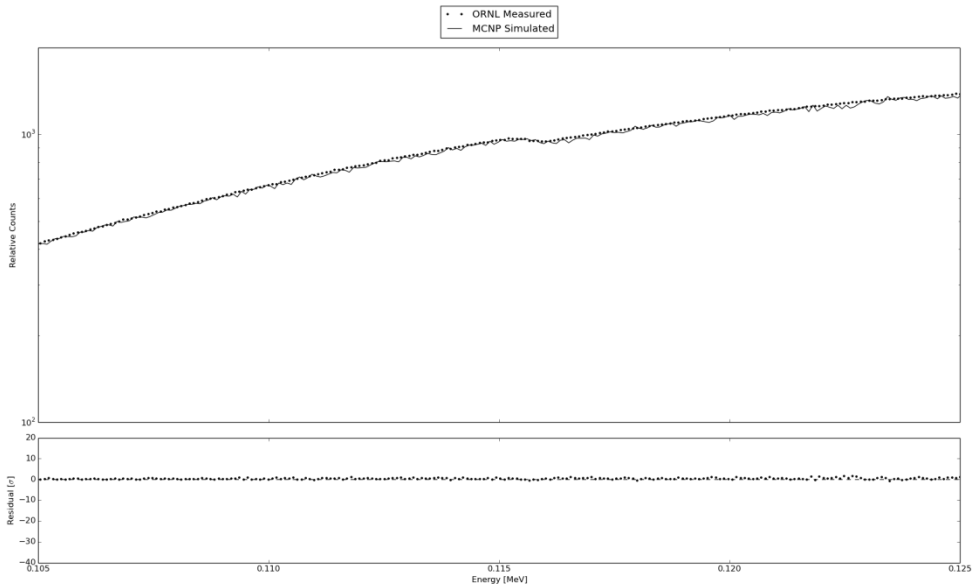

Figure A.28. Modeled and measured KED responses of the uranium K-edge magnitude for a uranium nitrite sample with approximately 16.119 g U/L with the residual shown in terms of sigma.

Below, the appendix illustrates only the XRF responses to the uranium and uranium-plutonium nitric acid based samples for the simulated HKED system for the 1:1 U:Pu actinide ratio calibration range, ranging from around 125 g/L uranium to 200 g/L uranium and 140 g/L plutonium to 182 g/L plutonium.

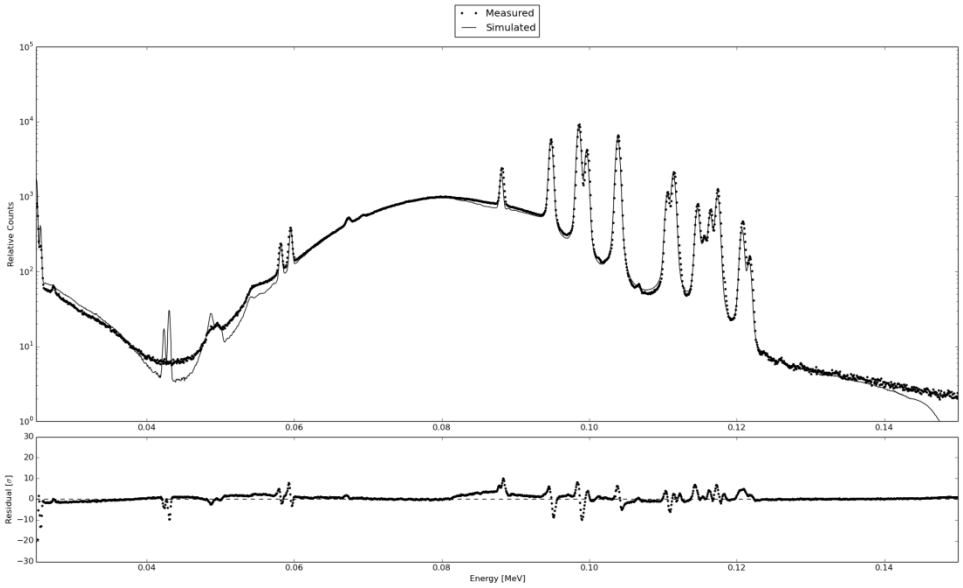

Figure A.29. Comparison plot between experimental HKED XRF results from a sample with a 1:1 U:Pu ratio and the corresponding MCNP simulation of a similar HKED system XRF results from a sample with 1:1 U:Pu ratio. Both results are generated using a sample with approximately 127.29 g U/L and 140.99 g Pu/L in nitric acid based matrix.

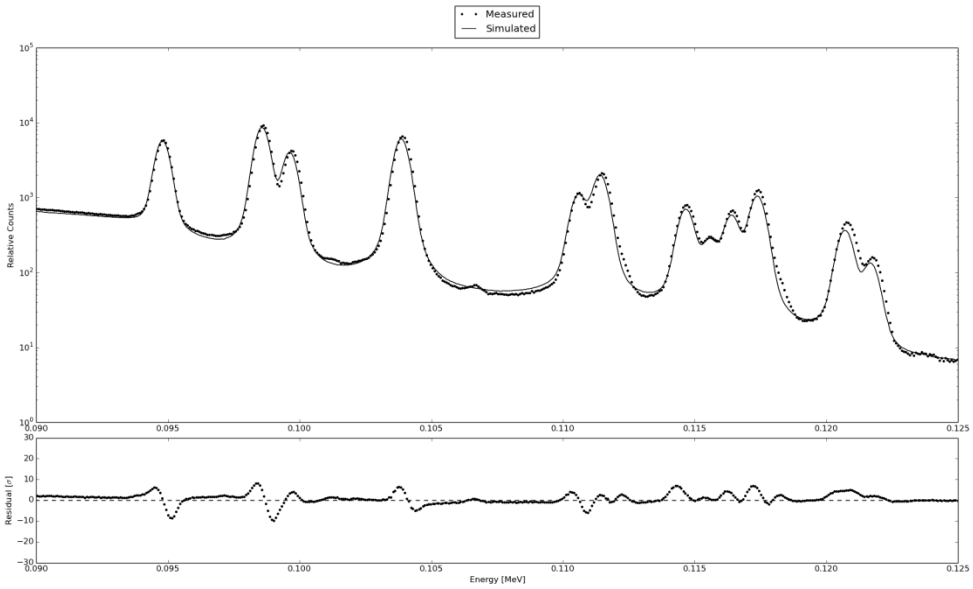

Figure A.30. Comparison plot between experimental HKED XRF results from a sample with a 1:1 U:Pu ratio and the corresponding MCNP simulation of a similar HKED system XRF results from a sample with 1:1 U:Pu ratio showing the energy range containing the K*α* and Kβ peaks for the actinides. Both results are generated using a sample with approximately 127.29 g U/L and 140.99 g Pu/L in nitric acid based matrix.

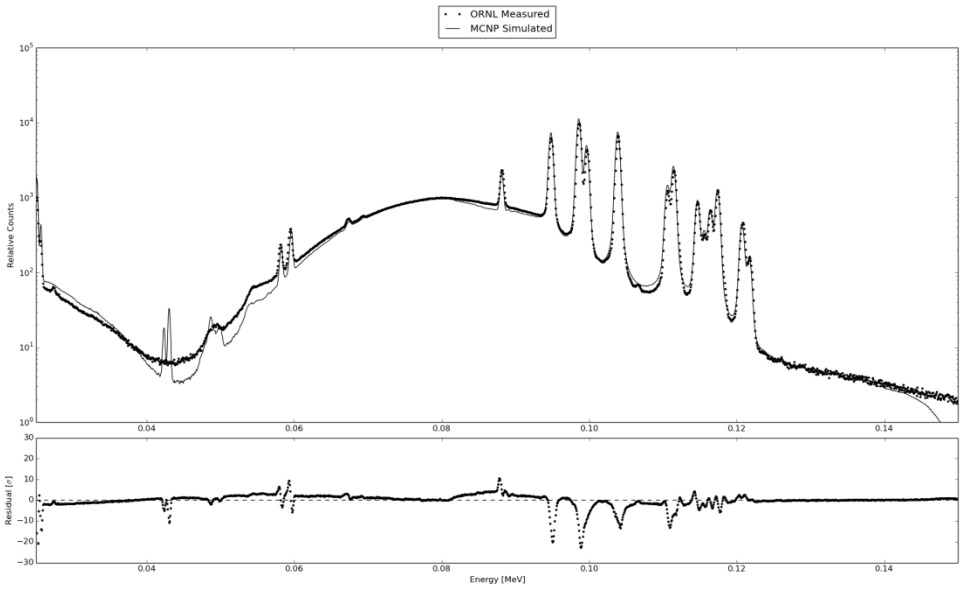

Figure A.31. Comparison plot between experimental HKED XRF results from a sample with a 1:1 U:Pu ratio and the corresponding MCNP simulation of a similar HKED system XRF results from a sample with 1:1 U:Pu ratio. Both results are generated using a sample with approximately 152.23 g U/L and 159.47 g Pu/L in nitric acid based matrix.

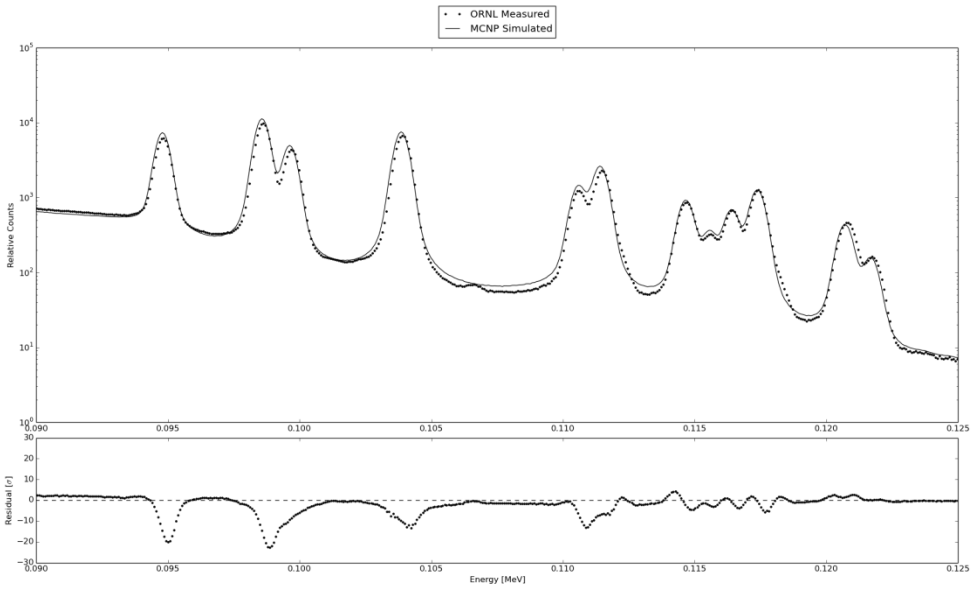

Figure A.32. Comparison plot between experimental HKED XRF results from a sample with a 1:1 U:Pu ratio and the corresponding MCNP simulation of a similar HKED system XRF results from a sample with 1:1 U:Pu ratio showing the energy range containing the K*α* and Kβ peaks for the actinides. Both results are generated using a sample with approximately 152.23 g U/L and 159.47 g Pu/L in nitric acid based matrix.

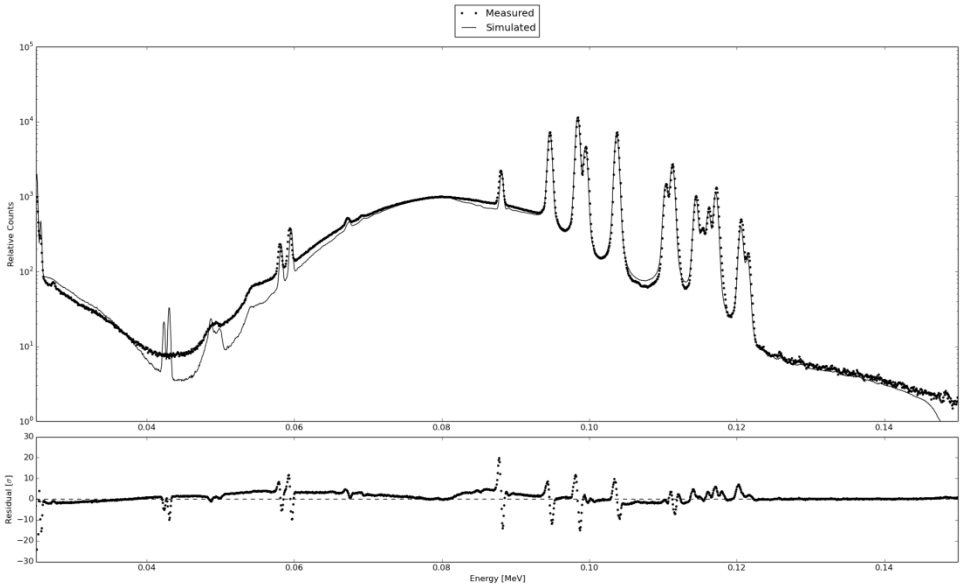

Figure A.33. Comparison plot between experimental HKED XRF results from a sample with a 1:1 U:Pu ratio and the corresponding MCNP simulation of a similar HKED system XRF results from a sample with 1:1 U:Pu ratio. Both results are generated using a sample with approximately 191.08 g U/L and 182.29 g Pu/L in nitric acid based matrix.

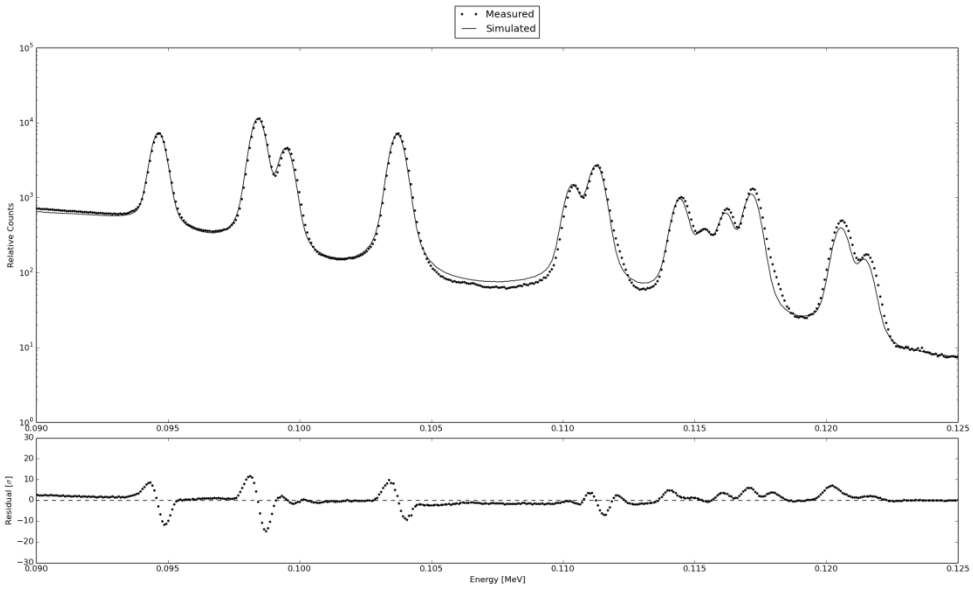

Figure A.34. Comparison plot between experimental HKED XRF results from a sample with a 1:1 U:Pu ratio and the corresponding MCNP simulation of a similar HKED system XRF results from a sample with 1:1 U:Pu ratio showing the energy range containing the K*α* and Kβ peaks for the actinides. Both results are generated using a sample with approximately 191.08 g U/L and 182.29 g Pu/L in nitric acid based matrix.

APPENDIX B

MCNP INPUT FILES

This appendix contains the representative MCNP input files used during the development of the simulation tool. The examples shown below are representative of the finalized versions.

MCNP Sample Input – apprx. 250 g U/L in Nitric Acid Sample Matrix

```
XRF Input for UPu250, SpekCalc source term, ring detector
c F5 optimized and F8 tallies, 1 um dead layer
c
c
c Cells
c ---------------------------------------------------------------------
c Sample
1  1 -1.402  -1 4 -11    u=1
c Sample Vial
2  2  -0.926 (1 -2 -3 4):(-5 -4 6):(-2 -9 3):
     (2 -7 8 -9):(-1 9 -10)  u=1
c Sample Carrier
3 3 -8  (13 -14 -15 16 -19 20):
     (13 -12 -15 16 -20 25 23 24):
     (13 -12 -26 16 -25 6 27 28 30 31 24):
     (13 -12 -15 26 -25 6 27 28 33 31 24):
     (13 -12 -15 16 -6 21)  u=1
c Stainless Steel Transfer Tube
4 3 -8 -41 42 -43 #(36 -35 39 -47 42 -43)
     #(38 -37 -40 47 42 -43)
     #(44 -45 -46 -48 49)
     #(-50 51 -48 52)
     #(-50 -52)
     #((-53 -51 57):(-58 59 -51 57 -55 56):
      (-54 -51 57))    u=1
5 3 -8 -60 -42 61   u=1
6 3 -8 -60 43 -62
     #(36 -35 39 -47 42 -62)
     #(38 -37 -40 47 42 -62)  u=1
c Stainless Steel KED Beam Filter
7 3 -8 (-63 -46 66):(-64 -66 65)   u=1
```

```
c KED Collimator
8 4  -19.25 ((-67 -46 70):(-68 -70 71):
     (-69 -71 72):(-68 -72 73))
     #(-63 -46 66) #(-64 -66 65)
     #(-74 -65 73)   u=1
c KED Shield with Collimator
9 4 -19.25 -48 49 -45 44 -46 75
     #((-67 -46 70):(-68 -70 71):
     (-69 -71 72):(-68 -72 75))   u=1
c KED Shield with Detector
10 4 -19.25 -48 49 -45 44 -75 76 77   u=1
c Copper foil for 109Cd Check Source on KED
11 5 -8.96  -78 -79 80   u=1
c Poly Cup KED Branch
12 2  -0.926 ((-81 -75 76):(-83 -76 82))
     #(-84 -85 82) #(-86) #(-87) u=1
c  Beryllium Window on KED LEGe
13 6 -1.85 -88 -85 89   u=1
c   Aluminum Container for KED LEGe Detector
14 7 -2.7 ((-90 -89 91):(-90 94 -89 93):(-90 -97 137))
     #(-94 -89 93) #(-92 -93 91)   u=1
c KED LEGe Detector
15 12 -5.5 -95 -96 97   u=1
c X-Ray Tube Shield
16 4 -19.25 (-50 51 -48 52) #(-98)
     #(-100 -99) #(-101 -102 51)
     #(-103 104 -105 106 102 -107) u=1
c     #(-108 -107)   u=1
c XRF SS Collimator EndCap
17 3 -8 -98 51 -109 112 u=1
c Gd XRF Collimator Beam Monitor
18 8 -7.9 -98 109 -110   u=1
c SS XRF Collimator Attenuator
19 3 -8 -98 110 -111   u=1
c XRF Collimator
20 4 -19.25 (-117 -114 113 112):
c 20 0 (-117 -114 113 112):
     (-98 -115 114 112):
     (-117 -116 115 112):
     (-98 111 -113 112) u=1 $  108) u=1
c     :(-113 111 -112)
c Be X-ray Filter
c 21 6 -1.85 -118 -120 119
c Cd X-ray Filter, Actually Steel
22  13 -8.65 -101 -102 121   u=1
c XRF Shield
```

```
23 4 -19.25 (113 -122 -124 125 -48 49 117):
    (122 -123 -124 125 -48 49 126)  u=1
c Copper foil for 109Cd Check Source on XRF
24 LIKE 11 BUT *TRCL=(-1.1485126377455  1.91144601803511 0
    -149 121 90 -59 -149 90 90 90 0)   u=1
c Poly Cup XRF Branch
25 LIKE 12 BUT *TRCL=( -1.1485126377455  1.91144601803511 0
    -149 121 90 -59 -149 90 90 90 0)  u=1
c  Beryllium Window on XRF LEGe
26 LIKE 13 BUT *TRCL=( -1.1485126377455  1.91144601803511 0
    -149 121 90 -59 -149 90 90 90 0)   u=1
c   Aluminum Container for XRF LEGe Detector
27 LIKE 14 BUT *TRCL=( -1.1485126377455  1.91144601803511 0
    -149 121 90 -59 -149 90 90 90 0)   u=1
c XRF LEGe Detector
28 LIKE 15 BUT *TRCL=( -1.1485126377455  1.91144601803511 0
    -149 121 90 -59 -149 90 90 90 0)   u=1
c Lead Tip of SS Beam Monitor Filter
c 29 11 -0.00121 (-108 -128 127):(-108 131 -129 128)  u=1
c SS Beam Monitor Filter
c 30 11 -0.00121 (-131 -129 128):(-108 -130 129)  u=1
c SS X-Ray Tube
31 3 -8 ((-100 -99 52):(-50 -52 133)) #(-132 -107)  u=1
c Lead Additional Beam Montitor Cup
c 32 11 -0.00121 (-108 -136 135):(-108 131 -135 134)   u=1
c Dead layer of KED Ge Crystal
33 12 -5.5 -95 -201 96   u=1
c Dead layer of XRF Ge Crystal
34 LIKE 33 BUT *TRCL=( -1.1485126377455  1.91144601803511 0
    -149 121 90 -59 -149 90 90 90 0)  u=1
c Void
99 11 -0.00121 #1 #2 #3 #4 #5 #6 #7 #8 #9 #10 #11 #12
    #13 #14 #15 #16 #17 #18 #19 #20
    #22 #23 #24 #25 #26 #27 #28
    #31 #33 #34 -9999  u=1
98 0 -999  fill=1 TRCL=18
100 0 999

c Surfaces
c ---------------------------------------------------------------------
c
c =Sample Vial=
1 cz 0.709
2 cz 0.948
3 pz  3.35
4 pz   -1.15
```

```
5 cz  1.1
6 pz  -1.3
7 cz  1.255
8 pz  2.85
9 pz  3.55
10 pz  4.25
c
c =Sample=
11 pz 1.8
c
c =Sample Carrier=
12 px  1.5
13 px -6.807
14 px -4.898
15 py  2.5765
16 py  -2.5765
17 py  0.25    $ UNUSED
18 py  -0.25        $ UNUSED
19 pz  2.3015
20 pz  0.9995
21 pz  -1.5515
22 pz  -1.9965
23 cz  0.9955
24 c/z  -1.699 0 1.372
25 pz 0.7525
26 py 0
27 c/y 0.3 0 0.7525
28 c/y -2.343 0 0.7525
29 pz -0.7525
30 rpp -2.343 0.3 -2.5765 0 -0.7525 0.7525
31 cz 1.372
32 c/y -1.566 0 0.7525
33 rpp -2.343 0.3 0 2.5765 -0.7525 0.7525
c
c =Stainless Steel Transfer Tube=
35 py 2.5995
36 py -2.5995
37 py 1.594
38 py -1.594
39 pz -2.5995
40 pz 4.51989
41 cx 6
42 px -8.48797
43 px 7.51203
44 px -4.98697
45 px 5.01103
```

```
46 py -2.7985
47 pz 2.5995
48 pz 5
49 pz -5
50 c/z 0 6.4875   5.5985
51 py 2.799
52 pz -4
53 c/y 0.3 0 0.7525
54 c/y -1.566 0 0.7525
55 pz 0.7525
56 pz -0.7525
57 py 2.6125
58 px 0.3
59 px -1.566
60 cx  6.55
61 px -10.48797
62 px  23.51203
c
c =Stainless Steel KED Beam Filter=
63 cy 0.239
64 cy 0.141
65 py -5.1665
66 py -3.1995
c
c =KED Collimator=
67 cy 0.899
68 cy 0.9975
69 cy 0.6995
70 py -9.2935
71 py -11.8355
72 py -12.3565
73 py -13.7955
74 cy 0.04
c
c =KED Shield with Collimator=
75 py -12.7955
c
c =KED Shield with Detector=
76 py -22.7805
77 cy 4.0115
c
c =Copper foil for 109Cd Check Source on KED=
78 c/y -2.113431305 0 1.2
79 py -13.8425
80 py -13.8505
c
```

```
c =Poly Cup=
81 cy 3.99
82 py -23.2925
83 cy 5.002
84 cy 3.851
85 py -13.9005
86 cy 1.27
87 c/y -2.115 0 1.27
c
c =Beryllium Window for KED LEGe Detector=
88 cy 3.5
89 py -13.9155
c
c =Aluminum Container for KED LEGe Detector=
90 cy 3.81
91 py -27.4025
92 cy 3.71
93 py -13.9655
94 cy 3.4
137 py -27.6025
c
c =KED LEGe Detector=
95 cy 0.7978845
96 py -14.9155
97 py -15.9155
c
200 rcc 0 -14.9155 0 0 -1 0 0.7978845
201 py -14.9154
c
c =X-Ray Tube Shield=
98 1 cy 0.701
99 pz 3.998
100 c/z 0 6.4875   2.5415
101 cy 0.839
102 py 2.985
103 px 0.1
104 px -0.1
105 pz 0.15
106 pz -0.15
107 py 6.5
108 2 cy 0.098
c
c =SS XRF Collimator EndCap=
109 py 2.999
c
c =Gd XRF Collimator Beam Monitor=
```

```
110 py 3.00154
c
c =SS XRF Collimator Attenuator=
111 py 3.00408
c
c =XRF Collimator=
112 1 cy 0.15
113 3 py 0
114 4 py 0
115 5 py 0
116 6 py 0
117 1 cy 0.9975
c
c =Be X-ray Filter=
118 cy 1.25
119 py 5.530263811
120 py 5.630263811
c
c =Cd X-ray Filter=
121 py  2.88
c
c =XRF Shield=
122 7 py 0
123 8 py 0
124 9 py 0
125 10 py 0
126 1 cy 4.0115
c
c =SS Lead Tipped Beam Monitor Filter=
127 11 py 0
128 12 py 0
129 13 py 0
130 14 py 0
131 2 cy 0.0625
c
c =X-Ray Tube=
132 cy 1.5
133 pz -10
c
c =Additional Lead Cup Beam Monitor=
134 15 py 0
135 16 py 0
136 17 py 0
c
c =Void=
999 so 31
```

```
9999 so 32

c Materials
c ---------------------------------------------------------------------
m1    $ =HNO3-UPu(UPu250)=
     92000 -0.182475036
     94000 -0.001839596
     7014  -0.09749761
     8016  -0.668973436
     1001  -0.049214323 PLIB 12p
m2      $ =Poly Vial=
     1001 1
     6012 1 PLIB 12p
m3   $ SS AISI 304
     26000 -69
     24000 -19
     6012  -0.08
     25055 -1.8
     28000 -9.05
     15031 -0.040
     16000 -0.03
     14000 -1 PLIB 12p
m4      $ Tungsten
     74000 1 PLIB 12p
m5    $ Copper
     29000 1 PLIB 12p
m6    $ Beryllium
     4000  1 PLIB 12p
m7     $ Aluminum
     13000  1 PLIB 12p
m8     $ Gadolinium
     64000 1 PLIB 12p
m9                        $ =U3O8=
     92234.51c    0.00090937   $ U-234
     92235.50c    0.12272727   $ U-235
     92238.50c    0.14909063   $ U-238
     8016.50c    0.72727273 PLIB 12p   $ O-16
m10                       $ =Pu Oxide=
     94238.51c   -0.000848     $ Pu-238
     94239.55c   -0.7886223    $ Pu-239
     94240.50c   -0.0507879    $ Pu-240
     94241.51c   -0.0050879    $ Pu-241
     94242.51c   -0.0025439    $ Pu-242
     8016.50c    -0.152019 PLIB 12p    $ O-16
m11                       $ =ANSI dry air=
     6000        -0.000124     $ Nat-C
```

```
    7000        -0.7555268    $ Nat-N
    8000        -0.231781     $ Nat-O
    18000       -0.012827 PLIB 12p    $ Nat-Ar
m12                         $ =HpGe Detector=
    32000        1.0   PLIB 12p       $ Nat-Ge
m13      $ Cadmium
    48000 1 PLIB 12p
m14          $ Lead
    82000 1 PLIB 12p
c
c Data Cards
c ---------------------------------------------------------------------
mode p $ photons
c NPS 1E8
c ctme 420
imp:p 1 18R 1 11R 1 0
rand seed=73524092663431 $ RNG
FCL:p 1 0 0 30R $ Use with Caution: Forced Collisions UPDATE for Variance Reduction
c
c Exponential Transform
c EXT:P 0 26R .8V1 .8V1 0 .8V1 0 0 3R
c EXT:P 0 26R .8V2 .8V2 0 .8V2 0 0 3R
EXT:P 0 19R .9V3 0 5R 0 0 0 3R
c non shifted vector: VECT V1 -1.805 3.004 0
c VECT V2 0.0 3.50466 0.0
VECT V2 0.0 3.50466 0.0 V3 -7.106 -11.8266 0
c
c Translation and Rotation
*TR1 0 0 0 -149 121 90 -59 -149 90 90 90 0
*TR2 -3.361683052 0 0
    -27.39221991 -117.39221991 90 62.60778009 -27.39221991 90 90 90 0
*TR3 0 13.966301272 0 31 -59 90 121 31 90 90 90 0
*TR4 0 15.39426055 0 31 -59 90 121 31 90 90 90 0
*TR5 0 16.040575452 0 31 -59 90 121 31 90 90 90 0
*TR6 0 18.028518761 0 31 -59 90 121 31 90 90 90 0
*TR7 0 17.476701164 0 31 -59 90 121 31 90 90 90 0
*TR8 0 29.143035136 0 31 -59 90 121 31 90 90 90 0
*TR9 0 9.713844944 0 -59 -149 90 31 -59 90 90 90 0
*TR10 0 -9.713844944  0 -59 -149 90 31 -59 90 90 90 0
*TR11 0 3.061916241 0
    -27.39221991 -117.39221991 90 62.60778009 -27.39221991 90 90 90 0
*TR12 0 3.129493103 0
    -27.39221991 -117.39221991 90 62.60778009 -27.39221991 90 90 90 0
*TR13 0 3.337855094 0
    -27.39221991 -117.39221991 90 62.60778009 -27.39221991 90 90 90 0
```

```
*TR14 0 3.625056757 0
    -27.39221991 -117.39221991 90 62.60778009 -27.39221991 90 90 90 0
*TR15 0 2.655465754 0
    -27.39221991 -117.39221991 90 62.60778009 -27.39221991 90 90 90 0
*TR16 0 2.863827744 0
    -27.39221991 -117.39221991 90 62.60778009 -27.39221991 90 90 90 0
*TR17 0 2.925773201 0
    -27.39221991 -117.39221991 90 62.60778009 -27.39221991 90 90 90 0
*TR18 0 0 0 -31 -121 90 59 -31 90 90 90 0
c
c Tallies
c ----------------------------------------------------------------------
c F25:p -8.907784908952014 14.825049665067276 0 1.0 ND $ 1.0 rad of exclusion
F25Y:p 17.1455 0.17 10 ND
c F25Y:p 17.1455 0.7978845 1.0 ND
E25 0.0000598138844716 8186i 0.154781402176
c FT25 GEB 0.0001 0.0012055 0.0 $ Gaussian Energy Broadening
PD25 1 1 31R
c
F45Y:p 17.1455 0.17 10 ND
E45 .12 .13
PD45 1 1 31R
TF45 6J 2
STOP F48 0.03873 $ With 60 indiv. Runs = 0.005 uncert
c
F55Y:p 17.1455 0.17 10 ND
E55 .12 .2
PD55 1 1 31R
TF55 6J 2
c
c Source Definition
c ----------------------------------------------------------------------
SDEF x=d5 y=6.4875 z=d6 vec=d8 dir=d7 erg=d3 TR=18
SI5 -0.1 0.1
SP5 0 1
SI6 -0.15 0.15
SP6 0 1
SI7 -1 .99984769515 1
SP7 0 0.1 100
SI8 L 0 -1 0 -0.46008 -0.88788 0 $ 27.39221991 degrees
SP8 1 0
SI3 H 0.0149 0.015 0.0151 0.0152 0.0153
    0.0154 0.0155 0.0156 0.0157 0.0158
    0.0159 0.016 0.0161 0.0162 0.0163
    …
    0.1479 0.148 0.1481 0.1482 0.1483
```

```
    0.1484 0.1485 0.1486 0.1487 0.1488
    0.1489
SP3 D 0.0 17970680.0 18033530.0 18099640.0 18169060.0
    18241850.0 18318060.0 18397750.0 18480980.0 18567830.0
    18658350.0 18752620.0 18791260.0 18832360.0 18875940.0
    …
    72179.07 65531.43 58900.35 52286.73 45690.52
    39111.66 32550.1 26005.79 19478.67 12968.7
    0.0
```

The information below is used to update the ring detector tally information to be used as the source term for the pulse height tally simulation.

```
c Tallies
c ------------------------------------------------------------------
F18:p 28
E18 0.0000598138844716 8186i 0.154781402176
FT18 GEB 7.13334966e-05 0.00128452846 0.0 $ Gaussian Energy Broadening
c
F48:p 28
E48 .12 .13
FT48 GEB 7.13334966e-05 0.00128452846 0.0 $ Gaussian Energy Broadening
TF48 6J 2
STOP F48 0.03873
c
F58:p 28
E58 .12 .2
FT58 GEB 7.13334966e-05 0.00128452846 0.0 $ Gaussian Energy Broadening
TF58 6J 2
c
c Source Definition
c ------------------------------------------------------------------
SDEF ERG=d1 POS=0.0 3.25 0.0 VEC=0 1 0 DIR=d2 RAD=d3 $ new source location
    AXS=0 1 0
SI2 -1 0 .999998477 1
SP2 0 0 90 10
SI3 0 0.2
SP3 -21 1
c source term information from F5 ring detector tally
SI1 H 5.9814e-05 7.8712e-05 9.7611e-05
    0.00011651 0.00013541 0.00015431
    0.0001732 0.0001921 0.000211
```

0.0002299 0.0002488 0.0002677
0.0002866 0.00030549 0.00032439
0.00034329 0.00036219 0.00038109
0.00039999 0.00041888 0.00043778
0.00045668 0.00047558 0.00049448
0.00051338 0.00053228 0.00055117
0.00057007 0.00058897 0.00060787
0.00062677 0.00064567 0.00066456
…
…
…
0.15399 0.15401 0.15403
0.15404 0.15406 0.15408
0.1541 0.15412 0.15414
0.15416 0.15418 0.1542
0.15421 0.15423 0.15425
0.15427 0.15429 0.15431
0.15433 0.15435 0.15437
0.15438 0.1544 0.15442
0.15444 0.15446 0.15448
0.1545 0.15452 0.15454
0.15455 0.15457 0.15459
0.15461 0.15463 0.15465
0.15467 0.15469 0.15471
0.15472 0.15474 0.15476
0.15478 0.15480
SP1 D 0.0 0.0 0.0
0.0 0.0 0.0
0.0 0.0 0.0
0.0 0.0 0.0
0.0 0.0 0.0
0.0 0.0 0.0
0.0 0.0 0.0
0.0 0.0 0.0
0.0 0.0 0.0
0.0 0.0 0.0
0.0 0.0 0.0
0.0 0.0 0.0
0.0 0.0 0.0
0.0 0.0 0.0
…
…
…

The tables below detail representative densities and weight percentages for the samples analyzed.

Table B.1. MCNP Uranium Sample Input Information for Nitric Acid Based Samples.

Sample	U Conc., mg/mL	Density, g/mL	U Mass Fraction	H mass Fraction	N Mass Fraction	O Mass Fraction
U001	1.07	1.063	0.001006585	0.060274201	0.119408137	0.819311076
U005	5.36	1.103	0.004859474	0.060041738	0.118947608	0.816151181
U015	16.119	1.111	0.014508551	0.059459561	0.117794268	0.80823762
U045	48.273	1.146	0.042123037	0.057793443	0.114493552	0.785589969
U100	107.3	1.218	0.088095238	0.055019713	0.108998565	0.747886483
U150	160.91	1.288	0.124930124	0.052797283	0.104595749	0.717676844
U200	214.61	1.355	0.158383764	0.05077886	0.100597087	0.69024029
U250	268.21	1.428	0.187822129	0.049002698	0.097078364	0.666096809
U300	321.91	1.527	0.21081205	0.047615603	0.094330415	0.647241933

Table B.2. MCNP Uranium-Plutonium Sample Input Information for Nitric Acid Based Samples.

Sample	U Conc., mg/mL	Pu Conc., mg/mL	Density, g/mL	U mass Fraction	Pu Mass Fraction
UPu100	107.3	1.041	1.23	0.087235772	0.0008463
UPu150	160.91	1.566	1.294	0.12435085	0.0012102
UPu200	214.65	2.082	1.357	0.158179808	0.0015343
UPu250	243.26	2.932	1.402	0.173509272	0.0020913

Table B.3. Additional Details of MCNP Uranium-Plutonium Sample Input Information for Nitric Acid Based Samples.

Sample	H mass fraction	N mass fraction	O mass fraction
UPu100	0.055021	0.109	0.747897
UPu150	0.052759	0.10452	0.717159
UPu200	0.050699	0.100438	0.689149
UPu250	0.04974	0.098539	0.67612

Table B.4. MCNP Uranium-Plutonium Sample Input Information for Nitric Acid Based Samples with the actinide ratio approximately at 1:1.

Sample	U Conc., mg/mL		Pu Conc., mg/mL	
Sample 2	127.29	+/- 0.50	140.99	+/- 0.48
Sample 1	140.22	+/- 0.37	145.96	+/- 0.50
Sample 3	152.23	+/- 0.27	159.47	+/- 0.27
Sample 4	154.72	+/- 0.57	160.82	+/- 0.41
Sample 5	165.22	+/- 0.07	157.50	+/- 0.50
Sample 6	191.08	+/- 0.32	182.29	+/- 0.50

Table B.5. MCNP Elemental Sample Input Information for Mark V Actinide Salt based Sample with room temperature density of 1.997 g/mL.

Element	Element Mass Fraction
Chlorine	0.732301
Lithium	0.054596
Potassium	0.158636
Sodium	0.016351
Rubidium	2.45E-05
Strontium	6.99E-05
Yttrium	5.08E-05
Cesium	0.000305
Barium	0.00019
Lanthanum	0.000129
Cerium	0.000235
Praseodymium	0.000107
Neodymium	0.000392
Promethium	8.06E-06
Samarium	0.000106
Europium	5.52E-06
Gadolinium	6.2E-06
Neptunium	2.97E-05
Uranium	0.012929
Plutonium	0.023524
Americium	5.32E-06

APPENDIX C

ANALYSIS ALGORITHMS

This appendix contains a representative set of the analysis algorithms used in post-processing the MCNP simulation data.

Peak Search Algorithm

```
# ------------------------------------------------------
# Define Peak Determination Subroutine
# ------------------------------------------------------

def peakdet(v, delta, x ):
    maxtab = []
    mintab = []
    if x is None:
        x = arange(len(v))
    v = asarray(v)
    if len(v) != len(x):
        sys.exit('Input vectors v and x must have same length')
    if not isscalar(delta):
        sys.exit('Input argument delta must be a scalar')
    if delta <= 0:
        sys.exit('Input argument delta must be positive')

    mn, mx = Inf, -Inf
    mnpos, mxpos = NaN, NaN
```

```
    lookformax = True
    for i in arange(len(v)):
        this = v[i]
        if this > mx:
            mx = this
            mxpos = x[i]
        if this < mn:
            mn = this
            mnpos = x[i]
        if lookformax:
            if this < mx-delta:
                maxtab.append((mxpos, mx))
                mn = this
                mnpos = x[i]
                lookformax = False
        else:
            if this > mn+delta:
                mintab.append((mnpos, mn))
                mx = this
                mxpos = x[i]
                lookformax = True
    return array(maxtab), array(mintab)
```

Smoothing Algorithm

```
# ------------------------------------------------------
# Define Smoothing Subroutine
# ------------------------------------------------------
def savitzky_golay(y, window_size, order, deriv=0, rate=1):
    import numpy as np
    from math import factorial
    try:
        window_size = np.abs(np.int(window_size))
        order = np.abs(np.int(order))
    except ValueError, msg:
        raise ValueError("window_size and order have to be of type int")
    if window_size % 2 != 1 or window_size < 1:
        raise TypeError("window_size size must be a positive odd number")
    if window_size < order + 2:
        raise TypeError("window_size is too small for the polynomials order")
    order_range = range(order+1)
    half_window = (window_size -1) // 2
    # precompute coefficients
    b = np.mat([[k**i for i in order_range] for k in range(-half_window, half_window+1)])
    m = np.linalg.pinv(b).A[deriv] * rate**deriv * factorial(deriv)
    # pad the signal at the extremes with
    # values taken from the signal itself
    firstvals = y[0] - np.abs( y[1:half_window+1][::-1] - y[0] )
    lastvals = y[-1] + np.abs(y[-half_window-1:-1][::-1] - y[-1])
    y = np.concatenate((firstvals, y, lastvals))
    return np.convolve( m[::-1], y, mode='valid')
```

Continuum Estimate Algorithm

```
# ------------------------------------------------------
# Define Continuum Removal Subroutine
# ------------------------------------------------------
def snipbg(y, yback, nchan, ich1, ich2, fwhm, niter):
    iw = math.floor(fwhm)
    i1 = max(ich1 - iw, 0)
    i2 = min(ich2 + iw, nchan - 1)
    yback = [math.sqrt(abs(l)) for l in y]
    redfac = 1
    nreduc = 8
    for p in range(1, niter):
        if p > (niter - nreduc):
            redfac = redfac/round(math.sqrt(2),4)
        iw = math.floor(redfac*fwhm)
        for q in range(ich1, ich2):
            i1 = int(max(q - iw, 0))
            i2 = int(min(q + iw, nchan - 1))
            yback[q] = min(yback[q], 0.5*(yback[i1] + yback[i2]))
    for r in range(ich1, ich2):
        yback[r] = yback[r]*yback[r]
    return yback
```

Broadening Subroutines

```
# ------------------------------------------------------
# Define Broadening Subroutines
# ------------------------------------------------------
def lorentzian(x,p):
    numerator =  ((p[0])**2 )
    denominator = ( x - (p[1]) )**2 + (p[0])**2
    y = p[2]*(numerator/denominator)
    return y
def czosnyka(x,p,q,r):
    lor_width = q*r
    gauss_sig = p[0]*r/2.35
    energy = x
    e0 = p[1]
    ka = [0.0, 1.09148, 2.30556]
    la = [0.0, 0.090227, 0.0035776]
    ma = [1.32272, 1.29081, 1.17417]
    na = [0.081905, 0.0093116,-0.0116099]
    a =  lor_width / 2 / gauss_sig
    v = (energy - e0) / gauss_sig
    v_sum = 0
    for i in range(0,3):
        x1 = (ka[i] * la[i] + na[i] * (a + ma[i]))
        y1 = (ka[i]**2 + (a + ma[i])**2 + v**2)
        z1 = (ka[i]**2 + (a + ma[i])**2 + v**2)**2 - 4 * ka[i]**2 * v**2
        tot = (x1 * y1 - 2 * ka[i] * la[i] * v**2) / z1
        v_sum = v_sum + tot
```

```
    czosnyka =  v_sum / a / gauss_sig**2 # norm with 1e-2 for UKalp1
    return czosnyka
def residuals(p,y,x):
    err = y - lorentzian(x,p)
    #print ptry
    return err
def tails(x,p):
    Lo_tail_area = 95.7983
    Lo_tail_decay = 0.0074455
    fast_tail_area = 0.0000
    fast_tail_decay = 0.0076843
    gauss_width = p[0]/2.35
    energy = x
    e0 = p[1]
    alpha = (-0.5)*gauss_width**2
    t = []
    for i in energy:
        if i < e0:
            t_x = (Lo_tail_area * math.exp(-Lo_tail_decay * (e0 - i)) \
                + fast_tail_area * math.exp(-fast_tail_decay * (e0 - i)))
        else:
            t_x = 0
        t.append(  t_x * (1-math.exp(0.4 * alpha * (e0 - i))) )
    tail_x = t
    counter = 0
    for ii in energy:
        if ii < e0:
```

```
        tail_x[counter] = tail_x[counter]
    else:
        tail_x[counter] = 0.0
    counter = counter + 1
return tail_x
```

Post-processing Code

```
# ===========ORNL REDC HKED Output File Analysis==========
# ==================Written by gsmickum=================
# ====================06/24/2014=======================

#                   IMPORTS
# *********************************************************
import re
import sys
import os
import math
from scipy.optimize import leastsq # Levenberg-Marquadt Algorithm #
from scipy.integrate import simps
import matplotlib.pyplot as plt
from matplotlib.pyplot import plot, scatter, show
import numpy as np
from numpy import NaN, Inf, arange, isscalar, asarray, array, ones, linalg
from pylab import *

#                   INPUTS
# *********************************************************
# !!! NOTE THAT Inputs required here!!!
Input0 = '250'
# Input file titles
Input1 = ['hh'] #'aa', 'bb', 'cc', 'dd', 'ee', 'ff'] #'a', 'b', 'c', 'd' ,'e', 'f', 'g', 'h', 'i'
filenumber = 10
Input1a = ['h']
```

```
filenumbera = 60
# Input file locations
Input2 = r'D:\My Documents\Current Work\Hybrid KEdge Densitometry\MCNP5HKED\hked data runs 3\3-18-2014 New Gd Filter KED XRF'
# Maxtab parameter for Peak Fitting
Input3 = 1e1; '"Input3aa = 1e1; Input3a = 1e2"'; Input3b = 2.5e1  #2e-7 Input3 ## 7e-5 2e-5; use 2e-6 for all the peaks, 2e-5 for most, and 7e-5 for short run on only tallest peaks
# Window for Smoothing approximation
Input4a = 11
# Order for Smoothing approximation
Input4b = 4
# Order for Continuum approximation
Input4c = 15 # 11
# Margin of MCNP Data Table xray energies from Actual Values
Input5 = 0.0001
# X-ray peak FWHM, Peak Location [MeV], and Peak Intensity [a.u.]
# UPDATE: The below values when calibration done.
#Input6 = [[0.00044839, 0.09895, 0.00090623], [6.14349811e-04, 0.1043, 1.04611092e-05]]
# for 100:1
# Input6 = [[0.00044839, 0.09895, 0.00090623], [0.00044839, 0.1043, 1.04611092e-05]] for 1:1 and 1:2
# Lorentzian shaping parameter, three tuples for UPu 100:1, 1:1 and 1:2
Input7 = 1 #[0.45, 0.5] # [(0.4, 0.4), (0.4, 0.4), (0.4, 0.4)] # [(0.35, 0.30), (0.35, 0.35), (0.35, 0.35)]
# Peak fitting normalization parameter
```

```
Input8 = 0.6 #0.6 #0.02 max(ornlynorm)/maxtab2[0][0] # for res ORNL calib file #0.03250 for sal ORNL calib file
# Broadening Paramter
Input9 = 1.115 #0.75 # for res ORNL calib file # 0.90 for sal ORNL calib file
# Normalization value for Exponential Tails
Input10 = 1 # [(1e-4,1e-3),(1e-4,1e-4),(1e-4,1e-4)] # 'g' [1e-4,1e-3]
# Optimum window for No. of Channels to analyze around peak max for fitting, three tuples for UPu 100:1, 1:1 and 1:2
#Input11 = [(75,25)] # for 100:1 # [(75,25),(75,75),(75,75)]
# Input11 = [(75,75)] for 1:1 and 1:2
# Cadmium counts normalization paramters
Input12 = 1e-1
# Cadmium counts normalization paramters for bkgd
Input12a = 1e-5
# Gadolinium counts normalization paramters
Input13 = 1e-2 #1e-1
# Gadolinium counts normalization paramters for bkgd
Input13a = 6e-6
# Number of channels in MCNP spectra
Input14 = 8188


Norm = 1e3      # Normalization constant used to avoid changing Input3 - Input7 for each run


#                    CLASSES
```

```
# ************************************************************
# ------------------------------------------------------
# Class to change working directory
# ------------------------------------------------------
class Chdir:
        def __init__( self, newPath ):
                self.newPath = newPath

        def __enter__( self ):
                self.savedPath = os.getcwd()
                os.chdir( self.newPath )

        def __exit__( self, etype, value, traceback ):
                os.chdir( self.savedPath )


#                BODY OF CODE
# ************************************************************
# ------------------------------------------------------
# Open File with Data to be Analyzed
# ------------------------------------------------------
filename = []; filenamebkgd = []
i,j = 0, 0
while i < len(Input1):
   filename.append('gsm_hked_UPu' + str(Input0) + '_2_' + str(Input1[i]) +
str(filenumber) + 'int.txt')
```

```
    filenamebkgd.append('gsm_hked_UPu' + str(Input0) + '_2_' + str(Input1a[i]) +
str(filenumbera) + 'int.txt')
    i = i + 1


# ------------------------------------------------------
# Import, Tally and Average Raw Data
# ------------------------------------------------------
rawenergies = []; rawcounts = []; rawbkgdcounts = []
for c in filename:
    with Chdir( Input2 ):
        infilename = str(c)
        infile = open(infilename, 'r') # open file for reading
    sepfile = infile.read().split('\n')
    infile.close()
    MCNPergs = []; MCNPcts = []
    for plotpair in sepfile[:-1]:
        xAndy = plotpair.split(',')
        MCNPergs.append(float(xAndy[0]))
        MCNPcts.append(float(xAndy[1]))
    rawenergies.append(MCNPergs)
    rawcounts.append(MCNPcts)
for c in filenamebkgd:
    with Chdir( Input2 ):
        infilename = str(c)
        infile = open(infilename, 'r') # open file for reading
    sepfile = infile.read().split('\n')
    infile.close()
```

```
    MCNPbkgdcts = []
    for plotpair in sepfile[:-1]:
        xAndy = plotpair.split(',')
        MCNPbkgdcts.append(float(xAndy[1]))
    rawbkgdcounts.append(MCNPbkgdcts)

# Add in Cd-109 Spectra
# ----------------------------------------------------
filename12 =r'D:\My Documents\Current Work\Hybrid KEdge Densitometry\MCNP5HKED\hked data runs 3\3-18-2014 New Gd Filter KED XRF\Solo Cd Source\gsm_hked_Cd_3_c60int.txt'

readfile12 = open(filename12, 'r')
sepfile12 = readfile12.read().split('\n')
readfile12.close()
cdcounts = [];
x12 = []
y12 = []
for plotpair12 in sepfile12[:-1]:
    xAndy12 = plotpair12.split(',')
    x12.append(float(xAndy12[0]))
    y12.append(float(xAndy12[1])*Input12)
cdcounts = [cdi * Norm for cdi in y12]
k = 0;


# Add in Gd Spectra
```

```
# ------------------------------------------------------
filename13 = r'D:\My Documents\Current Work\Hybrid KEdge Densitometry\MCNP5HKED\hked data runs 3\3-18-2014 New Gd Filter KED XRF\Solo Gd Beam Monitor\gsm_hked_Gd_3_d60int.txt'

readfile13 = open(filename13, 'r')
sepfile13 = readfile13.read().split('\n')
readfile13.close()
gdcounts = [];
x13 = []
y13 = []
for plotpair13 in sepfile13[:-1]:
    xAndy13 = plotpair13.split(',')
    x13.append(float(xAndy13[0]))
    y13.append(float(xAndy13[1])*Input13)
gdcounts = [gdi * Norm for gdi in y13]
k = 0;



rawcountstot=[]; rawbkgdcountstot=[];
rawcountstotnorm = []; bkgdcontnorm = []
for i in range(0,len(Input1)):
    totbkgdcounts = [(rawi + cdi*Input12a + gdi*Input13a) for rawi, cdi, gdi in zip(rawbkgdcounts[i], y12, y13)]
    rawbkgdcountstot.append(totbkgdcounts)
    totcounts = [(rawi + cdi + gdi) for rawi, cdi, gdi in zip(rawcounts[i], y12, y13)]
    rawcountstot.append(totcounts)
```

```
# Normalize data to single parameter

   rawcountstotnorm.append([ii*Norm/max(rawcountstot[i][4200:4300]) for ii in rawcountstot[i]])
   bkgdcontnorm.append([ii*Norm/max(rawbkgdcountstot[i][4200:4300]) for ii in rawbkgdcountstot[i]])

rawcountstotnormsm = np.asarray(rawcountstotnorm[0])
rawcountstotnormsg = savitzky_golay(rawcountstotnormsm, window_size=Input4a, order=Input4b)

# ----------------------------------------------------
# Locate and tabulate Peak Maximum values from Data
# ----------------------------------------------------

#Raw Data
# ----------------------------------------------------
maxtab11a = []; maxtab11b = []; maxtab11 = [];
maxtab22a = []; maxtab22 = [];
maxtab33a = []; maxtab33 = []
maxtab1 = []; maxtab1a = []; maxtab2 = []; energy = []
# PeakSearch for locale maximums only on Each of the Sets of Data(Sample, Gd and Cd)
for i in range(0,len(Input1)):
   index1a = []; index2a = []; index3a = []
   index1 = []; index2 = []; index3 = []
   energy.append(rawenergies[i])
```

```
maxtab11a.append(peakdet(rawcountstotnorm[i],Input3,energy[i])[0])
for j in range(0,len(maxtab11a[i])):
    if maxtab11a[i][j,0] > 9.40E-02:
        index1a.append(maxtab11a[i][j])
maxtab11.append(index1a)
maxtab33a.append(peakdet(rawcountstotnorm[i],Input3b,energy[i])[0])
for j in range(0,len(maxtab33a[i])):
    if maxtab33a[i][j,0] < 6.00E-02:
        index3a.append(maxtab33a[i][j])
maxtab33.append(index3a)
maxtab = np.concatenate((maxtab11, maxtab33), axis=1)
# Remove low energy peaks to save computational time
for j in range(0,len(maxtab[i])):
    if maxtab[i][j,0] > 3.00E-02 and maxtab[i][j,0] < 7.00E-02:
        index1.append(maxtab[i][j])
    if maxtab[i][j,0] > 9.00E-02:
        index1.append(maxtab[i][j])
maxtab1a.append(index1)
maxtab1 = np.asarray(maxtab1a)
maxtab2.append(index1)
# Add similar values from the lists of maximums
for j in range(0,len(maxtab1[i])):
    for k in range(0,len(maxtab1[i])):
        if j != k and maxtab1[i][j,0] == maxtab1[i][k,0] and maxtab1[i][j,0] not in index2:
            maxtab1[i][j,1] = maxtab1[i][j,1] + maxtab1[i][k,1]
            maxtab2[i][j] = maxtab1[i][j]
            index2.append(maxtab1[i][j,0])
```

```
            index3.append(k)
    # Remove repeated maximums
    index3.sort(); pop = 0
    for k in index3:
        l = k - pop
        maxtab2[0].pop(l)
        pop = pop + 1
    maxtab2 = np.asarray(maxtab2)


#Experimental Data
# ------------------------------------------------------
with Chdir( r"D:\My Documents\Current Work\Hybrid KEdge Densitometry\ORNL REDC HKED Meas Data ORGANIZED\CALIBRATED DATA w ERROR\3-18-2014 New Gd Filter KED XRF"):
    ornlfilename = 'c_z_upu250_red_x_201311151402_1_cnf_calout.txt'
    ornlfile = open(ornlfilename, 'r') # open file for reading
    sepfile = ornlfile.read().split('\n')
    ornlfile.close()
    ornlx = []; ornly = []
    for plotpair in sepfile[:-1]:
        xAndy = plotpair.split(',')
        ornlx.append(float(xAndy[0]))
        ornly.append(float(xAndy[1]))
maxtabORNL = []
ergperchannelexp = (ornlx[-1]-ornlx[1])/(len(ornlx)-1)
# Normalize ORNL results to compare with Simulated
maxtabORNL.append(peakdet(ornly,max(ornly)/1e3,ornlx)[0])
```

```
# ------------------------------------------------------
# Create Offset Curve to correct MCNP x-ray, k-edge energies
# ------------------------------------------------------

#MCNP Outputs for Kalpha1,2 x-rays
Pu = [1.04280000e-01] #, 9.99950000e-02]
U = [9.89360000e-02, 9.50810000e-02]
#Pb = [7.52570000e-02,7.30460000e-02]
W = [5.94950000e-02,5.81350000e-02]
Gd = [4.30730000e-02,4.23730000e-02]
#Xe = [2.97870000e-02,2.94660000e-02]

MCNPOffset = np.concatenate(( Pu, U,  W, Gd))

#Actual Outputs for Kalpha1,2 x-rays
# Reference: http://physics.nist.gov/PhysRefData/XrayTrans/Html/search.html
# Available: July 15, 2015
#NIST Pu239 Theoretical
APu = [1.037354e-01] #, 9.95260e-02]
APuerr = [39e-6,40e-6]
#NIST U238 Theoretical
AU = [9.84336e-02, 9.46531e-02]
AUerr = [36e-6,37e-6]
#NIST Theoretical
APb = [7.49702e-02,7.28066e-02]
```

```
APberr = [24e-6,25e-6]
#NIST Theoretical
AW = [5.93188e-02,5.79819e-02]
AWerr = [17e-6,19e-6]
#NIST Theoretical
AGd = [4.29968e-02,4.23097e-02]
AGderr = [12e-6,13e-6]
#NIST Theoretical
AXe = [2.97783e-02,2.945840000e-02]
AXeerr = [29e-6,30e-6]

OffsettoCheck = np.concatenate((APu, AU, AW, AGd))

# Obtain Experimental Outputs from MaxtabORNL
margin = Input5; ExpOffsettemp = []
for i in range(0,len(Input1)):
    for j in OffsettoCheck:
        ii = 0; chnldownmax, chnlupmax = j - margin, j + margin
        for ii in range(0,len(maxtabORNL[i])):
            if maxtabORNL[i][ii,0] > chnldownmax:
                if maxtabORNL[i][ii,0] < chnlupmax:
                    ExpOffsettemp.append(maxtabORNL[i][ii,0])
ExpOffset = np.asarray(ExpOffsettemp)

Offset = MCNPOffset - ExpOffset
# Change units for Plotting
OffsetkeV = [abs(i*1e3)  for i in Offset]
```

```
OffsetkeV = np.asarray(OffsetkeV)
Offset = np.asarray(Offset)

# calculate polynomial
#z = np.polyfit(MCNPOffset, Offset, 1)
z = np.polyfit(MCNPOffset, Offset, 2)
f = np.poly1d(z)
#eqn = 'y = ' + str(round(z[0],3)) + 'x + ' + str(round(z[1],3))
#eqn = 'y = ' + str(round(z[0],3)) + 'x$^2$ + ' + str(round(z[1],3)) + 'x + ' +
str(round(z[2],3))
#eqnlong = 'y = ' + str(z[0]) + 'x$^2$ + ' + str(z[1]) + 'x + ' + str(z[2])
# calculate trendline
fx = np.linspace(0,MCNPOffset[0],50)
fy = f(fx)

# ----------------------------------------------------
# Begin Run for Voigt Fitting procedure on All Peaks
# ----------------------------------------------------

bkgdcont = [];
xrayguesses = []
shiftedmaxtabs = []
# Parameters to define FWHM for HKED LEGe detectors
a = 7.13334966e-05; b = 0.00128452846
for i in range(0,len(Input1)):
    ergperchannel = (energy[i][-1]-energy[i][0])/len(energy[i])
    xrayguess = [];
```

```
    # Based on offsets from span of elements [Pu,U,Pb,W,Gd,Xe]
    OffsetEqn = z
    for j in range(0,len(maxtab2[i])):
        channeloffset = OffsetEqn[0]*maxtab2[i][j,0]**2 + OffsetEqn[1]*maxtab2[i][j,0] +
OffsetEqn[2]
        #channeloffset = OffsetEqn[0]*maxtab2[i][j,0] + OffsetEqn[1]
        shiftedmaxtab = maxtab2[i][j,0] - channeloffset
        shiftedmaxtabs.append(shiftedmaxtab)
        xrayguess.append(( a + b * math.sqrt(maxtab2[i][j,0]), shiftedmaxtab,
maxtab2[i][j,1] )) #fwhm, energy, intensity

    xrayguesses.append(xrayguess)

# ---------------------------------------------------------
# Determine background continuum from Raw Data, Using different Continuums before
and after 90 keV
# ---------------------------------------------------------

    yback1 = []; yback2 = []; fwhm = 45;
    continuum1 = rawcountstotnorm[i] # snipbg(bkgdcontnorm[i], yback2, len(energy[i]),
0, Input14, fwhm, Input4c-10) #
    continuum2 = snipbg(bkgdcontnorm[i], yback2, len(energy[i]), 0, Input14, fwhm,
Input4c-10)
    #Normalize snip background to ensure continuous backgroun when combined with
continuum1
    continuum2 = [ii * continuum1[4800]/continuum2[4800] for ii in continuum2]
    continuum = continuum1[:4800] + continuum2[4800:]
```

```
    bkgdcont.append(continuum)


# ------------------------------------------------------
# Shift on Individual peaks to Offset MCNP Data Error
# ------------------------------------------------------
# Develop hard code for correct peak locations based exactly off of Experimental Results
sigpeakloc = []
for i in range(0,len(Input1)):
    for j in range(0,len(xrayguesses[i])):
        for k in ExpOffset: #OffsettoCheck
            if xrayguesses[i][j][1] > k - Input5 and xrayguesses[i][j][1] < k + Input5:
                loc = (k,j)
                sigpeakloc.append(loc)
for i in range(0,len(Input1)):
    for j in sigpeakloc:
        xrayguesses[i][j[1]] = (xrayguesses[i][j[1]][0],j[0],xrayguesses[i][j[1]][2])


Numchannels = Input14
plottempfit = []; normplottempfit = [];
notailsplottempfit = []; notailsnormplottempfit = []
peakarea = []; peakareabkgd = []
# Natural Line Widths from
# Reference: Croft, S., McElroy, R., "On the Relationship between the Natural Line Width and Lifetime of X-ray Transitions," 2015 INMM Annual Conference, Indian Wells, CA.
lor_table = [(0.0, 90888.8e-6, 25e-6), (90888.8e-6, 93347.9e-6, 91.91e-6), (93347.9e-6, 95864.8e-6, 95.94e-6), \
```

```
   (95864.8e-6, 98433.6e-6, 100.07e-6), (98433.6e-6, 101057.3e-6, 104.5e-6),
(101057.3e-6, 103735.4e-6, 108.93e-6), \
   (103735.4e-6, 106470.4e-6, 113.06e-6), (106470.4e-6, 109263.1e-6, 117.09e-6),
(109263.1e-6, 200000.0e-6, 121.11e-6)]

# ------------------------------------------------------
# Run Czosnyka and Tails Definitions on individual peaks
# ------------------------------------------------------

for i in range(0,len(Input1)):
   tempfit = [0] * Numchannels; normtempfit = [0] * Numchannels; formfactor = [];
   for j in range(0,len(xrayguesses[i])):
      ptry = np.asarray(xrayguesses[i][j])
      for r in lor_table:
         if ptry[1] > r[0] and ptry[1] < r[1]:
            lor_width = r[2]
      temp = czosnyka(energy[i],ptry,lor_width,Input9)
#czosnyka(calibenergy[i],best_parameters,Input9[i][j])
      print('working... ', len(Input1) - i, len(xrayguesses[i]) - j)
      normtemp = [jj*ptry[2]*Input8/max(temp) for jj in temp]
      #tailnorm = max(normtemp)
      #temp2 = tails(energy[i],ptry) #tails(calibenergy[i],best_parameters)
      #normtemp2 = [m * n  for m,n in zip(normtemp, temp2)]

      #notailstempfit = [tempi + newtemp  for tempi, newtemp in zip(tempfit, temp)]
      #notailsnormtempfit = [tempi + newtemp  for tempi, newtemp in zip(normtempfit,
normtemp)]
```

```
        tempfit = [tempi + newtemp  for tempi, newtemp in zip(tempfit, temp)]
        normtempfit = [tempi + newtemp  for tempi, newtemp in zip(normtempfit, normtemp)]

    plottempfit.append( tempfit )
    normplottempfit.append( normtempfit )
    #notailsplottempfit.append( notailstempfit )
    #notailsnormplottempfit.append( notailsnormtempfit )

# Combine Broadened Peaks with Continuum
combine1plottotal = []
for i in range(0,len(Input1)):
    combine1plottotal.append( [bkgdi + voigti for bkgdi, voigti in zip(bkgdcont[i], normplottempfit[i])] )

# ------------------------------------------------------
# Include PulsePileup
# ------------------------------------------------------

pulsepileup = []; gate = 0.75E-8 # 0.25 #
for itr in range(0,len(Input1)):
    ppup = []
    for i in range(0,len(combine1plottotal[itr])):
        pptemp = 0
        for j in range(0,len(combine1plottotal[itr])):
            if j > i: break
            if i - j < 1: continue
```

```
            pptemp = pptemp + combine1plottotal[itr][j] * combine1plottotal[itr][i - j] * gate
        ppup.append( pptemp )
    pulsepileup.append( ppup )

plottotal = []; plottotalnorm = []
for i in range(0,len(Input1)):
    plottotal.append( [ppi + toti for ppi, toti in zip(pulsepileup[i], combine1plottotal[i])] )
    plottotalnorm.append([ii*Norm/max(plottotal[i][4200:4300]) for ii in plottotal[i]])
ornlynorm = [ii*Norm/max(ornly[1050:1070]) for ii in ornly]

# ------------------------------------------------------
# Peak Compare
# ------------------------------------------------------
# Uranium Kalpha1 Peak
AU = 9.84336e-02

maxtab_sim = []; maxtab_exp = []
# Simulation
maxtab_sim.append(peakdet(plottotalnorm[0],Input3,energy[0])[0])
# Experiment
maxtab_exp.append(peakdet(ornlynorm,max(ornlynorm)/1e3,ornlx)[0])
for i in maxtab_sim[0]:
    if i[0] > AU - Input5 and i[0] < AU + Input5:
        ukalpha1_sim = i[0]
# Experimental UKalpha1
for i in maxtab_exp[0]:
    if i[0] > AU - Input5 and i[0] < AU + Input5:
```

```
        ukalpha1_exp = i[0]


simlocation =  ukalpha1_sim # AU #
explocation =  ukalpha1_exp # AU #
FWHMUsim = a + b * np.sqrt(simlocation)
FWHMUexp = a + b * np.sqrt(explocation)
 # optimum window around the peak is 1.1 times the FWHM on either side * Ottmar Eberle Princ HKED
size = 1.1


upeakerg = []; upeakareatemp = []; itr = 0
for i in energy[0]:
    if i > simlocation-size*FWHMUsim and i < simlocation+size*FWHMUsim:
        upeakerg.append(i)
        upeakareatemp.append(plottotalnorm[0][itr])
    itr = itr + 1
upeakarea1 = trapz(upeakareatemp, dx=ergperchannel)
upeakarea2 = simps(upeakareatemp, dx=ergperchannel)


upeakexperg = []; upeakareaexptemp = []; itr = 0
for i in ornlx:
    if i > explocation-size*FWHMUexp and i < explocation+size*FWHMUexp:
        upeakexperg.append(i)
        upeakareaexptemp.append(ornlynorm[itr])
    itr = itr + 1
upeakareaexp1 = trapz(upeakareaexptemp, dx=ergperchannelexp)
upeakareaexp2 = simps(upeakareaexptemp, dx=ergperchannelexp)
```

```
#print('The ratio of UK$alpha_1$ peaks from Experiment and MCNP is =', (upeakarea2-upeakareaexp2)/upeakareaexp2)
print(upeakarea2, upeakareaexp2, 'Ratio =', (upeakarea2-upeakareaexp2)/upeakareaexp2, 'Error =', (upeakareaexp1 - upeakareaexp2))
sumu = 0
for u in upeakareatemp:
    sumu = sumu + u*ergperchannel
print(upeakarea2, 'Error =',sumu - upeakarea2)



# Plutonium Kalpha1 Peak
APu = [1.037354e-01]
FWHMPu = a + b * np.sqrt(APu)
 # optimum window around the peak is 1.1 times the FWHM on either side * Ottmar Eberle Princ HKED

Pupeakerg = []; Pupeakareatemp = []; itr = 0
for i in energy[0]:
    if i > APu-size*FWHMPu and i < APu+size*FWHMPu:
        Pupeakerg.append(i)
        Pupeakareatemp.append(plottotalnorm[0][itr])
    itr = itr + 1
Pupeakarea1 = trapz(Pupeakareatemp, dx=ergperchannel)
Pupeakarea2 = simps(Pupeakareatemp, dx=ergperchannel)

Pupeakexperg = []; Pupeakareaexptemp = []; itr = 0
```

```
for i in ornlx:
    if i > APu-size*FWHMPu and i < APu+size*FWHMPu:
        Pupeakexperg.append(i)
        Pupeakareaexptemp.append(ornlynorm[itr])
    itr = itr + 1
Pupeakareaexp1 = trapz(Pupeakareaexptemp, dx=ergperchannelexp)
Pupeakareaexp2 = simps(Pupeakareaexptemp, dx=ergperchannelexp)

#print('The ratio of PuK$alpha_1$ peaks from Experiment and MCNP is =',(Pupeakarea2-Pupeakareaexp2)/Pupeakareaexp2)
print(Pupeakarea2, Pupeakareaexp2, 'Ratio =',(Pupeakarea2-Pupeakareaexp2)/Pupeakareaexp2, 'Error =', (Pupeakareaexp1 - Pupeakareaexp2))
sumpu = 0
for pu in Pupeakareatemp:
    sumpu = sumpu + pu*ergperchannel
print(Pupeakarea2, 'Ratio =',sumpu - Pupeakarea2)



# ------------------------------------------------------
# Plotting
# ------------------------------------------------------

# Chop down size of simulated from 8192 to 2024 to compare channel to channel with experimental
plottotalchop = []; itr = 0; n = 0
for i in plottotalnorm[0]:
    itr = itr + i
```

```
    if n > 3:
        plottotalchop.append(itr)
        n = 0; itr = 0
    n = n + 1
plottotalchop.append(0)
plottotalchop.insert(0,0)
plottotalchopnorm = [ii*Norm/max(plottotalchop[1050:1075]) for ii in plottotalchop]
#ornlynorm = [ii*max(plottotalchop[1050:1075])/max(ornly[1050:1070]) for ii in ornly]

rawcountschop = []; itr = 0; n = 0
for i in rawcountstot[0]:
    itr = itr + i
    if n > 3:
        rawcountschop.append(itr)
        n = 0; itr = 0
    n = n + 1
rawcountschop.append(0)
rawcountschop.insert(0,0)
rawcountschopnorm = [ii*Norm/max(rawcountschop[1050:1075]) for ii in
rawcountschop]
#ornlynormraw = [ii*max(rawcountschop[1050:1075])/max(ornly[1050:1070]) for ii in
ornly]

chopenergy = list(energy[0])
chopenergy.insert(0,0)
chopenergy = chopenergy[::4]
```

```
x = range(0,2048)
xx = range(0,8188)

## RESIDUAL PLOT
fig1 = figure(1)
#Plot Data-model
frame1=fig1.add_axes((.1,.325,.8,.6))
l1, l2 = frame1.plot(ornlx, ornlynorm, '.k', chopenergy, plottotalchopnorm, 'k-')
fig1.set_facecolor('white')
#frame1.set_xlabel('Energy [MeV]')
frame1.set_ylabel('Relative Counts')
#frame1.set_xticklabels([]) #Remove x-tic labels for the first frame
frame1.set_ylim([1e0,1e5])
frame1.set_xlim([.090,.125])
#frame1.set_xlim([.025,.15])
frame1.set_yscale('log')
fig1.legend((l1, l2),('ORNL Measured','MCNP Simulated'), 'upper center')
plt.show()
#Residual plot
rawcountsres = np.array(ornlynorm)
normplottempfitres = np.array(plottotalchopnorm)
rcresdiff = np.array([math.sqrt(i) for i in rawcountsres])
#nptfresdiff = np.array([math.sqrt(i) for i in normplottempfitres])
#diff = rcresdiff - nptfresdiff
diff = [i - j for i,j in zip(rawcountsres,normplottempfitres)]
difference = [i/j for i,j in zip(diff,rcresdiff)]
```

```
frame2=fig1.add_axes((.1,.1,.8,.2))
#frame2.set_xlim([1150,1600])
frame2.set_xlim([0.090,.125])
#frame2.set_xlim([.025,.15])
frame2.set_ylim([-20,20])
frame2.set_xlabel('Energy [MeV]')
frame2.set_ylabel('Residual [$\sigma$]')
#frame2.set_yscale('log')
zeros = [0]*len(chopenergy)
plot(chopenergy,difference,'.k',chopenergy,zeros,'k--')
```

APPENDIX D

ANALOG MCNP RUNS FOR SOURCE AND SPECTRA

This appendix contains the analog source runs in MCNP to recreate the x-ray tube spectra, as well as the XRF and KED branch results for simulations without any variance reduction.

The MCNP code was used to recreate the x-ray tube spectrum for the HKED system to be used as the source term for the sample investigation simulations. However, the MCNP simulated x-ray tube spectra from a tungsten anode with or without filers was determined to be a poor representation of the actual spectral results. Therefore, a separate tool for generating tungsten anode x-ray tube spectra was used to generate the source term. The SpekCalc program was utilized for calculation of the x-ray spectra from the tungsten anode x-ray tube [87]. SpekCalc was chosen as a very fast, accurate means of generating the x-ray source spectral profile that could simply be formatted into the MCNP source term definition. Figure D.1 shows the comparison between the simulated x-ray tube spectra for the HKED system and the approximate results from a separate published result for the HKED system x-ray tube spectra [73]. Additionally, the results from the SpekCalc x-ray spectrum generating software is compared and is shown to match the published results better [87].

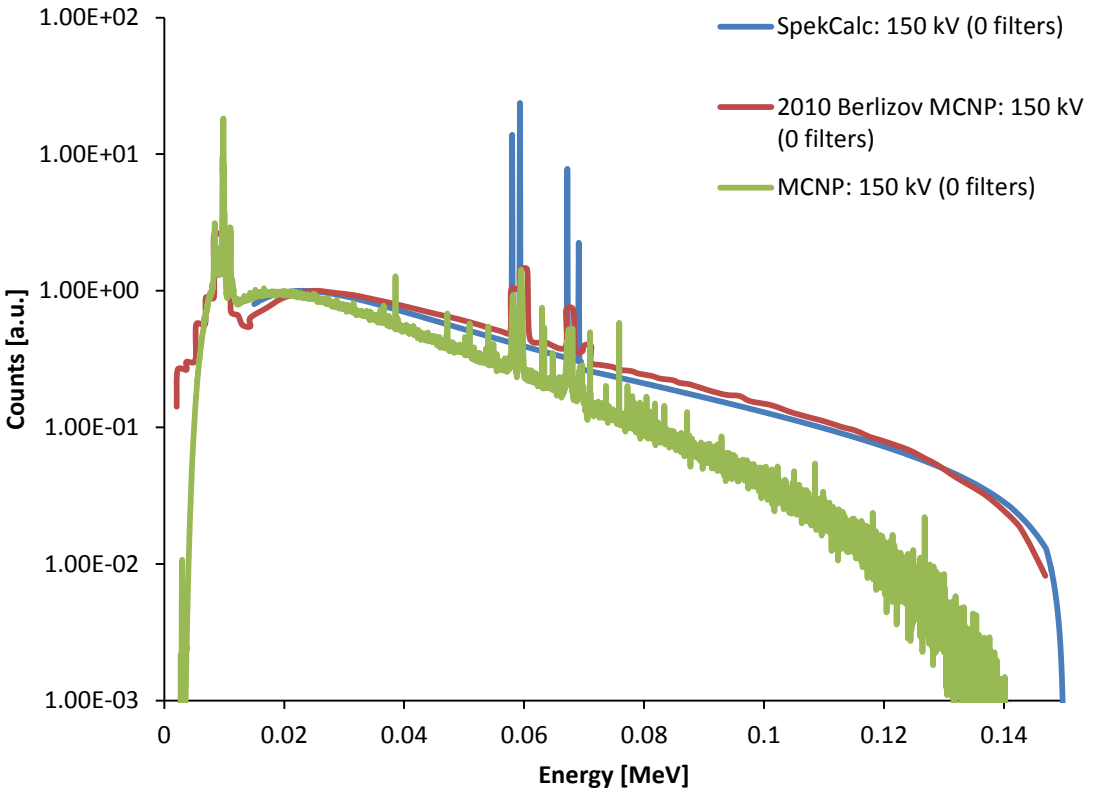

Figure D.1. Comparison plot between simulated HKED x-ray tube spectral results with a voltage of 150 kV and no filters and a similar x-ray tube spectral result from a Berlizov [73] as well as SpekCalc [87].

The simulated MCNP x-ray spectrum was also compared to published values by Ay et. al. for an x-ray tube at 140 kV with several filters: 1 mm of beryllium, 2.5 mm of aluminum, 0.1 mm of copper, and 100 mm of air [84].

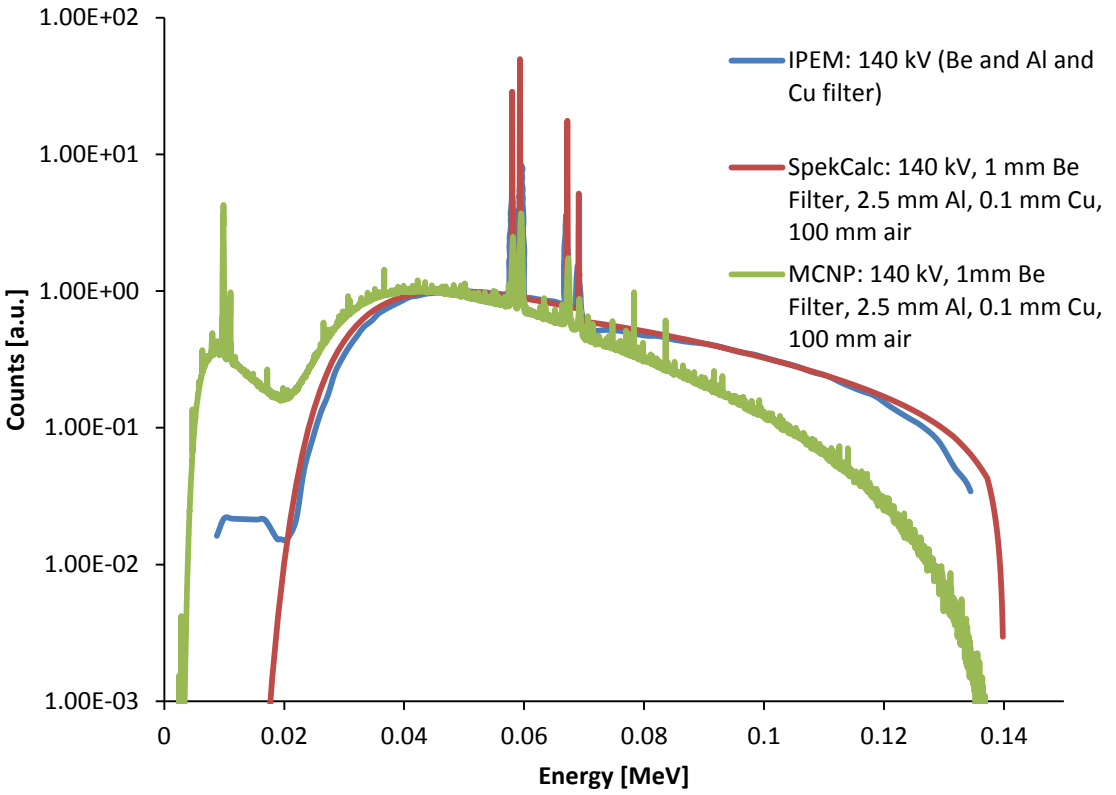

Figure D.2. Comparison plot between simulated HKED x-ray tube spectral results with a voltage of 140 kV and several filters and a similar x-ray tube spectral result from Ay et. al. [84]as well as SpekCalc [87].

Analog runs of the MCNP results for the XRF and KED branches were simulated in order to determine if any biases were introduced into the results when applying variance reduction techniques. The analog results for the KED branch matched extremely well to those results generated using variance reduction, shown in Figure D.3. However, due to the extremely limited x-ray current directed towards the XRF detector, the month long analog run for the XRF branch did not resolve into useful results as shown in Figure D.4. Thus the analog runs for the XRF branch were only used as a proof of concept result to show that the variance reduction approach can successfully overcome the computational difficulty of simulating this radiation transport.

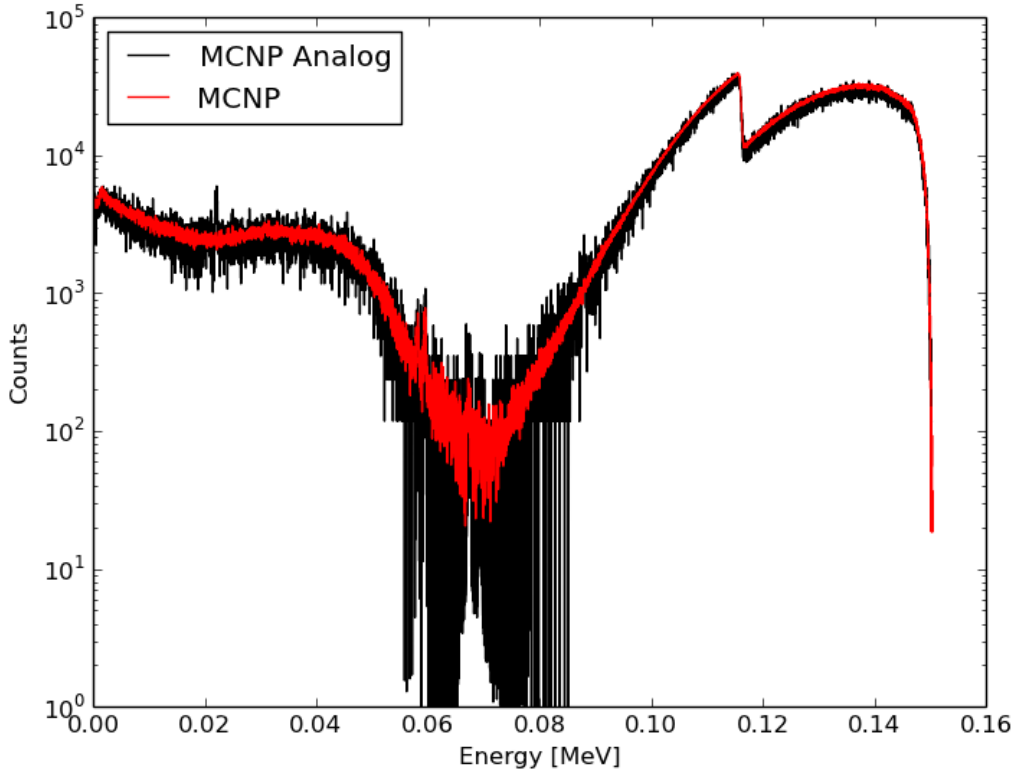

Figure D.3. Simulated HKED KED spectral results with MCNP analog results compared to MCNP results with variance reduction methods applied for a nitric acid based uranium sample with approximately 268.21 g U/L.

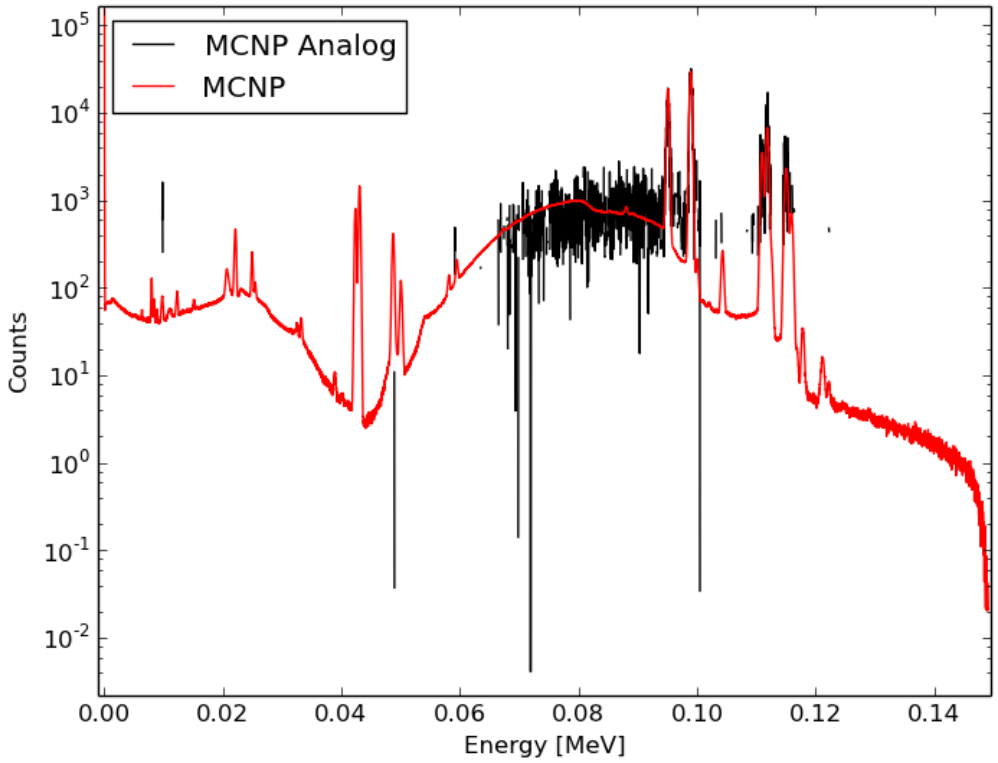

Figure D.4. Simulated HKED XRF spectral results with MCNP analog results compared to MCNP results with the variance reduction methods applied for a uranium-plutonium sample with approximately 243 g U/L and 2.93 g Pu/L nitric acid based sample.

REFERENCES

1. Cook, M.T., et al. *Current and Future State of Pyrochemical Reprocessing for Spent Nuclear Fuel*. in *54th Annual Institute of Nuclear Materials Management Meeting*. 2013. Palm Desert, CA.
2. World Nuclear Association. *Processing of Used Nuclear Fuel*. 2013 [cited 2013 July 29]; Available from: http://www.world-nuclear.org/info/Nuclear-Fuel-Cycle/Fuel-Recycling/Processing-of-Used-Nuclear-Fuel/.
3. Cipiti, B.B., et al., *Modeling and Design of Integrated Safeguards and Security for an Electrochemical Reprocessing Facility*. 2012, Sandia National Laboratories: Albuquerque.
4. Laidler, J.J., et al., *Development of pyroprocessing technology.* Progress in Nuclear Energy, 1997. **31**(1–2): p. 131-140.
5. Williamson, M.A. and J.L. Willit, *Pyroprocessing Flowsheets for Recycling Used Nuclear Fuel.* Nuclear Engineering and Technology, 2011. **43**(4): p. 329-334.
6. International Atomic Energy Agency, *Assessment of Partitioning Processes for Transmutation of Actinides*. 2010, International Atomic Energy Agency: Vienna.
7. Bean, R., *Project Report on Development of a Safeguards Approach for Pyroprocessing*, Idaho National Laboratory, Editor. 2010, Idaho National Laboratory: Idaho Falls.
8. Song, K., et al., *Status of Pyroprocessing Technology Development in Korea.* Nuclear Engineering and Technology, 2010. **42**(2): p. 131-144.
9. *OECD/NEA, Pyrochemical separations in nuclear applications, A Status Report, ISBN 92-64-02071-3 (2004).*
10. *Strategy of Nuclear Power Development in Russia in the First Half of the 21st Century, Ministry of Russian Federation for Atomic Energy, Summary, Moscow (2000).*
11. Phongikaroon, S. *Development of New Chemical Engineering Applications in Pyroprocessing Technology*. 2010; Available from: http://www.if.uidaho.edu/~phonst/research.html.
12. Yoo, J.H., et al., *A Conceptual Study of Pyroprocessing for Recovering Actinides from Spent Oxide Fuels.* Nuclear Engineering and Technology, 2008. **40**(7): p. 581-592.
13. Herrmann, S., S. Li, and M.F. Simpson, *Electrlytic Rduction of Spent Light Water Reactor Fuel.* Journal of Nuclear Science and Technology, 2007. **44**(3): p. 361-367.
14. Lee, S.Y., et al., *A Preliminary Study on the Safeguardability of A Korean Advanced Pyroprocessing Facility (KAPF)*, in *International Conference on Advanced Nuclear Fuel Cycles and Systems*. 2007. p. 362-371
15. Till, C.E. and Y.I. Chang, *Plentiful Energy: The Story of the Integral Fast Reactor*. 2011: CreateSpace Independent Publishing Platform
16. Abousahl, S., et al., *Development of quantitative analytical methods for the control of actinides in a pyrochmeical partitioning process.* Radiochimica Acta, 2005. **93**: p. 147-153.

17. Hamilton, L., et al., *Blue Ribbon Commission on America's Nuclear Future: Report to the Secretary of Energy.* Blue Ribbon Commission on America's Nuclear Future (BRC), Washington, DC, 2012.
18. *World Nuclear Association. (2015). Nuclear Power in Russia. Available: http://www.world-nuclear.org/info/Country-Profiles/Countries-O-S/Russia--Nuclear-Power/.*
19. *World Nuclear Association. (2015). Nuclear Power in China. Available: http://www.world-nuclear.org/info/Country-Profiles/Countries-A-F/China--Nuclear-Power/*
20. *Hecker, S., Braun, C. et. al., Nuclear Energy and Nuclear Security in the Republic of Korea. Center for International Security and Cooperation, p. 25, Dec. 2013. .*
21. *Nuclear regulators overwhelmed as China races to lauch worlds most powerful reactor. Bloomberg News. Available: http://www.bloomberg.com/news/2014-06-18/french-nuclear-regulator-says-china-cooperation-lacking.html, 2014. .*
22. *Jun Bong-Geun, The ROK-US Nuclear Partnership for the Peaceful Use and Nonproliferation, EAI-CSIS Workship on US-ROK Cooperation for Global Nuclear Governance, 16 Nov. 2012. .*
23. *Agreement for Cooperation between the Government of the United States of America and the Government of the Republic of Korea Concerning Civil Uses of Atomic Energy. Available: http://nnsa.energy.gov/sites/default/files/nnsa/05-13-multiplefiles/2013-05-02%20Korea_South_123.pdf.*
24. Durst, P.C., et al., *Advanced Safeguards Approaches for New Reprocessing Facilities*. 2007, Pacific Northwest National Laboratory: Richland.
25. Cipiti, B.B., *Separations and Safeguards Performance Modeling for Advanced Reprocessing Facility Design.* Journal of Nuclear Materials Management, 2011. **39**(2): p. 4-14.
26. Willit, J., W. Miller, and J. Battles, *Electrorefining of uranium and plutonium—a literature review.* Journal of nuclear materials, 1992. **195**(3): p. 229-249.
27. Itoh, T., et al. *Enhanced Cooperation between SSAC and IAEA through Joint Operation of On Site Laboratory for Safeguarding Rokkasho Reprocessing Plant*. in *41st Annual Meeting of the Institute of Nuclear Materials Management*. 2000.
28. Bari, R., et al. *Pyroprocessing, UREX and PUREX*. in *AAAS Workshop on Game-Changing Nuclear Technologies*. 2010.
29. Han, B.Y., et al. *Analysis of Material Unaccounted For Uncertainty for the Reference Pyroprocessing Facility*. in *51st Annual Meeting of the Institute of Nuclear Materials Management*. 2010. Baltimore, MD.
30. Han, B.Y., H.S. Shin, and H.D. Kim. *Evaluation of Material Unaccounted for Reference Pyropocessing Facility Model*. in *52nd Annual Meeting of the Institute of Nuclear Materials Management (INMM)*. 2011. Palm Desert, CA.
31. Kim, H.D., et al. *Application of Safeguards-by-Design for the Pyroprocessing Facilities in ROK*. in *53rd Annual Meeting of the Institute of Nuclear Materials Management*. 2012. Orlando, FL.
32. Pellechi, M., et al. *Inherent Challenges in Safeguading Pyroprocessing R&D, Demonstration and Commercial Facilities*. in *52nd Annual Meeting of the Institute of Nuclear Materials Management (INMM)*. 2011. Palm Desert, CA.

33. Shin, H.S., et al. *Development of a Simulation Program for the Pyroprocessing Material Flow and MUF Uncertainty*. in *52nd Annual Meeting of the Institute of Nuclear Materials Management (INMM)*. 2011. Palm Desert, CA.
34. Shin, H.S., et al. *Progress of a Member State Support Program (MSSP) for the Development of a Safeguards Approach for a Pyroprocessing Facility*. in *51st Annual Meeting of the Institute of Nuclear Materials Management*. 2010. Baltimore, MD.
35. Han, B.-Y., H.-S. Shin, and H.-D. Kim, *Analysis of Measurement Uncertainty of Material Unaccounted for in the Reference Pyroprocessing Facility.* Nuclear Technology, 2013. **182**(3): p. 369-377.
36. Schwalbach, P., et al. *The EURATOM Safeguards On-Site Laboratories at the Reprocessing Plants of La Hague and Sellafield - Ten Years of Operation*. in *Symposium on International Safeguards: Preparing for Future Verification Challenges* 2010. Vienna.
37. Texas A&M University. *Nuclear and Non-Nuclear Material: Basic Terms*. 2013; Available from: http://nsspi.tamu.edu/nsep/reference-modules/technical-safeguards-terminology/nuclear-and-non-nuclear-material-basic-terms/.
38. Bjornard, T., et al. *Safeguards-by-Design: Early Integration of Physical Protection and Safeguardability into Design of Nuclear Facilities*. in *Proceedings of GLOBAL*. 2009.
39. Kim, H.D. *Development of Safeguards Approach for Reference Engineering-scale Pyroprocessing facility*. in *2012 International Pyroprocessing Research Conference*. 2012. August 26-29, The Abbey Resort.
40. Bychkov, A. and O. Skiba, *Review of non-aqueous nuclear fuel reprocessing and separation methods*, in *Chemical Separation Technologies and Related Methods of Nuclear Waste Management*. 1999, Springer. p. 71-98.
41. International Atomic Energy Agency, *The Structure and Content of Agreements between the Agency and States Required in Connection with the Treaty on the Non-Proliferation of Nuclear Weapons*, in *INFCIRC 153 (corrected)*, International Atomic Energy Agency, Editor. 1972.
42. *IAEA Department of Safeguards Long-Term R&D Plan, 2012-2023*. 2013, International Atomic Energy Agency.
43. *Development and Implementation Support Pragromme for Nuclear Verification 2014-2015*. International Atomic Energy Agency, STR-377, 2013.
44. Garcia, H.E., et al., *Detecting Proliferation Activities via System-centric Integration and Interpretation of Multi-Modal Data Collected from a System of Sensors.* Proceedings of the 54th Annual INMM Meeting, Palm Desert, July 14-18, 2013
45. Gauld, I., *Strategies for application of isotopic uncertainties in burnup credit.* ORNL/TM-2001/257, Oak Ridge National Laboratory, 2003.
46. Borrelli, R., *Use of curium spontaneous fission neutrons for safeguardability of remotely-handled nuclear facilities: Fuel fabrication in pyroprocessing.* Nuclear Engineering and Design, 2013. **260**: p. 64-77.
47. Miura, N. and H. Menlove, *The use of curium neutrons to verify plutonium in spent fuel and reprocessing wastes*. 1994, Los Alamos National Lab., NM (United States).

48. Rinard, P. and H. Menlove, *Application of curium measurements for safeguarding at reprocessing plants. Study 1: High-level liquid waste and Study 2: Spent fuel assemblies and leached hulls*. 1996, Los Alamos National Lab., NM (United States).
49. Rinard, P. and H. Menlove, *Applications of curium measurements for safeguarding at large-scale reprocessing plants*. 1997, Los Alamos National Lab., NM (United States).
50. Mariani, R.D. and D. Vaden, *Modeled salt density for nuclear material estimation in the treatment of spent nuclear fuel.* Journal of Nuclear Materials, 2010. **404**(1): p. 25-32.
51. Vaden, D., et al., *Engineering-scale liquid cadmium cathode experiments.* Nuclear Technology, 2008. **162**(2): p. 124.
52. Abousahl, S., et al., *Development of quantitative analytical methods for the control of actinides in a pyrochemical partitioning process.* Radiochimica Acta, 2005. **93**(3): p. 147-153.
53. Koyama, T.J., T. R.; Fischer, D. F., *Distribution of Actinides in Molten Chloride Salt/Cadmium Metal Systems.* Journal of Alloys and Compounds, 1992. **189**: p. 37-44.
54. Ackerman, J.P. and J.L. Settle, *Distribution of plutonium, americium, and several rare earth fission product elements between liquid cadmium and LiCl-KCl eutectic.* Journal of alloys and compounds, 1993. **199**(1): p. 77-84.
55. Zhang, J., *Electrochemistry of actinides and fission products in molten salts-data review.* Journal of Nuclear Materials, 2014. **447**: p. 271-284.
56. Till, C.E. and Y.I. Chang, *Plentiful energy: the story of the integral fast reactor*. 2011.
57. Li, S.X., S.D. Herrmann, and M.F. Simpson, *Electrochemical analysis of actinides and rare earth constituents in liquid cadmium cathode product from spent fuel electrorefining.* Nuclear technology, 2010. **171**(3): p. 292-299.
58. Li, S.X., et al., *Actinide recovery experiments with bench-scale liquid cadmium cathode in real fission product-laden molten salt.* Nuclear technology, 2009. **165**(2): p. 190-199.
59. Osipenko, A., et al., *Electrochemical behaviour of curium (III) ions in fused 3LiCl–2KCl eutectic.* Journal of Electroanalytical Chemistry, 2011. **651**(1): p. 67-71.
60. Lee, T., et al., *Determination of Pu content of U/TRU ingot of pyroprocessing using passive neutron albedo reactivity technique*, in *53rd Annual Meeting of Institute of Nuclear Materials Management*. 2012. p. 3444.
61. Sanders, J., *Status of Activities to Implement a Sustainable System of MC&A Equipment and Methodological Support at Rosatom Facilities*. 2010, Idaho National Laboratory (INL).
62. Bean, R., *Project Report on Development of a Safeguards Approach for Pyroprocessing*, in *INL/EXT-10-20057*. Idaho National Laboratory, 2010.
63. Casteleyn, K. and L. Duinslaeger, *The Euratom Safeguards On-Site Laboratories at the Reprocessing Plants of La Hague and Sellafield*, in *JRC Reference Reports*, JRC-ITU, Editor. 2010, Joint Research Center - Institute for Transuranium Elements: Karlsruhe.

64. Ottmar, H., et al. *Demonstration of Measurement Technollogies for Neptunium and Amercium Verification in Reprocessing*. in *Symposium on International Safeguards: Verification and Nuclear Material Security*. 2001. Vienna: International Atomic Energy Agency.
65. Kessler, G., *Proliferation-Proof Uranium/Plutonium Fuel Cycles*, ed. K.I.f. Technologie. 2011, Karlsruhe.
66. Blohm-Hieber, U., et al. *Hybrid K-Edge Densitometer - More than 10 Years of EURATOM Safeguards Exerpeince*. in *39th Annual Meeting of the Institute of Nuclear Materials Management*. 1998.
67. Thorton, A., et al. *Reintroduction of Hybrid K=Edge Densitometry to United States Fuel Reprocessing Facilities*. in *49th Annual Meeting of the Institute of Nuclear Materials Management*. 2008.
68. Cipiti, B.B., *Advanced Instrumentation for Reprocessing*, Sandia National Laboratories, Editor. 2005, Sandia National Laboratories: Albuquerque.
69. Zendel, M., et al., *Nuclear Safeguards Verification Measurement Techniques*, in *Handbook of Nuclear Chemistry*, A. Vértes, et al., Editors. 2011, Springer US. p. 2893-3015.
70. Canberra Industries. *Hybrid K-Edge/XRF Analyzer*. 2008; Available from: http://www.canberra.com/products/waste_safeguard_systems/pdf/Hybrid-KEdge-SS-M3849.pdf.
71. EURATOM, M.M.B. and M.G. Renha Jr, *International Target Values 2010 for Measurement Uncertainties in Safeguarding Nuclear Materials.* 2010.
72. Ottmar, H., et al. *Demonstration of measurement technologies for neptunium and americium verification in reprocessing*. in *International Safeguards Verification and Nuclear Material Security (Proc. Int. Symp. Vienna, 2001), IAEA, Vienna*. 2001.
73. Berlizov, A.N., et al., *A quantitative Monte Carlo modelling of the uranium and plutonium X-ray fluorescence (XRF) response from a hybrid K-edge/K-XRF densitometer.* Nuclear Instruments and Methods in Physics Research Section A: Accelerators, Spectrometers, Detectors and Associated Equipment, 2010. **615**(1): p. 127-135.
74. Simpson, M.F., et al. *Management of salt waste from electrochemical processing of used nuclear fuel*. in *Global 2013 International Nuclear Fuel Cycle Conference in Salt Lake City, Utah, USA*. 2013.
75. Nuclear Energy Agency, *Spent Nuclear Fuel Reprocessing Flowsheet*. 2012, OECD.
76. Collins, M., N. Doubek, and H. Ottmar. *Fitting of Germanium X-Ray Escape Peaks in Hybrid Densitometer X-Ray Fluorescence Spectra*. in *48th Annual Meeting of the Institute of Nuclear Materials Management (INMM)*. 2007.
77. Bosko, A., S. Philips, and M. Villani. *Application of Multi-Elemental K-Edge Densitometry to MOX Solutions at a Commercial Plant Using a New Hybrid K-Edge Densitometry (HKED) Software Package*. in *53rd Annual Meeting of the Institute of Nuclear Materials Management*. 2012. Orlando, FL.
78. McElroy, R.D., et al. *Spectral Fitting Approach to the Hybrid K-Edge Densitometer: Preliminary Performance Results*. in *56th Annual INMM Meeting*. 2015. Indian Wells, CA.

79. Brown, F., *MCNP-a general Monte Carlo N-particle transport code, version 5 Report LA-UR-03-1987.* Los Alamos, NM: Los Alamos National Laboratory, 2003.
80. Pelowitz, D.B., *MCNP6 User's Manual*. 2013.
81. Ottmar, H. and H. Eberle, *The Hybrid K-Edge/K-XRF Densitometer: Principles - Design - Performance*. 1991: Kernforschungszentrum Karlsruhe.
82. Reilly, D., et al., *Passive nondestructive assay of nuclear materials*. 1991, Nuclear Regulatory Commission, Washington, DC (United States). Office of Nuclear Regulatory Research; Los Alamos National Lab., NM (United States).
83. B. Chyba, et al., *Calculation Methods of X-ray Spectra: A Comparative Study.* International Centre for Diffraction Data, 2010.
84. Ay, M., et al., *Monte Carlo simulation of x-ray spectra in diagnostic radiology and mammography using MCNP4C.* Physics in medicine and biology, 2004. **49**(21): p. 4897.
85. Ebel, H., *Fundamental Parameter Programs: Algorithms for the Description of K, L, and M Spectra of X-ray Tubes.* International Centre for Diffraction Data, 2006.
86. Bhat, M., et al., *Diagnostic x-ray spectra: A comparison of spectra generated by different computational methods with a measured spectrum.* Medical physics, 1998. **25**(1): p. 114-120.
87. Poludniowski, G., et al., *SpekCalc: a program to calculate photon spectra from tungsten anode x-ray tubes.* Physics in medicine and biology, 2009. **54**(19): p. N433.
88. Hughes III, H.G., *Recent developments in low-energy electron/photon transport for MCNP6*. 2012, Los Alamos National Laboratory (LANL).
89. Everett, C. and E. Cashwell, *MCP code fluorescence-routine revision.* 1973(LA-5240-MS).
90. Berlizov, A.N., et al., *Comprehensive modelling of the hybrid K-edge/K-XRF measurements of actinide solutions: development and experimental validation of a dedicated software program*, in *33rd Annual ESARDA Meeting*. 2011: Budapest, Hungary.
91. Canberra, *Low Energy Germanium Detector (LEGe)*, in *C39331 – 11/12*. 2012.
92. Knoll, G.F., *Radiation detection and measurement*. 2010: John Wiley & Sons.
93. McElroy, R.D., *Preliminary Performance Results for a Hybrid K-Edge Densitometer (HKED) Installed at the Radiochemical Engineering Development Center (REDC)*, in *53rd Annual Meeting of the Institute of Nuclear Materials Management* 2012: Orlando, FL. p. 1237.
94. Deslattes, R.D., et al., *X-ray Transition Energies (version 1.2)*. 2005, National Institute of Standards and Technology, Gaithersburg, MD.: [Online] Available: http://physics.nist.gov/XrayTrans [2015, May 15].
95. Van Grieken, R. and A. Markowicz, *Handbook of X-ray Spectrometry*. 2001: CRC Press.
96. Sanner, M.F., *Python: a programming language for software integration and development.* J Mol Graph Model, 1999. **17**(1): p. 57-61.
97. Savitzky, A. and M.J. Golay, *Smoothing and differentiation of data by simplified least squares procedures.* Analytical chemistry, 1964. **36**(8): p. 1627-1639.

98. Czosnyka, T. and A. Trzcińska, *Unified analytical approximation of Gaussian and Voigtian lineshapes.* Nuclear Instruments and Methods in Physics Research Section A: Accelerators, Spectrometers, Detectors and Associated Equipment, 1999. **431**(3): p. 548-550.
99. F. J. Schreier, Q.S.R.T., 1992. .
100. J. L. Campbell, T.P., *Widths of the Atomic K - N7 Levels*. 2001: Atomic Data and Nuclear Data Tables 77, 1-56.
101. Croft, S., et al. *On the Relationship Between the Natural Line Width and Lifetime of X-Ray Transitions*. in *56th Annual INMM Conference*. 2015. Indian Wells, CA.
102. Atkinson, K.E., *An introduction to numerical analysis*. 2008: John Wiley & Sons.
103. Sitko, R. and B. Zawisza, *Quantification in X-Ray Fluorescence Spectrometry*. 2012: INTECH Open Access Publisher.
104. Shizuma, T., et al., *Proposal for an advanced hybrid K-edge/XRF densitometry (HKED) using a monochromatic photon beam from laser Compton scattering.* Nuclear Instruments and Methods in Physics Research Section A: Accelerators, Spectrometers, Detectors and Associated Equipment, 2011. **654**(1): p. 597-603.
105. Phongikaroon, S., R.W. Bezzant, and M.F. Simpson, *Measurements and analysis of oxygen bubble distributions in LiCl–KCl molten salt.* Chemical Engineering Research and Design, 2013. **91**(3): p. 418-425.

VITA

GEORGE SPENCER MICKUM

MICKUM grew up in Houston, Texas. He attended public schools in Sugar Land, Texas, and received a B.S. in Nuclear Engineering from Texas A&M University, College Station, Texas in 2010 before coming to Georgia Institute of Technology to pursue both a M.S. degree and PhD in Nuclear Engineering. Mr. Mickum enjoys listening to audiobooks and language learning programs as they can be enjoyed on the move and pair well with an active lifestyle. When he is not working on his research, he enjoys going on adventures with his wife Megan and his dog, Lilly or sitting with his cat, Chloe in his lap and a book in his hands.